DISSERTATION/DOCTORAL THESIS

Titel der Dissertation/Title of the Doctoral Thesis

Tools for the Reinterpretation of BSM Searches with Simplified Models

verfasst von/submitted by

Dott. Mag. Federico Ambrogi

angestrebter akademischer Grad/in partial fulfilment of the requirements for the degree of
Doktor der Naturwissenschaften (Dr. rer. nat.)

Wien, im Dezember 2018 / Vienna, in December 2018

Studienkennzahl lt. Studienblatt / degree programme code as it appears on the student record sheet:	A 796 605 411
Dissertationsgebiet lt. Studienblatt / field of study as it appears on the student record sheet:	Physik
Betreut von / Supervisor:	Univ.-Prof. Dr. André H. Hoang Privatdoz. Dipl.-Ing. Dr. Wolfgang Waltenberger

Contents

List of Abbreviations

BR	**B**ranching **R**atio
BSM	**B**eyond **S**tandard **M**odel
CL	**C**onfidence **L**evel
CMB	**C**osmic **M**icrowave **B**ackground
CR	**C**osmic **R**ay
dSphs	**d**warf **Sph**eroidal Galaxie**s**
DM	**D**ark **M**atter
EM	**E**fficiency **M**ap
EWSB	**E**lectro**W**eak **S**ymmetry **B**reaking
GUT	**G**rand **U**nification **T**heory
Λ**CDM**	Λ(**L**ambda) **C**old **D**ark **M**atter
LHC	**L**arge **H**adron **C**ollider
LSP	**L**ightest **S**upersymmetric **P**article
MSSM	**M**inimal **S**upersymmetric **S**tandard **M**odel
NLSP	**N**ext-to **L**ightest **S**upersymmetric **P**article
PAD	**P**hysics **A**nalyses **D**atabase (from `MadAnalysis 5`)
PDF	**P**arton **D**istribution **F**unction
pMSSM	**p**henomenological **M**inimal **S**upersymmetric **S**tandard **M**odel
QCD	**Q**uantum **C**hromo **D**ynamics
RGE	**R**enormalization **G**roup **E**quations
SM	**S**tandard **M**odel
SMS	**S**implified **M**odel **S**pectra
SUSY	**S**upersymmetry
UL	**U**pper **L**imit
WIMP	**W**eakly **I**nteracting **M**assive **P**article

Abstract

The search for Beyond the Standard Model (BSM) physics is one of the main challenges for both experimentalists and theorists in particle physics. Astrophysical observations show that around 25% of the total energy content of the universe includes a form of particle dark matter (DM), that cannot be explained by the Standard Model (SM). Other shortcomings, like the hierarchy problem, suggest that the SM might not be the final theory of particle physics.

Supersymmetry (SUSY) is one of the most appealing extensions of the SM, able to solve both the DM and hierarchy problems. Despite the extensive experimental efforts, SUSY particles have not been discovered yet. The results of SUSY searches at the LHC are frequently interpreted with simplified model spectra (SMS). They aim at reducing the complicated parameter space of generic SUSY models to just a handful of new particles. Owing to their largely model independent assumptions, SMS allow to use the results for SUSY searches to constrain other BSM theories.

This thesis summarizes the contribution in the developments of three different tools designed to study the phenomenology of arbitrary BSM theories. First, the implementation of CMS-SUS-16-033 in the `MadAnalysis 5` recasting tool is described. This analysis represents the first "all hadronic" final state search at 13 TeV centre-of-mass energy implemented in this framework. Then, the version `v1.1` of the `SModelS` tool is introduced, with emphasis on the extension of the database of SMS results with homegrown recast results. As a concrete example it will be demonstrated how `SModelS` can efficiently constrain the parameter space of a specific SUSY model by taking full advantage of these new results. Finally, the new features of `v.3.0` of `MadDM`, such as the newly developed modules for DM indirect detection predictions and for the comparison with the latest experimental results, are discussed.

Kurzfassung

Die Suche nach Physik jenseits des Standardmodells (Beyond the Standard Model BSM) is eine der gröSSten gegenwärtigen Herausforderungen sowohl für Theoretiker als auch für Experimentatoren in der Teilchenphysik. Astrophysikalische Beobachtungen zeigen, dass etwa 25% des Energiegehalts des Universums aus einer unbekannten dunklen Materie besteht, die nicht innerhalb des Standardmodells der Teilchenphysik erklärt werden kann. Andere Probleme, wie etwas das Hierarchieproblem des Higgsbosons, legen ebenfalls nahe, dass das Standardmodell nicht der Weisheit letzter Schluss ist.

Die Supersymmetrie (SUSY) ist die wohl attraktivste Erweiterung des Standardmodells, liefert sie doch eine mögliche Erklärung sowohl für das Rätsel der dunklen Materie als auch für das Hierarchieproblem. Doch trotz eines umfangreichen Suchprogramms am LHC wurden bislang keine SUSY Teilchen gefunden. Das Ergebnis der SUSY Suchen wird häufig im Rahmen sogenannter vereinfachter Modelle (Simplified Model Spectra – SMS) publiziert. Diese Modelle reduzieren den komplizierten Parameterraum generischer SUSY Modelle, indem sie sich auf eine handvoll neuer Teilchen konzentrieren. Aufgrund ihrer groSSteils modellunabhängiger Annahmen erlauben es diese Modelle, die Resultate für SUSY Suchen auf andere BSM Theorien umzulegen.

Die vorliegende Arbeit umfasst die Beiträge zur Entwicklung dreier Softwarewerkzeuge, die alle darauf ausgelegt sind, die Phänomenologie verschiedener BSM Theorien zu disseminieren. Zuerst wird die Implementierung der CMS-SUS-16-033 Analyse im Softwarepaket `MadAnalysis 5` beschrieben. Diese Analyse beinhaltet die erste Suche nach rein hadronischen Endzuständen bei einer Schwerpunktsenergie von 13 TeV, die in `MadAnalysis 5` implementiert wurde. Danach stellt diese Arbeit die Version `1.1` des Softwarewerkzeugs `SModelS` vor, mit einer Betonung auf die Erweiterung der Datenbank der SMS Resultate mit selbst produzierten Resultaten. Als konkretes Beispiel wird gezeigt werden, wie `SModelS` unter Zuhilfenahme der neuen Resultate den Parameterraum von bestimmten SUSY Modellen effizient einschränken kann. Zuletzt werden die Neuerungen von `MadDM` Version `3.0` diskutiert, wie z.B. das neu entwickelte Modul, das Vorhersagen für die indirekte Detektion dunkler Materie mit den letzten experimentellen Ergebnissen vergleicht.

Chapter 1

Introduction

The announcement in 2012 of the discovery of the Higgs boson, or better of a scalar particle compatible with the Higgs Boson's properties as predicted by the Standard Model (SM) of particle physics, was probably the biggest achievement in the particle physics community in the recent years. After about 50 years from the first theoretical formulations, and after years of searches at various collider experiments, the last missing piece of the SM was finally found at The Large Hadron Collider (LHC). The SM in an incredibly successful theory, able to predict with extreme precision the properties of all known particles and their interactions. Nevertheless, there are still several open questions that cannot be answered without proper extensions of the SM to account for "new physics".

One of the most compelling evidences of the limitation of the SM is found in astrophysical measurements. The cosmological ΛCDM model seems to point to the existence of new particles that cannot be accommodated in the SM, adding up to around 25% of the total energy budget of our universe. Since this form of matter does not emit electromagnetic radiation, it is commonly called Dark Matter (DM). The gravitational potential due to DM is crucial for the formation and growth of the cosmic structures populating the universe, and gravity is so far the only established interaction between these new particles and ordinary matter.

Stringent limits on the cross section of elastic or inelastic scattering processes involving DM and SM particles could be set, for example, by several 'direct search' types of experiments, that look for scattering events of heavy nuclei with DM particles forming the galactic halo. Another possibility is to search for an increase of the cosmic rays flux, for example of gamma rays, due to the annihilation of DM into SM particles, which is expected to happen in regions of the universe with high DM density; such measurements are at the basis of 'indirect searches' type of experiments, able to set upper limit on the DM annihilation cross section. Moreover, by colliding particles at accelerators, we are given access to high energy regimes possibly allowing for the production of new particles, and hints of physics Beyond the Standard Model (BSM) might be observed in some deviations of particle properties as predicted by the SM.

So far no significant deviations from the SM predictions were found in the large amount of data collected by the various experiments, and upper limits on the cross sections of many processes involving DM or other BSM states could be obtained. By interpreting the results of the searches in the context of specific models, it is possible to point out the regions of the parameter space of the BSM theories which still survive the experimental constraints. This also suggests which regions should be investigated further by future searches, or eventually by building more sensitive and powerful experiments.

Ultimately, the goal of experimentalists is to provide the data necessary to verify or falsify possible new theories. Most of the BSM theories often possess a large number of free parameters, introducing challenges when trying to use the experimental results to constrain their parameter spaces. In fact, if such results are interpreted in the context of specific models assuming certain values of the parameters, it is problematic to re-use the results to constrain different models. A more practical way is instead to use model independent limits, and then derive the constraints on the parameters of some particular BSM theory. In this respect, a special class of models, called simplified models spectra (SMS), was developed and has become the standard way for the interpretation of searches for new physics, for example Supersymmetry at the LHC. These models depend only on a few basic quantities such as the mass spectra of the particles and their production cross sections. Results obtained within the SMS framework can thus be re-interpreted to constrain more general theories, once the theories are decomposed into their SMS.

This thesis work summarises the contributions to the developments of three tools for the re-interpretation of BSM searches, namely `MadAnalysis 5`, `SModelS` and `MadDM v.3.0`. These tools are designed to provide an interface between the worlds of experiment and theory. While the first two deal with results from the LHC experiments, the latter is designed to study the phenomenology of DM with astrophysical type of experiments.

Beside presenting the technical features of these tools, the other important aim of this work is to show concretely how simplified models can be efficiently used to constrain generic BSM theories. To this end, this thesis is structured as follows.

Chapter 2 is a short summary of our understanding of particle physics, listing the main properties of the SM as well as the most intriguing questions that this successful theory cannot answer. The theory of Supersymmetry (SUSY) and specifically the minimal supersymmetric Standard Model (MSSM), which will be the main BSM theory discussed throughout all this work, is presented as a potential extension of the SM.

Chapter 3 starts with a description of the Large Hadron Collider and the CMS experiment, used as an example of modern particle detector built for the discovery of new physics. The description of how searches for SUSY are performed is then outlined, together with the current status of the SUSY searches.

In Chapter 4 the `MadAnalysis 5` tool for the re-interpretation and recasting of BSM searches by the LHC experiments is described. Then follows the detailed description of the implementation and validation of the recent CMS-SUS-16-033 analysis, which searches for SUSY events in the 'all-hadronic' final state; the code was published in [1]. The theoretical framework of simplified model spectra is then introduced, as well as `SModelS`, a tool designed to make systematic use of LHC results interpreted with SMS. My personal contribution in this Chapter includes the implementation and validation of the aforementioned CMS analysis in `MadAnalysis 5`. Regarding the `SModelS` tool, my focus was the implementation and validation of a large part of the experimental results in the database from the LHC Run 1 (mainly at 8 TeV centre-of-mass energy, and some recent results at 13 TeV), under the form of upper limit and efficiency maps. The development of an infrastructure for the creation of homegrown results constitutes the basis for the extension of the database to include a plethora of new efficiency maps results. Most of the maps were made publicly available with the release of version 1.1 in [2], and in the recent version 1.2 documented in [3].

Chapter 5 describes how `SModelS` can be used to study a specific SUSY model, called phenomenological MSSM (pMSSM), by means of simplified models results. This exemplifies the power of the `SModelS` tool, highlighting the possibility to extend its database of experimental results to better constrain specific theories. This work was possible thanks to the inclusion of the complete set of 8 TeV results in the database available from the LHC experiments. While part of the work presented can be found in [4], the majority of the results shown is still unpublished, such as: the classification of the most important simplified models, divided for each analysis in the database; the impact of the simplified model results produced by the `FastLim` Collaboration; the study of the effects of including quarks and gluons in `SModelS` generic 'jet' definition; the production, implementation, and test of the impact of gluino-squark simplified models on the pMSSM (which constitutes an original publication in preparation).

In Chapter 6 an important assumption at the basis of the philosophy of the `SModelS` software is analysed. `SModelS` is able to extract results for arbitrary mass combinations of BSM states by interpolating between the fixed set of masses available. The concept of interpolation is here discussed, focussing on quantifying the related uncertainty in the case of specific analyses and simplified models. This study is a novelty for the `SModelS` tool, as the effects of interpolation could not be investigated prior to the extension of the database with homegrown efficiency maps.

The final Chapter 7 turns to astrophysics, by introducing the latest `MadDM v.3.0` [5]. This extends the abilities of the previous versions 1.0 and 2.0, namely the calculation of the DM relic density and the rates for direct detection experiments, to the calculation of theory predictions for DM annihilations. The prediction for gamma rays fluxes are then compared with the latest upper limits provided by the Fermi-LAT experiment. The contribution to this project mainly concerns technical aspects of the development of the code: the inclusion of annihilation spectra of DM candidates into SM channels in pre-computed tables, and their validations by comparison with the spectra simulated with Monte Carlo generators; the update of recent experimental limits for direct and indirect detection; the extension of the Fermi-LAT limits to new SM channels; the module for the propagation of cosmic rays, such as neutrinos accounting for the flavour oscillation, and positrons from existing tables; and the development of the general structure of the outputs, both in single run and scan mode.

The following published documents include part of the work presented in this thesis:

- F. Ambrogi and J. Sonneveld - *MadAnalysis 5 recast of CMS-SUS-16-033* (`https://inspirehep.net/record/1685439/`);
- F. Ambrogi, S. Kraml, S. Kulkarni, U. Laa, A. Lessa, V. Magerl, J. Sonneveld, M. Traub, and W. Waltenberger - *SModelS v1.1 user manual: Improving simplified model constraints with efficiency maps*, **Comput. Phys. Commun. 227 (2018) 7298** (`https://arxiv.org/abs/1701.06586`);
- F. Ambrogi, S. Kraml, S. Kulkarni, U. Laa, A. Lessa, and W. Waltenberger - *On the coverage of the pMSSM by simplified model results*, **Eur. Phys. J. C78 (2018), no. 3 215** (`https://arxiv.org/abs/1707.09036`);
- F. Ambrogi, J. Dutta, J. Heisig, S. Kraml, S. Kulkarni, U. Laa, A. Lessa, P. Neuhuber, H. Reyes-González, W. Waltenberger and M. Wolf - *SModelS v1.2: long-lived particles, combination of signal regions, and other novelties* (`https://arxiv.org/abs/1811.10624`);
- F. Ambrogi, C. Arina, M. Backovic, J. Heisig, F. Maltoni, L. Mantani, O. Mattelaer, and G. Mohlabeng - *MadDM v.3.0: a Comprehensive Tool for Dark Matter Studies* (`https://arxiv.org/abs/1804.00044`).

Chapter 2

The Standard Model of Particle Physics and Beyond

Contents

Everything that we know about particles is condensed in a very elegant theory called the Standard Model (SM) of particle physics. This theory can successfully explain almost the entire rich phenomenology that we observe at the sub-atomic level, and most notably predict the values of observables that can be experimentally measured. It is the summary of the work of almost a century of investigation, both from the theoretical and the experimental worlds. The two worlds were indeed complementarily pushing each other, from one side to develop new theories to interpret the new puzzling experimental results, and from the other to build more powerful and sensitive experiments to verify fascinating and intriguing conjectures.

But the SM alone is not enough to explain the entire microscopical world. In particular there are several experimental evidences that suggest we are still missing one or more pieces to complete the puzzle. This Chapter provides some theoretical and experimental motivations for Beyond the Standard Model (BSM) physics. I will first give in Section 2.1 a very concise summary of our present knowledge of the SM of particle physics, listing its main building blocks. Then I will introduce some of the most important open questions that the SM is not able to answer. In Section 2.2 I will introduce the theory of Supersymmetry (SUSY), an extension of the SM that is able to solve some of the most striking problems of modern particle physics.

2.1 The Standard Model

The SM has its basis on the relativistic formulation of quantum mechanics, called relativistic quantum field theory (QFT). This mathematical framework links together the two big families of particles that we so far know, represented by the families of bosons (with integer spin) and fermions (with half-integer spin). In fact, SM fermions constitute what we call 'matter', while bosons are responsible for mediating the interaction between particles. In the SM, only three out of the four known fundamental interactions are described: the electromagnetic, the weak and the strong force. The gravitational interaction cannot be still successfully included in the SM, and quantum gravity is currently a very active field of research. Nevertheless, gravity should play a role in particle physics only at the very beginning of the history of the universe, i.e. at the Planck scale, with no substantial impact on most of the particle physics experiments.

The forces between the particles are mediated by bosons: the photons (γ) are responsible for the mediation of the electromagnetic interaction, the gauge bosons W^-, W^+ and Z mediate the weak interaction, and the gluons (g) the strong interaction. Finally, the Higgs boson H plays a special role, since it is the only *spin-0* or scalar particle, and it is responsible for giving mass to all the massive fermionic particles through the Yukawa coupling.

Surprisingly, only a few particles of the SM form what we consider regular matter that is the fundamental constituent of everything stable in the universe: neutrons and protons are made of up and down quarks (uud and udd respectively), that in atoms are surrounded by clouds of electrons. Due to the color confinement of quantum chromodynamics, quarks cannot exist in isolated form, and they combine together to form hadrons: mesons, formed by two quarks, and baryons, made of three quarks. Differently from electrons, muon and tau leptons are unstable, and they decay; in particular, the mass of the tau lepton allows it to decay to quarks through an off-shell W boson, i.e. via charged weak interaction. For the latest observed values of the masses of particles together with a detailed summary of the physics of the SM and beyond, see e.g. the latest Review of Particle Physics of the Particle Data Group at [6].

2.1.1 QFT Formulation of the SM

Both the matter content and the allowed interactions of the SM are embedded in its symmetry groups, based on a local $SU(3)_C \times SU(2)_L \times U(1)_Y$ gauge symmetry and a space-time symmetry described by the Poincaré group. All the fermions and the bosons with their corresponding gauge quantum numbers are listed in Tab. 2.1, where only one of the three families of quarks/leptons is listed.

The $SU(3)_C$ symmetry is governed by the laws of quantum chromodynamics (QCD), the theory that describes the strong interactions between colour-charged fermions, i.e. the colour-triplets quarks, and the eight massless *gluons*. The three leptonic families are colour chargeless and do not interact through the strong interaction.

The electroweak interaction is described by the group $SU(2)_L \times U(1)_Y$, where the subscript "L" refers only to particle doublets with left chirality. The right-handed singlets do not interact via weak interaction. The definition of the weak hypercharge is such that the electric charge Q can be calculated as $Q = T_3 + Y$, with T_3 being the third component of the weak isospin. The weak interaction is mediated by massive vector bosons, the $W^{\pm}(\approx 80,3$ GeV) and the Z^0 ($\approx 91,2$ GeV).

The full SM Lagangian that described the all the possible interactions between all the fermionic and bosonic fields is quite complicated. For illustration purpose, I will take as an example the Lagrangian describing the electroweak interaction $\mathcal{L}_{EW}$ for a fermionic field ψ, that can be written

		Field	**SU(3)$_C$,SU(2)$_L$,U(1)$_Y$**
Fermions	**Leptons**	$\mathrm{l} = (\nu_e\ e_L)$	$(\bar{\mathbf{1}},\ \mathbf{1},\ \text{-}\frac{1}{2}\ )$
		$e_R^\dagger$	$(\bar{\mathbf{1}},\ \mathbf{1},\ 1\ )$
	Quarks	$q_L = (u_L d_L)$	$(\mathbf{3},\ \mathbf{2},\text{-}\frac{1}{6})$
		$u_R^\dagger$	$(\bar{\mathbf{3}},\ \mathbf{1},\ \text{-}\frac{2}{3})$
		$d_R^\dagger$	$(\bar{\mathbf{3}},\ \mathbf{1},\ \frac{2}{3})$
Bosons	Gluon	g	$(\mathbf{8},\ \mathbf{1},\ 0\ )$
	W	$(W^+W^0W^-)$	$(\mathbf{1},\ \mathbf{3},\ 0\ )$
	B	B^0	$(\ \mathbf{1}\ ,\ \mathbf{1},\ 0\ )$
	Higgs	$\Phi = (\phi^+\phi^0)$	$(\mathbf{1},\ \mathbf{2},\ \frac{1}{2}\ )$

TABLE 2.1: Bosons and fermions of the SM in terms of Weyl spinors. The hypercharge is defined so that the electric charge is calculated as Q = T$_3$ + Y , with T$_3$ being the third component of the weak isospin. Note that only one of the three families of leptons and quarks is listed.

as:

$$\mathcal{L}_{EW} = -\frac{1}{4}\vec{W}^{\mu\nu}\vec{W}_{\mu\nu} - \frac{1}{4}B^{\mu\nu}B_{\mu\nu} + i\psi_L\gamma_\mu D_\mu\psi_L + i\psi_R\gamma_\mu D_\mu\psi_R\ , \tag{2.1}$$

where the B_μ and the $\vec{W}^{\mu\nu}$ are the $U(1)_Y$ and $SU(2)_L$ gauge fields respectively, and the covariant derivative

$$D_\mu = \left(\partial_\mu - ig\frac{\tau_i W_{\mu_i}}{2} - ig'YB_\mu\right) \tag{2.2}$$

is introduced to preserve the invariance of the Lagrangian under gauge transformations; g' and g are the coupling constants for $U(1)_Y$ and $SU(2)_Y$. Note that τ_i for $i = 1, 2, 3$ represent the Pauli matrices, that are identically zero the case of right-handed fermions. This implies that there are no interactions between right handed fields mediated by charged currents.

A more general Lagrangian can be written by extending the $\mathcal{L}_{EW}$ described above to include the strong interaction, represented by the $SU(3)_C$ group, and the Yukawa interaction with the Higgs field. The covariant derivative is extended to include the strong interaction as

$$D_\mu = \left(\partial_\mu - ig\frac{\tau_i W_{\mu_i}}{2} - ig'YB_\mu - i\frac{g_s}{2}\lambda_\alpha G^\alpha_\mu\right) \tag{2.3}$$

where g_s is the strong coupling constant, the λ_α are the Gell-Man matrices and G^α_μ are the gluon fields.

In a short form, the SM Lagrangian can be decomposed into different components as

$$\mathcal{L}_{SM} = \mathcal{L}_{gauge} + \mathcal{L}_{fermion} + \mathcal{L}_{Higgs} + \mathcal{L}_{Yukawa} + V_{Higgs}. \tag{2.4}$$

The last two terms in Eq. 2.4 are related to the Higgs potential $V_{Higgs} \equiv V(\Phi)$ given by

$$V(\Phi) = \mu^2\Phi^\dagger\Phi + \lambda(\Phi^\dagger\Phi)^2\ , \tag{2.5}$$

and the Yukawa interaction that couples the Higgs field to the fermions. The Higgs potential $V(\Phi)$ assumes the shape of the 'Mexican hat' for $\mu^2{<}0$ and $\lambda{>}0$, with a local maximum at $\Phi{=}0$ and degenerate global minima for

$$\Phi^\dagger\Phi = -\frac{\mu}{2\lambda} = v^2, \tag{2.6}$$

where v is the vacuum expectation value of the Higgs field, related to the Fermi constant G_F by:

$$v = (\sqrt{2}G_F)^{-\frac{1}{2}} \approx 246\ [GeV]\ . \tag{2.7}$$

The shape of the potential is responsible for the spontaneous electroweak symmetry breaking (EWSB) or Higgs mechanism (developed thanks to the studies of Higgs[7], Englert and Brout[8] and Guralnik, Hagen and Kibble[9]) a process that gives masses to the W^-, W^+ and Z^0 bosons.

The scalar Higgs field itself assumes a mass of $m_H = \sqrt{\mu^2}$, while the photon remains massless. For a complete treatment of the Higgs mechanism see e.g. [10].

With the announcement of the discovery of the Higgs boson in 2012 [11, 12], the particle content of the SM is complete. The SM includes 19 free parameters:

- fermion masses: six quarks, three charged leptons;
- four parameters for the Cabibbo-Kobaiashi-Maskawa mixing matrix (allowing flavour changing neutral currents);
- three coupling constants (g_s, g and g' for the $\mathrm{SU}(3)_C$,$\mathrm{SU}(2)_L$,$\mathrm{U}(1)_Y$ respectively);
- μ^2 and λ (the parameters of the Higgs potential);
- the QCD vacuum angle θ (allowing CP violation in the strong sector).

2.1.2 Is the SM the Final Theory of Particle Physics?

Despite the huge number of experimental evidences of the validity of the SM, there are a series of anomalies and measurements that the SM fails to explain without introducing extra free parameters, new interactions or new particles. In the following I provide a list of what are commonly called the 'shortcomings' of the SM.

A Dark Universe: Dark Matter There is compelling evidence that a form of electrical and color charge-neutral form of matter constitutes more than 25% (from the latest Planck measurements in [13]) of the matter content of the universe, if the ΛCDM model for the thermal evolution is assumed. Without this form of matter, called 'dark' since it does not emit electromagnetic radiation, the evolution of the universe, the structure (cluster of galaxies and galaxies) formation and the observed matter distribution cannot be explained. Very little is known about dark matter (DM); all the information available comes from astrophysical observations and cosmological assumptions (see the introductory part of Chapter 7 for more details). I conclude here by reminding that, strictly from a particle physics perspective, there are no convincing indications of the existence of such elusive particles, except for the claim from the DAMA experiment[14] of detecting a phenomenon called DM annual modulation, linked to the motion of the Earth within the DM galactic halo. While the excess in the event counts is still present, other similar experiments failed to reproduce any signal compatible with the modulation.
At present, all our knowledge coincides with observation of gravitational anomalies and phenomena that cannot be explained by the SM physics and by Einstein's general relativity.

Grand Unification The electroweak theory described by the $SU(2)_L \times U(1)_Y$ symmetry group is an example of a successful unification at higher energies of two theories that behave very differently after the process of symmetry breaking, i.e. below the EWSB scale. The concept of a possible unification of distinct forces, indeed, was born with Maxwell who at the time unified the electric and magnetic forces in his theory of electrodynamics. The very appealing idea of extending the unification of forces to include also the strong interaction has been pursued for several decades by the theory community. This was particularly motivated by the observation that by running the coupling constants (electromagnetic, weak and strong) through the Renormalisation Group Equations (RGE), they all seem to converge to a common value at a scale of $O(10^{16})$ GeV, called Grand Unification Theory (GUT) scale. The exact unification however cannot be realised within the SM. A common way to allow for such unification are to extend the gauge groups of the SM to more large symmetries like *SU(5)* or *SO(10)* (see also Section 2.2.2.2 for the unification of forces in Supersymmetric models).

Neutrino Masses and Oscillation Neutrinos come in three different flavours, identified with the flavour of the charged leptons that are produced via weak-interaction. However it was found in several experiments that during their free propagation, neutrinos can change flavour i.e. the flavour eigenstates are not constant during propagation. The probability of changing the flavour, a process known as *flavour oscillation*, depends primarily on the length of the path considered, on the neutrino energy and on the squared difference of the mass eigenstates. More details will be given in Section 7.3.1.4, where the implementation of neutrinos oscillation in `MadDM v.3.0` is described. For now it suffices to remember that all the experimental observations regarding neutrino oscillations are compatible with the assumptions that at least two neutrino mass eigenstates have non-zero value (see e.g. [15] for a review). The exact mechanism that produces the neutrino mass is still object of research and, in some sense, requires an extension of the SM for which neutrinos are massless. Among the theories introducing mass terms for neutrinos, we find e.g. the 'seesaw' mechanism, that postulate that there exist companions of the SM neutrinos with very large mass, possibly around the GUT scale, which can explain the very small mass of $O(eV)$ of the SM neutrinos [16]. This argument is sometimes used as a motivation for GUT models.

The Hierarchy Problem and Naturalness One question which is, in some sense, more aesthetic than driven by unexplainable phenomena is the extremely large difference between the energy scale at which the EWSB takes place, and the Planck scale ($M_{Plank} = 1/\sqrt{8\pi G_{Newton}} \sim 10^{18}$ GeV). If we consider the mass of the heaviest know fundamental particle, the top quark (around 173 GeV[6]), no other SM particle is expected to exist before the $O(10^{16})$ GeV, which is believed to be the scale where new physics should appear, e.g. through the unification of forces and large quantum gravity effects. The very large gap in the energy scales between $O(10^2)$ and $O(10^{16})$ GeV is considered somehow 'unnatural', and ultimately the question is why the weak scale and the Planck scale are so different.

The Higgs boson couples to each massive SM fermion f through the Yukawa coupling λ_f, with an interaction of the form $\mathcal{L}_Y = -\lambda_f \bar{\psi} H \psi$ where ψ and H are the fermionic (Dirac) and Higgs fields respectively, and the Yukawa coupling is proportional to the fermion mass. The mass of the Higgs boson can be expressed as:

$$m_H = m_H^0 + \Delta m_H. \tag{2.8}$$

The equation above shows that the bare Higgs mass m_H^0 receives quantum corrections; for example the 1-loop radiative corrections due to the couplings to fermions is given by:

$$\Delta m_H^2 = -\frac{|\lambda_f|^2}{8\pi^2}\Lambda_{UV}^2 + ... \tag{2.9}$$

where the scale Λ_{UV} represents the scale at which the SM ceases to be valid and new physics is expected, and regulates the calculation of the corrections, that otherwise will be quadratically divergent. This is often taken to be the Planck scale, or the GUT scale where new interactions and mediators are predicted, leading to corrections that are indeed of $O(\Lambda_{UV})$. Note that the largest contribution from SM fermions come from the top quark, due to its large Yukawa coupling ($y_t \approx 0.94$). Since the physical Higgs mass is the sum of the bare mass and the various loop contributions, the latter must cancel out up to incredible precision in order to obtain the observed value of the Higgs mass $\approx O(100)$ GeV. This can be achieved only by a fine tuning of the parameters of the new physics appearing at the scale Λ_{UV}, that must cancel the corrections deriving from SM particles.

A possible solution of the fine tuning problem would be the presence of BSM particles at $O(1)$ TeV scale, which then would cancel out the contribution from SM particles without excessive tuning of the parameters. Such particles are predicted by theories like Supersymmetry, which introduce a fundamental symmetry between bosonic and fermionic particles that naturally solves the problem. The main characteristics of Supersymmetry, which will be the main BSM theory discussed in this thesis, will be now introduced, highlighting how this extension of the SM can solve the principal shortcomings that have been discussed.

2.2 Going Beyond the Standard Model: Supersymmetry

We have seen that the SM is incomplete, for example it does not accommodate any suitable DM candidate compatible with the astrophysical observations, and it has some unpleasant features from a theoretical point of view related to the unification of forces at higher scales and to the hierarchy problem. An extension of the SM, based on an additional symmetry of space-time that extends the Poincaré group, is able to elegantly solve the three problems above as well as provide a new rich particle phenomenology that can be potentially observed at various types of experiments, is called Supersymmetry (SUSY).

2.2.1 Basic Principles

The theory of Supersymmetry is based on the extension of the Poincaré group; the Supersymmetric algebra can be expressed in terms of Weyl spinors Q_i with the anti-commutating relation:

$$\{Q_\alpha, \bar{Q}_{\dot{\beta}}\} = 2(\sigma^\mu)_{\alpha\dot{\beta}} P_\mu \tag{2.10}$$

where σ^μ are the Pauli matrices and the $P_\mu = -i\partial_\mu$ are the generators of the translations; the indices with dots refer to the components of the complex conjugated spinors, while all the other anti-commutating relations between the Q and the P vanish.

These anticommuting relations transform bosonic and fermionic states into each other, i.e.

$$\begin{aligned} Q|Boson >&= |Fermion > \\ Q|Fermion >&= |Boson > . \end{aligned} \tag{2.11}$$

This has the direct consequence that in SUSY the number of particles is at least double the particles in the SM: we call Minimal Supersymmetric Standard Model (MSSM)[17, 18] a SUSY theory that adds the minimum number of new particles to the SM.

Gauge Superfield	**spin 1**	**spin $\frac{1}{2}$**	$\mathbf{SU(3)}_C$,$\mathbf{SU(2)}_L$,$\mathbf{U(1)}_Y$
Gluon, gluino	g	$\tilde{g}$	($\mathbf{8}$,$\mathbf{1}$,0)
W, Wino	(W^+, W^0, W^-)	$(\tilde{W}^+, \tilde{W}^0, \tilde{W}^-)$	($\mathbf{1}$,$\mathbf{3}$,0)
B, Bino	B^0	$\tilde{B}^0$	($\mathbf{1}$,$\mathbf{1}$,0)

Table 2.2: Gauge superfields in the MSSM.

In SUSY the notion of superfield $\mathcal{S}(x^\mu, \theta_a)$ is introduced, describing each field as constituted by a fermionic and bosonic component; the coordinates x^μ represent the space-time coordinates, while the $\theta_a, a = 1, ..., 4$ are Grassmann anticommuting coordinates.
The left and right handed components of SM fermions and their Supersymmetric partners are contained in "chiral superfields". Chiral superfields can describe spin $1/2$ as well as spin 0 particles, and this include SM leptons, quarks and the Higgs boson. Analogous to this chiral superfields representation is to consider the spin up and down states of fermions (see e.g. [19]).
In the same way, "gauge superfields" can be introduced, describing the SM gauge bosons (spin 1) and their Supersymmetric fermionic partners. With the notion of superfields, superpotentials are then introduced, which describe the interaction between the various chiral superfields. The description of the SUSY algebra and the derivation of the SUSY Lagrangian can be found e.g. in [20].

Contrary to what its name suggests, even Supersymmetry is not a perfect symmetry: so far, no particles with the same mass of any SM particle but with half-integer spin difference were found. This means that SUSY must be broken, i.e. there must be a SUSY breaking mechanism so that the superpartners acquire a mass that is different from the SM value. Unfortunately the theory does not predict the scale of the masses of the SUSY particles.

SUSY, despite being motivated primarily by abstract principles, has a solid theoretical appeal, and the modern formulation of the theory was developed by many theorists during the last 40 years. It is also very interesting from an experimental point of view, since the existence of SUSY partners provide a rich phenomenology to be studied and searched for with many types of experiments; in fact, all the searches for DM can be interpreted in the context of SUSY, since it can provide a natural DM candidate, as it will be explained in the next Section. In this work I wish to focus primarily on the phenomenological aspects of SUSY, in particular how it could be detected at particle colliders. In the following I will describe the particle content of the MSSM, and briefly demonstrate how SUSY can successfully solve some of the problems of the SM introduced in the previous sections. The next Chapter 3 will describe in some detail the phenomenology of SUSY at colliders, and how indeed the results of the searches for SUSY offer the opportunity to investigate other generic BSM theories, thanks to the use of simplified models.

2.2.2 The Minimal Supersymmetric Standard Model

The most general realisation of Supersymmetry that is constructed as an extension of the SM is called Minimal Supersymmetric Standard Model, or MSSM. The content of the MSSM in terms of chiral and gauge superfield is shown in Tables 2.2 and 2.3.

Given the extremely large dimensionality of its parameter space, the interpretation of searches in the context of such general model is an extremely hard achievement. This lead phenomenologists to consider special subsets of such a generic model, by requiring that some of its parameters are constrained by scaling relations or other assumption inspired for example by Grand Unification theories.

	Chiral Superfield	**spin $\frac{1}{2}$**	**spin 0**	**$\mathbf{SU(3)}_C$,$\mathbf{SU(2)}_L$,$\mathbf{U(1)}_Y$**
(S)quarks	Q	$(u_L\ d_L)$	$(\tilde{u}_L\ \tilde{d}_L)$	$(\mathbf{3},\mathbf{2},\frac{1}{6})$
	$\bar{U}$	$u_R^\dagger$	$\tilde{u}_R^*$	$(\bar{\mathbf{3}}, \mathbf{1}, -\frac{2}{3})$
	$\bar{D}$	$u_L\ d_L$	$(\tilde{u}_L\ \tilde{d}_L)$	$(\bar{\mathbf{3}}, \mathbf{2},\frac{1}{6})$
(S)leptons	L	$(\nu_L\ e_L)$	$(\tilde{\nu}_L\ \tilde{e}_L)$	$(\mathbf{1}, \mathbf{2},-\frac{1}{2})$
	$\bar{E}$	$e_R^\dagger$	$\tilde{e}_R^*$	$(\mathbf{1},\mathbf{1},1)$
Higgs(inos)	H_U	$(H_U^+ H_U^0)$	$(\tilde{H}_U^+ \tilde{H}_U^0)$	$(\mathbf{1}, \mathbf{2},-\frac{1}{2})$
	H_D	$(H_D^0 H_D^-)$	$(\tilde{H}_D^0 \tilde{H}_D^-)$	$(\mathbf{1},\mathbf{1},-\frac{1}{2})$

TABLE 2.3: Chiral superfields in the MSSM (left-handed superfields).

2.2.2.1 Solving the Hierarchy Problem

As seen in Eq. 2.9, the fermions couple to the Higgs and give corrections to the 1-loop calculation of its bare mass. This term is mostly sensitive to massive particles, and the top quark loop leads the various correction terms, with $\lambda_f \sim 0.94$, due to its very large mass of $m_t \approx 173$ GeV. Let us now consider two spin-0 complex scalar particles S coupling to the Higgs as $\lambda_s = |\lambda_f|^2$, and contributing to loop corrections as:

$$\Delta m_H^2 = 2 \times \frac{\lambda_s}{16\pi^2}\Lambda_{UV}^2 + \dots \,. \tag{2.12}$$

This term looks exactly like Eq. 2.9 but with positive sign, meaning that by introducing a bosonic (scalar) partner to any SM fermion, the sum of the contributions of the loop corrections will vanish, since all the particles and their partners will contribute with diagrams such as the ones sketched in Fig. 2.1. This also means that SUSY naturally solves the hierarchy problem thanks to the additional content of scalar partners to fermions, and in particular with the scalar partner of the SM top quarks (i.e. the stops). Note that the cancellations induced by these new particles hold at every order in perturbation theory for unbroken SUSY. However we know that SUSY must be broken; for SUSY to solve the hierarchy problem with a reasonable level of fine tuning of the parameters, the mass of the top squark $m_{\tilde{t}}$ should be of order $O(1)$ TeV.

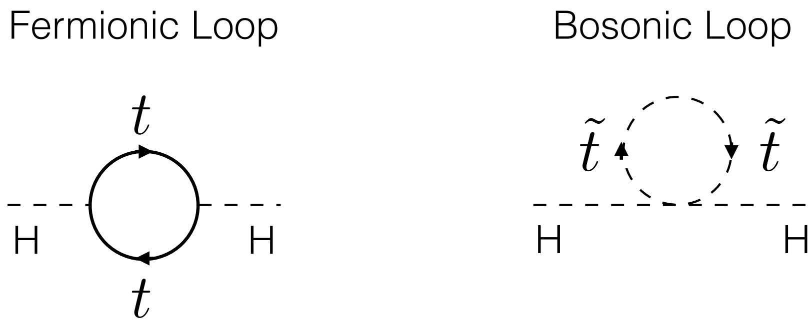

FIGURE 2.1: Loops correction to the Higgs mass by a fermionic (left) and bosonic (right) partner. In particular, the top quark and its scalar supersymmetric companion are considered since they.

2.2.2.2 GUT Unification

Finally, SUSY has the very pleasant feature of allowing for the unification of fundamental forces at higher scale (see e.g. [21]). This is shown in Fig. 2.2 that shows how for a specific realisation of the MSSM, the coupling constants unify at O(10^{16}). Here the coupling constants are expressed in units of $\alpha_i = g_1^2/4\pi$.

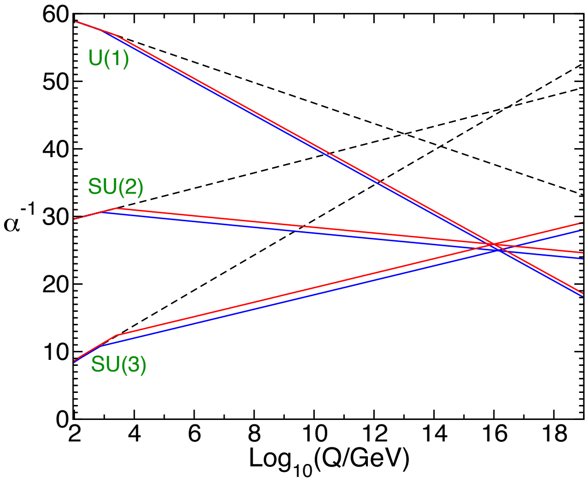

FIGURE 2.2: Evolution of the SM gauge coupling constants through the RGE. The dashed lines represent the evolution in the case of the SM, while the coloured lines show the case of the MSSM, where the different colours correspond to models with a common threshold of the SUSY masses of 500 GeV (blue) and 1.5 TeV (red). See Ref. [20] for more details.

2.2.2.3 R-Parity Symmetry and DM Candidate

An additional discrete symmetry that can be imposed on the MSSM, that enforces the conservation of the baryon and lepton numbers B and L, is called *R-Parity*. The B and L symmetries in the SM are ‘accidental’, but have the effect to prevent protons decay, so that protons have a lifetime greater than 10^{33} years (see e.g. the results from the SuperKamiokande experiment [22]). In the MSSM however these symmetries are absent, and B and L might be violated by extra terms present in the SUSY superpotential. The R-Parity symmetry is able to fix this problem. For each particle, the quantum number R is defined by:

$$R = (-1)^{2s+3B+L} \tag{2.13}$$

where s is the spin of the particle. The two possible eigenvalues are $R = 1$ for any SM particle, and $R = -1$ for SUSY particles. Due to the discrete nature of this symmetry, for a set of particles the total R is calculated as the product of the R-Parity value of each particle in the set. The requirement that the total R is conserved by any particle process considered leads to three important phenomenological consequences:

1. an even number of SUSY particles must be produced in processes with SM initial particles;
2. each SUSY particle decays to an odd number of SUSY particles;
3. the lightest SUSY particle is stable.

From point (1) it follows immediately that at colliders, through any e.g. $e^-e^+/p\bar{p}/pp$ collisions only pair productions of SUSY particles are expected (or even 4-SUSY particles production, though

kinematically disfavoured); the same holds for the decay of any resonant SM particle, like e.g. the Z bosons, or the Higgs/Heavy Higgses.
From (2) and (3), the decay of SUSY particles to other SUSY states ends with the lightest SUSY particle (LSP) that has to be stable. This makes the MSSM particularly interesting since it readily provides possible DM candidates. Models where the lightest of the neutralino species $\tilde{\chi}_1^0$ or the gravitino $\tilde{G}$ are the LSP are the most searched for at the LHC; though there also exist SUSY models where right-handed sneutrinos $\tilde{\nu}_R$ constitute a viable DM particle.

2.2.3 Other Supersymmetric Models

cMSSM and mSUGRA Minimal Supergravity (mSUGRA) and the Constrained MSSM (cMSSM) are subspaces of the MSSM parameter space; they are based on the assumption that there exists a hidden sector that can communicate with the SM only by gravity, and where SUSY is spontaneously broken (see e.g. [23]). The models have 4+1 free parameters at the GUT scale: the universal mass m_0 common to all the scalar particles, the ratio of the Higgs vacuum expectation values $tan\beta$, the sign of the Higgsino mass parameter $sign(\mu)$ that can be positive or negative defined, the gaugino mass parameters $M_{1/2}$, and the universal trilinear coupling A_0. From the GUT scale, the masses of the SUSY particles at low energies can be calculated by running down the renormalisation group equations. Thanks to the small parameter space and its predictive power, it has been largely studied both by theorists and experimentalists. Its parameter space is now tightly constrained due to the discovery of the Higgs boson mass as wells as constraints from collider experiments, precision measurements in flavour physics, and astrophysical observations (see e.g. [24, 25]). Note that, while nowadays the cMSSM and the mSUGRA models are considered equivalent, in the early literature the mSUGRA model required that also the gravitino parameter is unified (with $m_{\frac{3}{2}} = m_0$, see [6] for more details).

pMSSM The phenomenological MSSM[26] (pMSSM) will be the object of an extensive study in Chapter 5, where a detailed characterisation of the model will be presented. Very briefly, experimental measures that constrain additional sources of CP violation and flavour changing neutral currents, plus theoretically appealing motivation such as the first and second generation universality (for sleptons or squarks), reduce the total free parameters of the MSSM to *O(10)* parameters.

nSUSY Another extensively studied SUSY class of models is represented by 'natural' SUSY (see e.g.[27]). In this case, there are not fixed relations between any of the free parameters in the MSSM, but a requirement regarding the level of fine-tuning, in attempt to solve the hierarchy problem. A model is considered natural when the level of fine-tuning required is below a certain threshold (for example, see the Barbieri-Giudice measure [28]). However how much fine tuning should be considered acceptable is an arbitrary definition. It follows that also natural models include a large parameter space, depending also on the specific details of the model considered. In general, a low level of fine-tuning is obtained when the LSP and NLSP are Higgsino-like, and the lightest stops, which gives the largest contribution to the radiative correction to the Higgs boson mass, are not too heavy, roughly around the $O(TeV)$ scale. Also gluinos should not be too massive, since they contribute to the corrections at loop level to the stop mass. The masses of the other sparticles are less relevant. While current simplified models results at 13 TeV constrain the stop mass to be roughly above the TeV scale ([29],[30] and Section 3.2.4), in the context of full models this limit is much weaker, due to more complex decay patterns.

Chapter 3

Phenomenology of Supersymmetry at the LHC

Contents

As introduced in the previous Chapter, there are some questions that the SM cannot answer, and many theoretical considerations suggest that some new physics might be hiding at the TeV scale. If the theory of Supersymmetry is true, already within the MSSM, which is the most economical Supersymmetric extension of the SM in terms of new particles, a rich phenomenology can be tested experimentally.

This Chapter summarises the main distinct signatures of SUSY candidates at the Large Hadron Collider (LHC), the most powerful machine for high energy particle physics ever built. First, the main characteristics of the LHC are described (Section 3.1), followed by the description of the Compact Muon Solenoid (CMS) experiment, one of the two multi-purpose detectors able to look for new physics at O(TeV) mass scale.
Then the main concepts at the basis of BSM searches are introduced, with a focus on searches for Supersymmetry (Section 3.2). On the one hand, owing to the complex phenomenology offered by SUSY and its vast parameter space, the results for the searches are hard to interpret in the context of the full MSSM. On the other hand, many searches target final states which are common to many different BSM theories, and it is extremely useful to re-interpret the results of such searches to constrain several new models. I will then introduce simplified model spectra (SMS) (Section 3.2.2), which represent the standard way of the LHC collaborations to present the results of their searches for SUSY. Finally, the status of the current constraints on the most common simplified models will be summarised in Section 3.2.4.

3.1 The LHC and the Hunt for New Physics

The Large Hadron Collider (LHC) at the European Organisation for Nuclear Research (CERN) is the most powerful 'discovery machine' ever built, able to reach an unprecedented 7-8 TeV (LHC

Run 1, *2010-2012*) and 13 TeV (*2015-ongoing*) centre-of-mass energy, or $\sqrt{s}$, with proton-proton collisions. It is built at the border of France and Switzerland between the Jura Mountains and Lake Geneva; it uses the 26.7 km tunnel constructed for the Large Electron-Positron collider (LEP), at depths ranging from 50 to 150 m below the ground level.

The technical design foresees a future run at $\sqrt{s}$=14 TeV in the last years of operation, before an upgrade of the main components of the collider. These high energy collisions allow to investigate an unexplored energy regime in particle physics at colliders, and in particular they give access to the on-shell production of hypothetical new particles with masses at the $O(TeV)$ scale. Beside the hunt for new physics, at the various LHC experiments the properties of the SM can be probed with very high accuracy. Indeed, deviations from the SM predictions os some observable found in precision measurements of rare processes might suggest the presence of new physics, that give additional contributions to the known SM processes. Finally, thanks to the heavy ions program, for which heavy lead ions are circulated inside the beam pipe, the properties of QCD can be studied at its extreme in the form of a novel state of matter called quark-gluon plasma, which is supposed to constitute the primordial universe at the very beginning of its history ($O(10^{-6})$ s after the Big-Bang, with a temperature around 175 MeV).

So far, the biggest achievement of the LHC is the discovery of a particle compatible with the properties of the SM Higgs boson, announced in 2012 ([11, 12]), which had been hunted for more than 50 years and was one of the most compelling arguments for the construction of the machine. In the next Sections the main characteristics of the LHC and of the CMS particle detector, designed for new physics searches, will be described.

3.1.1 The Journey of the Protons

The LHC is a collider where two separate protons or heavy ions beams, circulating in opposite directions inside the tunnel, are made to collide in four specific interaction points, at the centre of the detectors of the experiments. The LHC is the very last accelerator in the journey of the particles, which is schematically represented in Fig. 3.1. Here I briefly summarise the main steps for the protons(for more details, see e.g. [31],[32]).

The preliminary phases of the proton injections into the LHC start with the Linear accelerator 2 (LINAC2) and the Proton Synchrotron Booster (PSB), that boost the protons to an energy of 1.4 GeV. The PSB, composed of four stacked rings, continues accelerating the protons and split them into four bunches into the Proton Synchrotron (PS); this increases the energy of the protons up to 26 GeV, before entering the Super Proton Synchrotron (SPS), the last step before the LHC tunnel. At an energy of 450 GeV, the protons finally enter the two parallel beams in the main LHC ring, travelling in opposite directions.

The beams are accelerated up to their nominal centre-of-mass energy of 7 TeV by eight radio-frequency resonant cavities, which oscillate at 400 MHz. The final beam is composed of around 3000 bunches of protons, each containing 10^{11} protons. The ultra relativistic protons require a strong magnetic field to bend in the ring, as well as to focus at the interaction points and to maximise the collision cross section. The two tasks are achieved by 1232 dipole and 392 quadrupole magnets respectively, made of Niobium-Titanium alloy. The magnets are kept at a temperature of 1.9 K by superfluid Helium, that enables them to work in the superconducting regime and produce a 8.33 Tesla magnetic field. Two different configurations of the magnetic field are needed, since the protons have the same charge but they need to travel in opposite directions in two separate beam

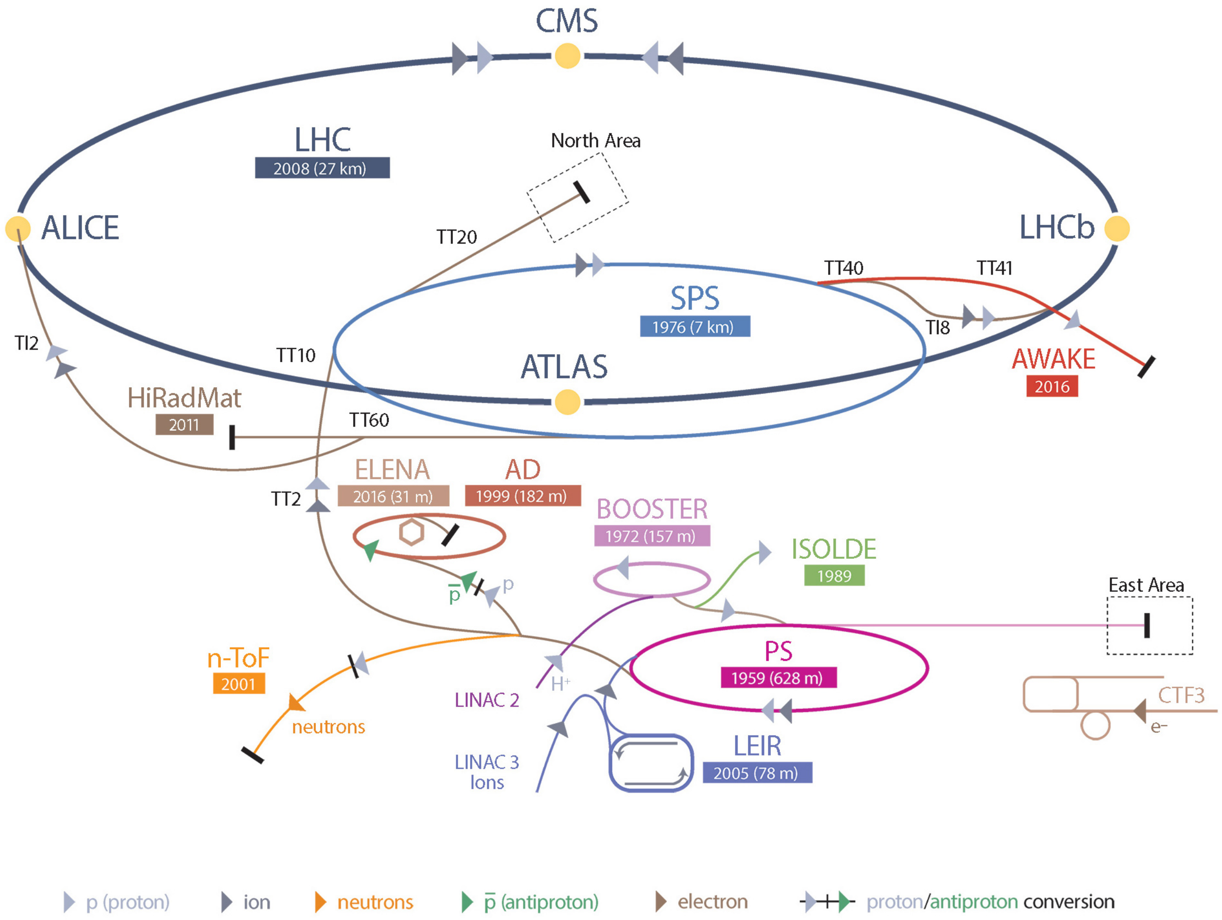

FIGURE 3.1: A schematic overview of the The Large Hadron Collider accelerator complex.

pipes.

Currently, during the last LHC Run 2 phase, the separation in time of each proton bunch is 25 ns; at each turn in the ring, the bunches gain an energy of 485 keV, meaning that the centre-of-mass energy of 13 TeV is achieved after around 20 minutes.

LHC Parameters, Event Rate, Luminosity

One of the crucial LHC parameters for physics studies is the total number of proton-proton interactions. The quantity controlling the total number of collision in the unit time is called *luminosity* ($\mathcal{L}$) and it is defined as:

$$\mathcal{L} = \gamma \frac{n_b N^2 f_{rev}}{4\pi \beta^* \epsilon_n} R \tag{3.1}$$

where γ is the proton beam energy in unit of rest mass, n_b is the number of bunches for each beam (which is 2808 for 25 ns bunch spacing); N is the number of protons in each bunch (1.15 $\times 10^{11}$ at 25 ns); f_{rev} is the revolution frequency (11.2 kHz); β^* is the focal length of the beam (around 0.55 m at the collision point); ϵ_n is the transverse emittance (3.75 μm); R is the reduction parameter that accounts for the angular separation of the beam crossings. All the values represent the design nominal values.

The total number of collisions over a time T can be finally calculated by integrating Eq. 3.1:

$$L = \int_T \mathcal{L} dt \tag{3.2}$$

The luminosity enters the calculation of the total rate N for a given physics process of cross section σ, as:

$$N = \sigma \cdot \ L \tag{3.3}$$

For Run 1, a maximum instantaneous luminosity of $\mathcal{L} = 7.7 \times 10^{33} cm^{-2} s^{-1}$ was achieved, and a total luminosity of around 23 fb^{-1} was delivered to the two general purpose experiments (ATLAS and CMS), at 8 TeV centre-of-mass energy.

The LHC is designed to operate at $\sqrt{s}$=14 TeV; the bunch crossing rate will be 40 MHz, at the peak instantaneous luminosity of $\mathcal{L} = 10^{34} cm^{-2} s^{-1}$. A total integrated luminosity of 300 fb^{-1} is expected to be collected by the year 2023 (LHC Run 3)[33].

3.1.2 The CMS detector

The LHC houses six principal particle detectors and experiments: A Toroidal LHC ApparatuS (ATLAS)[34], the Compact Muon Solenoid (CMS)[35], LHC-beauty (LHCb)[36], A Large Ion Collider Experiment (ALICE)[37], TOTal Elastic and diffractive cross section Measurement (TOTEM)[38] and LHC-forward (LHCf)[39]. In particular the first two, the ATLAS and CMS experiments, constitute the biggest scientific collaborations in the world, each with more than 3,000 among scientists, technicians and students. These multi-purpose detectors are designed to cover the largest range of physics goals, from precision measurements of SM properties to the discovery of new particles.

Both the generic purpose detectors have a similar design, typically referred to as ‘onion shape’: they surround hermetically the interaction point of the beams, and guarantee an almost most complete coverage of the 4π steradians solid angle. From right the interaction point outwards, a series of subdetectors, each one aiming at measuring different particle species, is located. Especially when searching for new physics, it is important to collect the data of all the particles produced in the event, since an imbalance in the conservation of the total momentum or energy can point to the existence of new physics. For example, in R-Parity conserving SUSY, a large imbalance in the transverse momentum (see Section 3.1.2) is expected to appear due to the presence of the neutralinos, that escape detection. In the following I will shortly describe the CMS detector and highlight its main features.

As the name suggest, the design of the CMS detector is very compact, with a diameter of around 15 m, a maximum length of 29 m and a weight of around 14,000 tonnes (for comparison, the ATLAS detector has a length of 46 m, a diameter of 25 m and weights ‘only’ 7,000 tonnes), making it the heaviest particle detector ever built. Almost 80% of its volume is occupied by the muon chamber, that surrounds the solenoid.

The ‘onion’ like structure develops as follows. The inner part hosts the solenoid, which extends up to a radius of 6 m. This is surrounded by the inner tracker, which extends to the proximity of the interaction point. Going outwards, we find the electromagnetic (ECAL) and hadronic (HCAL) calorimeters. Then the large system of muon trackers is located. A sketch of the CMS detector can be seen in Fig. 3.2. The coordinate systems used to describe the positions of the sub-detectors and the particles inside CMS will be now introduced, before describing the various sub systems.

Coordinates System

To describe the coordinates inside the CMS detector, a possible choice is to define a right-handed Cartesian system centred at the collision point. In this case, the x-axis is directed towards the center of the LHC circumference, the y-axis points upward, and the z-axis is aligned with the beam direction. The x-y plane is called transverse plane (with respect to the beam direction). However a more natural choice that follows the symmetry of the detector is to define a cylindrical system of coordinates (r, η, ϕ), where r is the radial distance of the point from the beam, ϕ is the azimuthal angle measured from the x-axis, and θ the polar angle measured from the z-axis.
The variable η, called *pseudorapidity*, is related to the polar angle θ by the following relation:

$$\eta = -ln\left[tan\left(\frac{\theta}{2}\right)\right] \tag{3.4}$$

The pseudorapidity η can be obtained in the limit of massless particles from the *rapidity* y defined as:

$$y = ln\sqrt{\frac{E+p_z}{E-p_z}}\ , \tag{3.5}$$

and in the case of highly energetic particles, the two definitions converge. It is preferred to use the pseudorapidity as a coordinate since the rapidity takes into account the Lorenz boost, while the angular difference $\Delta\theta$ is not a Lorenz invariant quantity. The reference systems and the values of the pseudorapidity for a set of polar angles are shown in Fig. 3.3

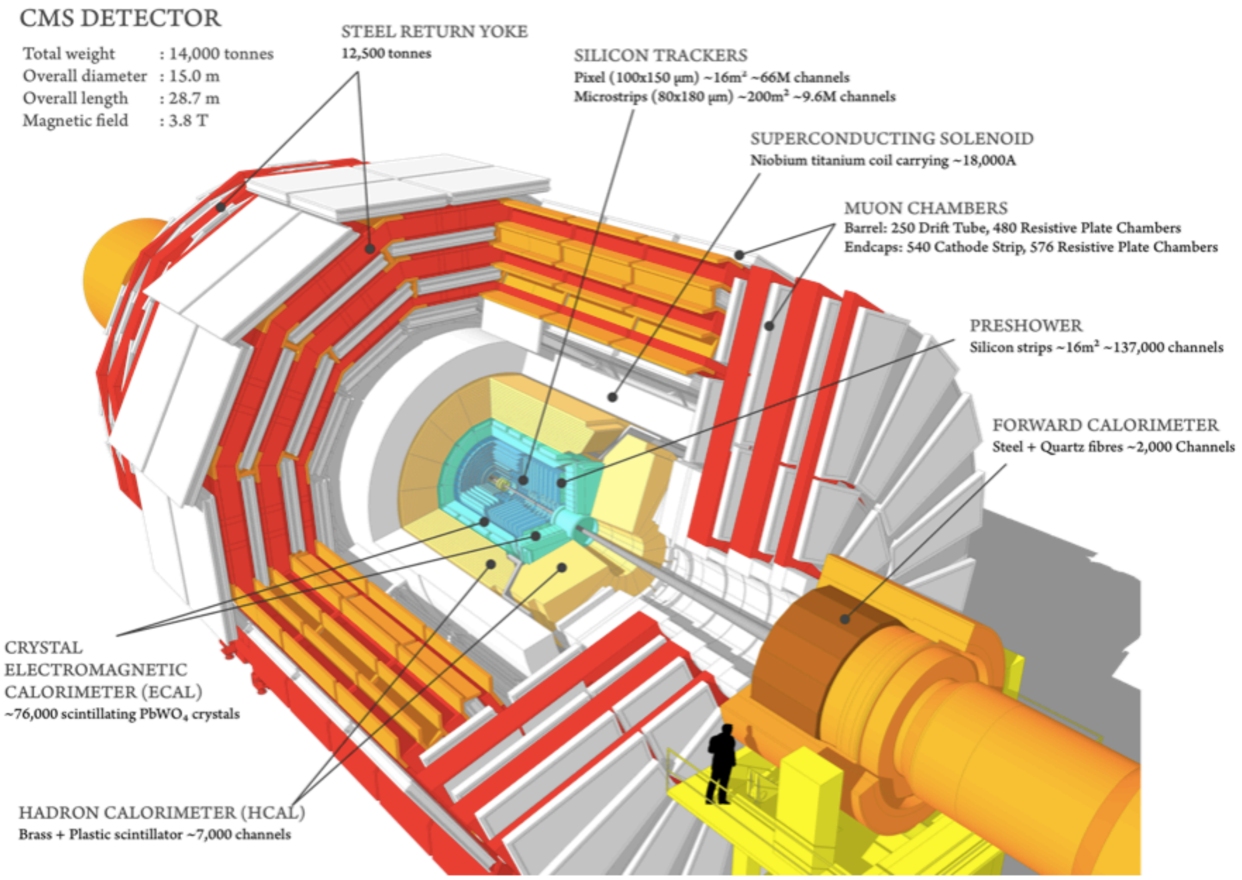

FIGURE 3.2: The CMS detector.

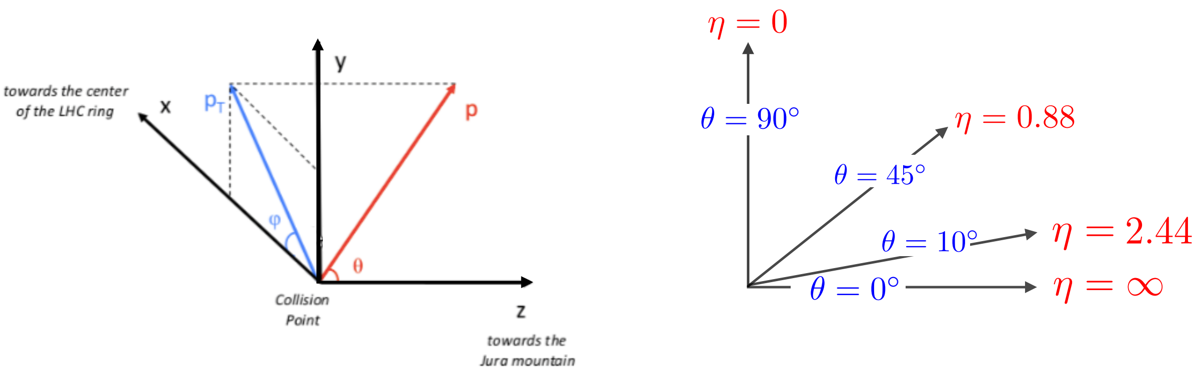

(a) (b)

FIGURE 3.3: The coordinates system for the CMS detector. Figure a) shows the (x, y, z) Cartesian system with black lines. The $\vec{p}_T$ vector (blue) is the projection in the transverse mass plane of the momentum $\vec{p}$ (blue). Figures b) shows the value of the pseudorapity for some polar angles θ.

Due to mechanical reasons, particles with high pseudorapidity that fly almost along the beam line cannot be detected since they fall out of the detector region, or cannot be reconstructed efficiently. Typically the particle objects considered by the CMS analyses require $\eta \leq 5$.
The azimuthal angle and the pseudorapity are used to define a measure of angular separation:

$$\Delta R = \sqrt{(\Delta\eta)^2 + (\Delta\phi)^2} \tag{3.6}$$

which is frequently used to discriminate if the tracks of two particles fall inside the same isolation cone (see Section 4.1.4.1).

Tracking System

The tracking system is the first detector encountered by the particles originating from the collisions, placed right around the interaction point. It is composed of a set of 1,440 silicon pixel and 15,148 silicon strip detectors, covering a surface of around 200 m^2. The system is designed to measure the trajectories of charged particles, i.e. tracks, such as electrons, muons and charged hadrons, or sufficiently long-lived new BSM charged particles. Charged particles are bent by the almost uniform 3.8 Tesla magnetic field present in the volume of the tracker due to the Lorentz force, and their curvature radius is used to determine their momentum. Tracks originating directly from the collisions of the two proton bunches converge into the primary vertex; secondary vertices can also be found, for example caused by the decay of B-mesons (mesons containing bottom quarks), that can fly with a certain life-time before decaying, of order $O(10^{-12})$ s. The charged particles coming from such decays will all point to a secondary vertex.

The CMS tracking system allows to efficiently record and measure tracks up to $|\eta| \leq 2.5$. In the case of non-isolated particles with $|\eta| \leq 1.4$ and transverse momentum $1 \leq p_T \leq 10$ GeV, the tracker system can measure the p_T with a relative uncertainty of 1.5 %; for isolated particles with p_T=100 GeV, the uncertainty is around 3 %. More details about the tracking efficiencies and uncertainties, as well as a complete description of the tracking system in the barrel and in the endcap regions can be found in [40].

Electromagnetic Calorimeter

The electromagnetic calorimeter (ECAL) is designed to measure the energy deposited by electrons and photons. This is achieved by inducing a cascade electromagnetic shower of low energy secondary particles. Photons will produce pairs of e^+e^-, and electrons and positrons will emit bremsstrahlung radiation. The electrons produce scintillation light inside a dense, thick layer of lead-tungstate crystals ($PbWO_4$): the atoms of the scintillator are ionised, and the de-excitation light emitted is collected by photodiodes which convert the photons to electric signals. The shower develops until the energy of the particle fall below a critical threshold energy. The radiation length (i.e. the average distance traveled by an electron before losing $(1 - 1/e)$ of the total initial energy) for this material is 0.89 cm; the total thickness of the ECAL in the barrel and in the endcap is 23 (25.8 times the radiation length) and 22 cm (24.9 times the radiation length) respectively, so the ECAL contains almost the entire energy of the photons and electrons.

The ECAL covers the pseudorapidity range up to $\eta \leq 3$, with a gap between $1.479 \leq |\eta| \leq 1.653$. 61,200 crystals form the ECAL of the barrel region, and 7,324 form the ECAL in the endcap region. Beside a high resistance to radiation damage, the $PbWO_4$ crystals offer a very quick response, and emit around 80 % of the light before the next bunch crossing.
A complete description of the CMS ECAL is given in [41].

Hadronic Calorimeter

The measurement of the hadronic activity is carried out by the hadronic calorimeter (HCAL). The CMS HCAL is a sampling calorimeter; it consists of 16 different pairs of an absorbing material (brass), which causes the formation of hadronic showers due to nuclear interaction, followed by plastic layers which again produce scintillating light in the blue-violet range and allow to collect the energy deposit. The initial and last layer of absorber are made of steel, for structural reasons. The HCAL is almost entirely contained inside the solenoid, extending from just outside the ECAL (r = 1.77 m) to the inner radius of the magnet coil (r = 2.95 m). This compact design is achieved thanks to the short nuclear interaction length of brass, which is only 16.4 cm.

The HCAL is divided into four parts: the hadron barrel (HB), the hadronic endcap (HE), the hadronic outer barrel (HO) and the hadronic forward calorimeter (HF). All the absorbing layers of the HB add up to 5.8 at η=0, and up to 10.6 at η=1.3 in units of total radiation lengths. Since some hadronic showers cannot be confined in the HB or have a late development, the HO uses the material of the coil as an absorber, extending the total absorbing length to 11.8 radiation lengths. Finally the HF is placed in the very forward region surrounding the beam, with $2.85 \leq |\eta| \leq 5.19$. This subdetector is made of steel absorbers, followed by quartz fibers that collect the Cherenkov light produced by the passage of highly energetic charged hadrons.
The technical report of the HCAL can be consulted at [42].

Muon System

The CMS experiment carries in the name the importance of its muon system, which covers the external part of the detector up to $\eta \leq 2.4$. Muons have highly penetrating power: they leave traces in the tracking systems but then propagate without energy loss through the calorimeters. Energy loss via bremsstrahlung is limited and less important than in the case of electrons, since the radiated power is proportional to e.g. m^{-4} in the case of circular motion, and muons are about 200 times more massive than electrons.

The muon system comprises three sub-systems, consisting of drift tubes (DT), cathode strip chambers (CSC) and resistive plate chambers (RPC). The four cylindrical layers of DT are placed in a region of an almost uniform magnetic field, between the plates of the magnet return yoke, extending up to $|\eta| \leq 1.2$. Each layer contain several tiny tubes filled with a gaseous mixture of argon and carbon dioxide. When the gas is ionised by the passage of muons, an electromagnetic cascade is produced. The induced electric signal is collected by positively charged metal wires placed inside the tubes. The signals from the electrical current allows to measure the position of the particle.

For the region $0.9 < |\eta| < 2.4$, CSC are used to take advantage of their fast response; in this region, in fact, the magnetic field is stronger and inhomogeneous, and the particle flux is typically higher. The CSC consist of a series of wires, positively charged, crossed with negatively charged copper strips. The wires attract the electrons that are scattered off by the impact with the muons, while the copper attracts the positive ions; the radial position of muons can thus be reconstructed.

Finally, the RPC extend up to $|\eta| \leq 1.6$; despite their low resolution, they provide a very fast response (around 1 ns), so they are used as a muon triggering system, independent from the other sub-detectors. They are made of positively and negatively charged metallic plates, placed in between a gaseous volume. The electric signals from the ionisation of the gas is collected by metallic strips parallel to the beam.

Since muons tracks are also reconstructed by the tracking system, the combination of the information of the tracker and the muon system allows to achieve the highest resolution of $1.3 - 2$ % in for transverse momenta in the range $20 \leq p_T \leq 100$ GeV in the barrel region.

The design of the muon system is documented in [43].

Triggers and Data Acquisition System

In addition to the main components of the CMS detector, complex triggers and data acquisition systems are used complementarily to filter the enormous amount of events that are produced at each bunch crossing, at the rate of 40 MHz (or 25 ns spacing) at the current Run 2 configuration. In fact, each single event requires from 1 to 2 Mb of disk space after zero removing, adding up to 40 Terabyte/s of data that would have to be recorded, an enormous quantity that cannot be handled by the system. Since the majority of the events are produced in soft collisions or *minimum bias* events, which are not the main target of any CMS physics study, an efficient system to discriminate interesting events was developed.

A two-tiered trigger system [44] is employed to reduce the initial frequency of nominal bunch crossing rate of 40 MHz to $O(1)$ kHz. This is achieved in two following steps. The first trigger system, called *Level* - trigger or L1, is built with low latency hardware. It uses the information from the calorimeters and muon system to decide if the event should be analysed further, in around 4 microseconds. The L1 trigger was specifically designed to work with 25 ns bunch spacing. If the event is considered interesting from the L1, the *data acquisition system* reads out the data and passes it to the software-based HLT trigger, at a rate of $O(100)$ kHz; this is the maximum rate that the detector front end electronics is able to sustain. The HLT uses a series of complex reconstruction algorithms to finally discriminate if the event is to be recorded or discarded, analysing fully reconstructed particle objects such as jets (i.e. hadronic particles contained in an arbitrarily defined narrow cone) and muons. The task is performed running several thousand of CPUs in parallel. The HLT includes also the information from the tracking system. The description of the algorithms used for the reconstruction of the event are included in the *trigger menu*. The events passing the two trigger systems are then recorded and stored for physics analysis.

3.2 Basic Principles of SUSY Searches

In this Section I wish to briefly describe how searches for BSM physics, with a particular focus on SUSY, are performed by the ATLAS and CMS collaborations. However BSM searches are typically generic, and could be potentially sensitive to a broad spectrum of new theories. This is why the re-interpretation of existing searches is a very active field of investigation by phenomenologists; common approaches for re-interpretation will be discussed in Chapters 4 and 7, while a concrete example of a re-interpretation study will be the subject of Chapter 5.

3.2.1 Supersymmetry at the LHC

Since the LHC is a proton-proton machine, the production cross sections for coloured sparticles are dominant with respect to electroweak processes. This means that, for a given mass scale, squarks and gluinos have a much larger cross section than gauginos and sleptons. The cross section for some relevant strong processes are shown in Fig. 3.4. The plot shows processes at $\sqrt{s} = 8$ TeV since results for SUSY searches at this energy will be largely discussed and used in the following

Chapters, but cross sections behave similarly at $\sqrt{s} = 13$ TeV, exponentially falling with increasing mass (the values are in logarithmic scale).

Note that the $\tilde{g}\tilde{g}$ and $\tilde{q}\tilde{q}'$ processes have the largest cross section among all SUSY production processes at the LHC, owing to the strong interaction; for the same reason, gluino-squark associated production cross section is also important. Here squarks $\tilde{q}$ include only the first and second generations, which benefit from the parton distribution function (PDF) of light quarks inside the protons. Sbottoms and stops, on the opposite, have lower cross sections since they are penalised by small or almost null PDFs for bottom and top quarks. The cross section shown in Fig. 3.4 assumes that all the other particles are decoupled. In realistic models, where the masses of all sparticles can be comparable, the cross sections might get enhanced or decreased by additional t-channel exchange of light sparticles and interference terms.

We also how much electroweak production is less important compared to the strong processes. For the same mass of the SUSY particles, typically the cross section is reduced by more than $O(10^{-2})$. This makes electroweak processes more challenging to be constrained at the LHC, and the current limits on gauginos and sleptons are around 1 TeV weaker than the limits for gluinos (see Section 3.2.3).

3.2.2 Simplified Models for SUSY Searches

Hunting for SUSY and in general for new physics at the LHC is a challenging task. From the experimental point of view, a deep understanding of the detector performance and particle object reconstruction is needed, in order not to miss potentially interesting signs of new physics and at the same time not to mistake rare SM events with something exotic. From the theoretical point of view, even within the MSSM, an excess of events with some particular signatures does not in general point unambiguously to the existence of specific SUSY particles. In fact the opposite is quite true: given the large number of free parameters in the MSSM, in primis the unknown masses of the sparticles, the same signature can be produced by several SUSY signals. This makes it hard to identify which particles are responsible for the signals, how these particles decay to the LSP, and if other particles are simultaneously produced so that the signal is indeed a mixture of final

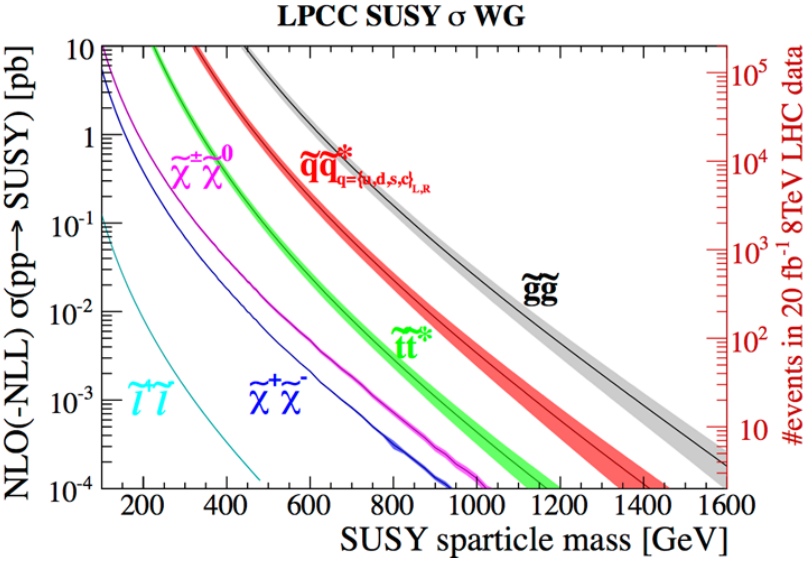

FIGURE 3.4: Production cross section for a selection of processes at the LHC for $\sqrt{s}$ =8 TeV. The expected number of events for the various processes corresponding to an integrated luminosity of 20 fb^{-1} is shown on the right. Taken from [45].

states from several production modes.

To ease the characterisation of hypothetical signals, theorists have developed a framework that reduces the complexity of the parameter space of generic BSM models to a handful of new parameters. The new models, which represent only a subset of the full theory, are called *simplified models*, and the sets of new particles constitute the *simplified models spectra*[46, 47, 48](SMS). Beside the reduction in the number of parameters, the quantities describing simplified models can be often related directly to collider physics observables, such as the masses of the particles and the production cross sections. In addition, SMS assume a specific branching fraction for the particle decays. These three parameters completely describe the results of SUSY searches in the context of SMS. While making use of a limited set of parameters, results interpreted with simplified models can be be used to reconstruct the limits of a full theory (see Section 4.2.2 when efficiency maps results are introduced).

Finally, the sensitivity of the searches of the LHC experiments depend mostly on the mass spectrum of the model tested, that affects directly the energy of the SM particle in the final state, for example jets, leptons, and the magnitude of the missing transverse energy of the events, which can point to the presence of the charge neutral LSP escaping detection. This dependency on the mass array makes SMS results largely model independent, in the sense that any BMS theory with similar mass spectra and final states will leave the same signature in the detector. In particular, any other quantum number is expected to produce only minor effects in the final state. SMS limits can thus be used for the re-interpretation of searches for a variety of other BSM theories; this will be discussed in Section 4.2 when the `SModelS` tool is introduced.

3.2.3 Searches for R-parity conserving SUSY at the LHC

Searches for R-parity conserving SUSY at the LHC typically rely on signatures with a large imbalance in the total transverse momentum; the magnitude of such vector is called transverse missing energy E_T^{miss}:

$$E_T^{miss} = \left|\vec{p_T}^{miss}\right| = \left|\sum_i \vec{p_T}^i\right| \tag{3.7}$$

This is mainly due to the presence of the neutralinos, which escape detection. Note however that events with missing energy are also expected in the SM, such as events with Z bosons that decay to neutrinos. Particles that fall outside the acceptance of the detector will also result in missing energy of the events.

The visible SM final state can be categorised as:

- large hadronic activity without any leptons (for example in the case of squark production that decay directly to the LSP);
- large hadronic activity and leptons (for example gluinos that undergo cascade decays via gauginos);
- leptonic final state without significant hadronic activity (as it is expected for example in slepton decaying to the LSP).

Photons are typically used to constrain specific models of SUSY, with the LSP being a massless gravitino.
It is also frequent to consider reconstructed vector bosons (W or Z) as final state particles. Due to the different branching fractions of the W and Z bosons, that can decay hadronically or leptonically,

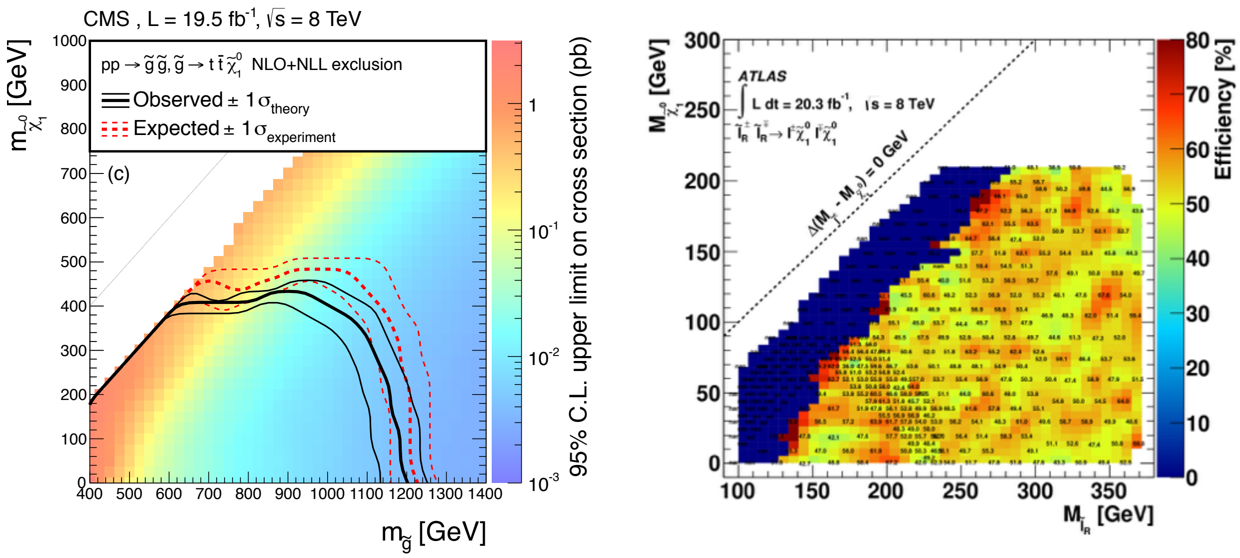

FIGURE 3.5: Example of results from the LHC experiments interpreted with SUSY simplified models. Left: upper limit map from the analysis CMS-SUS-13-012[49] for the *T1tttt* simplified model. Right: efficiencies for one signal region of the ATLAS-SUSY-2013-11[50] analysis for the *TSlepSlep* ($pp \to \tilde{l}^- \tilde{l}^+, \tilde{l} \to l\tilde{\chi}_1^0$) simplified model, where $l = (e, \mu)$.

the same simplified models can be constrained by looking at different experimental signatures. A simple example is the search for stop pair production, where each stop decays to a top quarks and the LSP. The top quark will then decay to a bottom quark and a W boson. The search for this simplified model can be performed e.g. in the all hadronic final state (for hadronically decaying W bosons), where two jets should be identified as originating from bottom quarks (b-tagged jets). However final states with a single lepton or opposite-sign leptons final state are also possible, in addition to two b-tagged jets.

Generally the SUSY analyses select interesting events by applying cuts on the kinematic variables of the particle object of interest, or on their multiplicity, in order to separate the potential SUSY events from the SM background. For example, searches for gluino typically require a high number of jets, large missing energy, b-tagged jets if in the decay chain of the gluino stops appear, and then a certain number of leptons. This analysis strategy is usually called *cut-and-count*, since it aims at removing the uninteresting events from the SM background and then counting the surviving events to determine the efficiency of the analysis. This strategy will be described more extensively in Section 4.1.4, where it will be shown how a simple analysis can be reproduced with sufficient accuracy outside the LHC collaborations. A series of cuts define a specific signal region (SR); in each search there are typically several SRs (from a few tens up to a few hundreds), since different kinematic selections might improve the analysis sensitivity to different SUSY models, or different mass spectra of the same model, that share the same final state. By comparing the number of events taken from the collision data with the expectation of the SM background and an hypothetical SUSY signal, limits on the production cross section can be computed.

Examples of two types of results from the LHC results are shown in Fig. 3.5. On the left we see an upper limit map for the *T1tttt* ($pp \to \tilde{g}\tilde{g}, \tilde{g} \to t\bar{t}\tilde{\chi}_1^0$) model, where the gluino decays via an off-shell stop, from the analysis CMS-SUS-13-012[49]. This simplified model is described by the two masses of the gluino and the LSP, the theoretical production cross section for the gluino, and a fixed branching ratio of 100% of the gluino in the way described above. These four parameters are sufficient to describe the simplified models; all the rest of the SUSY particles are neglected. For each mass combination, i.e. for each choice of $(m_{\tilde{g}}, m_{\tilde{\chi}_1^0})$, the experimental limit on the production cross section is calculated, and indicated by the temperature map.

Note that the values of the upper limit cross section provided by the experimental collaborations do not depend on the theoretical cross section of the specific simplified model taken into considerations. On the contrary, the black lines or exclusion curves delimit the region in the mass plane that this particular analysis can exclude, at a 95 % confidence level; these curves are indeed derived assuming a specific value of the production cross section. The regions that a specific analysis can exclude depend then both on the sensitivity of the analysis to the model, and on the value of the production cross section. For the non excluded regions, either the search is not sensitive enough, for example because the SM final state are below the CMS detector acceptance, or the theoretical cross section is so small that too few SUSY events are expected to be found in the total dataset collected. The last case can be understood by looking at the vertical edge that almost all the simplified model present for high SUSY mass: at increasing SUSY particle masses, the value of the cross section drops as shown e.g. in Fig. 3.4.

The results on the left of Fig. 3.5 is an efficiency map of a specific SR of the analysis, which shows the number of events that survive all the cuts of the analysis, for the simulated simplified model *TSlepSlep* ($pp \to \tilde{l}^-\tilde{l}^+, \tilde{l} \to l\tilde{\chi}_1^0$) simplified model, where $l = (e, \mu)$. The number of events is normalised by the total number of events generated in the simulation. In practise this number corresponds to the fraction of the simulated SUSY events that the analysis is able to detect. This information is used by the experimentalists, and also by the theoreticians (in specific and simple cases), to calculate the upper limit like the one show in the left plot. Likewise, the analysis shows a different sensitivity for each mass point $(m_{\tilde{l}}, m_{\tilde{\chi}_1^0})$.

3.2.4 Statuts of SUSY Searches

Here I briefly summarise the status of SUSY searches at the LHC when this thesis was written (Winter 2018). The CMS results are taken as an example, but ATLAS analyses show similar reach in the exclusion of the various SUSY models.

Figure 3.6, produced for the CMS collaboration, represents one of the standard ways of summarising the status of the searches for specific SUSY particles and decay modes. The left plot shows the exclusion curves for the *T1tttt* simplified model, where $\tilde{g} \to t\bar{t} + \tilde{\chi}_1^0$, with 100% BR. With the Run 1 data, gluino masses of up to ≈1.4 TeV could be excluded under the simplified model assumptions. Different analyses targeting different final states show different exclusion power through the mass plane, demonstrating the importance of performing multiple searches, targeting the same model. It is to be noted, in addition, that even in the regions where many analyses exclude a specific model, the cross section UL might be different; this information can only be extracted from the UL maps provided by the collaborations.

The right plot of Figure 3.6 represents the summary of the results for the *T2tt* simplified model $pp \to \tilde{t}\tilde{t}, \tilde{t} \to t\tilde{\chi}_1^0$; the dashed oblique lines separate the mass plane into three regions, depending on the $\Delta(m_{\tilde{t}}, m_{\tilde{\chi}_1^0})$ mass gap, that might induce the stop to decay via off-shell tops, i.e. 3-body decays ($\tilde{t} \to bW\tilde{\chi}_1^0$) or 4-body decays($\tilde{t} \to bW^*\tilde{\chi}_1^0$). Flavour changing neutral current mediated by the neutralino can also favour the stop decay to a charm quark and the LSP. Each analysis often targets a limited region of the mass plane. We see that stops can be excluded up to almost $m_{\tilde{t}} =$ 800 GeV for a massless LSP; however, for lighter stops, a large part of the mass plane cannot be excluded, due to the small mass gap between the stops and the LSP.

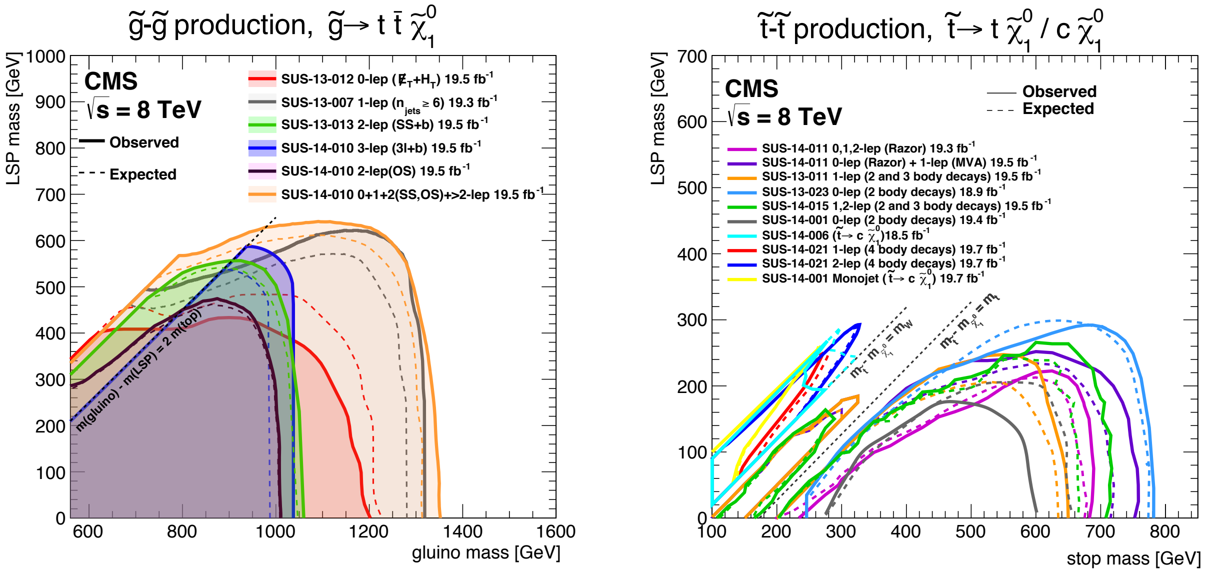

FIGURE 3.6: Run 1 results for the CMS collaboration for the *T1tttt*$(pp \to \tilde{g}\tilde{g}, \tilde{g} \to t\bar{t}\tilde{\chi}_1^0)$ and *T2tt*$(pp \to \tilde{t}\tilde{t}, \tilde{t} \to t\tilde{\chi}_1^0)$ simplified models. The dashed lines indicate the kinematic region where the SM tops are off-shell.

In Fig. 3.7 the production cross section for selected EW processes is shown (left), as well as the summary of the EW searches for charginos, neutralinos and staus from the ATLAS collaboration[51] (right). The highest reach in the exclusion for massless LSP is obtained by interpreting the searches with cascade decays simplified models, in this case where the mass of the intermediate sparticle is equal to the average of the mother and the LSP (i.e. calculated with the parameter x=0.50). However some care should be taken when interpreting the results for such cascade decays simplified models; in fact, contrary to the gluino and stops described above, where only two particles appear in the SMS, in this case we have a third one, which assume a fixed value that depends on the first two. The results are then projected onto a slice of the 3-dimensional mass parameter space of the model. In general, by assuming a different relation to fix the intermediate mass, very different limits and exclusions will be obtained. Also note that this mass relations are completely arbitrary, and do not reflect the properties of the mass spectra of any realistic model. Whenever upper limits or efficiencies for several mass combinations are available, one can interpolate to obtain the results for arbitrary mass combinations. The interpolation procedure and its related uncertainty will be extensively discussed in Section 4.2.4, in Chapter 6 and in Appendix F.

Figure 3.8 represents the summary of the results of the CMS searches, interpreted with simplified models, for early 13 TeV (Run 2) CMS analyses, up to Moriond 2017 results, with the full dataset available at the time (35.6 fb^{-1}), with blue bars. Only a few results have been published afterwards. A comparison with the preliminary results obtained with a smaller dataset (around 14 fb^{-1}) is also shown, with orange bars. Additional results, categorised by their production channels, can be found at [52] for the CMS and at [53] for the ATLAS experiments.

We see that currently the most constraining result for gluino simplified models come from *T1bbbb*, where $\tilde{g} \to b\bar{b} + \tilde{\chi}_1^0$, pushing the exclusion for $m_{\tilde{g}}$ up to 2 TeV and improving the previous Run 1 limit by almost 700 GeV [1].

---

[1] `https://twiki.cern.ch/twiki/pub/CMSPublic/SUSYSMSSummaryPlots8TeV/T1bbbb_ICHEP2014.pdf`

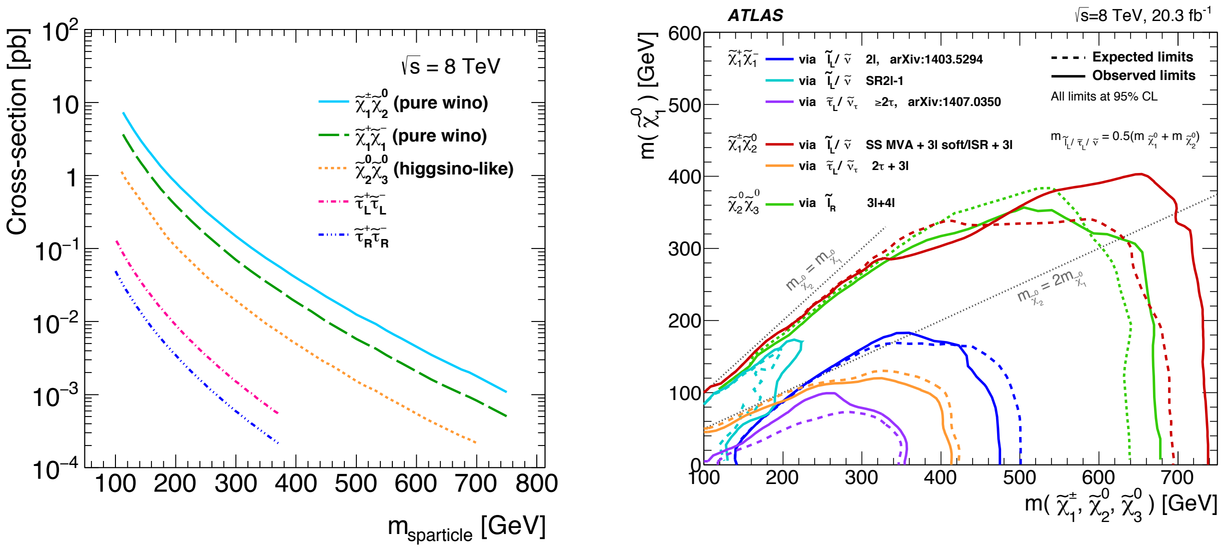

Figure 3.7: Run 1 summary plot of the EW SUSY searches results from the ATLAS collaboration[51]. Left: cross section for relevant electroweak processes and different nature of the neutralinos (Bino,Higgsino or Wino-like). Right: exclusion curves from the various ATLAS searches. The parameter x is set to 0.50 in the case of cascade decays.

As for the stops, the limits were pushed up to 1.1 TeV, from the previous 800 GeV.

Finally, the current simplified model limits for electroweak particles lies in the 1.1 TeV range, in the case of cascade decays. For chargino-neutralino production the limit is much lower, sightly exceeding 200 GeV for the models with $\tilde{\chi}_2^0 \to H\tilde{\chi}_1^0$ and 400 GeV for $\tilde{\chi}_2^0 \to Z\tilde{\chi}_1^0$. The limits obtained from the combination of several searches reaches around 500 GeV (See [54]).

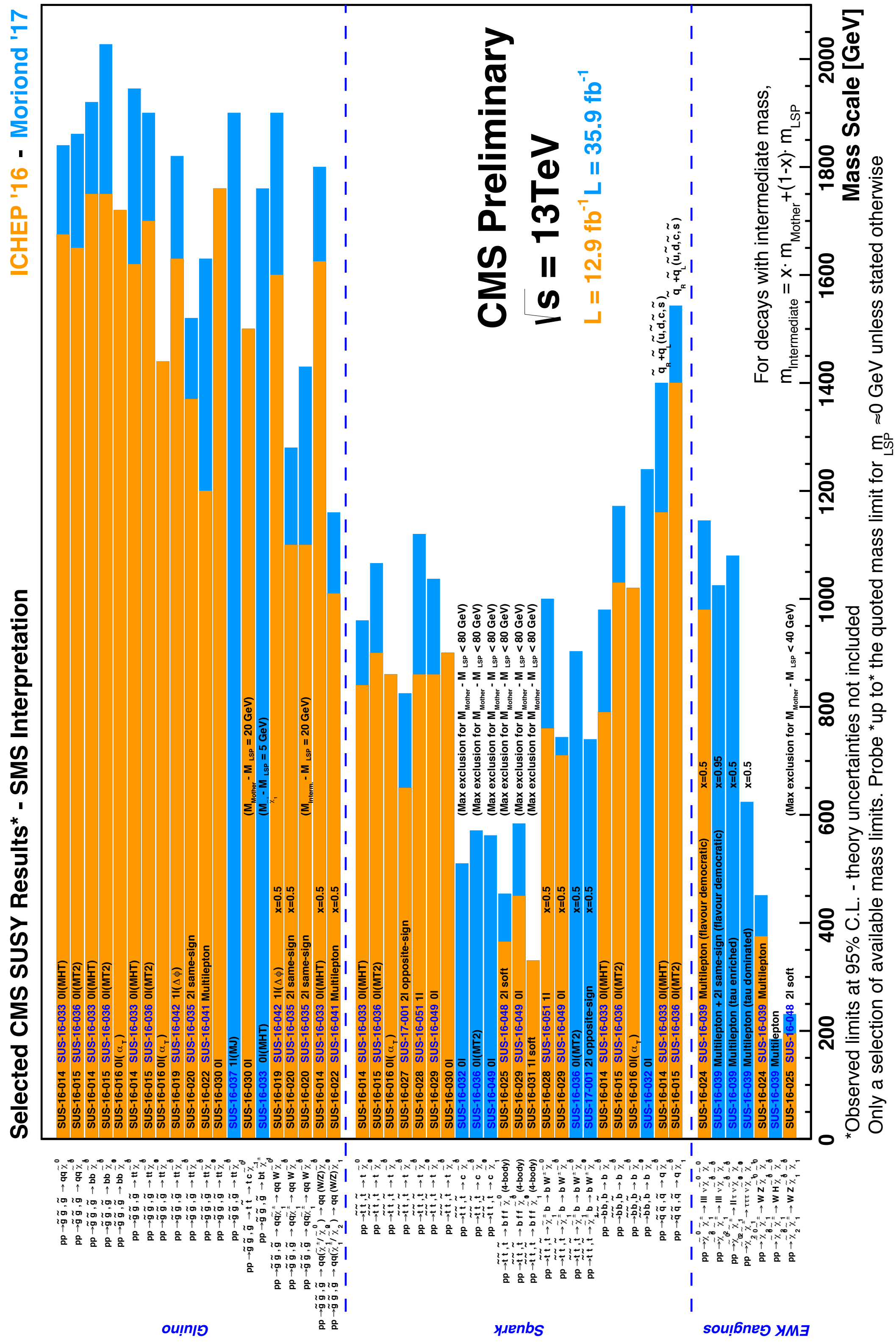

FIGURE 3.8: Summary of the SUSY searches results of the CMS experiment for Run 2 analyses (as of Moriond 2017) with SMS interpretation. Each bar corresponds to a specific SMS result, and the x-axis indicates the reach in the exclusion for the mother particle with massless LSP, or as specified for each bar in the plot. In the case of cascade decays, the x mass parametrization used is also reported, defined as $x = \frac{m_I - m_M}{m_M - m_{LSP}}$ where M and I indicate the mother and intermediate SUSY particles.

Chapter 4

Methods for Reinterpreting BSM Searches at the LHC

Contents

Presenting the results of searches for BSM physics in terms of simplified models has become the standard method adopted by the ATLAS and CMS collaborations. However the re-interpretation of such results in the context of full and more realistic models is a non-trivial task. Re-interpreting existing searches is extremely useful, since they are often sensitive to a large variety of models that share similar signatures. The experimental results from those searches can be efficiently used to constrain the parameter space of different models without the need of a separate analysis. However, due to limited computing resources, the collaborations are forced to limit their interpretation efforts to a few selected (simplified) models.

As it was shown in the previous Chapter, so far there have been no exciting discoveries of new BSM physics from the plethora of LHC searches, so that the "allowed" parameter space of many theories has sensibly shrunk, pushing further and further the hope to find new physics at the LHC, at least for the most popular BSM theories. However there are many theories that are still poorly constrained.

Many tools have been developed by phenomenologists to re-interpret the LHC searches in the context of arbitrary BSM models. On one side, there are tools that make efficient use of the simplified model results provided directly from the experimental collaborations. By mapping a general BSM model onto its simplified model spectra, direct comparison between the theoretical cross section of the tested model and the experimental results is possible, for example using the upper limits or the efficiency maps provided by the LHC experiments. This is the basic philosophy of tools such as `Fastlim` [55], *XQCUT*[56] and `SModelS` [57]. This method of re-interpretation is efficient and fast, since no Monte Carlo sample generation is involved. However, by definition, simplified models constitute only a fraction of the total signal of a complete model, that might be too complex to be reconstructed by means of simplified models results.

Other frameworks called *recasting tools* overcome the restrictions imposed by simplified models by re-running a fast version of the experimental analysis to constrain arbitrarily complex models, and derive cross section upper limits. The recasting procedure is more convoluted and lengthy, since it requires the production of simulated events at various levels of accuracy depending on the study to be performed. The advantage is that this method is more flexible and it usually leads to more constraining results. Tools of such types are CheckMATE[58], GAMBIT(ColliderBit)[59] and `MadAnalysis 5` [60]. Unfortunately the full recasting process involves the Monte Carlo generation of samples, followed by the simulation of the detector effects, and finally the proper analysis recast. The complete chain is computationally expensive, so it is not suitable for testing very large scans of parameter points.

A large part of this thesis involved the development and extension of three different re-interpretation tools: `SModelS`, `MadAnalysis 5` and `MadDM`. In this Chapter the main features of the first two tools, which are designed specifically for the re-interpretation of the LHC searches for BSM physics, are introduced, as well as the novelties developed in this work. The entire Chapter 7 is dedicated to present the new features of the latter, which is designed for phenomenological studies of DM from an astrophysical point of view.

This Chapter is structured as follows: first, the recasting tools are introduced in Section 4.1, with a particular focus on the `MadAnalysis 5` package and the validation of a recent 13 TeV CMS analysis, searching for SUSY particles in events with jets and missing transverse energy. The implementation of this analysis constitutes an important piece in the `MadAnalysis 5` database of analyses, since it is the first one targeting all-hadronic final state BSM signals using the full dataset available at 13 TeV. Then, the tool `SModelS` is introduced in Section 4.2. While this tool has already been used in several publications (see [61] for a complete list), it is worth to describe in detail the new features of v1.1, in particular regarding the extension of the capabilities of the database to include efficiency map types of results. A major effort of this work was the update and maintenance of the database. Thanks to the usage of efficiency maps, the `SModelS` database can incorporate also results produced by phenomenologists, for example with the usage of recasting tools. Even more importantly, new results can be produced by oneself to extend the constraining power of `SModelS` in the case of specific BSM theories tested. To this end, Section 4.3 describes the automated framework I developed to recast SUSY results for new simplified models and increase the number of efficiency maps available in the database. This procedure represents a synthesis between the approaches of full-recasting and the fast reinterpretation philosophy, and allows to extend the `SModelS` database significantly. The physics cases studied in Chapters 5 and 6 will show concretely the application of the entire `SModelS` procedure and the benefit coming from the newly created results.

4.1 Recasting Tools

As stated in the introduction, a few tools have been developed to re-interpret the searches for new physics performed by the LHC collaboration with generic BSM models. The experimental analyses typically provide only a few interpretations of searches in the context of simplified models. Also models with a limited set of free parameters, e.g. the cMSSM and mSUGRA models, are at times used as benchmarks to show the impact of the presented analysis on more complete models (see e.g. [62]). Both the ATLAS and CMS collaborations, at the end of the Run 1 of the LHC, performed a dedicated study paper to analyse the constraints on the pMSSM-19 (this will be treated extensively in the Chapter 5).

Specialised tools have been developed that allow, from outside the experimental community, to reproduce the basic workflow of the experimental analyses and thus constrain new theories with existing analyses. Starting from a Monte Carlo sample containing any generic BSM signal, they are able to extract the signal efficiency for the various signal regions of the analysis and set upper limits on the production cross sections of the BSM particles. External tools like `Delphes`[63] are then used to simulate the detector response.

The signal $(\epsilon \times \mathcal{A})$[1] is defined by the product of the efficiency ϵ (defined by the cuts of the analysis) times the acceptance $\mathcal{A}$ (that accounts for the detector response). It is calculated as the ratio of the events surviving each signal region selection divided by the initial number of events generated. Reimplementing the analysis workflow is usually possible for relatively simple experimental searches based on a *cut-and-count* approach. For this type of analyses, the selection of the events is based on simple cuts on specific kinematic variable or quantities (such as the transverse momentum, angular separation, object multiplicities, etc.) of the objects in the final state (e.g. leptons, photons, jets). Each signal region is thus unambiguously defined by a series of cuts. When more complicated analyses are considered, for example ones based on multivariate analysis techniques, the results cannot be so easily reproduced outside the LHC collaborations. Fortunately a large number of experimental searches, both targeting SUSY or more exotic signals, are based on this simple cut-and-count approach.

Among the recasting tools, we find e.g. the CheckMATE[58] and `MadAnalysis 5` [64, 60] frameworks. They are both written in C++, and offer a python interface as well. They allow the users to either develop their own analysis implementation and to design new analyses, or use the available recast analyses to test any input BSM model. In conclusion, they are essentially a compact and simplified version of the big software packages used by the experimentalists from ATLAS and CMS to perform their searches.

In the following I will give a brief overview of the various steps involved in the recasting procedure.

4.1.1 Basics of Analysis Recasting

It is useful to briefly remind here the typical workflow of an analysis recast, divided into three main steps: the Monte Carlo sample production, the simulation of the detector response, and finally the proper analysis recast.

---

[1] For the rest of the thesis, unless otherwise specified, the term ‘efficiency’ will always refer to the product $(\epsilon \times \mathcal{A})$.

Monte Carlo Simulation

Monte Carlo generators are needed to produce the events that will then be analysed by the recasting tools. `MadGraph`[65], `Pythia`[66] or Herwig[67] are only some known examples. Generally the generators accept standardised input files containing the implementation of the Lagrangian of desired BSM model, for example in a UFO[68] file format. The `MadGraph` tool calculates the *matrix elements* (up to NLO accuracy) for the processes involved, using the Feynman rules at different order of the coupling constant involved (e.g. α_s). The other tools are based on the *parton shower* formalism, based on the application of subsequent QCD evolution equations and splitting functions to *2-to-2* types of process.
It is well known that the matrix-element formalism is advantageous to describe highly energetic or well separated partons, which is the case for example of extra parton emission. At the same time it poorly describes soft and collinear partons and the structure of jets, which are on the contrary better modelled by the parton shower formalism. It is then advisable to use the two methods in combination and simulate the most accurate events for the entire phase space. In this case, a matching procedure is needed to avoid the double counting of events. The partonic events are then hadronised and showered.

Detector Simulation

Tools like DELPHES 3.4.0 [63] are designed to quickly simulate the detector response to the various simulated particles. Such tools make use of simplified parametrizations of the various subdetectors (tracker, electromagnetic and hadronic calorimeter, etc.) and simple equations that describe the efficiencies of object reconstruction. Typically the efficiencies of electrons and muons depend primarily on their energy and on their coordinates inside the detector. At this time also the clustering of hadrons into *jets* is performed, e.g. by FASTJET[69]. Jets can be further classified according to the flavour of the initial quark. I mention here briefly the *b-tagging* class of algorithms, which aim at identifying jets originating from a bottom quark. Each experimental analysis uses different jet selection criteria as well as different clustering and jet flavour tagging algorithm, so in general no unique parametrization universally suitable for all the different analyses.

Analysis Recast

After the detector simulation, the events are ready to be passed to the proper analysis recast, which extracts the values of the efficiency for each SR. The efficiency, or precisely the $(\mathcal{A} \times \epsilon)$ is used to calculate the estimated yield y (or number of BSM events), defined as:

$$y = (\mathcal{A} \times \epsilon) \times \mathcal{L} \times \sigma \tag{4.1}$$

where $\mathcal{L}$ is the total integrated luminosity, and σ is the production cross section of the process considered. This yield can then be compared to the SR cross section upper limit, to determine if the signal is compatible with the observed data. This procedure is described in the following Section.

4.1.2 Limit Setting: the CLs Method

For each SR of an analysis, it is possible to calculate a model independent cross section UL (*'signal region UL'*), also called upper limit on the visible cross section σ_{vis}, usually calculated at 95% confidence level. ULs for the various SRs are often quoted in the publications of the LHC experiments;

otherwise, it is possible to calculate an approximate limit using the total number of estimated SM background events n_{bkg}, its total uncertainty Δn_{bkg}, and the number of observed events in the data n_{obs}.
The accurate estimation of the SM background is indeed one of the main challenges for any experimental search for new physics. This complicated evaluation can make use of Monte Carlo simulations, or can be based on a 'data driven' approach. The latter is typically the case when the simulation of the background might not be well performed by the Monte Carlo generators, for example when the signals considered are expected to lie in the extreme tails of the kinematic distributions.

The procedure used to calculate the UL is based on the CL$_s$ method[70, 71], and it is summarised below.

The simplified likelihood used in `SModelS` is defined as:

$$L_{s+b}(\sigma_{sig}, n_{bkg}, \mathcal{A} \times \epsilon, \mathcal{L}) = \mathcal{P}(n_{obs}|n_{bkg} + \sigma_{sig} \times (\mathcal{A} \times \epsilon) \times \mathcal{L}) \times \mathcal{G}(n_{bkg}|\hat{n}_{bkg}, \Delta n_{bkg}) \tag{4.2}$$

where $\mathcal{L}$ is the total integrated luminosity, σ_{sig} is the hypothetical production cross section of a BSM signal, and the $\mathcal{G}$ and $\mathcal{P}$ functions are respectively a Gaussian and Poissonian distribution. Additionally, if available, one can implement other terms which account for the uncertainty of $\mathcal{L}$, of the cross section σ and of the $\mathcal{A} \times \epsilon$, typically using Gaussian approximations.

By fixing $\sigma = 0$, one obtains the likelihood for the background only or null hypothesis L$_b$, which explains the data without the need of introducing new physics. On the other hand, the hypothesis L_{s+b} is needed to understand the data in case of a signal, i.e. when the null hypothesis is rejected.

One can use the likelihood functions to define a test statistic T as:

$$T = \frac{L_{s+b}}{L_b} \tag{4.3}$$

Using the test statistic T, it is possible to set a limit on the signal strength of the hypothetical signal that is still compatible with observation with a confidence level:

$$CL_{s+b} = P_{s+b}(T \leq T_{obs}) \tag{4.4}$$

where P_{s+b} is the probability distribution of the test statistic. This formula implies that the signal hypothesis can be rejected at the $(1 - CL_{s+b})$ confidence level, so that e.g. a 95% CL corresponds to $CL_{s+b} = 0.05$.
However, this procedure does not take into account cases that are not well explained neither by the signal nor by the background hypothesis. To account for those, a modified limit is often used:

$$CL_s = \frac{CL_{s+b}}{CL_b} \tag{4.5}$$

where CL_b is evaluated using the background only hypothesis. One can thus calculate a cross section upper limit at the 95% by requiring that $CL_s = 0.05$.

Numerically, the test statistic T is constructed using Monte Carlo toy experiments. The CL_s method can be used for two distinct purposes. On the one hand, given a certain BSM process with a specific cross section σ_{sig}, it is possible to calculate at which CL the model is excluded by the LHC data. On the other hand, one can extract the value of the visible cross section σ_{vis} upper limit calculated at a given CL, for a given SR (since the Likelihood includes the value of the efficiency). These σ_{vis}^{SR} will be used by the `SModelS` tool to determine if an input BSM model is excluded by the efficiency maps results, as will be described in Section 4.2.2.

The procedure just described can be applied to each signal region of the analysis, but can be extended to derive a global limit using the results of all the different SRs. This can be done by calculating the product of the likelihoods for all the SRs when they are statistically uncorrelated, i.e. the series of cuts that define them are exclusive, so that events cannot belong to multiple signal regions, and the background estimates are uncorrelated (which is never exactly true). The caveat is that correlations between the SRs are neglected, both in terms of $(A \times \epsilon)$ and in the estimation of the background events. Recently, the CMS collaboration has started providing the covariance matrices and prescriptions [72] to enable outside users to combine the results. The recent release 1.2 of `SModelS` [3] includes the ability of combining signal regions, if such information is available. In this thesis, only the limits for individual SRs will be considered.

4.1.3 The `MadAnalysis 5` Recasting Tool

I wish now to introduce briefly the `MadAnalysis 5` package, which was extensively used for this thesis. In addition, *Public Analyses Database* or *PAD*[73] was extended with the implementation and validation of the recasting code for the analysis CMS-SUS-16-033, presented in Section 4.1.4.

The *PAD* is a fundamental part of the tool; it contains a large set of recast codes of experimental searches from the ATLAS and CMS collaborations, together with detailed notes that validate the results of the implementation (see e.g. [74, 75]). An analysis is considered validated if, in general, the recasting procedure can reproduce the results provided by the experimental collaborations within 20% discrepancy. Among the results, cutflow tables (reporting the number of events surviving after applying a specific cut), kinematic distributions for the most significant variables, efficiency maps and cross section upper limits are often provided.

Reaching the desired 20% level of accuracy is, at times, impossible, mainly due to the lack of sufficient information of the experimental analyses, regarding for example the selection efficiencies of objects, or details regarding the generation of Monte Carlo samples. The validation note serves as a guideline for the user to decide if the level of accuracy of the recast results are sufficient for his/her intentions, and eventually highlight which step of the analysis implementation is problematic. By recasting the analyses included in the *PAD*, the user can confront the prediction of his/her model with the current experimental limits from the LHC.

The extension of the *PAD* with a new 13 TeV search from CMS will be the centre of the following discussion.

4.1.4 Implementation and Validation of CMS-SUS-16-033 in `MadAnalysis 5`

This Section focusses on the implementation and validation of the analysis CMS-SUS-16-033[76]. There are three main reasons that made the recasting of this analysis quite interesting among all the available published by the ATLAS and CMS collaborations. First, as it will be thoroughly explained in Chapter, searches for coloured SUSY particles in the generic hadronic final state (also called *inclusive* searches) can provide strong constraints on full models like the MSSM. The second reason is the availability of the covariance matrix, which enables tools like `SModelS v1.1.3` to combine the contributions of the signal in different signal regions; more constraining limits, with respect to the usage of a single signal region, can thus be obtained. Third, the analysis is well documented and provides extensive validation material.

4.1.4.1 Analysis Description

The analysis CMS-SUS-16-033[76] searches for SUSY particles in the '*all hadronic*' final state, a generic description that will be used for SUSY analyses searching for events with large hadronic activity, a high jets multiplicity and veto the presence of isolated leptons. The search was performed using data collected with proton-proton collisions at a centre-of-mass energy of 13 TeV, with a total integrated luminosity of 35.9 fb^{-1}.
All the information used for the recasting and the validation is available in the official wiki page of the analysis[2].

The search is performed using four main variables: the light flavour and b-tagged jets multiplicity, the hadronic transverse energy (H_T) and the missing transverse energy ($\not{H}_T$). The variable H_T is defined as the scalar sum of the p_T of the signal jets:

$$H_T = \sum_{jets(p_T>30)} |\vec{p}_T| \tag{4.6}$$

where only the 'tight signal jets' with $p_T > 30\ GeV$ and $|\eta| < 2.4$ are used.

The variable $\not{H}_T$ on the other hand considers the jets momenta's vectorial sum

$$\not{H}_T = |\vec{\not{H}}_T| = \left| \sum_{jets(p_T>30)} \vec{p}_T \right| \tag{4.7}$$

for jets with $|\eta| < 5.0$.

Events with isolated leptons (electrons or muons) are rejected; the radius of the isolation cones depends on the p_T of the lepton considered. The isolation requirements are imposed to discriminate true leptons originating from the decay of hadrons and jets that are erroneously identified as leptons. For each lepton, an isolation variable I_l is defined as:

$$I_l = \frac{\sum_{\Delta R} p_T(h,c) + p_T(h,n) + p_T(\gamma)}{p_T(l)}$$

where the sum at the numerator includes the scalar p_T of the charged (h,c) and neutral (h,n) hadrons and the photons, divided by the transverse momentum of the considered lepton $p_T(l)$. The sum is performed over all the objects included in a radius

$$\Delta R = \sqrt{(\Delta\phi)^2 + (\Delta\eta)^2}$$

---

[2] http://cms-results.web.cern.ch/cms-results/public-results/publications/SUS-16-033/index.html

arund the lepton direction. The size of the radius considered depends on the lepton momentum, accounting for an increase in the collimation of the decay product depending on the Lorentz boost of the mother particle:

- $\Delta R \leq 0.2$ for $p_T < 50$ GeV ;
- $\Delta R \leq (10 \text{ GeV } /p_T)$ for $50 \leq p_T \leq 200$ GeV ;
- $\Delta R \leq 0.05$ for $p_T > 200$ GeV.

Electrons and muons are considered isolated if I_e <0.2 and I_μ <0.1, respectively.

The analysis also vetoes isolated tracks, with again isolation requirements depending on the type and momentum of tracks being considered. In particular, the isolation requirement is applied to tracks with a transverse momentum exceeding 5 GeV, and a the transverse mass $m_T(\vec{E}_T^{miss}, \vec{p}_T(track))$ below 100 GeV to eliminate tracks compatible with the decay of a W boson. The isolation variable calculated for a track of transverse momentum p_T is:

$$I_{track} = \frac{\sum_{\Delta R \leq 0.3} |p_T(all\ tracks)|}{p_T}$$

and the isolation must satisfy:

- $I_{track,electron} < 0.2$;
- $I_{track,muon} < 0.2$;
- $I_{track,other} < 0.1$;

where these requirements on tracks help discard events with hadronically decaying tau leptons, and events with electrons and muons that do not pass the identification requirements.

Additional event selections require an angular separation of the azimuthal angle $\Delta\phi(\vec{\not{H}}_T, \vec{p_T})$ between the jets up to the fourth highest p_T jet: the two-highest p_T jets must satisfy $\Delta\phi$ >0.5, while for the 3rd and 4th-highest, if present in the signal jets collection, $\Delta\phi$ >0.3 is required.

The results are interpreted in the context of simplified models, targeting both squark (light and 3rd generation) and gluino production. A total of 174 exclusive, non-overlapping signal regions are defined according to different values of the four kinematic variables above. In addition, 12 'aggregated signal regions' are also defined, for the sake of easing the usage of the analysis for re-interpretation purposes. These signal regions are defined in an inclusive way, so that the same events might fall in more than one signal regions. These aggregated regions were implemented in the recast code and validated.

4.1.4.2 Samples Generation

The CMS collaboration did not provide any specific details about the production of their SUSY Monte Carlo signals, hence it was not possible to tune the sample production. The matrix-element based generator `MadGraph5_aMC@NLO v.2.6.2` [77] was used to simulate the hard scattering process with up to 1 additional parton, and `Pythia 6` took care of the hadronization, showering and decay of the particles. The MLM merging scheme[78, 79] was used, and the parameters $(XQcut, Qcut) = (30, 65), (30, 135)$ were chosen for the case of squark and gluino production respectively. Processes with up to 2 additional partons were also tested and validated, but they did not change sensibly the final results; moreover the production of 2 additional partons lower

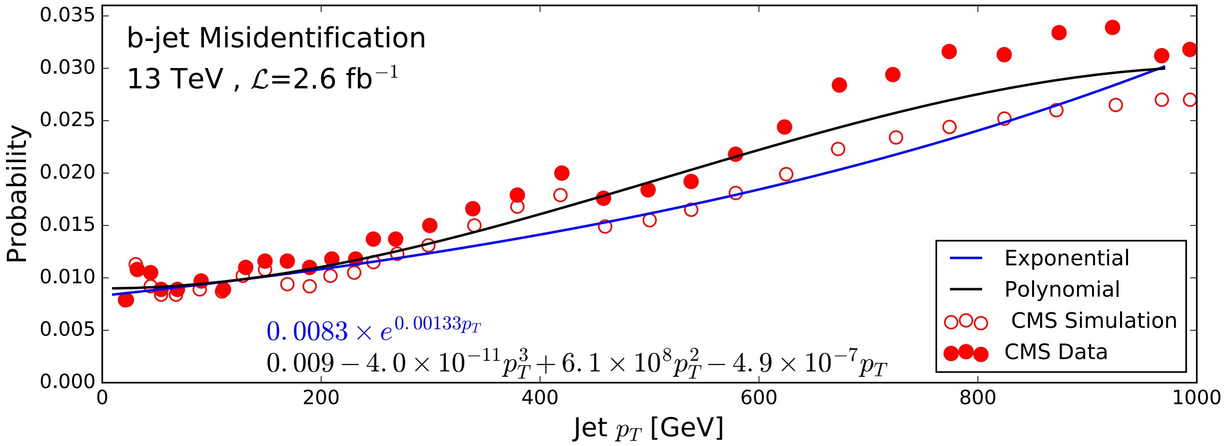

FIGURE 4.1: CMS data (full dots) and simulation (empty dots) for the b-tag misidentification probability, used to extract the indicated fitting formulas, implemented in DELPHES 3.4.0.

the merging efficiency, reducing the sample statistics (for a fixed initial number of matrix element events generated), and more computational time is required to produce enough events to be passed to the analysis recast.

The simulation of the CMS detector response was performed with DELPHES 3.4.0 [63], using FASTJET 3.2.1[69] for the jet clustering. The analysis requires jets clustered with the $anti - k_T$ [80] algorithm, with the requirement $\Delta R = 0.4$. The b-jet tagging efficiency was described with the fitting formula suggested from the CMS collaboration[3], which parametrises the b-tagging efficiency as a function of the jet transverse momentum. The b-jet misidentification probability, was obtained from Fig. 18 in [81] by digitising the data and extracting the fitting formula. The b-jet misidentification probability accounts for the incorrect identification of light jets (especially jets originating from initial charm quarks) or leptonic signatures.

Fig. 4.1 shows the b-tagging misidentification probability using two different fitting formulas extracted from CMS data, as a function of the jet p_T. It can be seen that in the region of low p_T, the probability is around 1 %, while it goes up to around 3% in the region of highly energetic jets. The two fitted formulas, one parametrized with an exponential and the other one with a polynomial curve, show a similar behaviour up to jet $p_T \sim 300$ GeV, while a deviation of around 20% arises when considering the high p_T region. In any case the formulas were obtained based on the CMS simulation which is performed internally by CMS, and both curves show a good level of agreement. For 8 TeV results, as well as more recent 13 TeV, a value of 1% is quoted as the standard magnitude of the misidentification probability. Given the simpler analytical formula, the exponential function was implemented in the DELPHES 3.4.0 card. Nevertheless, also the polynomial formula was tested and compared against the validation data, giving similar results.

4.1.4.3 Validation

In the case of the CMS-SUS-16-033 analysis, the validation material available is quite extensive, and the basic cuts of the analysis with the definition of the key kinematic variables are well described. Details regarding samples generation are however missing, but the overall validation seems in good agreement with the results from CMS. The validation material includes cutflow tables (for the preselection cuts common to all the signal regions), the yields in the aggregated signal regions, and

---

[3] `https://twiki.cern.ch/twiki/bin/view/CMSPublic/SUSICHEP2016ObjectsEfficiency`.

txName	**Model**	**Particles**	**Uncompressed**	**Compressed**
T2	$\tilde{q}\tilde{q}, \tilde{q} \to q\tilde{\chi}_1^0$	$(m_{\tilde{q}}, m_{\tilde{\chi}_1^0})$	(1000,800)	(700,400)
T2bb	$\tilde{b}\tilde{b}, \tilde{b} \to b\tilde{\chi}_1^0$	$(m_{\tilde{b}}, m_{\tilde{\chi}_1^0})$	(650,1)	(500,300)
T2tt	$\tilde{t}\tilde{t}, \tilde{t} \to t\tilde{\chi}_1^0$	$(m_{\tilde{t}}, m_{\tilde{\chi}_1^0})$	(700,50)	(300,200)
T1	$\tilde{g}\tilde{g}, \tilde{g} \to q\bar{q}\tilde{\chi}_1^0$	$(m_{\tilde{g}}, m_{\tilde{\chi}_1^0})$	(1400,100)	(1000,800)
T1bbbb	$\tilde{g}\tilde{g}, \tilde{g} \to b\bar{b}\tilde{\chi}_1^0$	$(m_{\tilde{g}}, m_{\tilde{\chi}_1^0})$	(1500,100)	(1000,900)

Table 4.1: Summary of the simplified model used for the validation of the MA5 recast code for CMS-SUS-16-033. Masses are expressed in GeV.

the kinematic histograms for H_T,$\not{H}_T$, jets and b-tagged jets multiplicity after the preselection cuts. The recast code was validated against the simplified models listed in Tab. 4.1.

For each model the data for two different mass points is available, the first including particles with a large mass splitting between the mother and the LSP, the second with a more compressed mass spectrum. Whenever the LSP is close in mass to the mother, the tuning of the Monte Carlo production becomes more and more important, but unfortunately the CMS collaboration does not provide detailed information about the generation of the samples. Also the systematic error typically increases in this region, due for example to lower experimental sensitivity to soft (low energy) objects, so typically it is difficult to obtain good agreement between official data and recast results in this regions of the parameter space. This is also true for the regions of the tails of the kinematic distributions, where simulations are often problematic.
I omit to include here the complete set of validated results, which can be found in the official validation document [82] on the `MadAnalysis 5` PAD webpage [73], focussing on the *T2* and *T2tt* results.

The comparisons of the kinematic distributions are shown respectively in Figures 4.2 and 4.3, for the n_{jet}, n_b, $H_T$and $\not{H}_T$variables. Similarly to the calculation of signal yields, for each *bin* of the `MadAnalysis 5` distributions, the normalised bin counts bin_n were obtained with:

$$bin_n = \frac{bin \times \sigma \times \mathcal{L}}{N_{events}}$$

where σ is the production cross section, $\mathcal{L}$=35.9 fb^{-1} is the total integrated luminosity, and N_{events} the total number of Monte Carlo events entering the analysis recast after the detector simulation step. The official CMS distributions are plotted with dashed lines, while the `MadAnalysis 5` recast results are superimposed with dots. The distributions are obtained by applying all the pre-selection cuts except the one regarding the variable shown. For example the H_T distribution includes all the cuts in the pre-selection cutflow but the one on H_T itself.

In Fig. 4.2 the results for light squarks are shown, and overall they are in good agreement with the official results, for both the compressed and uncompressed mass scenario. However, a big discrepancy can be seen in Fig. 4.3, where this time the model with large mass gap *T2tt(700,50)* GeV shows very good agreement, while the compressed case *T2tt(300,200)* GeV shows a large discrepancy. To date there is no understanding of the source of this discrepancy. Despite producing samples with large statistics, the `MadAnalysis 5` histograms suffer from lack of events in the tails of the distributions. On a purely speculative level, the mass compressed point data provided might not correspond to $(m_{\tilde{t}}, m_{\tilde{\chi}_1^0})$=(300,200) GeV as indicated by the collaboration, since for all the other models no large difference was found between the compressed and uncompressed mass points.

The validation of the pre-selection cutflow, i.e. cuts common to all the signal regions (aggregated or not), and the aggregated SRs are presented next. Each aggregated SR is defined by a specific requirement for each of the four kinematic variables. Tables 4.2 reports the comparisons of the pre-selection cuts; the numbers report the absolute number of events passing the cut, and the relative drop with respect to the previous cut. In particular, an agreement at the level of $O(\%)$ is found for the absolute values of the efficiency, as well as the relative % drop of each cut in the pre-selection cuts. The only exception is the cut regarding the isolation of leptons for the *T2tt* model, which can be due to the lack of specific information from the CMS collaboration, which does not provide the efficiencies for lepton-veto, but only for the selection of signal leptons. This information is not available and hence the agreement for this cut cannot be improved.

Finally, the Tables 4.4 and 4.5 list the yields in the aggregated signal regions for the *T2* and *T2tt* simplified models. Again, a good overall agreement is found in most of the signal regions, while the discrepancy reaches up to 50% for a few SRs, e.g. the *SR1* of the *T2(700,400)* GeV model point. The discrepancy is not understood, since there is good agreement in the kinematic distributions, and it does not systematically affect all the SRs for all the models. The recast code is now available on `INSPIRE` at [1] and is implemented in the current version of the `MadAnalysis 5` *PAD*; the validation note is available at [82].

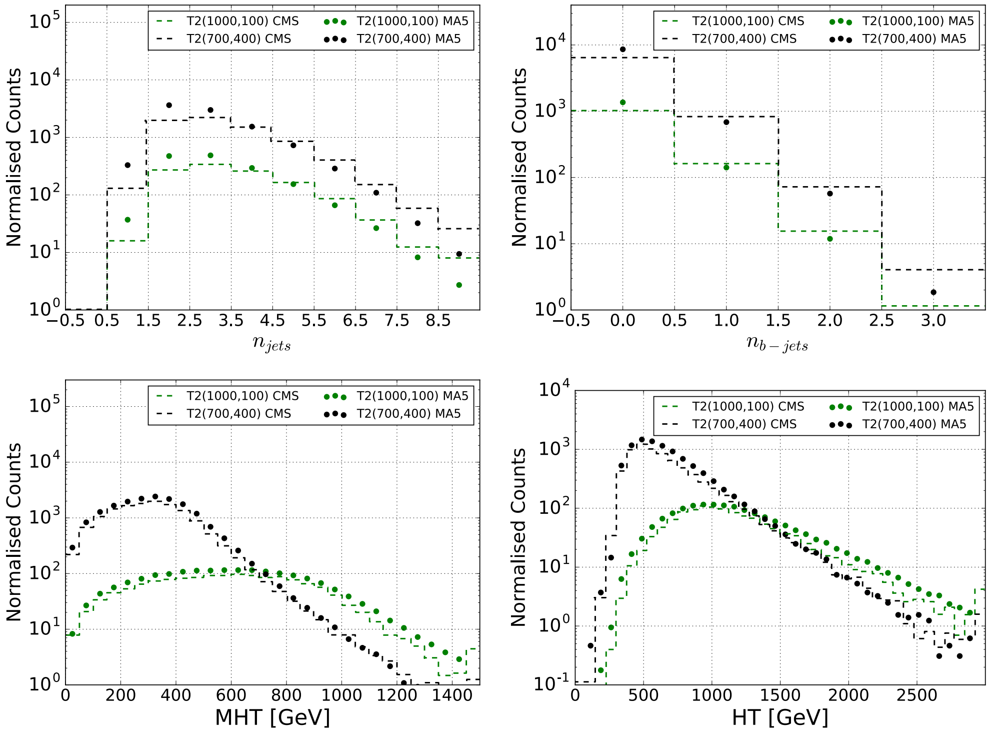

FIGURE 4.2: Validation of the kinematic distributions of the `MadAnalysis 5` implementation of the analysis CMS-SUS-16-033 for the *T2* model.

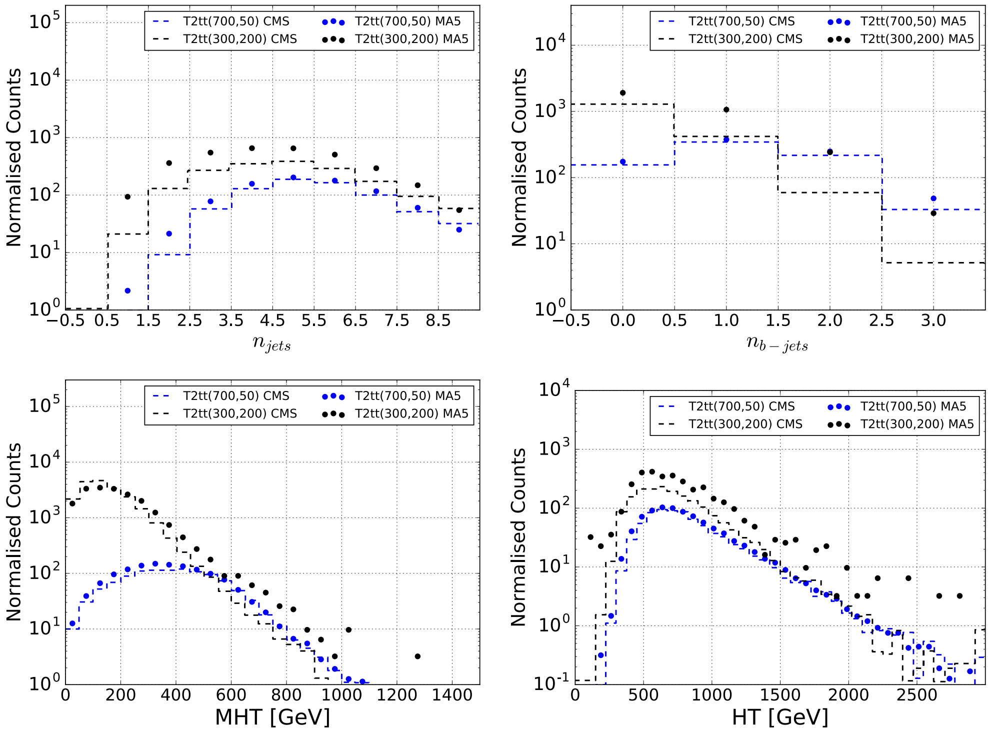

FIGURE 4.3: Validation of the kinematic distributions of the `MadAnalysis 5` implementation of the analysis CMS-SUS-16-033 for the *T2tt* model. See the text for the discussion regarding the large discrepancy for the compressed point $(m_{\tilde{t}}, m_{\tilde{\chi}_1^0})$=(300,200) GeV.

	T2=(700,400)					**T2=(1000,100)**				
	Absolute			Relative		Absolute			Relative	
Cut	**MA5**	**CMS**	**Diff**(%)	**MA5**	**CMS**	**MA5**	**CMS**	**Diff**(%)	**MA5**	**CMS**
n_{jet} ≥2	96.18	98.00	1.86	-3.82	158.58	97.82	98.90	1.09	-2.18	45.66
H_T >300	87.85	91.30	3.78	-8.66	-6.84	97.12	98.60	1.50	-0.72	-0.30
$\not{H}_T$ >300	43.63	43.80	0.39	-50.34	-52.03	79.16	80.00	1.04	-18.49	-18.86
NoIsoMuons	43.63	43.80	0.39	0.00	0.00	79.16	79.90	0.92	-0.00	-0.12
NoMuonsTracks	43.61	43.70	0.20	-0.04	-0.23	79.14	79.80	0.82	-0.03	-0.13
NoIsoElectrons	43.61	43.50	-0.26	0.00	-0.46	79.14	79.60	0.57	0.00	-0.25
NoElectronsTracks	43.59	43.40	-0.45	-0.05	-0.23	79.12	79.30	0.23	-0.03	-0.38
NoIsoTracks	43.44	43.00	-1.03	-0.35	-0.92	78.96	78.70	-0.33	-0.20	-0.76
$\Delta\phi(\not{H}_T$,j1)>0.5	43.41	42.90	-1.19	-0.07	-0.23	78.89	78.60	-0.36	-0.09	-0.13
$\Delta\phi(\not{H}_T$,j2)>0.5	40.97	41.10	0.32	-5.62	-4.20	73.58	74.50	1.24	-6.73	-5.22
$\Delta\phi(\not{H}_T$,j3)>0.3	39.57	39.60	0.08	-3.41	-3.65	70.24	70.60	0.50	-4.53	-5.23
$\Delta\phi(\not{H}_T$,j4)>0.3	38.46	37.90	-1.46	-2.82	-4.29	67.65	67.90	0.36	-3.69	-3.82

Table 4.2: Pre-selection cutflow for the *T2* simplified model.

	T2tt=(300,200)					**T2tt=(700,50)**				
	Absolute			Relative		Absolute			Relative	
Cut	**MA5**	**CMS**	**Diff**(%)	**MA5**	**CMS**	**MA5**	**CMS**	**Diff**(%)	**MA5**	**CMS**
n_{jet} ≥2	72.96	86.90	16.05	-27.04	11804.11	98.90	99.80	0.90	-1.10	213.84
H_T >300	15.71	23.30	32.58	-78.47	-73.19	92.30	96.40	4.25	-6.67	-3.41
$\not{H}_T$ >300	3.34	2.84	-17.64	-78.73	-87.81	54.13	57.80	6.35	-41.36	-40.04
NoIsoMuons	2.69	2.16	-24.38	-19.58	-23.94	48.16	46.60	-3.35	-11.02	-19.38
NoMuonsTracks	2.61	2.10	-24.17	-2.94	-2.78	47.74	46.10	-3.55	-0.88	-1.07
NoIsoElectrons	2.17	1.60	-35.65	-16.77	-23.81	43.32	37.40	-15.82	-9.26	-18.87
NoElectronsTracks	2.07	1.52	-36.13	-4.66	-5.00	42.78	36.90	-15.94	-1.23	-1.34
NoIsoTracks	1.97	1.41	-39.88	-4.68	-7.24	42.16	35.80	-17.77	-1.45	-2.98
$\Delta\phi(\not{H}_T$,j1)>0.5	1.97	1.40	-40.58	-0.21	-0.71	42.03	35.70	-17.74	-0.30	-0.28
$\Delta\phi(\not{H}_T$,j2)>0.5	1.40	1.03	-36.04	-28.80	-26.43	40.03	34.00	-17.73	-4.77	-4.76
$\Delta\phi(\not{H}_T$,j3)>0.3	1.15	0.85	-35.35	-17.89	-17.48	38.77	33.10	-17.13	-3.14	-2.65
$\Delta\phi(\not{H}_T$,j4)>0.3	1.06	0.73	-45.34	-7.78	-14.12	35.45	31.80	-11.48	-8.56	-3.93

Table 4.3: Pre-selection cutflow for the *T2tt* simplified model.

	T2(700,400)		**T2(1000,100)**	
Aggregated Signal Region	**MA5**	**CMS**	**MA5**	**CMS**
SR1-Njet2-Nb0-HT500-MHT500	1620.33	1055.38	988.50	729.30
SR2-Njet3-Nb0-HT1500-MHT750	22.23	25.55	84.27	58.40
SR3-Njet5-Nb0-HT500-MHT-500	279.11	337.33	152.72	179.20
SR4-Njet5-Nb0-HT1500-MHT750	14.51	18.24	29.50	27.98
SR5-Njet9-Nb0-HT1500-MHT750	0.15	1.03	0.68	1.16
SR6-Njet2-Nb2-HT500-MHT500	17.75	16.87	9.41	11.60
SR7-Njet3-Nb1-HT750-MHT750	17.44	21.71	46.10	50.15
SR8-Njet5-Nb3-HT500-MHT500	0.62	0.94	0.49	0.56
SR9-NJet5-Nb2-HT1500-MHT750	0.31	0.78	1.24	1.13
SR10-Njet9-Nb3-HT750-MHT750	0.00	0.05	0.01	0.04
SR11-Njet7-Nb1-HT300-MHT300	39.52	59.26	10.06	16.50
SR12-Njet5-Nb1-HT750-MHT750	10.19	13.41	17.30	21.82

Table 4.4: Aggregated signal region yields for the *T2* simplified model.

	T2tt(300,200)		**T2tt(700,50)**	
Aggregated Signal Region	**MA5**	**CMS**	**MA5**	**CMS**
SR1-Njet2-Nb0-HT500-MHT500	254.46	133.03	65.04	59.80
SR2-Njet3-Nb0-HT1500-MHT750	22.55	4.11	1.96	1.38
SR3-Njet5-Nb0-HT500-MHT-500	132.06	81.48	39.23	38.63
SR4-Njet5-Nb0-HT1500-MHT750	22.55	3.84	1.45	1.08
SR5-Njet9-Nb0-HT1500-MHT750	9.66	0.58	0.23	0.26
SR6-Njet2-Nb2-HT500-MHT500	48.32	10.15	106.59	95.29
SR7-Njet3-Nb1-HT750-MHT750	41.87	7.26	22.58	21.46
SR8-Njet5-Nb3-HT500-MHT500	6.44	0.92	17.76	11.34
SR9-NJet5-Nb2-HT1500-MHT750	0.00	0.83	2.44	2.29
SR10-Njet9-Nb3-HT750-MHT750	0.00	0.06	0.29	0.30
SR11-Njet7-Nb1-HT300-MHT300	296.34	192.22	183.37	152.21
SR12-Njet5-Nb1-HT750-MHT750	32.21	5.60	16.44	15.66

Table 4.5: Aggregated signal region yields for the *T2tt* simplified model. See the text for a discussion of the large discrepancy found for the compressed *T2tt(300,200)* GeV model.

4.2 Making Systematic Use of Simplified Models Results with `SModelS`

Section 3.2.2 described how the LHC collaborations make extensive use of simplified models to interpret the outcome of the searches for new physics. The big limitation of such interpretations however lies in the rigid assumption that the decay pattern of the model is fixed with 100% BR, while the contributions of all the remaining decoupled sparticles can be neglected. This does not apply in generic models, where the complex particle spectra increase the number of allowed decays. It is thus nontrivial to use SMS results to constrain generic BSM theories.

Nevertheless, since SMS represent a small subset of a full model, it is possible to decompose a theory into a set of simplified models. Taking as example the R-Parity conserving MSSM, for each SUSY process, e.g. gluino pair production, all the possible decay patterns of the gluino to the LSP must be considered; each of them map onto a specific simplified model. This is called *decomposition* procedure, and it consists of extracting all the possible simplified models from the general theory considered, by taking into account all the possible possible production channels and all the possible decay modes. Each mode will have a proper theoretical cross section times branching ratio $\sigma_{th} \times BR$, called *weight*. Once the correct weight of each simplified model has been calculated, it is straightforward to compare the theoretical prediction with cross section upper limits from the LHC experiments.

The procedure described above in an automatic fashion is the central idea behind `SModelS` . This tool, written in python, allows to automatically decompose an input BSM model with a $\mathbb{Z}_2$ symmetry into its SMS components, calculate the proper theory prediction and confront it with the results from BSM searches from the LHC experiments. Contrary to the method of a full recast, this procedure has the big advantage that if the input model can be provided in a standard SLHA format, no Monte Carlo simulation is required. This is very practical when testing high-dimensional parameter spaces, like in the case of the MSSM.

Before detailing on the main characteristics of `SModelS` , the concept of *'SMS assumptions'* must be introduced, since it lies at the very basis of the `SModelS` idea. It is assumed that the sensitivity of searches for SUSY, or BSM particles, mostly depends on the masses of the new states. Effects coming from other properties such as the color structure, the spin, or other quantum numbers can be neglected and should not strongly affect the sensitivity of an experimental search. This is a valid approximation for SUSY analyses with a classical cut-and-count approach, since most of the time the selection cuts only depend on global properties such as the momentum or multiplicity of SM particles, that are expected to depend primarily on the masses of the BSM states they originate from. `SModelS` approach relies strongly on the SMS assumption for the decomposition and comparison with the experimental limits, restricting the number of important properties of the model to the $\sigma_{th} \times BR$ and mass array of the model considered.

For the rest of the discussion the R-parity conserving MSSM will be used, but the concepts can be extended to any model with the required $\mathbb{Z}_2$, i.e. any model with pair production of BSM particles that decay promptly in the detector up to the stable DM candidate. SUSY particles are $\mathbb{Z}_2$-odd states, while SM particles are $\mathbb{Z}_2$-even; this means that for `SModelS`, the vector bosons and the top quarks are considered final state particles, as well as bottom and charm quarks, muon and tau leptons.

A complete description of the `SModelS` tool and database can be found in [83](v1.0) and [2](v.1.1)[4] In the following I will only introduce the main aspects of the `SModelS` working principles, and will focus on the new features introduced in v1.1 of the database.

Txnames Convention

`SModelS` uses a naming convention which was borrowed and adapted from the CMS collaboration[46], as seen for example in the summary plots in Section 3.2.4; simplified models are called *'Txnames'*. All the *'Txnames'* that will be relevant in this work are summarised in Appendix A; a more complete characterisation of the SMS in `SModelS` can be found on the dedicated wiki page [85].

Models where the particle produced by the proton-proton interaction decays directly to the LSP are referred to as *direct decays*; models where the SUSY particles produced decay via intermediate states with several steps up to the LSP, are called *cascade decays.* In particular, in *1-step cascade decays*, the produced SUSY particles decay to one intermediate SUSY state, that must then decay to the LSP.

While there are no strict prescriptions to build Txnames for given simplified models, a general set of rules that help identify the models is the following:

- squark simplified models are named *'T<number>_SM_SM'* , where *number*=(2,6) for direct and 1-step cascade decays respectively;
- gluino simplified models are named *'T<number>_SM_SM'* , where *number*=(1,5) for direct and 1-step cascade decays respectively;
- slepton simplified models are named *'T_slepton_slepton'*, where *slepton* include either combination of particles like selectrons and smuons, or can be one specific species like 'stau';
- gauginos simplified models are named *'T_Chi'*, followed by various gauginos/SM bosons or sleptons/leptons.

Note that the CMS collaboration defines also models starting with *T3* and *T4* for asymmetric gluino and squark models, where the first branch has a direct decay while the second branch has a cascade decay to the LSP. Such models however are not present in the database.

To give a few examples, the *T2bb* Txname refers to a squark pair production for which the squark decays directly to a bottom quark and the LSP; *T6ttWW* refers to a pair production of squarks that decay to a top quark and intermediate SUSY particle, that then decays into a W boson and the LSP. In both cases, a possible model could be a sbottom production followed by a direct decay (former), or that undergoes a 1-step decay to a top plus chargino (latter). Note that, since in the `SModelS` framework and in the simplified model assumption all the quantum numbers are neglected, there could be several SUSY processes mapping onto the same Txname.

The Txnames for gauginos and sleptons simplified models are less intuitive; the simplest model *'TChiWZ'* corresponds to a charginos/heavy neutralinos production, followed by the direct decay to W/Z vector bosons and the LSP, while *'TSlepSlep'* to a generic slepton pair production (selectrons, smuons or staus), decaying to the corresponding SM lepton and the LSP. All the Txnames will be explained when introduced, as well as the names of asymmetric models which do not follow any particular rule.

---

[4] An extension of the database, including the latest CMS results at 13 TeV was made public in [84].

4.2.1 The SModelS Principles

I will now give a general description of the basic principles at the basis of the `SModelS` tool. The workflow of the entire procedure is schematically depicted in Fig. 4.4.

The chain starts with an input model that can be provided in the form of an SLHA[86] or LHE[87] file. The former contains the mass spectrum of the BSM particles, together with information on the quantum numbers, decay widths, branching ratios etc.; the latter is a standardized type of file containing events at the parton level produced by Monte Carlo generators. While SLHAs files are certainly the preferred format, since they do not require long computing time for the Monte Carlo simulation, they cannot be used for completely arbitrary BSM models.

The LHE files produced by generators typically contain the information of the production cross sections, while in the case of SLHAs, the information must be added to the files. For this purpose, `SModelS` provides a utility called `xseccomputer`: it calculates the cross sections of the relevant SUSY processes and adds them to the files in separate blocks for each production mechanism, according to the established convention for the SLHA format. The cross sections are calculated using `PYTHIA6`[88] or `PYTHIA8`[66] at leading order in perturbative expansion, while `NLLfast`[89, 90] can be used for strong production up to next-to leading logarithmic order. If the files contain cross sections at different order of perturbative expansion, the highest order will be considered. The cross section information is required for the calculation of the weights and thus the final comparison with the experimental limits.

The input file must first pass a series of preliminary checks, for example the absence of stable charged BSM particles that would produced characteristics signature in the detector. Then the file is decomposed into its SMS. The SUSY pair production cross section are read, and for each mother particle in the two branches, all the possible decay modes up to the LSP are considered. The value of the $w = \sigma \times BR$ is calculated and updated at each sparticle decay. The parameter `sigmacut` can be set by the user to discard elements with $w = \sigma \times BR \leq$ `sigmacut`, that will not be decomposed further; because of their very low weights, these SMS could not be anyhow constrained by any experimental search. The default value is `sigmacut`=0.03 fb. This parameter is important since it majorly influences the computational time required to complete the decomposition, otherwise the full decomposition might take several minutes in the case of complex mass spectra.

Finally, the theory prediction is compared against the results contained in the `SModelS` database, in the form of upper limit (UL) or $(\mathcal{A} \times \epsilon)$ maps (EM), to determine if the model can be excluded by one or more SMS results.

In Appendix B, more details about how to run `SModelS` with a concrete example can be found, as well as the main parameters that can be set by the user in the `parameters.ini` input card.

The entire `SModelS` procedure makes use of important objects called *elements*, that will be now described.

Elements

The main building block of the `SModelS` decomposition procedure is called *element*, of which an example is sketched on the left diagram in Fig. 4.5. An element is characterised by two branches, one for each of the pair-produced SUSY particles, with an associated σ_{th}.

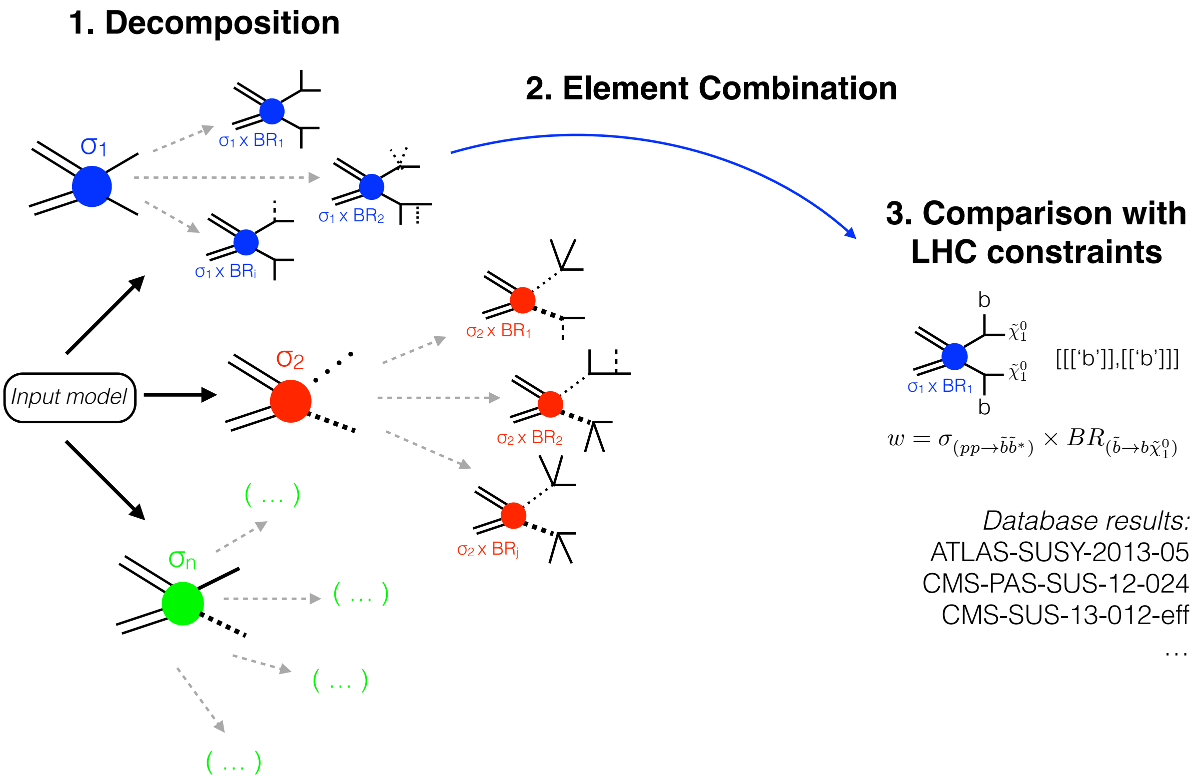

FIGURE 4.4: Workflow of the `SModelS` working principle. The input file (SLHA or LHE), containing the BSM particle spectrum, the pair production cross section and the branching ratio information, is decomposed into a set of elements, each of them characterised by a proper $w = \sigma \times BR$. The elements are eventually clustered and the theory prediction is calculated. Finally the element are confronted against the experimental results in the database.

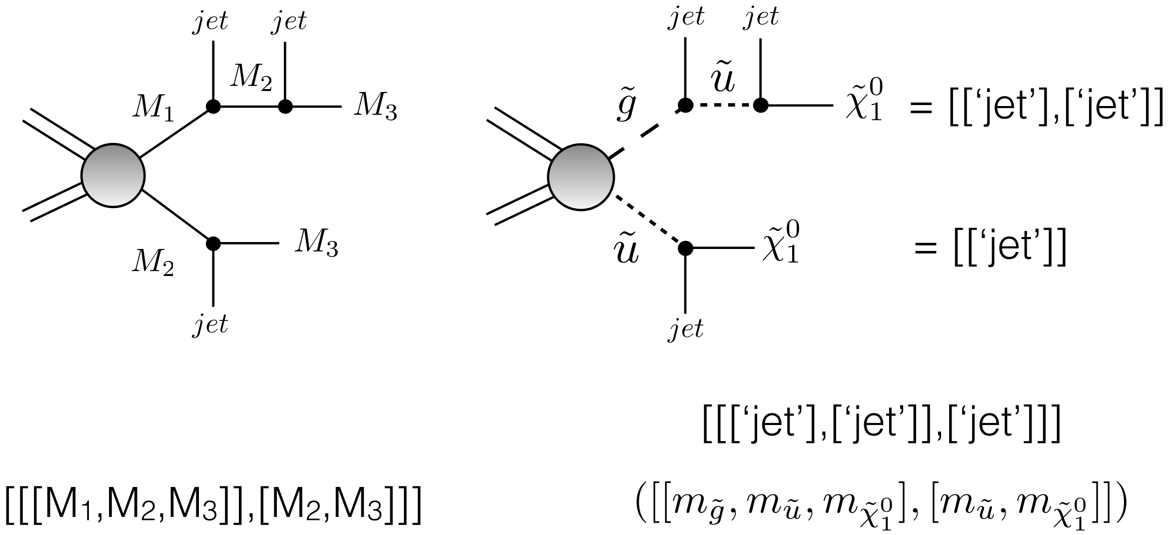

FIGURE 4.5: On the left, an example of *element*, the building block of `SModelS` decomposition procedure. The structure underneath the element, characterised by the mass array and the vertices with the insertion of the SM particles, is called topology. On the right, one of the possible simplified models that can be mapped to the described element, with the corresponding identification by the bracket notation of each branch. The parameter space of the model consists of three dimensions.

According to the sketched element, the mother particle (M_1) will decay with a 100% BR, to some SM hadronic particle forming a jet particles plus other intermediate SUSY (I) in the upper branch, while (M_2) decays directly to the LSP in the lower branch. Under the SMS assumption, this model is completely determined by the mass arrays *[Mother,Intermediate,LSP]* and *[Mother,LSP]*, the branching fractions ($M \to I, I \to LSP$) and ($M \to LSP$), and the pair production cross section. In terms of masses, it covers a 3-dimensional parameter space. Each branch is also characterised by a number of vertices, holding the information of the SM particles that originate in the decay. These SM particles form the targets of the searches at the LHC (for example, leptons, jets, photons etc.), along with the missing energy due to the LSP. The branches, the vertices and the SM particles identify a structure called *topology*.

A dedicated *bracket notation*, consisting of a 3-level nested series of squared brackets, was developed to unambiguously identify the elements by listing the particles in the vertices of each branch. For the case illustrated here, it is an asymmetric model where in each vertex the SUSY particle decays to a jet, written as *[[['jet'],['jet']],['jet']]]*. This notation is called *constraint*, and it corresponds to the SM final state of the simplified model. The v.1.1 of `SModelS` can only deal with signatures with missing energy, which is omitted in the constraint.

The diagram on the right of Fig. 4.5 shows a concrete simplified model that can be identified by that element and constraint, for example a gluino-squark associated production decaying to hadronic particles and the LSP. However this is just one of the possible simplified models that can be mapped to the *[[['jet'],['jet']],['jet']]]* constraint. In fact, one simplified model can be mapped to strictly one constraint, but one constraint can correspond with multiple simplified models. From an experimental point view it means that the same signature can constraint several different BSM signals. The upper branch *[['jet']],['jet']]* can map to the gluino production followed by the decay into the intermediate squark, where the *['jet']* is inserted, and the decay to the LSP with the last *['jet']* insertion.

Before comparing with the experimental limits, a series of procedures are applied to the decomposed elements. Depending on the mass spectrum of the BSM particles appearing in an element, and on the type of SM particle in the vertices, it is possible to compress elements. The *mass compression* reduces a complex element to a simpler one, reducing by one unit the dimensionality of the BSM mass array characterising the element; for example, a compressed 2-steps decay model will reduce to 1-step decay. This is helpful due to the intrinsic limitation of the number of free parameters reasonable for simplified models. Currently there are no models with more than three free mass parameters implemented in `SModelS`; examples of such 3-dimensional mass parameters models are e.g. all the *T5*** models for gluino production, *T6*** models for squark production or the asymmetric gluino-squark associated production *T3GQon*.

Mass compression

If an element includes the decay of two BSM states close in mass, the SM particles in the vertex will have a small momentum. They will fall outside the detector sensitivity and will act for all practical purposes as invisible particles; in this case, one element can be mass compressed. This is schematically drawn in Fig. 4.6.

In the compressed element, the BSM state of mass M_j is replaced by the element of mass M_{j+1}

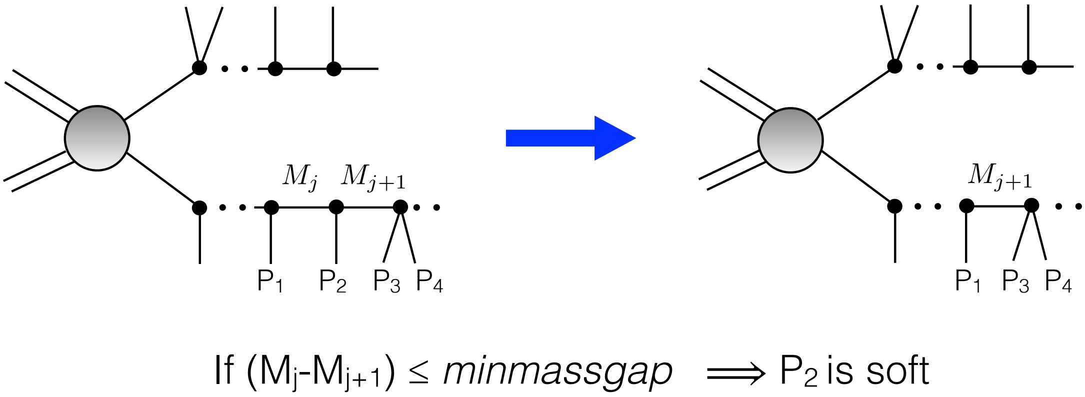

FIGURE 4.6: Mass compression of an element: if $M_j - M_{j+1} \leq$ *minmassgap*, the SM states P are considered too soft for detection. The BSM states with M_j is then replaced by M_{j+1}.

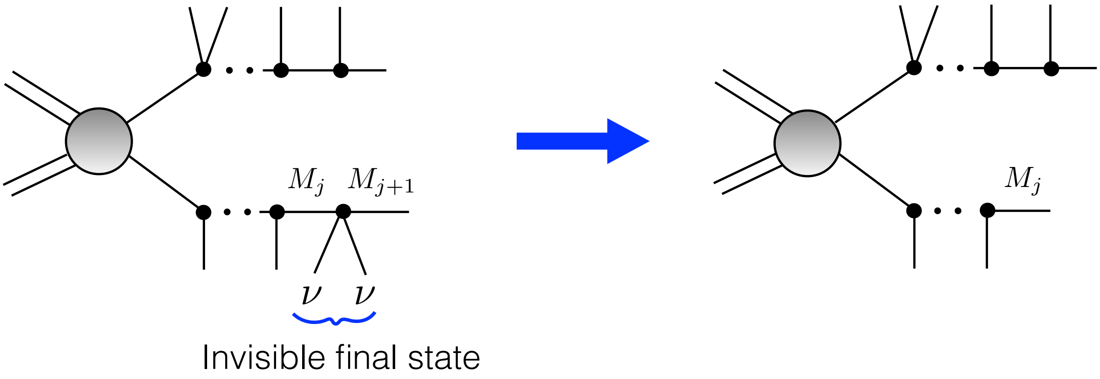

FIGURE 4.7: Invisible compression of an element, only possible at the end of the decay chain.

which followed in the original decay chain, and the intermediate state M_j as well as the invisibile SM particle P are removed. The user is allowed to choose if the mass compression should be activated, with the parameter doCompress, and to specify the value when it is applied with the parameter minmassgap in the `parameters.ini` input card. By default, `minmassgap` $= 5$ GeV, meaning that whenever $M_{j+1} - M_j \leq 5$ GeV, the element will be mass compressed. However it should be noted that in case of boosted (high p_T) BSM particles, the validity of the assumption should be verified. More details can be found in Appendix B.

Invisible compression

The other type of element reduction is called invisible compression; this happens when the particles appearing in a vertex are invisible, for example neutrinos, acting as missing energy of the events (Fig. 4.7). This compression is only possible at the end of a decay chain. The invisible mass compression is activated by parameter *doInvisible* in the input card `parameters.ini`.

4.2.2 Theory Predictions and Comparison with Experimental Limits

After the decomposition procedure, a series of elements is obtained. While each element owns a specific $w = \sigma \times BR$, additional steps have to be taken to obtain the total theory prediction to be compared with the limits in the database. In particular there are differences in the calculation of predictions for the UL and EM results.

Upper Limits Results

To compute the theory prediction, elements must be first selected and then clustered. The *element selection* procedure is common for both UL and EM results, and it consists of selecting the elements that can be mapped to an experimental result in the database. As an example, frequently the results for sleptons searches are interpreted combining electron and muon signatures, and the constraint can be written as *[[['l']],[['l']]]* with $l = (e, \mu)$. The elements *[[['e']],[['e']]]* and *[[['μ']],[['μ']]]* in the decomposition can be constrained by such results but only if combined together, so that effectively one has to calculate the sum of the two elements *[[['e']],[['e']]]+[[['μ']],[['μ']]]*.
However this is possible only if the mass arrays of the elements are equal, or almost equal, since the results in the database assume that the mother particle mass is the same for all the elements. Nevertheless small mass differences should be allowed since they are not expected to have a large impact on the limits. The definition of 'similar' mass array is implemented by requiring that the quantity:

$$\begin{aligned}\text{Element } A\ (M_A = [[M1, M2, ...], [m1, m2, ...]]) \rightarrow\ \text{Upper Limit}(M_A) = u_A\\ \text{Element } B\ (M_B = [[M1', M2', ...], [m1', m2', ...]]) \rightarrow\ \text{Upper Limit}(M_B) = u_B\\ \Rightarrow \text{mass distance}(A, B) = \frac{|u_A - u_B|}{(u_A + u_B)/2}\end{aligned} \tag{4.8}$$

is smaller than an arbitrary maximum value called *maxDist*. The quantity above takes into account the limits for the two different mass arrays extracted from the database, and if the condition *mass distance(A,B)<maxDist* is verified, then the elements are clustered and the corresponding weights added together. It is also checked that masses with very different values but similar upper limits are not clustered together.

The final step is the comparison with the results with UL maps. Trivially, the 95%CL upper limits on the production cross section are looked up in the database (one for each experimental results that can be applied to the clustered element), and compared with the total theory prediction. The parameter *r-value* is calculated as:

$$r = \frac{\sigma_{th}}{UL} \tag{4.9}$$

and if $r \geq 1$, the model is considered excluded at 95% CL by the specific experimental result. The `SModelS` output will report the r-value and the theory prediction for each different cluster.

Efficiency Maps Results

Contrary to the case of UL, which can be used to constrain only one specific topology at a time, EMs results from a single signal region can be combined together, to reconstruct the total signal efficiency by adding up the contribution of the different simplified models.

As explained Section 4.1, the $(\mathcal{A} \times \epsilon)$ of a BSM signal is defined as the number of events passing all the cuts characterising a specific signal region, normalised by the number of generated events. The expected yield of a signal can be calculated as the product of the efficiency times the luminosity and the production cross section:

$$\epsilon \times \mathcal{L} \times (\sigma \times BR) \equiv \sigma_{vis} \times \mathcal{L} \tag{4.10}$$

where σ_{vis} is called visible cross section.

The total efficiency of an input model can be decomposed in the product of $\mathcal{A} \times \epsilon_i$ of each simplified model appearing in the decomposition. After selecting the elements that can be constrained by the EM results, the total number of SUSY events of the model in each SR can be reconstructed as

$$N^{SR} = \sum_i \epsilon^{SR} \times (\sigma_i \times BR) \times \mathcal{L} \equiv \sigma_{vis}^{SR} \times \mathcal{L}, \tag{4.11}$$

where $\sum_i \equiv \sum$ *over all the topologies* . In other words it is possible to "reconstruct" the total signal of a SUSY model, and a better signal reconstruction is obtained if, for a given analysis, efficiency maps are available for several SMS. The combination of the signals is possible only within each signal region of each analysis[5].

In the case of EM, there is no need for clustering of the element according to their mass arrays, since the mass difference of the various elements are accounted for by the different values of the efficiencies. Once the visible cross section σ_{vis} has been computed, it is possible to compare this value with the observed upper limit on the visible cross section for each SR. Such UL is either provided directly from the experimental collaboration, or can be computed with the simplified *CLs procedure*(see Section 4.1.2), using for each SR the information of the observed number of events n_{obs}, the number of expected background events n_{bkg} and its uncertainty Δn_{bkg}. By assuming $n_{obs} = n_{bkg}$, i.e. by considering no BSM signal, the expected UL is calculated, based only on the SM background estimation. Both the expected and observed upper limits are stored in the database, and calculated at the time of implementation of the analysis in the database if not provided directly in the experimental papers.

Finally, the r-value:

$$r^{SR} = \frac{\sigma_{vis}}{\sigma_{ul}^{SR}} \tag{4.12}$$

is computed. Among the several search regions that are available, the one which maximises the ratio $\sigma_{vis}/\sigma_{UL}^{exp}$ is called *best signal region* (best SR). The observed UL for this best SR will be used to determine the exclusion of the point. The ratio $\sigma_{vis}/\sigma_{UL}^{obs}$ for the best SR is computed, and if $r \geq 1$ the model points is considered excluded the analysis. To summarise: the point is excluded if σ_{vis} exceeds the value of the observed UL for the signal region providing the best expected UL.

Currently the `SModelS` database contains EMs results from three different sources:

- official ATLAS and CMS results;
- EMs produced by the `Fastlim` collaboration;
- ‘homegrown’ EMs (described in Section 4.3).

---

[5] The combination of signal regions is possible for a few selected 13 TeV CMS analyses starting from `SModelS` v1.1.3.

4.2.3 Missing Topologies

Testing the input model against the available experimental results in the database is the essential feature of `SModelS` , but it is not the only relevant physics information one can obtain. Equally interesting is in fact the characterisation of the elements that currently escape simplified model constraints, due to the lack of the relevant topologies in the database: we call this class of models *missing topologies*. A dedicated coverage module, selected by assigning *testCoverage=True* in the `parameters.ini` input file, returns a list of the most relevant missing topologies, sorted by weight $w = \sigma \times BR$. Elements are further classified into two categories:

- *longCascade*: elements that have more than two intermediate sparticles in one of the branches (i.e. equal or longer than 2-steps cascade decays);
- *asymmetricBranches*: elements where the two branches are different.

Note that these two categories are exclusive, meaning that *longCascade* models do not enter the *asymmetricBranch* category, and vice versa.

How the information from the coverage module can be used for extending the `SModelS` database and improve the constraints on a tested model will be concretely shown in Chapter 5. There I will stress how EMs for a specific simplified model, created with recasting tools, provide additional constraints to the pMSSM. However the available recast analyses might not be sensitive enough to the signatures of the missing topologies to constrain the model. Missing topologies, nevertheless, could be used as a guide by the experimental collaboration for testing new simplified models interpretation for existing searches, or desirably for designing new searches that cover unexplored regions of the parameter space.

Finally, the mass array of the decomposed element might fall outside the interpolated grid of some experimental results in the database. In this case, the model will appear in the *outsideGrid* list, i.e. simplified model results for which the parameter space is not sufficiently well covered by the available results.

4.2.4 `SModelS` Database

In this Section the content of the `SModelS` database is described. The database is a structured collection of text files, organised in a fixed scheme of nested directories, that contain both the experimental results, in the form of upper limits and efficiency maps, and useful accessory information regarding the analysis. The schematic structure of the directories in the database is shown in Fig. 4.8.

The database is divided according to the centre-of-mass energy of 8 and 13 TeV, and further split into ATLAS and CMS results. In v1.1, all the 8 TeV results from the ATLAS and CMS collaboration are included, with the following requirements. Whenever a cascade decay is considered, only results with at least three mass planes are included, with the exception of a few topologies for which we allowed the presence of two mass planes only, for reasons of backward compatibility with previous releases. Several mass planes are necessary to ensure that the interpolation procedure is performed between points that are reasonably close in mass, so that the limits or efficiencies are supposed to vary linearly with no large fluctuations. However in some cases even when three mass planes are available, large fluctuations can be found; this will be discussed for EM results in Chapter 6.

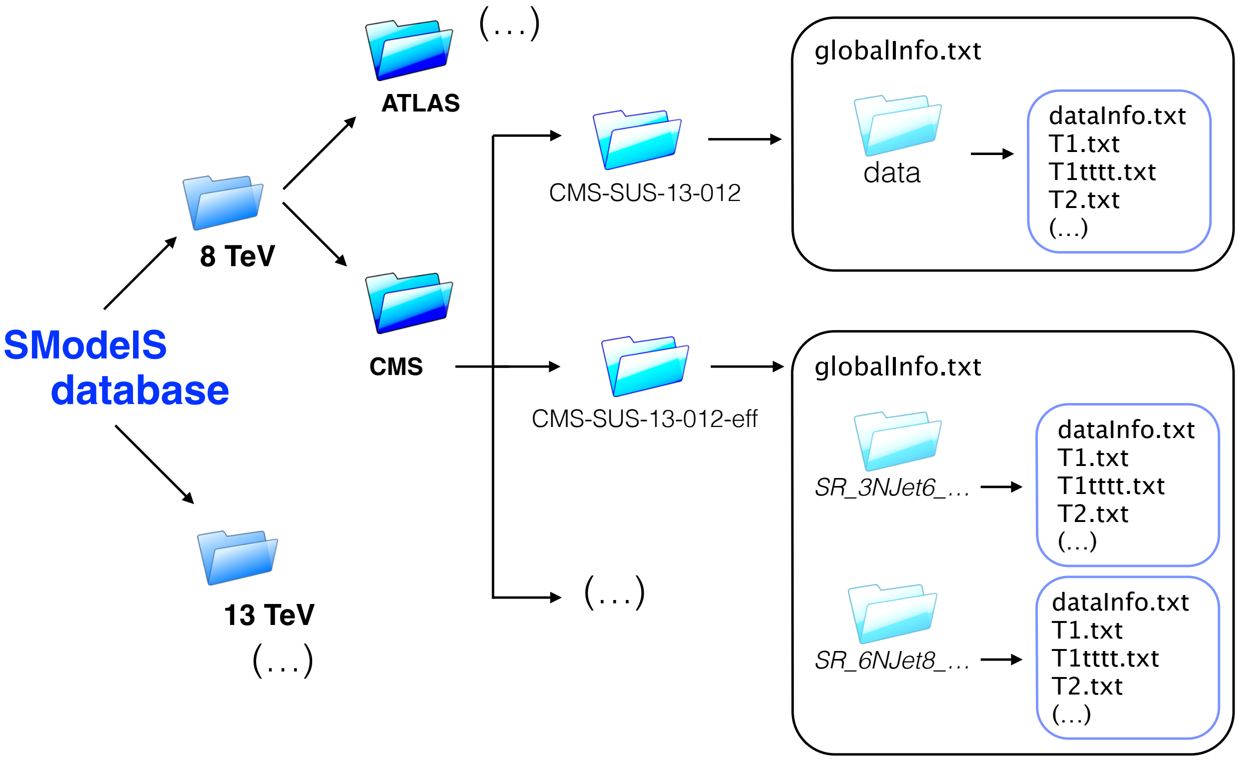

FIGURE 4.8: Schematic view of the structure of the `SModelS` database.

Taking as an example the 8 TeV CMS sub-directory, a list of folders named after the official CMS analyses names can be found. In the case of EMs results, the suffix *'-eff'* is attached to the analysis name, so that e.g. the directories *'CMS-SUS-13-012'* and *'CMS-SUS-13-012-eff'* contain the UL and EM results respectively. For UL results, only two files are found in each analysis directory: the *'data'* folder and the *'globalInfo.txt'* text file. The *'globalInfo.txt'* file contains the general information about the analysis, e.g. the official wiki page or `hepData` urls where the information was collected, the *arXiv* or publication links, the luminosity, the name of the person who implemented the analysis:

```
id: CMS-SUS-13-012
sqrts: 8.0*TeV
lumi: 19.5/fb
url: https://twiki.cern.ch/twiki/bin/view/CMSPublic/PhysicsResultsSUS13012
arxiv: http://arxiv.org/abs/1402.4770
publication: JHEP06(2014)055
contact: cms-pag-conveners-sus@cern.ch
implementedBy: Federico A
lastUpdate: 2016/9/29
```

The 'data' directory contains the UL results for each Txname available in text files named as '<Txname>.txt'.
In the case of EMs, the summary file *'globalInfo.txt'* contains the same information as in the case of UL results. The 'data' folder however is replaced by a series of 'datasets' directories, each of them named after a specific signal region defined by the analysis. Inside each dataset directory, a file called *'dataInfo.txt'* summarises the most important information regarding the dataset:

```
dataId: SR_3NJet6_500HT800_200MHT300
dataType: efficiencyMap
observedN: 6159
expectedBG: 6088
```

```
bgError: 665
upperLimit: 69.5*fb
expectedUpperLimit: 67.3*fb
```

The values of the observed number of events, the expected background and its uncertainty are inserted (taken from the official publication), and used to calculate the expected and observed signal region (*'dataId'*) upper limits if not provided in the experimental papers. Note that this file is also present in the 'data' folder for UL results, with only the entries *'dataType: upperLimit'* and *'dataId: None'* since the datasets are not defined for UL results.

As an example, the 'T2.txt' efficiency maps data looks like:

```
txName: T2
constraint: [[['jet']],[['jet']]]
condition: None
conditionDescription: None
figureUrl: https://twiki.cern.ch/twiki/pub/CMSPublic/PhysicsResultsSUS13012/Fig_7a.pdf
source: CMS
validated: True
axes: [[x, y], [x, y]]
efficiencyMap: [[[[3.1250E+02*GeV,1.2500E+01*GeV],[3.1250E+02*GeV,1.2500E+01*GeV]],0.025849],
[[[3.1250E+02*GeV,6.2500E+01*GeV],[3.1250E+02*GeV,6.2500E+01*GeV]],0.024862], (...)
```

The first lines report the *Txname* naming convention used by `SModelS` , and the corresponding constraint in the bracket notation language. The *'condition'* and *'conditionDescription'* are used whenever restricting conditions should be applied when using these constraints to generic BSM models according to the details of the search. The 'source' field describes the origin of the results, that can be ATLAS or CMS, `Fastlim` or `SModelS` for homegrown efficiency maps. Finally, the field *'efficiencyMap'* (*'upperLimits'*) contains the values of the efficiency (cross section upper limits) for the mass points available, according to the convention described in *'axes:[[x, y], [x, y]]'*, where in this case x and y are the mother particle and the LSP respectively.

Interpolation

The first time the database is loaded, a series of operations is performed as a first step before using it for testing models. In particular a pickle file is built out of the text files contained in the database providing the values of the upper limits and efficiencies. Not only will this render the loading of the database much faster for the follow-up use of `SModelS`, but it also includes the preparatory steps necessary to interpolate between the discrete grid of mass points contained in the files. Specifically, a principal component analysis and Delaunay triangulation are performed. The results for arbitrary mass vector belong to 'convex hull' individuated by the simplices can be computed via linear interpolation. More detailed information can be found on the online manual at [6].

List of 8 TeV Analyses Included in v.1.1

A list of 8 TeV analyses implemented in the `SModelS` database v1.1 is provided in this Section. The ATLAS directory contains many preliminary results, that were superseded by final publications; the published analyses are listed in Tab. 4.6. For several CMS preliminary analyses however more updated results are not available, and the complete list can be found in Tab. 4.7. Both lists of analyses include official results in the form of UL and EM, and homegrown results.

---

[6] `http://smodels.readthedocs.io/en/latest/DatabaseStructure.html`

Published ATLAS Analyses in `SModelS` Database v1.1

Analysis	**Ref.**	**ID**
Gluino and Squark		
0-lepton + 2–6 jets + E_T^{miss}	[91]	SUSY-2013-02
0-lepton + 7–10 jets + E_T^{miss}	[92]	SUSY-2013-04
SS/3-leptons + jets + E_T^{miss}	[93]	SUSY-2013-09
0/1-lepton + 3b-jets + E_T^{miss}	[94]	SUSY-2013-18
1-lepton + jets + E_T^{miss}	[95]	SUSY-2013-20
Sbottom and Stop		
2b-jets + E_T^{miss}	[96]	SUSY-2013-05
Stop with Z boson	[97]	SUSY-2013-08
1-lepton stop	[98]	SUSY-2013-15
0-lepton stop	[99]	SUSY-2013-16
2-leptons stop	[100]	SUSY-2013-19
Monojet stop	[101]	SUSY-2013-21
Electroweak		
2-leptons	[50]	SUSY-2013-11
3-leptons	[102]	SUSY-2013-12
ℓh	[103]	SUSY-2013-23

TABLE 4.6: Run 1 ATLAS analyses implemented in the `SModelS` database. Only the final published analyses are listed.

CMS Analyses in `SModelS` Database v1.1

Analysis	**Ref.**	**ID**
Gluino and Squark		
jets + E_T^{miss}, α_T	[104]	SUS-12-028
3(1b-)jets + E_T^{miss}	[105]	SUS-12-024
jet multiplicity + H_T^{miss}	[49]	SUS-13-012
$\geq$ 2 jets + E_T^{miss}, M_{T2}	[106]	SUS-13-019
$\geq 1b$ + E_T^{miss}, Razor	[107]	SUS-13-004
1 lepton + $\geq 2b$-jets + E_T^{miss}	[108]	SUS-13-007
2 OS lept. + $\geq$4(2b-)jets + E_T^{miss}	[109]	PAS-SUS-13-016
2 SS leptons + b-jets + E_T^{miss}	[110]	SUS-13-013
b-jets + 4 Ws + E_T^{miss}	[111]	SUS-14-010
Sbottom and Stop		
0 lepton + $\geq$ 5(1b-)jets + E_T^{miss}	[112]	PAS-SUS-13-015
0 lepton + $\geq$ 6(1b-)jets + E_T^{miss}	[113]	PAS-SUS-13-023
1 lepton + $\geq$ 4(1b-)jets + E_T^{miss}	[114]	SUS-13-011
b-jets + E_T^{miss}	[115]	PAS-SUS-13-018
soft leptons, few jets + E_T^{miss}	[116]	SUS-14-021
Electroweak		
multi-leptons + E_T^{miss}	[117]	SUS-13-006

Table 4.7: Run 1 CMS analyses implemented in the `SModelS` database. The analyses named with PAS provide preliminary results.

`Fastlim` Results in `SModelS` Database v1.1

Analysis	Ref.	ID
Gluino and Squark		
0-lepton + 2–6 jets + E_T^{miss}	[119]	ATLAS-CONF-2013-047
0-lepton + 7–10 jets + E_T^{miss}	[120]	ATLAS-CONF-2013-054
1-lepton + jets + E_T^{miss}	[121]	ATLAS-CONF-2013-062
0/1-lepton + 3b-jets + E_T^{miss}	[122]	ATLAS-CONF-2013-061
Sbottom and Stop		
0-lepton stop	[123]	ATLAS-CONF-2013-024
1-lepton stop	[124]	ATLAS-CONF-2013-037
2-leptons stop	[125]	ATLAS-CONF-2013-048
2b-jets + E_T^{miss}	[126]	ATLAS-CONF-2013-053
Electroweak Production		
ℓh	[127]	ATLAS-CONF-2013-093

TABLE 4.8: Results recast by the `Fastlim` collaboration included in v1.1 of the `SModelS` database.

Fastlim Efficiency Maps

The `Fastlim` collaboration[118] produced several efficiency maps for a set of simplified models targeting a natural SUSY scenario [7]. Similar to what is done systematically by `SModelS` with EMs results, `Fastlim` [55] tests an SLHA input model against a database of results for a set of preliminary Run 1 $\not{E}_T^{miss}$ based ATLAS searches for SUSY with the full luminosity dataset (20.1 fb^{-1} - 20.7 fb^{-1}). The theory cross section for the set of available simplified models are read from pre-computed tables. Finally, for each signal region, `Fastlim` computes the visible cross section by interpolating the values of the efficiencies from the grids available, compares the value with the theory prediction and calculates a quantity like the `SModelS` r-value.

The results converted into `SModelS` format and implemented in the version 1.1 of the database are listed in Tab. 4.8. The steps for the production of the results follow the usual chain of producing the Monte Carlo samples with a matrix-element generator followed by a tool for the showering and hadronization, while the detector simulation and analysis recast was performed with a dedicated tool called ATOM (Automated Tests of Models), which however is still not publicly available. All the implemented analyses have a validation note on the `Fastlim` website [118]. Note that, due to very low efficiency and correspondingly large statistical error, the efficiencies with uncertainty above 25% are set to zero, and discarded. This is due to the fact that the recast analyses were not sensitive to the simplified models tested.

The available Txnames are:

- *gluino direct decay*: *T1*, *T1bbbb*, *T1bbbt*, *T1bbqq*, *T1bbtt*, *T1btbt*, *T1btqq*, *T1bttt*, *T1qqtt*, *T1tttt*;
- *gluino 1-step cascade decay*: *T5bbbb*, *T5bbbt*, *T5btbt*, *T5tbtt*, *T5tttt*;
- *squark*: *T2*, *T2bb*, *T2tt*, *T2bt*;
- *gluino asymmetric*: *TGQ* , *TGQbbq* , *TGQbtq*, *TGQqtt* ;

---

[7] Here, natural spectra are defined as spectra with the masses of $\tilde{g}, \tilde{t}_{L/R}, \tilde{b}_L, \tilde{h}_u, \tilde{h}_d$ are below the TeV scale

Despite being obtained with the recast of preliminary analyses, these results contain many topologies that still today, after Run 1 and in the middle of Run 2, have never been provided officially neither by ATLAS nor CMS.

The *gluino asymmetric* topologies deserve a particular mention. These were produced considering gluino pair production in which the *BR* was shared between 2-body decay to gluon-LSP (via a loop decay) and a 3-body decay through an off-shell squark (light or 3rd generation). These must not be confused with the *T3GQ* topologies that will be discussed thoroughly in Chapter 5, corresponding to gluino-squark associated production. As will be shown, the hadronization of gluon and quark and successive clustering into jets has an impact on the efficiency of certain analyses; currently `SModelS` treats gluon and quark jets equally, and it will be shown how much this affects the exclusion of a realistic model.

4.2.5 `SModelS` Validation of the Analyses

Irrespectively of the sources, only the experimental results that successfully pass a dedicated validation procedure enter the database. The `SModelS` validation procedure follows the working flow of a usual `SModelS` run over a specific set of SLHA files for a specific Txname. The grid of SLHA points is created from a template by varying the masses of the particles appearing in the simplified model considered, while all the other masses are decoupled.

For each SLHA, `SModelS` calculates the decomposed spectra and confronts the theory prediction with the experimental limit from the database. Finally the *r-value* is calculated. By connecting the points for which *r-value* =1, an exclusion curve is produced. Fig. 4.9 shows four selected validation plots for the analyses ATLAS-SUSY-2013-04(*T5WW*), ATLAS-SUSY-2013-05(*T2bb*), ATLAS-SUSY-2013-11(*TChipChimSlepSnu*,*TSlepSlep*), for homegrown EM results. The complete set of validation plots for all the analyses released with public versions of the `SModelS` databases can be found on the official validation webpage[8]. A result is considered validated if the exclusion obtained is contained within the uncertainty bands of the official curve if available, or if it looks reasonably close to the official central value curve.

Validating the analyses is especially important for recast results, due to the additional uncertainties involved in the recasting procedure. The validation plots shown here are indeed relative to homegrown efficiency maps results. Note that in the case of EM results, the best signal region is used to calculate the exclusion, so it is also possible to obtain a 'best SR map'. This type of information will be used in the next Chapters 5 and 6 to highlight possible recasting-related discrepancies that affect the limit calculation. In fact, differences in the efficiencies might lead to different choice of best SR, and this affects the limit calculation.

4.3 Extending the LHC SMS Results: EM Bakery

In Section 4.1 recasting tools were introduced, describing how they can be used to extract $(\mathcal{A} \times \epsilon)$ for arbitrary BSM models; then, in Section 4.2, it was shown how `SModelS` makes systematic use of these efficiency maps. This is possible both with maps provided by the experiments, as well as with the ones produced from phenomenologists like the `Fastlim` group. It was then natural to consider the idea of extending the `SModelS` database with recast results and fill the gap for missing simplified

---

[8] `http://smodels.hephy.at/wiki/Validationv112`

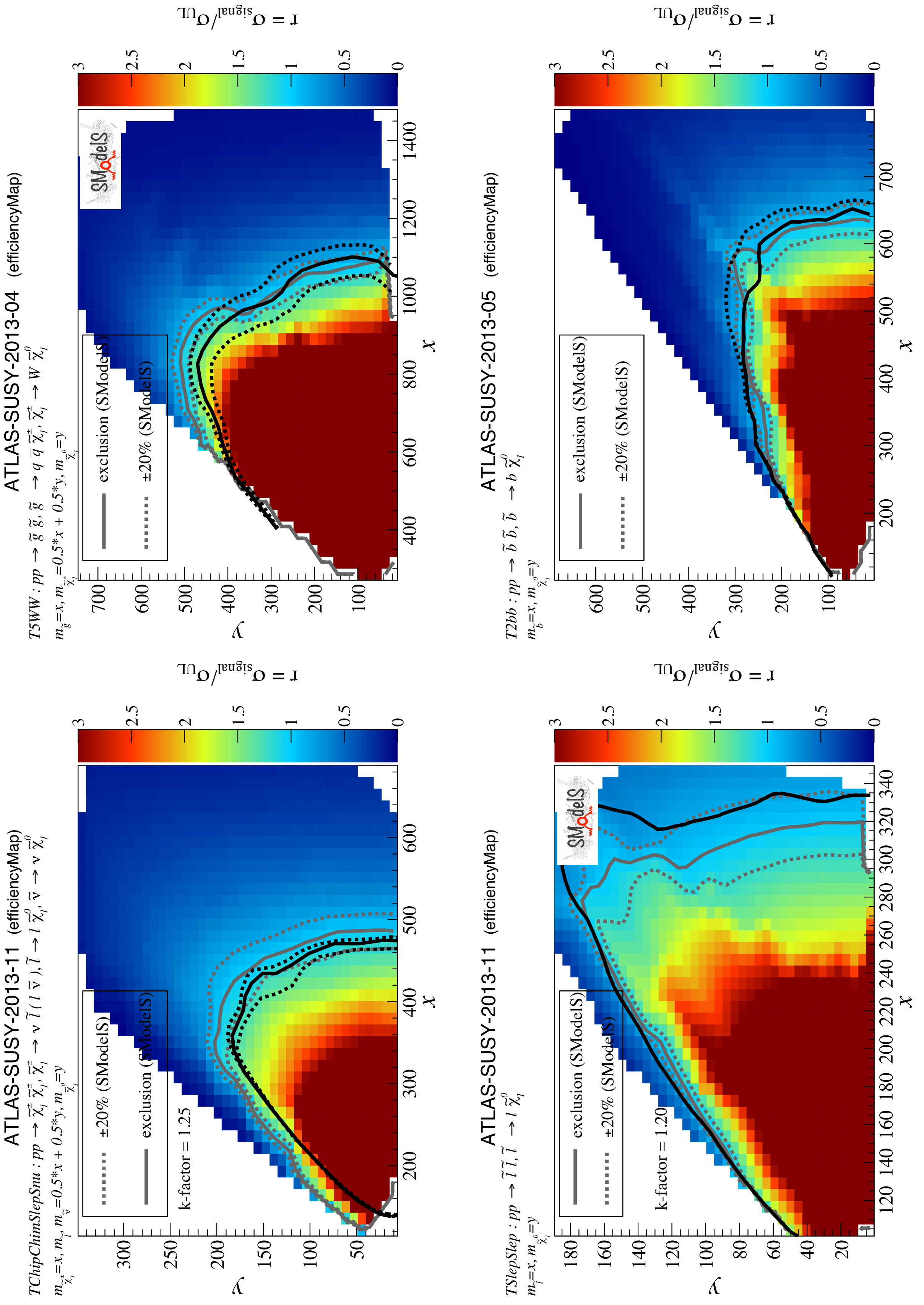

Figure 4.9: Validation plots for selected 'homegrown' efficiency maps results implemented in the `SModelS` database. The color map shows the *r-value*(ratio of the theory predictions over the experimental limit); the solid lines compare the `SModelS` exclusion (grey), obtained by connecting the points for which *r-value*=1, and the official ATLAS exclusion curve (black). The dashed lines correspond to ±20% variation in the `SModelS` cross section normalisation, or the ATLAS $\pm1\sigma$ band uncertainty.

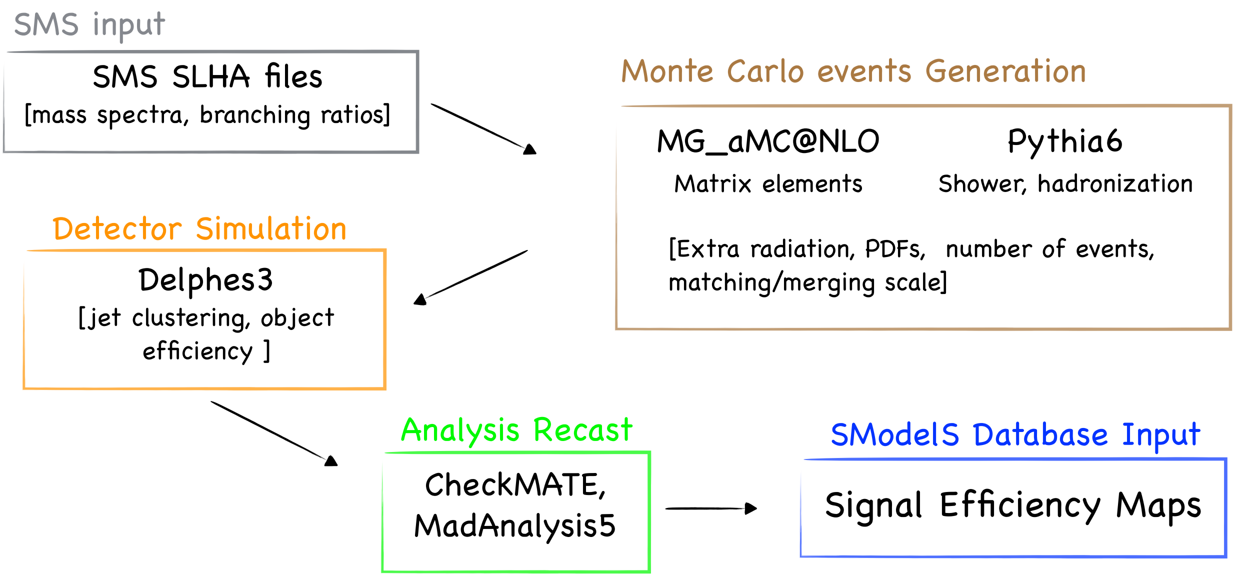

FIGURE 4.10: Workflow of the EM_Bakery machinery. For each SLHA file extracted from a grid, the signal Monte Carlo samples are produced; the output file is then passed to the detector simulation, and to the analysis recast. The EMs for the set of points are finally created and converted to a `SModelS` friendly format.

model interpretations. A large part of this thesis work was dedicated to the development of an infrastructure, friendly called *EM Bakery*, to systematically recast EM results and implement them in the `SModelS` database. The general working flow and a summary of the EM results obtained will be now described.

4.3.1 The EM Bakery Workflow

The working flow of the *EM Bakery* closely follows what was described for generic model testing with recasting tools: it is composed of the Monte Carlo sample production, the simulation of the detector effects, and the proper analysis recast. This is done in a systematic and automated way so to take advantage of the use of scientific computing clusters. The overall scheme is drawn in Fig. 4.10, and can be divided into the following steps:

1. creation of the SLHA files grid to be processed;
2. Monte Carlo event generation;
3. detector simulation;
4. analysis recast;
5. extraction of EMs.

The first ingredient necessary for the production is the definition of a grid of points of a given simplified model to be processed. Since quantum numbers are neglected according to the simplified model assumptions, no SUSY spectrum calculators are needed for the creation of SLHA files. For each model, a template SLHA file is written with arbitrary mixing matrices for the neutralinos and charginos, and branching fractions correspond at 100% to the fixed model. Typically Bino-like LSP and Wino-like charginos are assumed, but this should not effect the results for the final analysis efficiency. The masses of the SUSY particles involved are the only free parameters to be replaced in the template, while all the other SUSY masses can be set to large values so that they do not contribute to the production cross section. The decay widths must however be compatible with the narrow width approximation.

The mass grids adopted for homegrown maps production used a binning in the (mother,LSP) mass of (50,40) GeV and (60,50) GeV for squark and gluino production respectively. In the case of coloured sparticle production, the maximum mother mass considered for gluinos was 1.5 TeV, while for squark 1 TeV was chosen; the LSP mass considered went up to 700 GeV. These mass limits identify roughly the area of the mass planes excluded in the simplified model context. In the case of electroweak models, since the Monte Carlo production is typically faster, a finer grid was used.

Currently the automatised implementation of results in the `SModelS` database requires that in the

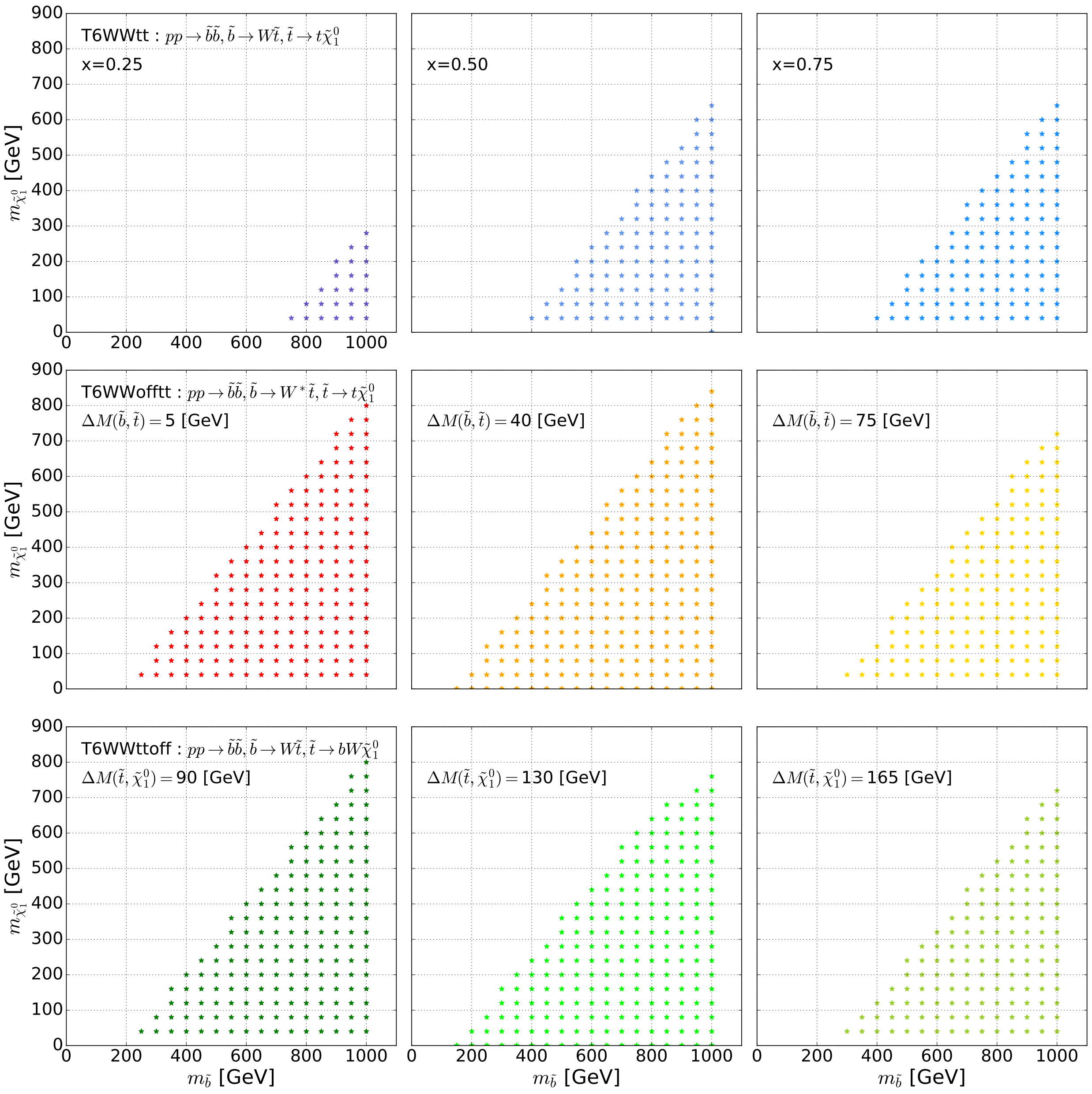

FIGURE 4.11: Example of the SLHA grid used to produce EMs for the *T6WWtt* model; for a total of 9 mass planes (including the off-shell decay of the W boson and of the top quark $t \to bW$. The x-axis shows $m_{\tilde{b}}$ while the y-axis shows $m_{\tilde{\chi}_1^0}$. The value of the intermediate sparticle $m_{\tilde{t}}$ is written in the label.

case of cascade decays, only two mass parameters can be varied freely (and read from a file source) while the third mass must be expressed as a function of the former two, or fixed to a constant value. This follows the habit of the LHC experiments to project the results onto a 'slice' of the parameter space when considering simplified models with more than two free mass parameters. The issue of parametrization of cascade-decays simplified models is the subject of Chapter 6. For the rest of this discussion, it is enough to remind that `SModelS` requires the mass of the third particle to be expressed as a mathematical function of the other two, or to assume a fixed value.

In Fig. 4.11, an example of the mass grids used for the production of the recast EMs for the *T6WWtt* model is shown. This model corresponds to a 1-step decay of sbottoms to intermediate stops. Since all SM particles are considered final states in `SModelS` , the case of off-shell particles must be treated separately; this means that according to the mass splitting between the sbottom and the chargino, the first vertex might contain on- or off-shell W bosons, while the second vertex on- or off-shell top quarks. The case of 4-body decays of the stop, including also an off-shell W boson, is not considered. Several mass parametrizations of $(m_{\tilde{b}}, m_{\tilde{\chi}_1^\pm}, m_{\tilde{\chi}_1^0})$ where employed; this allows the interpolation procedure to extract efficiencies for generic mass combinations. In the top row, the parametrization $x = (0.25, 0.50, 0.95)$ is used for the case of on-shell SM particles, i.e. the proper *T6WWtt* model. For the parametrization of the *T6WWtt* and *T6WWttoff*, the choice of fixing the mass difference between the sparticles involved in each vertex was adopted. For this model, the SLHA grids for nine mass planes were defined and processed.

The grid of SLHA is the input for the EMs creation. The next step is the actual production of the event files. All the external tools used by the *EM Bakery*, i.e. `MadGraph`, `Delphes`,`CheckMATE 1/2` and `MadAnalysis 5` and must be compiled in a dedicated directory.

The events are generated by `MadGraph v.2.4.3` and `Pythia 6.4`. The input parameters to be chosen are the specific SUSY process to be generated (e.g. gluino pair production, gluino-squark associated production, squark pair production etc.), the number of extra partons emitted, the center of mass energy of the collision (all the results were produced at 8 TeV), the numbers of events to be generated (all the samples were produced with a minimum of 100k events at the parton level), and the $(XQcut, Qcut)$ relevant for the jet matching. The parameters can be directly set in the basic input card read by the EM Bakery, and will be replaced inside template cards created for the two generators. Once the sample has been generated, it is passed to the recasting tools; both `MadAnalysis 5` and CheckMATE have dedicated modules for the detector simulation based on `Delphes`.

The analysis recast is then performed; in the case of `CheckMATE`, all the analyses compatible with the centre-of-mass energy chosen for the sample production will be run, since the ATLAS or CMS detector simulation is performed only once, and a fast smearing procedure is then applied to account for the specific object efficiencies of each analysis. In the case of `MadAnalysis 5` , each analysis requires a specific , so a dedicated detector simulation for each analysis, which takes several hours, is needed. Since it is expected that only few analyses are sensitive to the signature of the simplified models considered, the user can choose the analyses to be recast.

Finally, the standard output files from the two recasting tools are stored in a centralised directory, that at the end of the process will contain the efficiencies for each one of the SLHA point selected at the beginning. Then, the efficiency for each signal region and analysis is extracted and written to a text file suitable for implementation in the `SModelS` database.

Recast Results Included in `SModelS` v1.1 database

Process	txName	Decay	Mass Plane	Analyses
$pp \to \tilde{g}\tilde{g}$	T1bbbb	$\tilde{g} \to b\bar{b}\tilde{\chi}_1^0$	-	[1],[2]
	T1btbt	$\tilde{g} \to bt\tilde{\chi}_1^0$	-	[1],[2]
	T5	$\tilde{g} \to q\tilde{q}, \tilde{q} \to q\tilde{\chi}_1^0$	$x = (0.05, 0.50, 0.95)$	[1],[2]
	T5bbbb	$\tilde{g} \to b\tilde{b}_1, \tilde{b}_1 \to b\tilde{\chi}_1^0$	$x = (0.05, 0.50, 0.95)$	[1],[2]
	T5tttt	$\tilde{g} \to t\tilde{t}_1, \tilde{t}_1 \to t\tilde{\chi}_1^0$	$x = 0.5$	[1],[2]
			$\Delta M(\tilde{g}, \tilde{t}_1) = 177$ GeV	
			$\Delta M(\tilde{t}_1, \tilde{\chi}_1^0) = 177$ GeV	
	T5WW	$\tilde{g} \to q\bar{q}'\tilde{\chi}_1^\pm,\ \tilde{\chi}_1^\pm \to W^\pm\tilde{\chi}_1^0$	$x = (0.05, 0.50, 0.95)$	[1],[2]
			$\Delta M(\tilde{\chi}_1^\pm, \tilde{\chi}_1^0) = (10, 75)$ GeV	
	T5ZZ	$\tilde{g} \to q\bar{q}\tilde{\chi}_2^0,\ \tilde{\chi}_2^0 \to Z\tilde{\chi}_1^0$	$x = (0.05, 0.50, 0.95)$	[1],[2]
$pp \to \tilde{b}_1\tilde{b}_1^*$	T2bb	$\tilde{b}_1 \to b\tilde{\chi}_1^0$	-	[1],[3]
$pp \to \tilde{t}_1\tilde{t}_1^*$	T2tt	$\tilde{t}_1 \to t\tilde{\chi}_1^0$	-	[1],[2]
	T6bbWW	$\tilde{t}_1 \to b\tilde{\chi}_1^+,\ \tilde{\chi}_1^+ \to W^+\tilde{\chi}_1^0$	$x = (0.10, 0.50, .090)$	[1],[2]
			$\Delta M(\tilde{\chi}_1^\pm, \tilde{\chi}_1^0) = (10, 75)$ GeV	
$pp \to \tilde{\chi}_1^+\tilde{\chi}_1^-$	TChiWW	$\tilde{\chi}_1^\pm \to W^\pm\tilde{\chi}_1^0$	-	[1],[4]
	TChipChimSlepSnu	$\tilde{\chi}_1^\pm \to l^\pm(\nu_l)\tilde{\nu}_l(\tilde{l}^\pm),\ \tilde{\nu}_l(\tilde{l}) \to \nu_l(l)\tilde{\chi}_1^0$	$x = (0.05, 0.25, 0.50, 0.75, 0.95)$	[4]
			$\Delta M(\tilde{\chi}_1^\pm, \tilde{l}) = (5, 10, 15)$ GeV	
			$\Delta M(\tilde{l}, \tilde{\chi}_1^0) = (5, 10, 15)$ GeV	
$pp \to \tilde{\chi}_1^\pm\tilde{\chi}_2^0$	TChiWZ	$\tilde{\chi}_1^\pm \to W^\pm\tilde{\chi}_1^0,\ \tilde{\chi}_2^0 \to Z\tilde{\chi}_1^0$	-	[1]
$pp \to \tilde{\chi}_2^0\tilde{\chi}_2^0$	TChiZZ	$\tilde{\chi}_2^0 \to Z\tilde{\chi}_1^0$	-	[1]
$pp \to \tilde{l}^+l^-$	TSlepSlep	$\tilde{l}^\pm \to l^\pm\tilde{\chi}_1^0$	-	[4]

Table 4.9: Summary of the recast EM results included from v1.1 in the `SModelS` database. Numbers for ΔM mass differences are expressed in [GeV]. The recast analyses used are: [1]: CMS-SUS-13-012 (MA5) , [2]: ATLAS-SUSY-2013-04 (MA5), [3]: ATLAS-SUSY-2013-05 (CM), [4]: ATLAS-SUSY-2013-11 (MA5).

All of the described steps are performed in an systematic way, so that by changing only a few input parameter files, all the relevant parameter cards of the tools involved in the chain are automatically updated. Since the code is used internally by the `SModelS` developers and kept private, specific details about how to run the scripts will not be provided.

4.3.2 Summary of Homegrown EM Results

This EM Bakery was extensively used to produce several EM results, summarised in Tabs. 4.9 and 4.10. The first lists results available from v1.1 in the `SModelS` database; the second contains several additional models, mainly regarding third generation SUSY particles with 1-step cascade decays. The *T3GQon* model will be treated extensively in the next Chapter 5; the EMs for this topology were published in [3].

Additional Recast Results

Process	Txname	Decay	Mass Plane	Analyses
$pp \to \tilde{g}\tilde{g}$	T5WW	$\tilde{g} \to q\bar{q}'\tilde{\chi}_1^\pm,\ \tilde{\chi}_1^\pm \to W^\pm\tilde{\chi}_1^0$	$x = (0.25)$	[1]
$pp \to \tilde{q}\tilde{q}^*$ $[\tilde{q} = (\tilde{u}, \tilde{d}, \tilde{c}, \tilde{s})_{L,R}]$	T6WW	$\tilde{q} \to q'\tilde{\chi}_1^\pm\ ,\ \tilde{\chi}_1^\pm \to W\tilde{\chi}_1^0$	$x = (0.50, 0.95)$ $\Delta M(\tilde{\chi}_1^\pm, \tilde{\chi}_1^0) = (5, 40, 75)$ GeV	[1]
$pp \to \tilde{b}_1\tilde{b}_1^*$	T6bbZZ	$\tilde{b}_1 \to b\tilde{\chi}_2^0,\ \tilde{\chi}_2^0 \to Z\tilde{\chi}_1^0$	$x = (0.25, 0.50, 0.95)$ $\Delta M(\tilde{\chi}_2^0, \tilde{\chi}_1^0) = (5, 50, 75)$ GeV	[1]
	T6WWtt	$\tilde{b}_1 \to t\tilde{\chi}_1^\pm,\ \tilde{\chi}_1^\pm \to W\tilde{\chi}_1^0$	$x = (0.25, 0.50, 0.75)$ $\Delta M(\tilde{b}_1, \tilde{t}_1) = (5, 40, 75)$ GeV $\Delta M(\tilde{t}_1, \tilde{\chi}_1^0) = (90, 130, 165)$ GeV	[1]
	T6ttWW	$\tilde{b}_1 \to W\tilde{t}_1,\ \tilde{t}_1 \to t\tilde{\chi}_1^0$	$x = (0.25, 0.50, 0.75)$ $\Delta M(\tilde{b}_1, \tilde{\chi}_1^\pm) = (130, 165)$ GeV	[1]
			$\Delta M(\tilde{\chi}_1^\pm, \tilde{\chi}_1^0) = (5, 40, 75)$ GeV	
$pp \to \tilde{b}_2\tilde{b}_2^*$	T6ZZbb	$\tilde{b}_2 \to Z\tilde{b}_1,\ \tilde{b}_1 \to b\tilde{\chi}_1^0$	$x = (0.10, 0.50, 0.95)$ $\Delta M(\tilde{b}_2, \tilde{b}_1) = (5, 50, 75)$ GeV	[1]
$pp \to \tilde{t}_1\tilde{t}_1^*$	T6ttZZ	$\tilde{t}_1 \to t\tilde{\chi}_2^0,\ \tilde{\chi}_2^0 \to Z\tilde{\chi}_1^0$	$x = (0.50, 0.70)$ $\Delta M(\tilde{\chi}_2^0, \tilde{\chi}_1^0) = (5, 45, 85)$ GeV $\Delta M(\tilde{t}_1, \tilde{\chi}_2^0) = (200)$ GeV	[1]
	T6WWbb	$\tilde{t}_1 \to W\tilde{b}_1,\ \tilde{b}_1 \to b\tilde{\chi}_1^0$	$x = (0.05, 0.50, 0.75)$ $\Delta M(\tilde{b}_1, \tilde{\chi}_1^0) = 5$ GeV $\Delta M(\tilde{t}_1, \tilde{b}_1) = (10, 40, 75)$ GeV	[1]
$pp \to \tilde{t}_2\tilde{t}_2^*$	T6ZZtt	$\tilde{t}_2 \to Z\tilde{t}_1,\ \tilde{t}_1 \to t\tilde{\chi}_1^0$	$x = (0.10, 0.50, 0.95)$ $\Delta M(\tilde{t}_2, \tilde{t}_1) = (5, 40, 80)$ GeV $\Delta M(\tilde{t}_1, \chi_1^0) = (90, 160)$ GeV	[1]
$pp \to \tilde{l}^+\tilde{l}^-$	TSlepSlepWW	$\nu_l\tilde{l}^\pm \to \chi_1^\pm,\ \chi_1^\pm \to W^\pm\tilde{\chi}_1^0$	$x = (0.2, 0.50, 0.90)$ $\Delta M(\tilde{\chi}_1^\pm, \tilde{\chi}_1^0) = (10, 40, 75)$ GeV	[1],[4],[5]
$pp \to \tilde{g}\tilde{\chi}_1^0$	TGN	$\tilde{g} \to q\bar{q}\chi_1^0$	-	[1],[5]

TABLE 4.10: Additional unpublished EM results. See caption of Tab. 4.9 for details.

Summary

In this Chapter, two of the main methods for the re-interpretation of BSM searches at the LHC were presented: the recast approach, based on the full simulation of the signal, and the simplified model approach, that aims at constraining a full model by looking at its SMS decomposition. The former is certainly more constraining, since it can be applied to any generic BSM model that can be simulated with Monte Carlo generators. Nevertheless it suffers from long computing time needed in order to completely process the input model up to the final recast.

As for the simplified model approach, the positive aspect is that it can directly make use of the constraints provided by the LHC experiments, without any further processing or event simulation: it is enough to extract the elements from the full model that can be mapped onto existing SMS results from the experiment. This approach is however limited on the one hand by the number of results provided by the collaborations; on the other hand, it fails to efficiently constrain models with complex mass spectra, for which the description with simplified models might not be accurate enough.

Both approaches can be combined together: EMs for new simplified models can be recast and implemented in the `SModelS` database to extend the number of the available experimental results. This will be demonstrated in the next Chapter with a concrete example, for how the pMSSM can be probed by `SModelS` to highlight unconstrained elements, and how the production of EMs for such SMS can then improve the exclusion power. It was also shown that `SModelS` flexibility allows to use results produced by other groups of phenomenologist, as is the case of the `Fastlim` EM results, which cover interesting simplified models not investigated by the official LHC experiments.

Finally, for the future extensions of the database with more $\sqrt{s} = 13$ TeV results, the CMS-SUS-16-033 analysis was implemented in the `MadAnalysis 5` framework. This is the first inclusive analysis searching for coloured SUSY particles implemented in the framework; the importance of this particular type of searches will be demonstrated in the next Chapter. It will also serve as an interesting test case for the combination of different SR available from `SModelS` v.1.2[3], thanks to the available covariance matrix from the CMS collaboration that accounts for the correlation of the background systematic uncertainties.

Chapter 5

Constraining the pMSSM with Simplified Models

Contents

After discussing the technical aspects of the `SModelS` software, this Chapter is dedicated to testing the performance of the simplified model machinery with a realistic SUSY model. Specifically the phenomenological minimal supersymmetric model[26], or shortly pMSSM, will be used as a benchmark. This model was used by the ATLAS experimentalists to re-interpret several Run 1 SUSY searches, and to analyse how well the full parameter space of the theory is constrained[128]. They performed a large scan in the parameter space, and selected around 300k points, for which they produced the Monte Carlo signal events and re-ran the selected analyses. Since both the SLHA files as well as a detailed summary of the constraints provided by each analysis considered were made publicly available, it was possible to compare the official ATLAS results with the ones obtained with `SModelS`. Part of the material discussed in this Chapter was published in [4], which focused on the study of the global coverage of the pMSSM, and pointing out the relevant missing topologies found by `SModelS` .

However in the `SModelS` paper[4] several interesting aspects were not covered. For example an interesting question regards the performance of the different analyses targeting the same SMS interpretation, or so to say, which search strategy provides the best limits for a given SMS. Moreover, it is interesting to highlight which are the most useful results in the context of re-interpretation of new theories with simplified models.

The published results, based on the database in v1.1, used three types of EMs:

- official results from ATLAS and CMS;
- homegrown results;
- `Fastlim` results

The results produced by the `Fastlim` collaboration (introduced in Section 4.2.4) are noteworthy since they contains several topologies for which no official results exist. Understanding the impact on the pMSSM of these maps, despite being designed for a natural SUSY scenario, can constitute a concrete guideline for the future production of 'homegrown' results. On the other hand, the analysis of the missing topologies appearing in the `SModelS` pMSSM study demonstrates which are the most constraining signatures that must be prioritised for improving the coverage of the model. Both pieces of information are necessary and complementary for the future development of recast results.

This Chapter is structured as follows. In Section 5.1 the pMSSM is introduced, followed by a brief description of the ATLAS study and results in Section 5.2. Section 5.3 shows an in- depth comparison between the ATLAS and the `SModelS` results as already published in [4]. The rest of the Chapter contains unpublished results. First, a detailed analysis of the most constraining experimental results contained in the database is presented. In particular the most constraining simplified models will be highlighted, both for the official (ULs) and recast (`Fastlim` and homegrown EMs) results. This study can be used as a guideline to extend the coverage of the pMSSM using the recent 13 TeV recast analyses, e.g. the CMS-SUS-16-033 analyses described in the previous Chapter.

The final Section 5.4 concretely shows that using iteratively `SModelS` to first identify important missing simplified models, and then using the EMs Bakery machinery to produce dedicated results, improve the coverage of the pMSSM and the constraining power of the `SModelS` framework.

5.1 The pMSSM interpretation of SUSY searches

The full MSSM possess a too large parameter space to be considered for any reasonable phenomenological study, not only from a computational point of view, but also since the outcome of such a complicated study would be difficult to interpret. At the same time, simplified model results do not give a clear understanding of the current constraints on the parameter space of the full MSSM; for this, we then need to re-interpret the searches in the context of a full realistic model and abandon the naive SMS assumptions.

Contrary to simplified models, where typically only a few SUSY particles have masses accessible at LHC energies while all the other particles are decoupled, in realistic models a rich spectrum of SUSY particles opens many possible production modes with possibly complicated decay chains. This decreases drastically the weight $w = \sigma \times BR$ of each single decomposed simplified model, since the total production cross section is shared between several competing decay modes.

When considering complex decay chains, the sensitivity of searches might also decrease: on the one hand, since many SM particles are found in the final state, there might be limits in the usage of exclusive searches, looking e.g. for a fixed number of leptons or jets. Typically searches are designed to look for very distinct signatures of some simplified models, and might not be effective in constraining general models. Inclusive hadronic searches benefit from very general definition of the selection cuts, which make them sensitive to a multitude of simplified models for squark and gluino prompt decays. Thanks also to the large production cross section of coloured particle at the

LHC, they prove very effective to constrain the pMSSM.

On the other hand, in case of small mass differences in the SUSY mass spectrum, all the SM objects will become low energetic and possibly fail to pass the selection cuts of the analysis. It is no surprise that SUSY particle with masses below the current naive exclusion limits provided by some SMS results can be unconstrained by the same search when considering a full model with a full particle spectrum. In synthesis, realistic models are needed to capture *"the complex effects that can result from large numbers of competing production and decay processes"* (quote from[128]), but they come with serious experimental challenges as well as a non trivial theoretical interpretation.

Parameters of the pMSSM-19	
tan β	Ratio of the Higgs vacuum expectation values
M_A	Mass of the pseudoscalar Higgs boson
μ	Higgsino parameter
M_1 , M_2 , M_3	Gaugino mass parameters for Binos, Winos and Gluinos
$m_{\tilde{q}}$, $m_{\tilde{u}R}$, $m_{\tilde{d}R}$, $m_{\tilde{l}}$, $m_{\tilde{e}R}$	Masses of 2nd generation sfermions
$m_{\tilde{Q}}$, $m_{\tilde{t}R}$, $m_{\tilde{b}R}$, $m_{\tilde{L}}$, $m_{\tilde{\tau}R}$	Masses of 3rd generation sfermions
A_t , A_b , A_τ	Trilinear couplings for 3rd generation sfermions

TABLE 5.1: Description of the free parameters in the pMSSM-19 used by the ATLAS and CMS Collaborations for the re-interpretation study of LHC Run 1 analyses. The label $\tilde{q}$ denotes left-handed squarks, $\tilde{l}$ denotes left-handed sleptons and $\tilde{Q}$ left-handed stops and sbottoms.

Given the above considerations, an interesting model that is more complex than the SMS but that still possesses a reasonable number of free parameters is the phenomenological supersymmetric standard model, or pMSSM[26]. It is defined as subspace of the MSSM in which the number of free parameters is reduced by experimental constraints on new sources of CP violation and neutral currents producing large flavour violation. The former are avoided by imposing that all the elements in the soft SUSY breaking potential are real (i.e. the phases are zero); the latter, by requiring that the matrices of the sfermions and the trilinear couplings are diagonal in flavour space.

The pMSSM realisation considered in this thesis is described by a set of 19 parameters, listed in Table 5.1. All these assumptions are independent on any mechanism of SUSY breaking or unification of SUSY masse at higher (GUT) scales, and are mostly motivated by a pure phenomenological point of view and theoretical simplicity.

Owing to the large reduction of parameters from the complete MSSM, the pMSSM-19 is suitable to make phenomenological studies; the number of parameters can be reduced further by looking for example at individual sectors of the model, characterised by only a selection of a few parameters. Since this will acquire a certain relevance in the next sections, I stress the fact that there are three different values of the masses of light squarks, specifically left-handed up and down type, right handed up type and right-handed down type. This gives a rich phenomenology when considering SMS with gluinos and squarks, depending on the specific mass hierarchy. R-Parity conservation ensures the presence of a viable DM candidate, which is the lightest neutralino $\tilde{\chi}_1^0$.

5.2 ATLAS Run 1 Results on the pMSSM

Both the ATLAS[128] and CMS[129] Collaborations published an extensive study of the constraints on the pMSSM-19 by re-running many Run 1 analyses on a large set of pMSSM parameter points. They re-interpreted several SUSY searches from the LHC Run 1, with data collected with collisions at 7 and 8 TeV, with the addition of other searches for more exotic signatures. What renders the ATLAS pMSSM study special is the quantity and quality of information made public by the Collaboration on the HepData website [130], including all the SLHA files of the point tested, and information on the constraint provided by each of the 22 analyses with an integrated luminosity of up to 20.3 fb^{-1} used for the re-interpretation. These include the majority of classical SUSY searches plus searches for monojet-like signatures, disappearing tracks and Heavy Higgs resonant searches. The list of such analyses can be retrieved in Table 1 in [128].

Definition of the ATLAS scan

Due to the large number of parameters, only a sub-space of the full pMSSM can be probed, and some criteria to define the set of points that will be simulated with Monte Carlo generators and tested against the selected ATLAS searches need to be defined. A model point is defined by a specific choice of the 19 free parameters. Due to the rapid drop of the production cross section at the LHC with increasing mass, as shown in Fig. 3.4, a 4 TeV upper bound on the masses was applied for all the sparticles. The model space was sampled with a flat probability distribution for all the parameters. After the SUSY parameter selection, the SLHA files were created using various SUSY spectrum calculators, such as SoftSUSY[131] and SUSY-HIT[132]. Finally, several experimental constraints from e.g. electroweak precision measurement, flavour physics, Higgs physics, LEP results, DM relic density and direct detection limits etc. were applied to the points.

Three separate sets of LSP, according to the nature of the $\tilde{\chi}_1^0$, were defined. If N_{ij} are the entries in the neutralino mixing matrix, the three LSP sets are defined as:

- **Bino-like LSP** when $N_{11}^2 > max(N_{12}^2, N_{13}^2 + N_{14}^2)$ [103,410];
- **Wino-like LSP** when $N_{12}^2 > max(N_{11}^2, N_{13}^2 + N_{14}^2)$ [80,233];
- **Higgsino-like LSP** when $(N_{13}^2 + N_{14}^2) > max(N_{11}^2, N_{12}^2)$ [126,684],

where the number in square bracket is the total number of parameters points tested by the ATLAS collaboration.

ATLAS Results

Because of the high dimensionality of the model, results can be presented only by projecting the results onto specific mass planes (i.e. single slices of the full parameter space) e.g. using the $(\tilde{g}, \tilde{\chi}_1^0)$ and $(\tilde{g}, min(\tilde{q}))$ mass planes. Although such planes give immediate information on the reach in the mass limits for gluinos and squarks, the mass spectrum of the other particles are left unspecified. Examples of plots from the ATLAS pMSSM interpretation study can be found in Fig. 5.1, showing the fraction of excluded points as a function of the masses of light squarks vs LSP and gluino vs light squark. The corresponding exclusion curves from the analysis ATLAS-SUSY-2013-02(0l,2-6jets) are also drawn as a comparison.

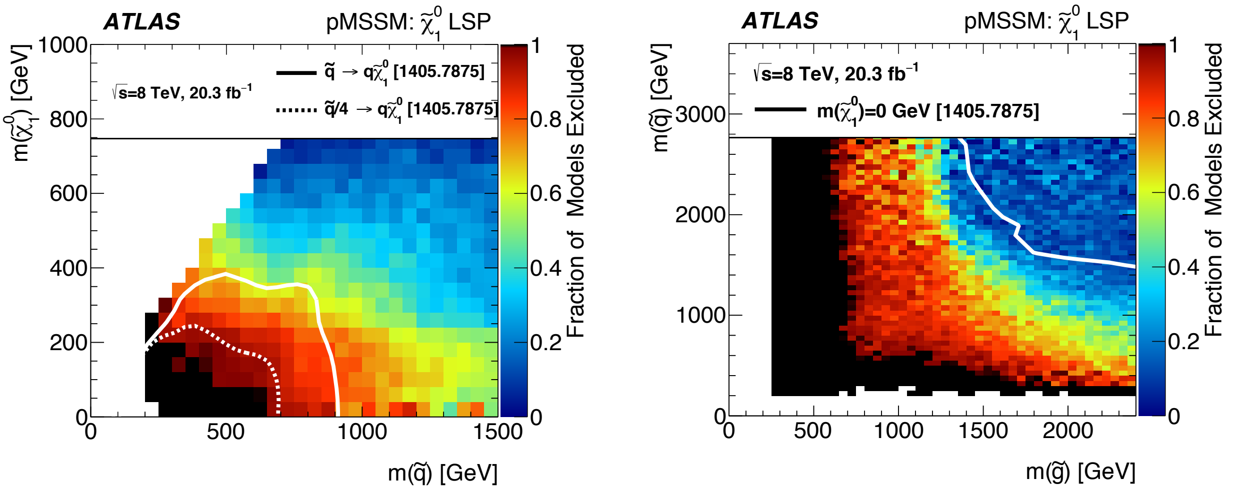

(b) Lightest (1st/2nd gen) squark / LSP (a) All LSP types

Figure 5.1: ATLAS results on the pMSSM interpretation for light squarks (left) and gluinos vs light squarks (right). The exclusion curve for the *T2* simplified model is superimposed as a reference on the left plot; the exclusion curve on the right is obtained by considering a set of pMSSM points where only gluino and squarks are light, and the other sparticles are decoupled. Both lines are taken from [91]).

Such plots however do not provide information about the source of the constraint, or in other words, why the model can be constrained. For example, even if a gluino is reasonably light, depending on the full mass spectrum, it can undergo complicated cascade decays to the LSP, and analyses targeting gluino production might have low efficiencies and exclusion power. At the same time, if other particles are sufficiently light, the point can be excluded by other dedicated searches, e.g. for sleptons or stops. As a consequence, the model point with the light gluino is excluded, but not because of gluino searches. This information is not encapsulated in such plots, unless only results for specific analyses are considered e.g. targeting third generation squarks or electroweak production. However this becomes crucial when considering simplified models results alone, as it will appear evident in the following discussion regarding `SModelS` constraints on the pMSSM.

5.3 SModelS Coverage of the pMSSM

The scope of this Section is to analyze how well a full model like the pMSSM can be constrained by SMS results only, as compared to the full analysis re-interpretation performed by ATLAS. This work was recently published in [4]; there, a great importance was given to highlight the most important SMS missing topologies (defined in Section 4.2.3), i.e. the topologies with a large ($\sigma \times BR$) weight that are not included in the database. After a general discussion of those findings, I will focus on discussing in detail the additional constraining power from recast EMs, either coming from new signatures implemented in the database (some of them never used for the official ATLAS and CMS interpretations) or from the combination of multiple signal topologies.

5.3.1 Analysis Setup

The main ingredients for the study are the complete set of SLHA files used by ATLAS, and a detailed list of the analyses which excluded a specific parameter point (provided at [130]). In the `SModelS` analysis only points that:

- were excluded by at least one of the ATLAS SUSY analyses , and

- did not include long lived charged particles

were considered. Points excluded only by heavy Higgs searches were removed from the tested sample since no corresponding simplified models are implemented in the database, as well as the Wino-like LSP set, which implied numerous long lived charged particles (the Bino and Higgsino-like LSP dataset contained only a few thousands long-lived sparticles that were excluded from our study). Even though a customised version of `SModelS` was used in [133] to study constraints on long lived BSM states, a public version of the tool is still in preparation. The total number of points passing our selection is 38575 for the Bino and 45594 points for Higgsino-like LSP respectively.

Version v1.1.1 of `SModelS` was employed, including both UL and EMs results (see 4.2.4). The `SModelS` cross section calculator, which provides a useful interface with `Pythia 8` (`v.8.226`)[66], `Pythia 6.4` [88] and `NLLfast` [89, 90, 134, 135, 136, 137, 138, 139] was used to compute the production cross sections, up to NLO+NLL order for strong production, and LO for electroweak processes; `Pythia 6.4` was instead used for slepton production. The other two relevant parameters selected in the configuration file `parameters.ini` are the `sigmacut` = 0.03 fb (controlling the minimum weight for a decomposed elements) and `minmassgap` = 5 GeV (standard value for BSM particles mass compression, below which the SM products in the vertex are considered invisible).

5.3.2 SModelS Results: pMSSM Coverage

I begin the comparison between the `SModelS` and ATLAS results with the discussion on the global coverage of the pMSSM parameter space; additional results obtained after the publication will be the last topic of this Chapter. The results for the Bino and Higgsino-like LSP datasets are presented separately, since they exhibit interesting peculiarities that depend on the nature of the LSP. Table 5.2 shows a summary of the total numbers of points excluded in the two categories: when using only UL results from the ATLAS and CMS Collaborations, `SModelS` reaches around 44% and 55% of the exclusion (obtained by ATLAS), which rises up to 55% and 63% when considering the full database containing official and recast EMs results, for the Bino and Higgsino-like LSP case respectively.

We see that on average in the Higgsino case the coverage looks more effective, and that the impact of EMs results is less relevant compared to the Bino case (+25% versus +14%). We proceeded then by analysing the coverage for specific SUSY particles, and here only gluinos will be treated. Fig. 5.2 shows the distribution of the number of excluded points as a function of $m_{\tilde{g}}$. The differently coloured histograms show the contribution from the different types of results used, namely the official UL and EM results, the homegrown and `Fastlim` EMs. The coverage of the SMS results is not able to match ATLAS reach even in the very low mass region $m_{\tilde{g}} \leq 1.4$ TeV. This is surprising for the reason that simple decay chains of gluinos to the LSP are expected (i.e. the gluinos BR should not be split between several decay modes), and the SMS results for direct gluino decays to the LSP in the database, such as *T1* and *T1bbbb*, plus several cascade decays models such as *T5*, *T5WW* and *T5ZZ* naively should constrain the points with low gluino mass.

Number of Points	**Bino-like** LSP	**Higgsino-like LSP**
Total	38575	45594
Excluded by UL	16957 (44 %)	25024 (55 %)
Excluded by UL+EM	21151 (55 %)	28669 (63 %)

TABLE 5.2: Summary of `SModelS` constraints for the Bino and Higgsino-like LSP. EMs include official, homegrown and `Fastlim` results.

A trivial consideration regards the grid of points defined in the experimental results in the database. First, as already noted before, an experimental analysis might not be sensitive in regions of compressed mass spectra, e.g. where the mass gap between the mother particle and the LSP is small. Ultimately this implies large systematic uncertainties and difficult background estimations. For this reason, the easiest choice from the experimentalists is not to provide results for regions where uncertainties are large or difficult to estimate accurately. Other times, simply the Monte Carlo signal samples were not available for the full simplified model parameter space. Whenever this happens, it is identified by the contribution of the elements falling outside of the available mass grid in the `SModelS` output (see Appendix B). This is to say that the mass compression between the gluino and the neutralino might make it problematic to constrain those points with gluino simplified models, and the actual constraints should come from other channels. In fact, the points are considered excluded if, for any analysis and any SMS, at least one result gives $r \geq 1$. Strictly speaking, a low mass gluino can be constrained thanks to SMS results that do not originate from gluino decays. Clearly the majority of points excluded for high gluino mass must be excluded by some other simplified models.

Figure 5.3 shows a direct comparison between the naive exclusion of a *T1* simplified model from the analysis ATLAS-SUSY-2013-02 [91], and the exclusion in the full pMSSM parameter space, projected in the $(m_{\tilde{g}}, m_{\tilde{\chi}_1^0})$ mass plane. It is clear that the coverage, even using the full sets of SMS results, is far away from the naive SMS interpretation exclusion, at least for the Bino-LSP case. A better coverage in the Higgsino-like LSP case can be seen, which can be explained by the mass compression between the $\tilde{\chi}_2^0/\tilde{\chi}_1^\pm$ and $\tilde{\chi}_1^0$. In the Bino-like LSP, the direct decay of the gluino to the LSP is quite rare, while decays to quarks and intermediate gauginos are more likely, resulting in long cascade decays. In the Higgsino-like LSP case, on the contrary, the mass compression functionality in `SModelS` will simplify most of the long cascade decays. The `Fastlim` dataset contains several asymmetric gluino decay, that can be combined together, explaining the increase in the coverage in the low gluino mass region. This improves the coverage wrt UL results, since efficiencies for models of the type *T1btbt-T1bttt-T1bbbt* (i.e. models where the gluino decays via intermediate chargino in at least one of the branch), *T1-T1bbbb-T1tttt*(direct decays of the gluino to the LSP via off-shell squarks), etc. can all be added up.

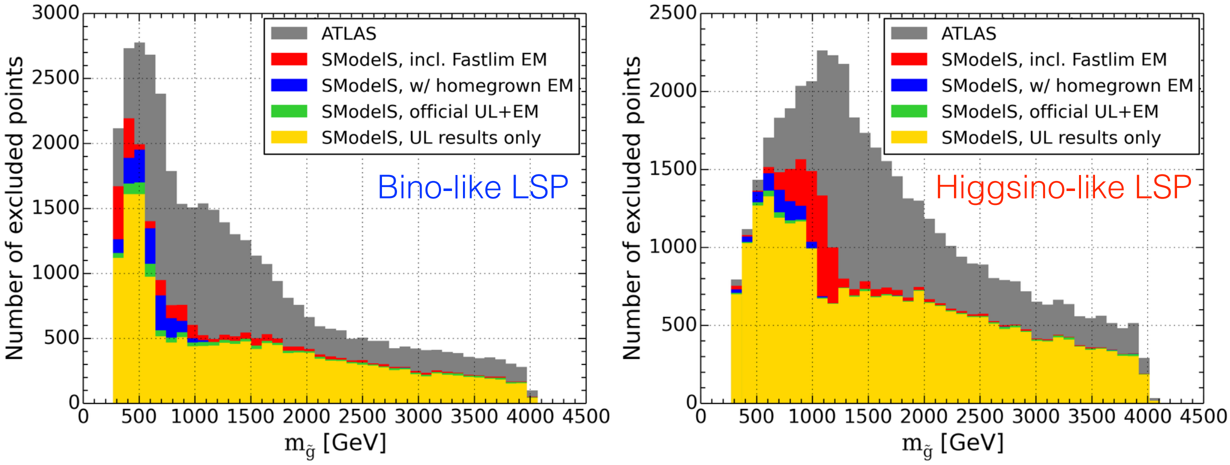

FIGURE 5.2: Distribution of the excluded points for the Bino (left) and Higgsino-LSP (right) dataset as a function of $m_{\tilde{g}}$. The yellow colour represents the number of points excluded by UL results, while the remaining represent the additional constraints provided by official (green), homegrown (blue) and `Fastlim` (red) EMs results.

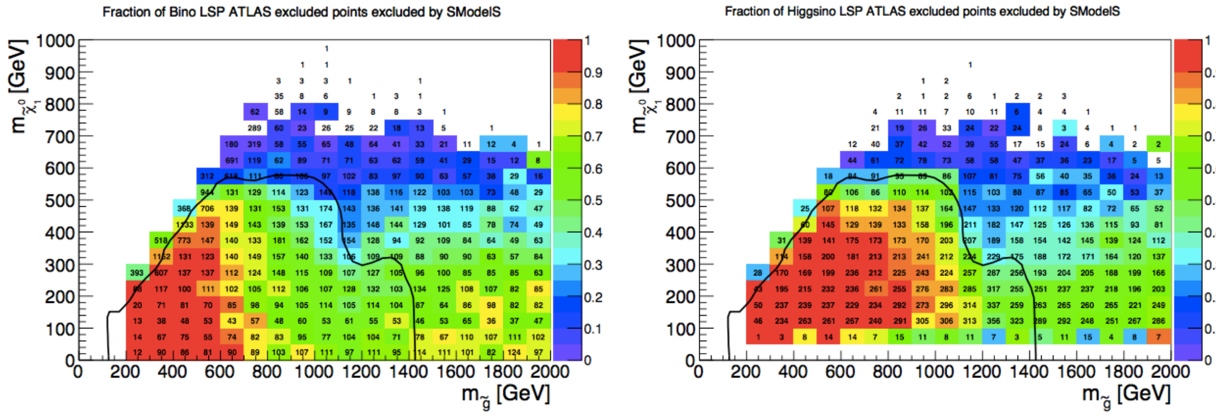

FIGURE 5.3: Distribution of the excluded points for the Bino (left) and Higgsino-LSP (right) dataset in the $(m_{\tilde{g}}, m_{\tilde{\chi}_1^0})$ mass plane. The black line drawn as a reference is the exclusion for a *T1* SMS interpretation of ATLAS-SUSY-2013-02. The numbers in each bin report the total points tested, and the colour code corresponds to the fraction covered by `SModelS`.

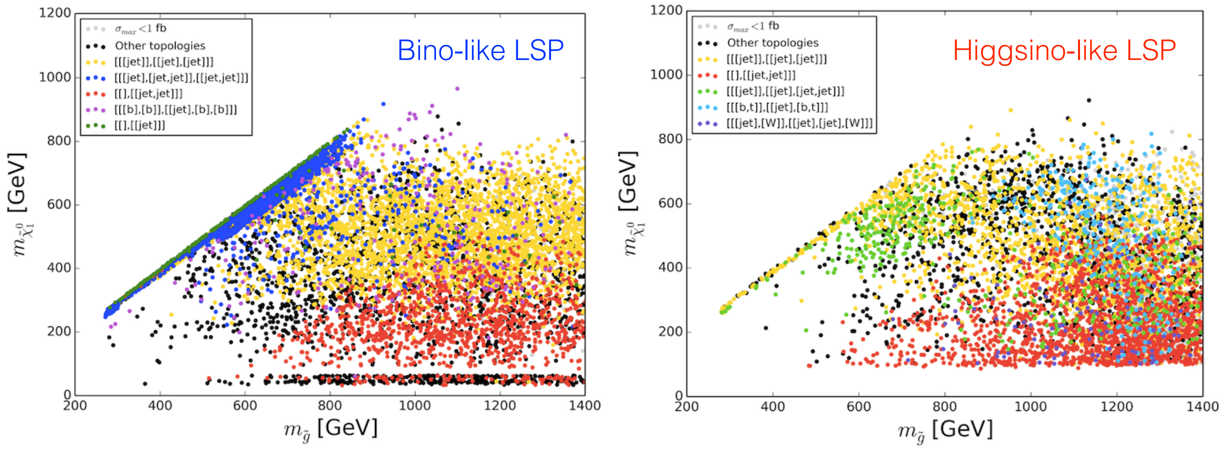

FIGURE 5.4: Missing topologies sorted by frequency of appearance for the Bino (left) and Higgsino-like LSP (right).

Missing Topology in the pMSSM

One of the main features of `SModelS` is the ability of identifying the most important missing topologies. They are a useful guideline to understand which SMS results could potentially improve the constraints on the tested model. However, in general, only the presence of a SMS in the database does not guarantee a proper and complete coverage of a particular experimental signature, since the extracted upper limit may be weak. Different analysis targeting similar final states have different sensitivity with respect to the mass spectra of the SMS, so by recasting a different analysis for an already available SMS might already improve the exclusion.

The most important missing topologies for the Bino and Higgsino-like LSP, sorted by frequency, are shown in Fig. 5.4. We see that in both cases the leading one is identified by the "[[[‘jet’],[[‘jet’],[‘jet’]]]" constraints or "TGQ" in `SModelS` *Txnames* convention, that can come from gluino-squark associated production via two different cascade decays depending on the mass spectrum:

- $pp \to \tilde{g}\tilde{q}, \tilde{g} \to \tilde{q}q, \tilde{q} \to q\chi_1^0$ if $m_{\tilde{g}} > m_{\tilde{q}}$;
- $pp \to \tilde{g}\tilde{q}, \tilde{g} \to g\chi_1^0, \tilde{q} \to \tilde{g}q$ if $m_{\tilde{q}} > m_{\tilde{g}}$;

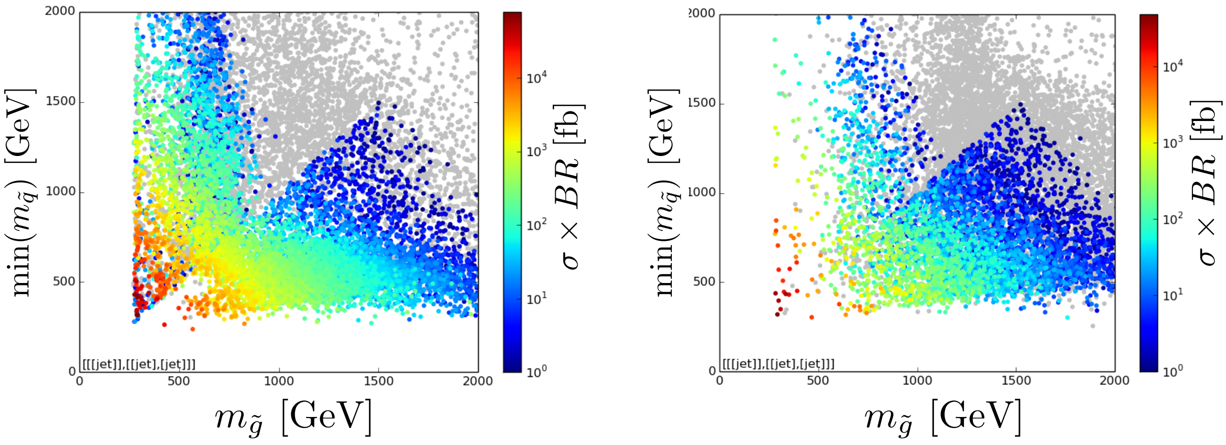

FIGURE 5.5: Total ($\sigma \times BR$) for the "[[['jet'],[['jet'],['jet']]]" constraint for the Bino (left) and Higgsino-like LSP(right), projected in the ($m_{\tilde{g}}, min(m_{\tilde{q}})$) mass plane, for `SModelS` allowed points.

The relevance of this missing topology is understandable since the cross section for gluino-squark associated production is large at the LHC, and there are three different mass parameters for the left-handed, up-type right-handed and down-type right-handed squark in the pMSSM, so that one of the two decay chains can have a large BR. This is visible in Fig. 5.5 showing, for the non excluded points, the value of the ($\sigma \times BR$) , which is quite sizeable especially for light gluinos and squarks. This topology belongs to the poorly covered category of asymmetric SMS, that includes either models with different SUSY mother particles, for example the *TGQ* $pp \rightarrow \tilde{g}\tilde{q}$, or models where the same SUSY particle decays in different ways in the two branches, for example $pp \rightarrow \tilde{g}\tilde{g}, \tilde{g} \rightarrow q\bar{q}\tilde{\chi}_1^0$ or $\tilde{g} \rightarrow b\bar{b}\tilde{\chi}_1^0$. Most frequently all the SMS results provided by the experimental collaborations assume symmetric topologies; due to this, a large ($\sigma \times BR$) cannot be constrained.
The constraining power of the *TGQ* (or more precisely *T3GQon*) simplified model will be extensively treated in Section 5.4.2.

The importance of asymmetric missing topologies is shown in Fig. 5.6. For each un-excluded model point with $\sigma_{tot} \geq 10$ fb, the total unconstrained weight ($\sigma \times BR$) coming from asymmetric models, normalised to the total 8 TeV cross section, is shown. Only the asymmetric model with at most 1-step decay are considered. It can be immediately seen that for a large number of points the fraction of missing cross section from asymmetric topologies is above 50%, with peaks at over 90%. Whenever the production cross section of a particle, e.g. gluinos, is shared among several decay

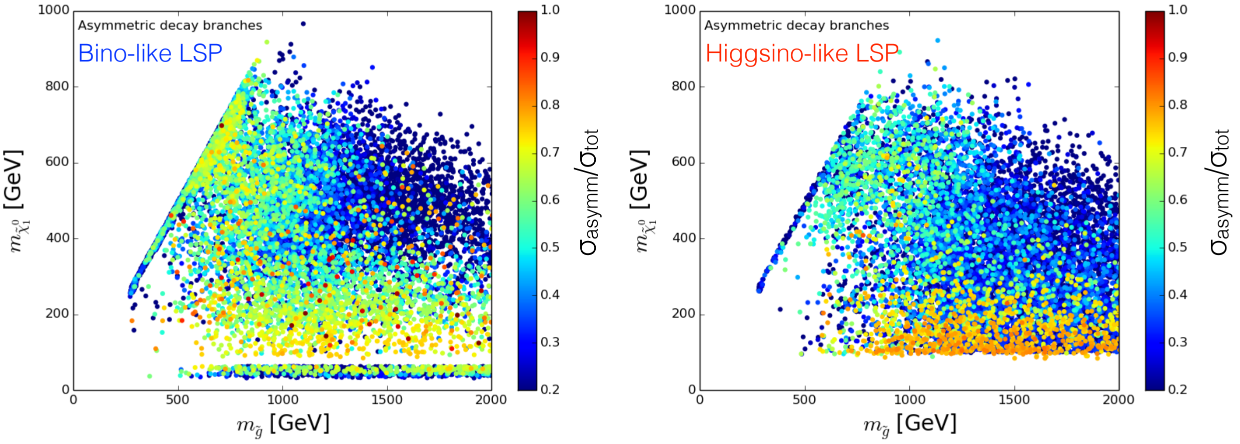

FIGURE 5.6: Total contributions of asymmetric branches to the full 8 TeV cross section (for points with σ_{tot}>10 fb) for the Bino (left) and Higgsino-like LSP (right).

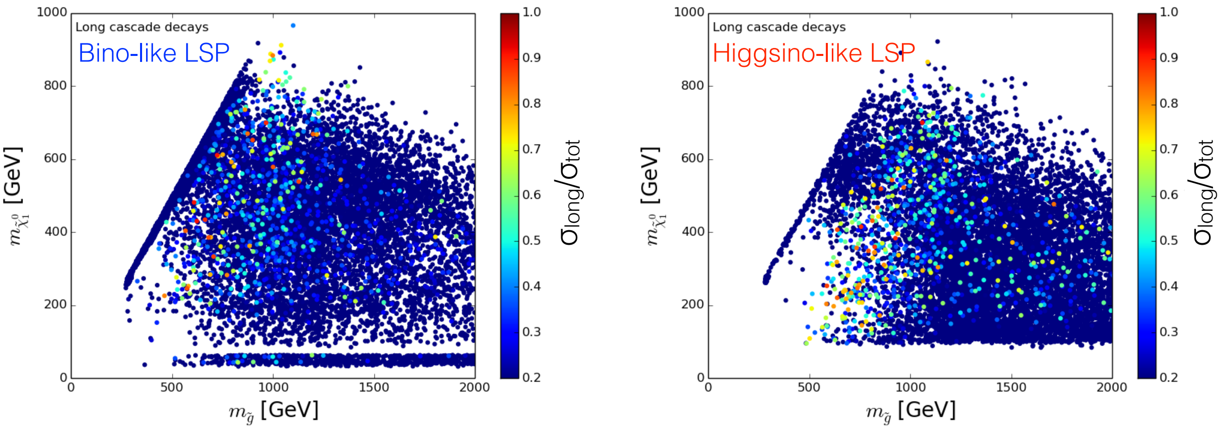

FIGURE 5.7: Total contributions of long decay chains, defined as supersymmetric models with more than one-step decay to the LSP, to the total cross section for the Bino (left) and Higgsino-like LSP (right).

patterns, asymmetric topologies (from the same mother particle) become automatically relevant.

I conclude this Section on the global coverage of the pMSSM with Fig. 5.7, showing again for not excluded points with $\sigma_{tot} \geq 10$ fb, the fraction of the total cross section missed by SMS with long decay chains (defined as topologies with more than one intermediate BSM particles, i.e. decaying to the LSP in more than one step). This is a very important and useful outcome of this study: it shows that indeed one of the assumptions at the basis of simplified models, i.e. that signals can be efficiently described by only a few parameters, does not largely reduce the ability to reconstruct a full model, since only a small number of points has long cascade decays contributions.

I remind that the maximum number of free parameters considered by `SModelS` for a feasible simplified model characterisation is three, corresponding to *[mother,intermediate,LSP]* masses in one-step decay models, or *[mother1,mother2,LSP]* in models with asymmetric branches. The main reason for this limitation is the required number of mass planes to properly cover the mass parameter space of the SMS.

5.3.3 Constraints from ATLAS and CMS Official Results

This Section and the following are meant to provide a detailed characterisation of the constraints provided by the different SMS results included in the `SModelS` database. For this reason, the attention is now shifted to the points that can be excluded by the SMS results. This is done to highlight the most interesting topologies already available, as well as the most powerful analyses providing the best limits. In fact, contrary to the expectation coming from the large variety of SMS results implemented in the database, most of the constraints come from only a few results. This analysis is useful since it gives a concrete guideline to produce additional recast results and further extending the database. Specifically the results produced by the `Fastlim` Collaboration include simplified models that were never employed by the LHC Collaborations, so it is worthy to quantify in detail their impact on the pMSSM.

The exclusion by official ATLAS and CMS results wills be treated separately. For the ATLAS case, I will include only the results from published analyses, since they supersede the preliminary results also available in the database. In the case of CMS, four preliminary results are also considered since the corresponding published results could not be implemented in the database. Given the limited

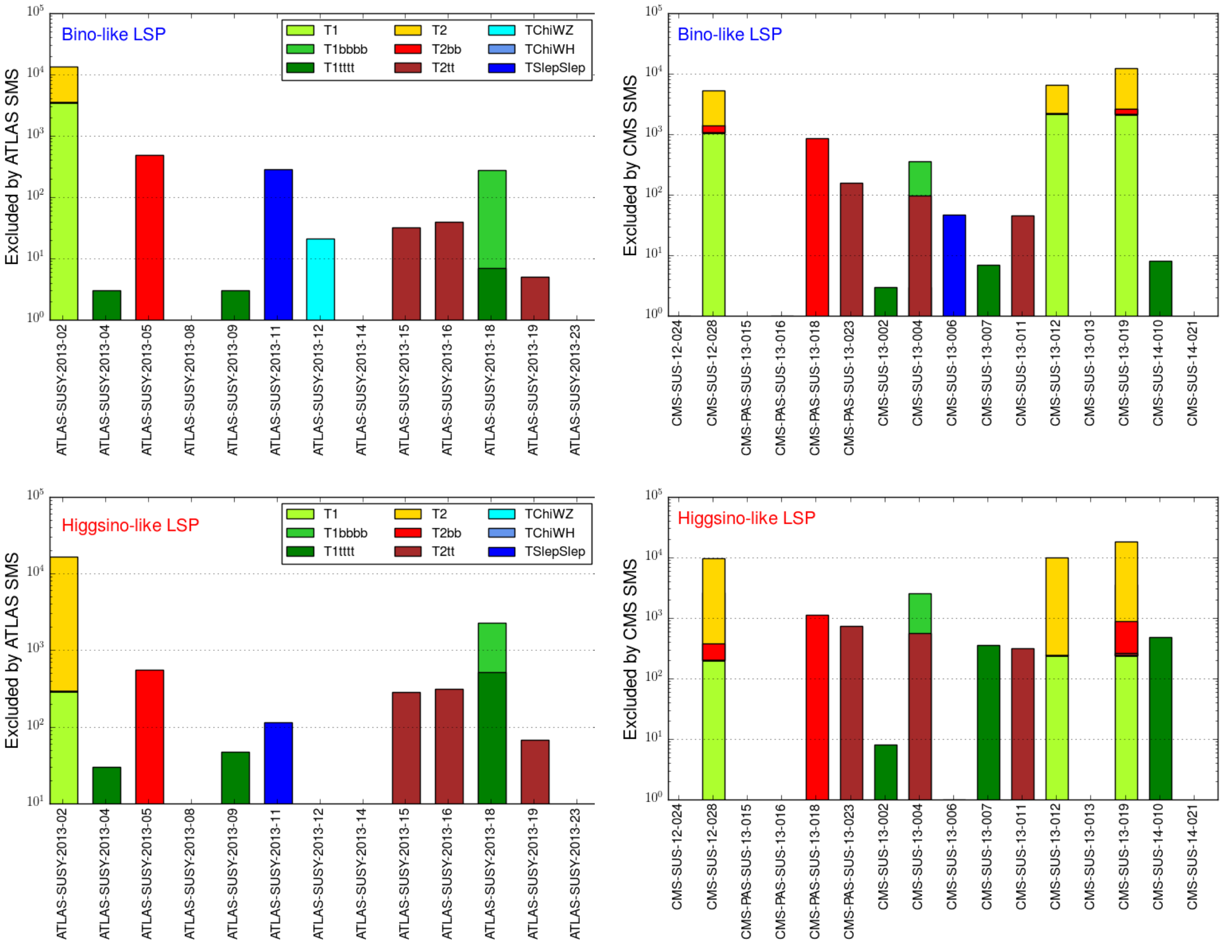

FIGURE 5.8: Excluded points for the Bino (top) and Higgsino-like (bottom) LSP dataset from selected ATLAS and CMS UL results. Only the most common direct decays and most constraining SMS results are shown. Note that the y-axis is in log scale. A complete summary of UL exclusion is given in Appendix D.

number as well as the small contribution to the `SModelS` exclusion as seen in Fig. 5.2, EMs results will be omitted. Finally, only UL results for the most common and most constraining simplified models are shown.

The exclusion provided by each UL result is presented in Fig. 5.8; note that the plots are in log scale. It can be immediately seen that the exclusion power in terms of simplified models come essentially from analyses designed to look for gluinos and squarks in the hadronic final state, also known as the *inclusive* SUSY searches: ATLAS-SUSY-2013-02($0l, 2-6jets$)[91], CMS-SUS-12-024(α_T)[104],CMS-SUS-13-012($H_T, \not{H}_T$)[49], and CMS-SUS-13-019(m_{T2})[106]. This is compatible what was found also by ATLAS pMSSM study, showing that the ATLAS-SUSY-2013-02 analysis is the one providing the best constraining power in terms of number of excluded points. Note that this does not mean, in general, that the UL provided by these analyses are the best for each point tested. In terms of SMS, the $T2: \; pp \to \tilde{q}\tilde{q}, \tilde{q} \to q\tilde{\chi}_1^0$ drives the exclusion for both LSP datasets, and is the most constraining SMS. In addition, for the Bino-like and the Higgsino-like LSP, the $T1: \; pp \to \tilde{g}\tilde{g}, \tilde{g} \to q\bar{q}\tilde{\chi}_1^0$ and $T1bbbb: \; pp \to \tilde{g}\tilde{g}, \tilde{g} \to b\bar{b}\tilde{\chi}_1^0$ models respectively become relevant. SMS results for EW models, either sleptons or gauginos (charginos,neutralinos) searches, are able to exclude only a few hundred points in total. This can be understood by considering that the SMS interpretation provided for the *TChiWZ* or *TChiWH* ($pp \to \tilde{\chi}_1^\pm\tilde{\chi}_2^0, \tilde{\chi}_1^\pm \to W\tilde{\chi}_1^0, \tilde{\chi}_2^0 \to Z/H\tilde{\chi}_1^0$ always assume that $m_{\tilde{\chi}_2^0} = m_{\tilde{\chi}_1^\pm}$, a condition that is seldom satisfied in the general pMSSM model.

A full summary of the exclusion provided by all the UL results included in the database v1.1 is given in Appendix D, including one-step cascade decays for gluino, stop and slepton production. Due to the specific mass assumptions for the SMS interpretation and the limited availability of mass planes, models with cascade decays cannot constrain efficiently within the pMSSM. Note however that, in the spirit of simplified models, it is worth to include all the possible signatures in the database, since other BSM models might be indeed constrained by such results.

The exclusion provided by the four *T1* results implemented in the database, targeting gluino production, is shown in Fig. 5.9; the presence of various patches of points excluded by a specific analysis highlight how different types of searches are sensitive to different regions in the mass space. It is difficult however to make more precise quantitative statements. Many CMS analyses combine several SRs to calculate the UL, so a single SR might not prove sufficiently constraining, and even if EMs were available, it would be impossible from the outside to combine them within `SModelS` .

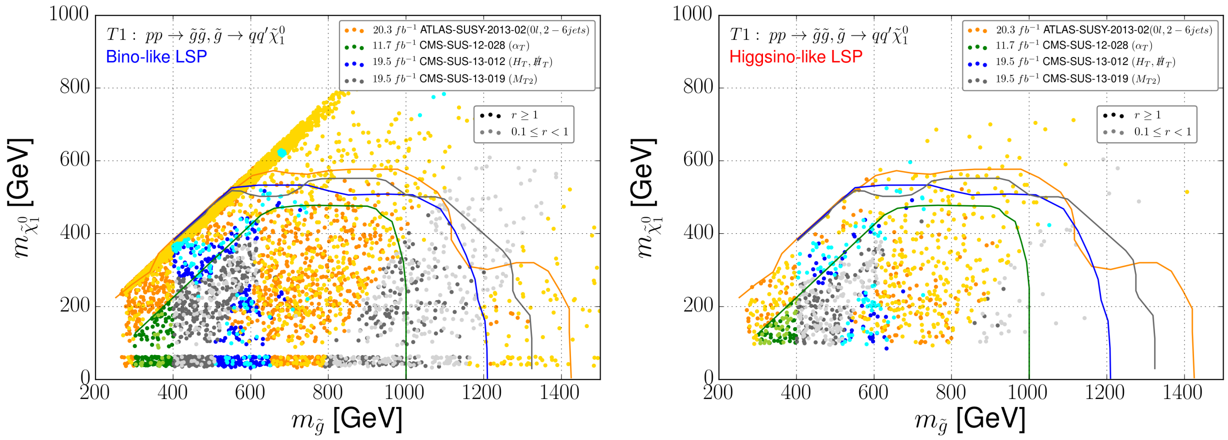

FIGURE 5.9: Distribution of the points excluded (dark shade) by the T1 SMS for the ATLAS and CMS analyses. The analysis providing the best limit is shown in different color. Non-excluded points, in lighter shades, have $0.1 \leq r < 1.0$.

Nevertheless it shows that, in general, the best UL is not necessarily given by the analysis with the highest exclusion power (in terms of higher gluino mass) over the whole mass plane. Indeed often the searches are designed to push the exclusion to higher and higher masses. Finally note that UL maps might be defined using different grids of simulated points, e.g. the CMS-SUS-13-012 and CMS-SUS-13-019 results are not given for $\Delta m(\tilde{g},\tilde{q}) \leq 400\ GeV$, making the analysis CMS-SUS-12-028 (which does not use the full luminosity dataset of Run 1) more constraining in the low gluino mass region. It is impossible to state if those analyses could provide better limits in the same region.

5.3.4 Constraints from Fastlim Results

As explained in detail in Section 4.2.4, the `SModelS` database was enriched with homegrown EM results, as well as several EMs created by the `Fastlim` Collaboration and adapted to the `SModelS` format. In this Section I aim at characterising the simplified models results contained in the `Fastlim` datasets that provides the best exclusion. This is of interest since the `Fastlim` SMS interpretation was specifically meant for a ‘natural SUSY’ scenario, while homegrown results targeted mostly gluino pair production. Both these classes of results include SMS interpretation that were not provided by the experimental collaboration, hence understanding the impact in detail gives a powerful indication on how to proceed further for future extensions of the database.

ATLAS-CONF-2013-047

From the list of `Fastlim` analyses included in the database (Tab. 4.8), I will focus on the ATLAS-CONF-2013-047[119], which is the preliminary analysis later superseded by the ATLAS-SUSY-2013-02. This inclusive search looks for events with a large jet multiplicity and missing transverse energy while vetoing isolated leptons. The key kinematic variable of the analysis is the effective mass m_{eff}, defined as the scalar sum of the p_T of the leading jets and the missing transverse energy:

$$m_{eff} = \sum_j |\mathbf{p_T}^j| + |\not{E}_T^{miss}| \tag{5.1}$$

This variable helps reduce the QCD background by requiring the quantities $\not{E}_T^{miss}/m_{eff}$ or $\not{E}_T^{miss}/\sqrt{H_T}$, where H_T is the scalar sum of the jets p_T, to lie above a certain threshold; this threshold is different for the different signal regions. The signal regions are defined by selecting signal jets with low, medium, or high transverse momentum and different jet multiplicities.

The distributions of excluded points for this analysis, as a function of the gluino mass, is given in Fig. 5.10 . The histogram shows the contributions of each SMS results: each colour corresponds to the points excluded exclusively by the SMS considered. For clarity, consider the *T2* model distribution. Those points can be excluded only by *T2*, meaning that the $r(T2) \geq 1$ while $\sum_{SMS \neq T2} r < 1$, or in other words, those points are excluded only because the *T2* results is available. The grey area of the plot shows instead the points excluded only by the combination of signals coming from at least two different SMS, i.e. the maximum r-value of any SMS does not exceed unity. The total number of points is also reported inside the brackets in the legend. It is evident that in the Higgsino-like LSP case, the exclusion gains significantly from the signal combination with EM, while this is more modest in the case of the Bino-like LSP case.

The other consideration regards the *T2* model, that maps to the "[[[‘jet’]],[[‘jet’]]]" `SModelS` constraint notation. This is again is confirmed to be the most powerful results, constraining alone

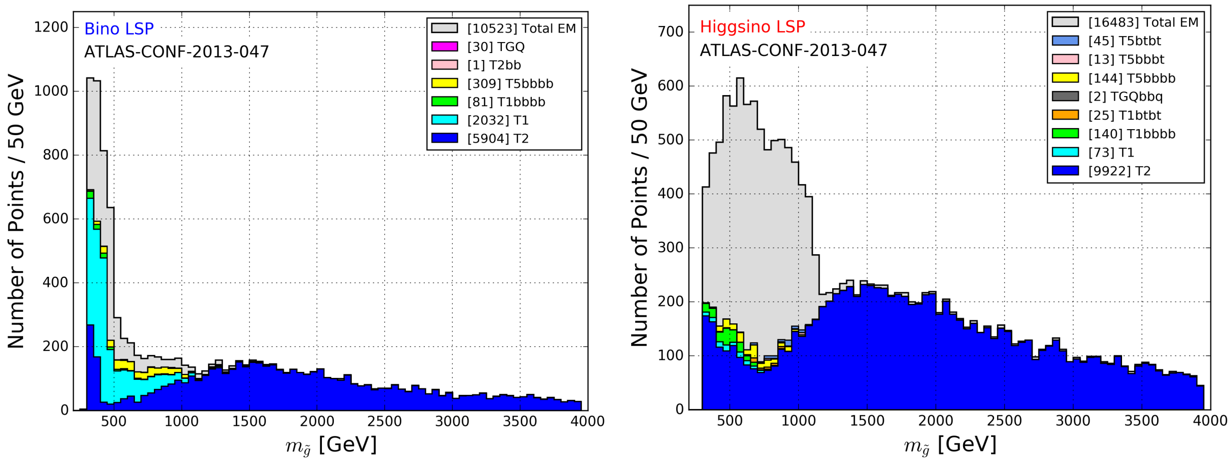

FIGURE 5.10: Distribution of the points excluded by the SMS results, recast by the `Fastlim` Collaboration, for the ATLAS-CONF-2013-047 analysis. Each entry in the legend shows the points excluded exclusively by the specific SMS only; in brackets, the number of excluded points is given. The grey area corresponds to the sets of points excluded by a the combination of two or more SMS signals.

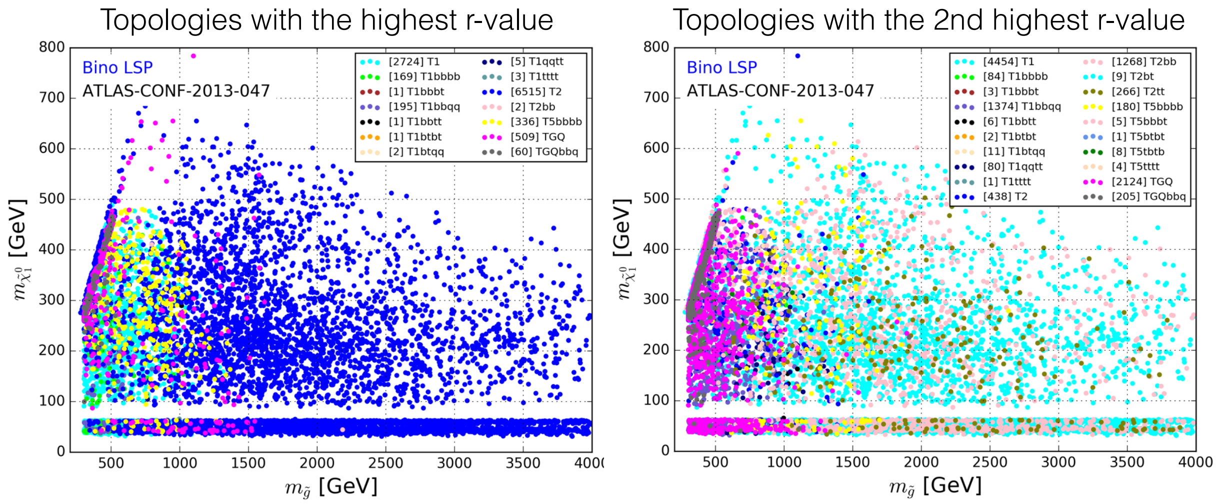

FIGURE 5.11: Distribution of the topologies providing the `SModelS` best (left) and second best r-value (right) the Bino-like LSP dataset in the $(m_{\tilde{g}}, m_{\tilde{\chi}_1^0})$ mass plane.

60% of the points. The aim of the rest of the Section is to analyse which models can be effectively combined together to improve the exclusion, one of the most important benefits of using efficiency maps. Figures 5.11 and 5.12 show, for each point excluded by ATLAS-CONF-2013-047, the distributions of the topologies providing the best limit, i.e. the highest r-value. Besides the *T2* model, also the *T1* model is important, and for a large number of points the *T1* and *T2* models are the respectively the most and second-most constraining models.

5.4 Extending the Coverage with Gluino-Squark Simplified Models

In this final Section dedicated to the pMSSM coverage I will discuss the improvement in the coverage on the pMSSM from to the inclusion of *TGQ* results constraining the "[[['jet']],[['jet'],['jet']]]" or *3jets*+E_T^{miss} signature, which was found to be the most important missing topologies in both the Bino and Higgsino-like LSP scenarios (see Fig. 5.4 and related discussion). This model will be

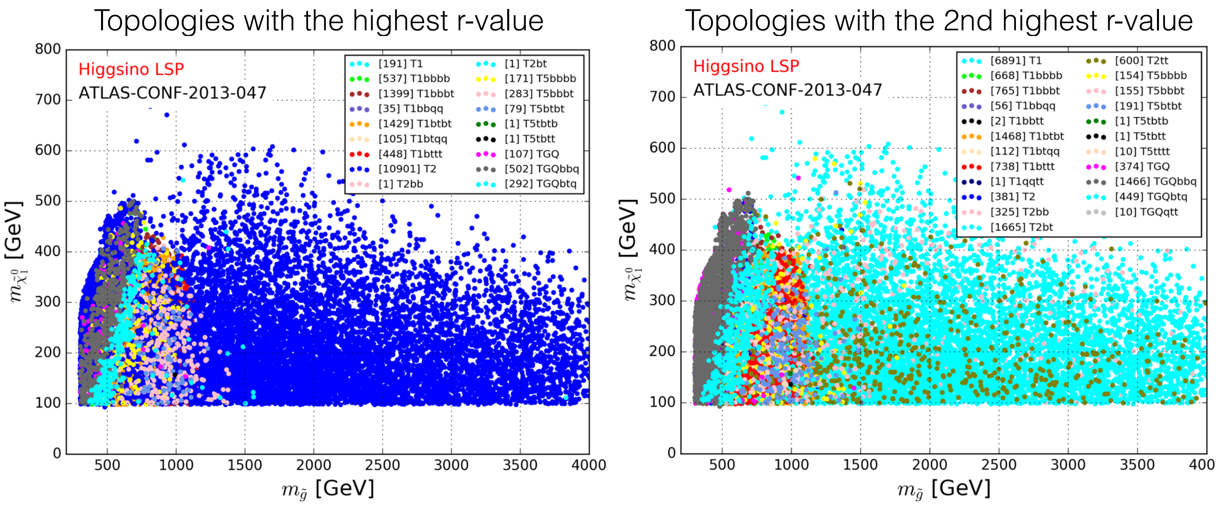

FIGURE 5.12: Same as Fig. 5.11 for the Higgsino-like LSP dataset.

labelled *T3GQon* for the reason soon explained. Note that also other missing topologies from the pMSSM include generic gluino-squark associated production, but they involve more complicated decay patterns.

Along with the results from *TGQ*, the power of combining the *T2* and *T5* models will be explored. In fact the asymmetric *TGQ* model is the combination of one branch from the *T2* and one from the *T5*. The branch with the *[‘jet’]* constraint requires a SUSY particle decaying to a jet and the LSP, while in the second *[[‘jet’],[‘jet’]]* branch there is a cascade decay to the LSP via an intermediate SUSY, producing a jet in each of the two vertices. Since the aim is to constrain points for which the total gluino+squark associated production is large, both the squark and gluino pair production cross section will be large, and the *T2* and *T5* models will naively constrain models in the same region of the parameter space where the *TGQ* is important. With EMs results, where the contribution coming from different signals is added up, the full reconstruction pf the signal *T2+T5+TGQ* can be obtained. As summarised by Tab. 5.1, in generic pMSSM points there are three free squark mass parameters plus the mass of the gluinos, that can result in different allowed mass hierarchies. When considering one single squark mass with $m_{\tilde{g}} > m_{\tilde{q}}$ (and the other third generation squark set to a high scale), then the gluino will decay to an on-shell intermediate squark, and the squark directly to a quark plus the LSP. However, for inverted hierarchies where all the squarks are heavier than the gluino, the squark will decay to an on-shell intermediate gluino, while the gluino will decay either via loop decay to the LSP, or for a small enough mass gap between the gluino and the lightest squark, via a three-body decay from off-shell squark $\tilde{g} \to q\bar{q}\tilde{\chi}_1^0$. This model

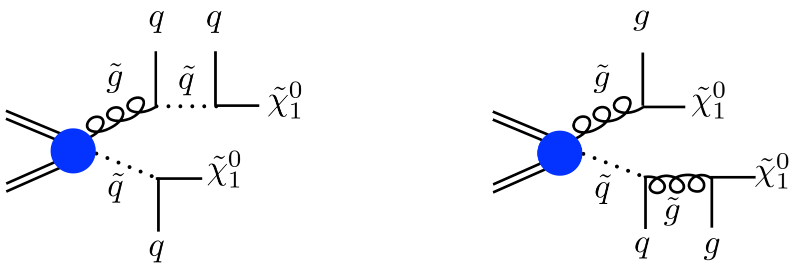

T3GQon: [[[‘jet’]],[‘jet’]], [[‘jet’]]] T3GonQ: [[[‘jet’]],[[‘jet’], [‘jet’]]]

FIGURE 5.13: Diagrams for the simplified models T3GQon (left) and T3GonQ (right).

will not be considered here, and it gives a 4-jets "[[[‘jet’,‘jet’]],[[‘jet’],[‘jet’]]]" signature. In another possible case, the gluino mass is set as intermediate between two squark families: the heavy squark will decay to intermediate on-shell gluinos, the gluino will decay to a lighter on-shell squark, and this will decay directly to the LSP.

In Fig. 5.13 the diagrams for the models with gluino-squark associated production that produce the "[[[‘jet’]],[[‘jet’],[‘jet’]]]" or *3jets+*E_T^{miss} signature, for the two different gluino-squark mass hierarchies, are shown. Only the lightest squark family is considered for simplicity.

An assumption underlying the `SModelS` framework is that the analysis efficiencies primarily depend on the mass array of the BSM particles involved, while all the other parameters of the theory only produce negligible effect.
However the case illustrated has a subtle difference, since it is basically assuming that the experimental constraints cannot distinguish between jet originating from gluons of jets originating from quarks. This means to assume that the hadronization and subsequent clustering in jets of gluons and quarks is equivalent at the level of Monte Carlo production. This assumption will be tested in the following part of the Chapter for a similar but simpler simplified model producing quark or gluons in the final state. Then, in Section 5.4.2, we will see how the pMSSM constraints improve significantly when the *T2*,*T5* and *T3GQon* are combined.

5.4.1 Gluon vs Quark jets under SModelS Assumptions

As introduced when discussing the constraints provided by official UL results in Section 5.3.3, the most powerful analyses, in terms of number of excluded points of generic pMSSM scans, are the searches for SUSY in events with large jets multiplicity and $\not{E}_T^{miss}$, such as the two multijets analyses described above. Additionally, the CMS-SUS-13-019 m_{T2} analysis alone is able to exclude roughly 9,900 and 17,800 points of the Bino and Higgsino-LSP dataset with the *T2* UL results (from Appendix D).

The first important point to be stressed is that in `SModelS` formalism, the class of particle defined generically as *‘jet’* in the experimental constraints include both jets originating from light (1st and 2nd generation) quarks, and jets coming from gluons. This implies that a constraint like *[[[‘jet’]],[[‘jet’]]]*, will be applied to any decomposed element with two jets in the final state irrespectively of weather they are light quarks or gluons. More concretely, the same constraint applies to *[[[‘q’]],[[‘q’]]]*, *[[[‘g’]],[[‘g’]]]* and *[[[‘g’]],[[‘q’]]]* where ‘g’ (gluon) and ‘q ’(quark).

The distinction of the three above cases is not currently applied in the `SModelS` framework, hence for the pMSSM study all the generic *2-jets* elements were mapped onto the *T2* simplified model results described by *[[[‘jet’]],[[‘jet’]]]*. Like the case of the *T3GQon* and *T3GonQ*, I introduce a different nomenclature for simplicity: the model *T2*, currently available in the database and used by the LHC experiments, will be called *T2qq*; this corresponds, strictly speaking, to the *[[[‘q’]],[[‘q’]]]* constraint. The model *T2gg*, which was never used by the experiments to interpret searches, corresponds to the *[[[‘g’]],[[‘g’]]]* constraint. To briefly recap, `SModelS` uses the *T2qq* results to constrain also the *T2gg* gluino loop decays.

The task of quantifying how much this assumption impacts the limits is the object of this Section, as well as investigating the large exclusion power of the generic *T2qq* results. I start the discussion with Fig. 5.14, that compares the exclusion provided by the *T2* UL results available in the database for the analysis ATLAS-SUSY-2013-02($0l, 2-6jets$, CMS-SUS-12-028(α_T), CMS-SUS-13-012($H_T, \not{H}_T$) and CMS-SUS-13-019(m_{T2}). For each point only the analysis providing the highest r-value is indicated. In the left plot, corresponding to the Bino-like dataset, the exclusion curve from the analysis CMS-SUS-13-019 is drawn in comparison with the naive simplified model limit, distinguishing the case where only one squark type is reasonably light to be produced at the LHC, and the case where all the eight types are light. On the right, a visualisation of the exclusion in a different mass plane, for the Higgsino-like LSP dataset is shown.

It is clear that a very large number of the points excluded by the *T2* results are not relatable to light squarks in the pMSSM points considered. In fact, by looking at the left plot, the exclusion exceeds way beyond the naive SMS exclusion, and even considering an increase in the cross section due to the presence of other light SUSY particles, that might contribute with electroweak processes with t-channel exchange of neutralinos and charginos or strong processes like the exchange of t-channel gluinos. Even in the case of completely degenerate squarks, masses much above 1 TeV should not be excluded. In the left plot, particularly interesting is that the whole region with 300 GeV $\leq m_{\tilde{\chi}_1^0} \leq$ 500 GeV is efficiently constrained. Likewise, in the right plot, there is a clear correlation of the excluded points with the region of low gluino mass, again around 500 GeV.

Combining this information, it seems that the exclusion of a large number of points is due to gluino that undergoes a radiative decay $\tilde{g} \to g\tilde{\chi}_1^0$. In particular this is a very efficient decay mode whenever only gauginos are light and the SUSY scalar sector is decoupled. For specific regions of the parameter space, the loop decay is the most prominent decay mode, and it can dominate over the 3-body decays via off-shell squarks like e.g. $\tilde{g} \to q\bar{q}\tilde{\chi}_1^0$ or $\tilde{g} \to b\bar{b}/t\bar{t}\tilde{\chi}_1^0$ (see e.g. [140] for an extensive review of gluino loop decays). To further prove this, in Fig. 5.15 the BR of the radiative decay is shown as a function of the mass difference between the gluino and the LSP, and the lightest squark mass, considering all the three generations. The value of the BR reaches up to 100 % for a large number of points, especially in the Bino-like LSP dataset. While in the Higgsino case the BR seems generally lower, the loop decay dominates over a larger range of $\Delta M(\tilde{g}, \tilde{\chi}_1^0)$ with respect to the Bino case, for which the majority of points with high BR is located in the compressed region $\Delta M(\tilde{g}, \tilde{\chi}_1^0) \lesssim 0.50$.

In Fig. 5.16 BR($\tilde{g} \to g\tilde{\chi}_1^0$) and BR($\tilde{q} \to q\tilde{\chi}_1^0$) are compared against each other, and the color

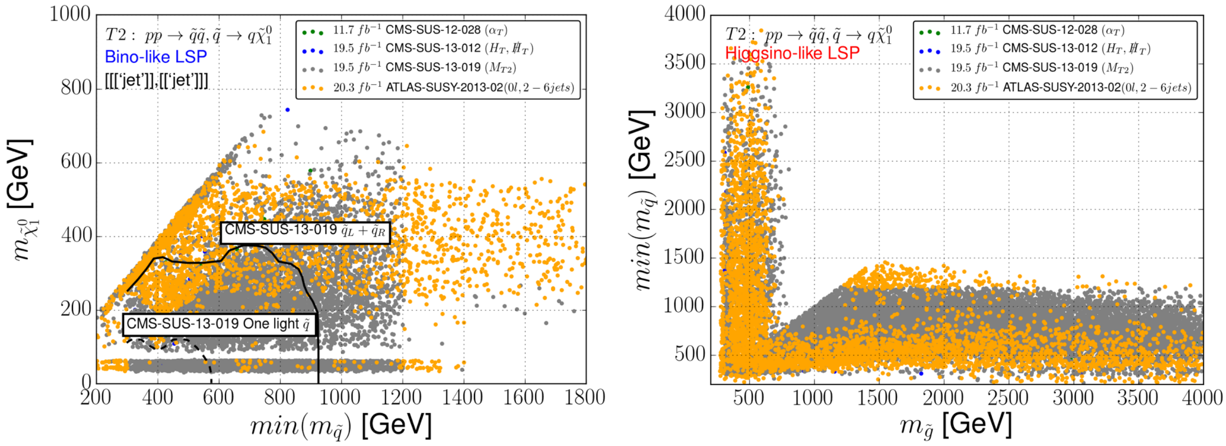

FIGURE 5.14: Distributions of the points excluded by the *T2* UL results (r-value ≥1), for the analysis giving the maximum r-value described in the legend. Left: Bino-like LSP dataset, in the squark-LSP mass plane. In addition, the exclusion curves for the analysis CMS-SUS-13-019 are provided for the case of one single light squark type (dashed line), and 8 degenerate types (solid line). Right: Higgsino-like dataset, in the gluino-lightest squark mass plane.

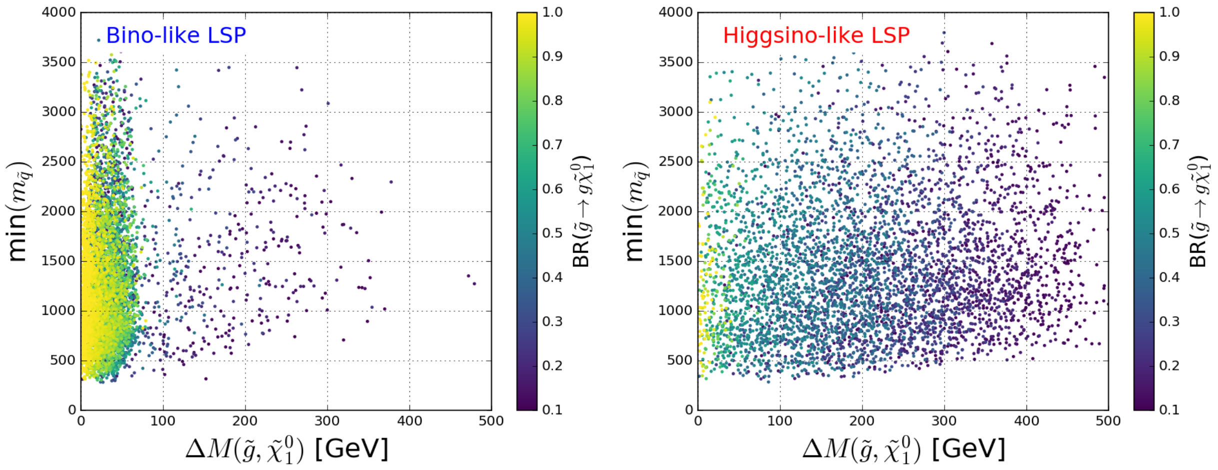

FIGURE 5.15: BR $\tilde{g} \to g\tilde{\chi}_1^0$ for the Bino(left) and Higgsino(right)-like LSP as a function of the mass difference $\tilde{g} - \tilde{\chi}_1^0$ and the lightest squark. Contrary to the Bino-like LSP case, where the loop decay dominates only for $\Delta M(\tilde{g},\tilde{\chi}_1^0) \leq$50 GeV, in the Higgsino the distributions of high BR points spreads up to 400 GeV mass difference, while on average the BR is smaller than the Bino case. Points with BR<0.1 are not shown.

	$\mathrm{BR}(\tilde{g}\to g\tilde{\chi}_1^0)$		$\mathrm{BR}(\tilde{q}\to q\tilde{\chi}_1^0)$	
Branching Ratio	Bino	Higgsino	Bino	Higgsino
$0.05 \leq \mathrm{BR} \leq 0.20$	1121	2533	1365	1953
$0.20 < \mathrm{BR} \leq 0.40$	636	1574	399	3679
$0.40 < \mathrm{BR} \leq 0.60$	586	1460	1090	10008
$0.60 < \mathrm{BR} \leq 0.80$	995	178	2739	5103
$0.80 < \mathrm{BR} \leq 1.0$	2752	117	5540	572

TABLE 5.3: Number of points divided according to their $\mathrm{BR}(\tilde{g}\to g\tilde{\chi}_1^0)$ and $\mathrm{BR}(\tilde{q}\to q\tilde{\chi}_1^0)$, where $\tilde{q}$ is the lightest squark of the first two generations. The set of points with large BRs for both modes is small, as shown in Fig. 5.16.

maps indicate the mass difference between the gluino and the lightest squark. The purpose of the comparison is to highlight if there is a large fraction of pMSSM possessing both a large fraction of gluino decaying via the radiative loop and where the lightest squark decay directly to the LSP, i.e. where the same *T2* experimental results will be applied to both elements. Only in Bino-like LSP there is a non negligible fraction of points where both decays modes have decent BR.

Next, the efficiencies and upper limits of the *T2qq* and *T2gg* models are estimated individually. For this purpose, efficiencies for the *T2qq* and *T2gg* were produced and implemented separately in the `SModelS` database. Two inclusive searches were considered: CMS-SUS-13-012 (code and validation available at [141],[75]) and ATLAS-SUSY-2013-02 (code and validation available at [142],[74]).

The results for the *T2qq* model, despite official results being provided by the collaborations, were produced for two main reasons: first, because of the mass plane coverage, which was not optimal in the official results; the second reason was to decrease possible uncertainties due to the Monte Carlo settings, and again the usual setup described in Chap. 4 was used.

Unfortunately the CMS-SUS-13-019, providing the strongest exclusion for the *T2qq* model, is not implemented in the available recasting tools.

Following the `SModelS` validation procedure (see Section 4.2.5), exclusion curves were extracted and compared in Fig. 5.17 and Fig. 5.18. For comparison, also the official exclusion curves are plotted, as well as the exclusion obtained by `SModelS` using the official EM results from the Collaboration. Note that the under-exclusion in the case of the CMS analysis is due to the impossibility of combining the 36 SRs defined in the analysis. This also explains the erratic behaviour of the curve, due to the jumps in the selection of the signal regions driving the limit.

For each analysis, also the map of the best SR over the whole mass plane is also provided. This information is important to understand discrepancies when comparing limits obtained using different EM results. In fact the simplified limit procedure first determines the best expected limit among all the SR; then the observed limit of the best SR is quoted as the experimental limit of the analysis.

It is clear that in case efficiencies between SRs vary greatly, also the selection of the best SR may vary, producing differences in the quoted limits hence in the exclusion. Regarding the ATLAS analysis, the *T2qq* and *T2gg* results both over-exclude the official curve in the small gluino/squark region, while the *T2qq* tends to over-exclude also in the high squark mass region. However, looking at the best SR map, this is not explainable with the choice of a different signal best region that indeed looks consistent through all the plane.
The SR *2jm* leads the exclusion for $m_{\tilde{q}} \approx 500$ GeV. Since official values are available, it is interesting to compare the recast efficiencies, as in Fig. 5.19, where the ratio of the recast over official values is shown. While a difference below 20% is achieved in most of the mass plane, the ratio increases exactly in the region of the over-exclusion up to 60%. Since the `MadAnalysis 5` validation does not provide the recast exclusion curve nor mention any specific issue relative to higher efficiency for some SRs, it quite difficult to further investigate the source of the discrepancy, that is in any case acceptable.

To the contrary, in the case of the CMS analysis a major difference in the choice of the best SR is seen, and in the *T2gg* case SRs with higher jet multiplicity seem to be favoured. This is most likely an effect of the different extra parton emission from initial gluinos or squarks: the difference is in fact most dominant in the region of average mother mass, where the signal is fully captured

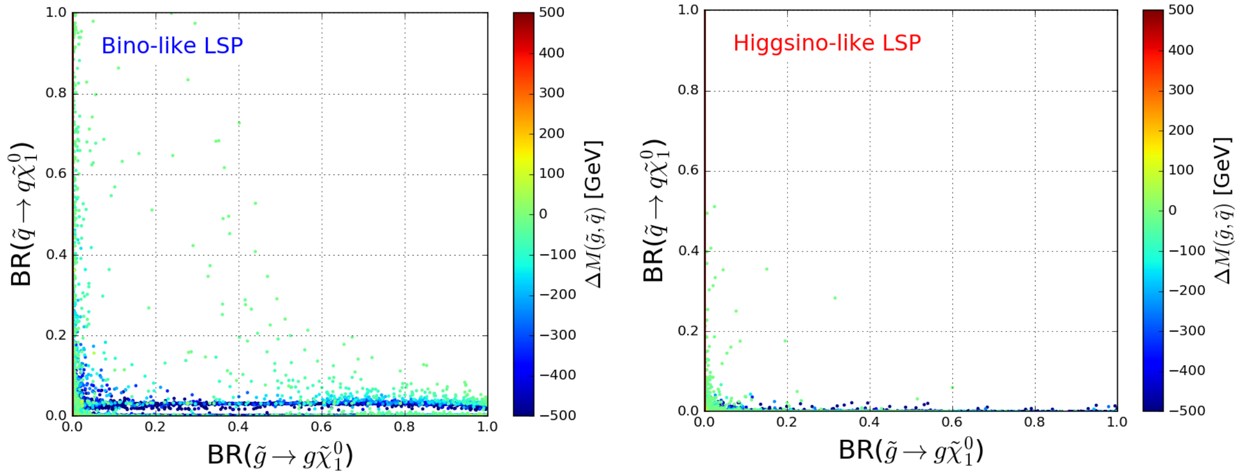

FIGURE 5.16: BR $\tilde{g} \to g\tilde{\chi}_1^0$ and $\tilde{q} \to q\tilde{\chi}_1^0$ for the Bino(left) and Higgsino(right)-like LSP. The color map gives the mass difference $\Delta M(\tilde{g}, \tilde{\chi}_1^0)$. Only in the Bino-like LSP case, a few tens of points possess large gluino loop decay BR and direct squark decay.

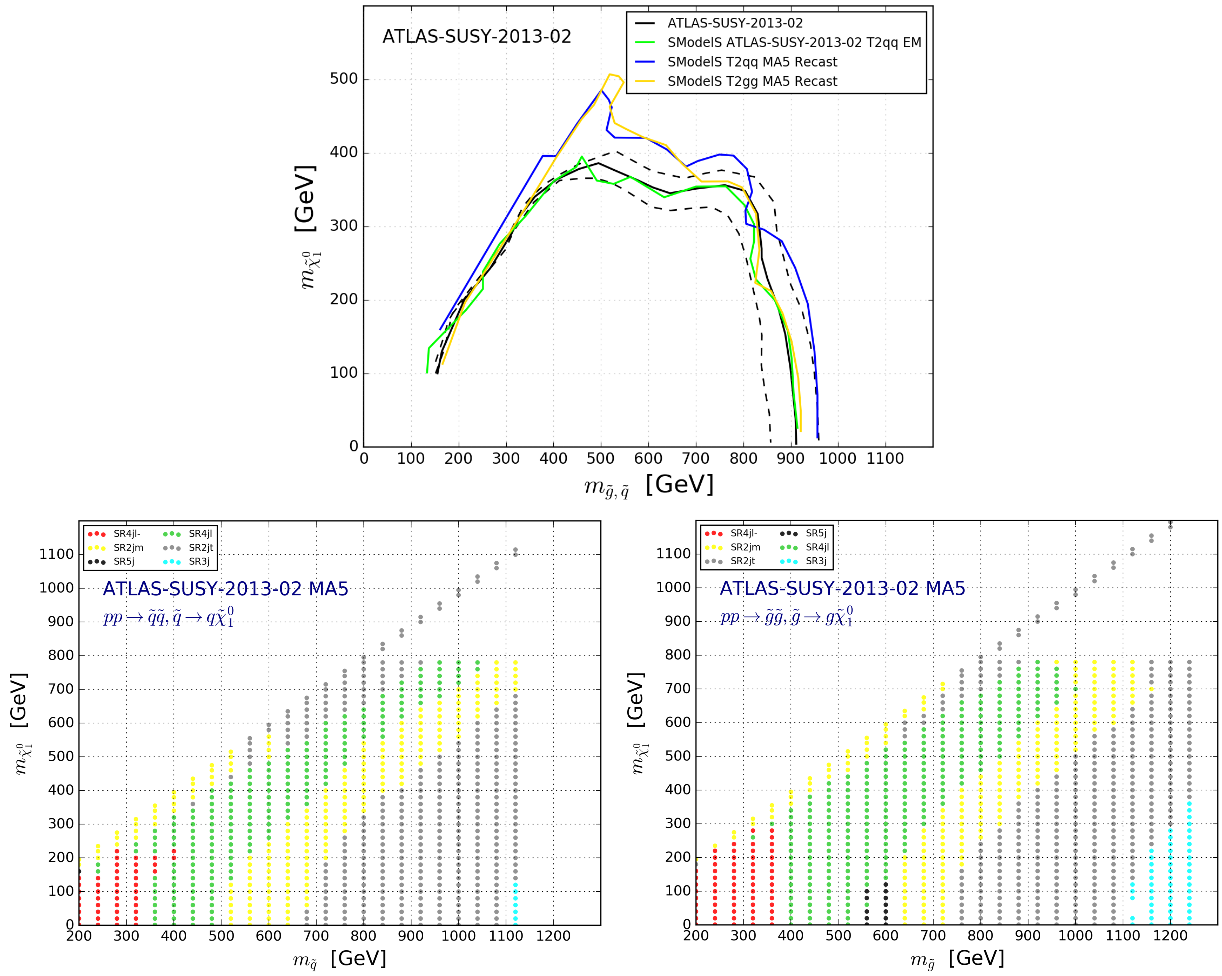

FIGURE 5.17: Exclusion curves for the ATLAS-SUSY-2013-02 analysis (top). The black lines show the official exclusion (solid) with the $\pm 1\sigma$ uncertainty band (dashed), and the green line the `SModelS` exclusion obtained with official EM results. The blue and yellow lines show the exclusion obtained with the MA5 recast EMs for the *T2qq* and *T2gg* models respectively. Bottom: best SR map for the *T2qq*(left) and *T2gg*(right) models.

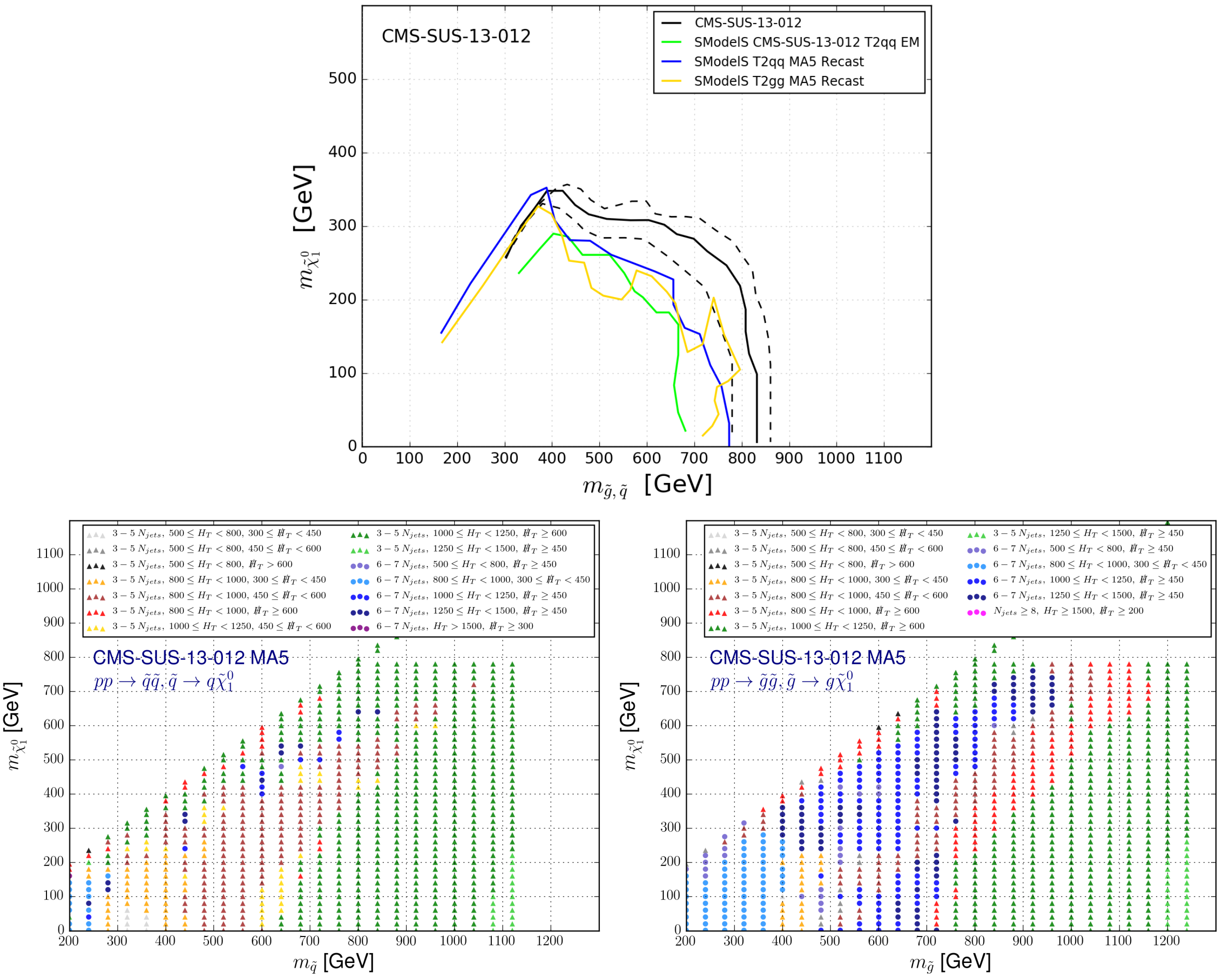

FIGURE 5.18: Same as Fig. 5.17 for the CMS-SUS-13-012 analysis.

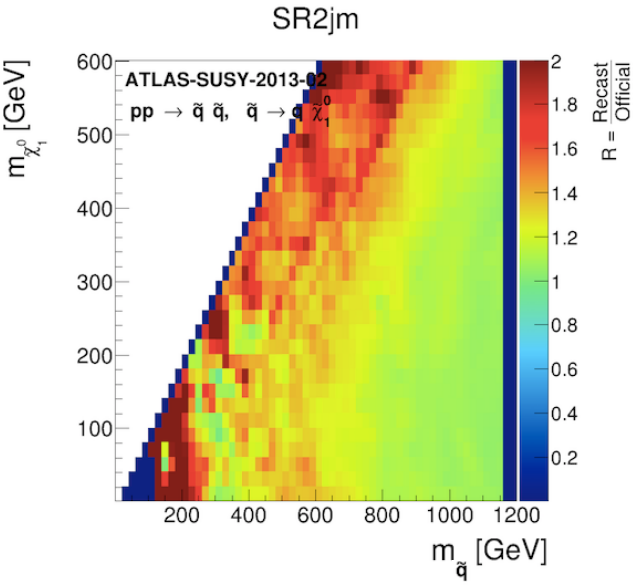

FIGURE 5.19: Ratio of recast versus official ATLAS values for the *2jm* SR efficiencies of ATLAS-SUSY-2013-02 for the *T2qq* model. The dark red area, showing the region where the difference in the efficiencies is large, is found for small mass gap between the squark and LSP.

by the selection cuts only when the mass gap between the mother and LSP is enough. For large mother mass and large mass gap, on the opposite, the choice of the SR is consistent, since the final state jets are hard and the ISR modelling should play a smaller role.

The ratio of the efficiency obtained with the *T2gg* model divided by the efficiency for the *T2qq* model, for two selected SRs of ATLAS-SUSY-2013-02, is shown in Fig. 5.20. The SR *2jt*, which drives the exclusion in the high mother mass region, clearly shows that on average the efficiency for the *T2qq* model is higher than the *T2gg* model. This in fact explains the different reach in the exclusion as seen in Fig. 5.17. If such a behaviour were found in all the SRs, a natural choice would be to produce the EMs with quark production, and limits in the gluino case would be automatically conservative. Sadly this is not the case as highlighted by the ratio for the SR *4jl-* on the right, which exhibits exactly the opposite behaviour with respect to the previous SRs. Monte Carlo related uncertainties, that can induce large fluctuations in the case of small efficiency values, are irrelevant since the ratio is calculated only when the value of the absolute efficiency for both models exceeds the value of 0.001.

For completeness, the kinematic distributions for the H_T, $\not{H}_T$ and n_{jet} variables are plotted in Fig. 5.21, for three selected mass points. As already noticed in the case of the best SR map for the CMS analysis, the distributions of the jets multiplicity seems to prefer a large multiplicity in the case of the *T2gg* model, for points with large mass splitting between mother and LSP. A similar behaviour is seen in the H_T distributions. Due to the exclusive binning in the kinematic variables, the CMS analysis is very sensitive to variation in the kinematic distributions, that causes to the different choice of the best SR. The ATLAS analysis suffers from the problem to a lesser extent thanks to the very inclusive definition of the cuts of the SRs.

Impact on the pMSSM

As described in the previous Section, there are differences in the efficiencies of the ATLAS and CMS analyses considered if EMs results are recast for gluino or squark production. At the same

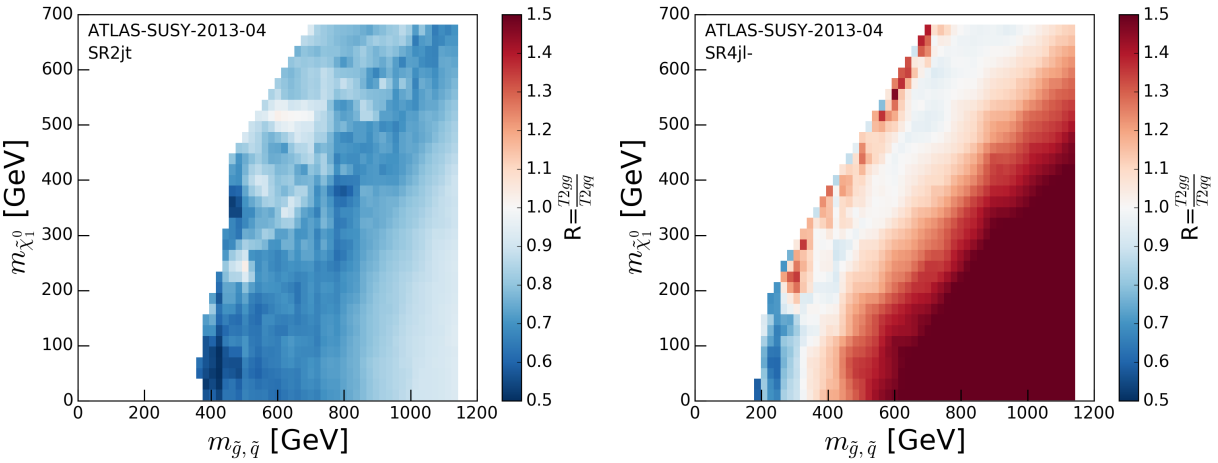

FIGURE 5.20: Ratio of the efficiency of *T2gg* over *T2* for the ATLAS-SUSY-2013-02 *2jt*(left) and *4jl-*(right) SRs. For the former, the squark model has a higher efficiency, resulting in a higher reach in mother mass compared to the gluino production. The opposite happens for the latter, where instead the *T2gg* model shows a higher efficiency in the large mother mass region. Only points with efficiency greater than 0.001 for both model are considered.

time, `SModelS` assumes that the differences are sufficiently small to be safely neglected, and it is worth to use the *T2* EMs or ULs to constrain also the gluino loop decays. Testing this hypothesis is the object of this Section. Based on the results shown in Fig. 5.16, the Higgsino-like LSP dataset includes points for which the contributions from direct squark decays or gluino loop decays are well distinguished, i.e. only one BR is large. From the dataset, points for which either BR($\tilde{g} \to g\tilde{\chi}_1^0$)>0.2 or BR($\tilde{q} \to q\tilde{\chi}_1^0$)>0.2 were selected (adding up to around 22,000 points). EMs for the *T2qq* and *T2gg* were implemented in distinct experimental results in the `SModelS` database, each described by the generic *[[['jet']],[['jet']]]* constraint, so that it was possible to separate the contribution from each specific EM result.

The `SModelS` results are shown in Fig. 5.22 for the ATLAS analysis (left) and CMS (right), where the colour code correspond to the ratio of the r-value obtained with the *T2qq* and *T2gg*. Different marks are used to show different types of points. Circles show points that are excluded by *T2qq* EMs results but not by *T2gg*; vice-versa for the triangles. Points indicated by crosses are excluded by both types of EMs. The numbers in the legend provide an important information regarding the absolute numbers of such points: for each category they report the total number of points excluded by a specific result (*T2qq*,*T2gg*, both) for the two different regions divided by the diagonal line,

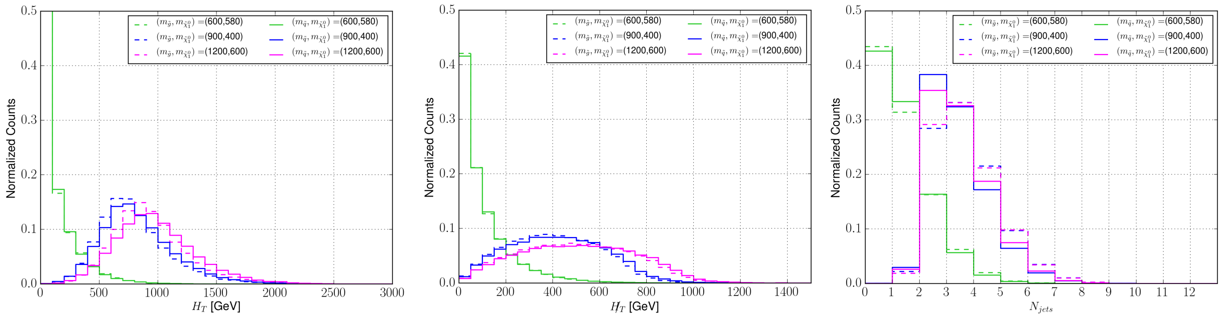

FIGURE 5.21: Kinematic distributions for the H_T (left),$\not{H}_T$ (middle) and n_{jet} (right) kinematic variables defined in the CMS-SUS-13-012 analysis for three mass points $(m_{\tilde{g}/\tilde{q}}, m_{\tilde{\chi}_1^0}) = (600, 580), (900, 400), (1200, 600)$. The solid lines show the distributions for the *T2gg* model, while the dashed line the distributions of the *T2qq* model.

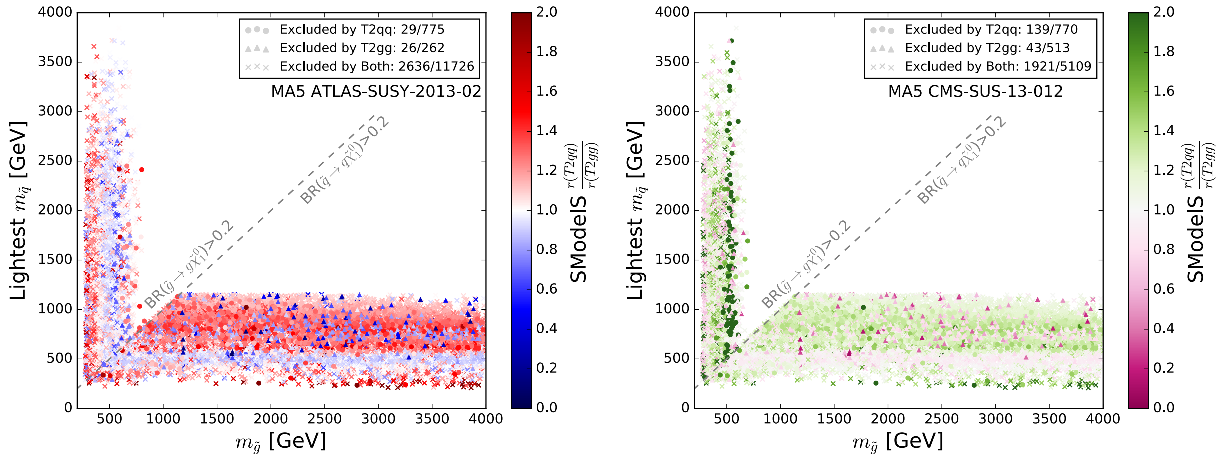

FIGURE 5.22: r-values for the Higgsino-like set of points provided by the *T2qq* and *T2gg* simplified model results for the ATLAS-SUSY-2013-02 (left) and CMS-SUS-13-012 (right) analyses, where the colour code shows the ratio of the r-values. The circle marks correspond to points excluded only by *T2qq* EMs results only, while the triangles show the points excluded only by *T2gg* results; with crosses, points excluded by both results. The numbers quoted in the legend refer to the points excluded in the region of BR($\tilde{g} \to g\tilde{\chi}_1^0$)>0.2 (left number) and BR($\tilde{g} \to q\tilde{\chi}_1^0$)>0.2 (right number).

that divides the plane into one region where the BR of the gluino loop decay is high (left) and one where the BR of squark direct decay is high (right). The numbers on the left side in the legend refer to the points falling in the left region of high BR($\tilde{g} \to q\tilde{\chi}_1^0$), while the numbers on the right side refer to the region of high BR($\tilde{g} \to g\tilde{\chi}_1^0$). Focussing on the ATLAS results, the number of points excluded by *T2gg* results only is of order of a few hundred, with respect to points excluded by both that exceeds 14,000 in total. Moreover the points falling in the right region, for which the proper *T2qq* is most frequently and correctly used (at least in the case of UL results), are the majority. To conclude, with the exception of few points for which the r-value ratio appears to be sensibly different from unity, the usage of *T2qq* results does not produce a large over-exclusion even when applied to gluino loop decays.

5.4.1.1 T3GQon vs T3GonQ

While not aiming at a detailed comparison as done for the *T2* vs *T2gg* case, I wish to show an example case of efficiencies and cutflow comparison for the more complicated case *T3GQon* vs *T3GonQ*. Differences in the efficiencies for the two different models are plotted in Fig. 5.23 for the selected mass points $(m_1, m_2, \tilde{\chi}_1^0) = (1000, 200, \Delta M(m_2, \tilde{\chi}_1^0))$, as a function of the mass splitting between the NLSP and the LSP. The efficiencies exhibit differences, up to 40% for e.g. the *2jm* ATLAS SR, as well as the choice of the best SR, which is indicated with the different marks for the two models. Also to be noted is the more erratic behaviour for the efficiencies of the CMS analysis. Focusing for example on the blue line, it shows that up to ΔM= 15 GeV the *T3GonQ* has a greater efficiency, while for ΔM > 15 GeV the *T3GQon* has higher efficiency. The same behaviour is found for several SRs for other mass point combinations, which are not included here.

Finally, in Appendix E, the UL computation for each SR of the ATLAS-SUSY-2013-02, and for a selection of SRs for the CMS-SUS-13-012 is presented for the same mass point above. For the rest of the discussion, if not stated otherwise, with the generic name *TGQ* I will refer to the *T3GQon* model with the mass hierarchy $m_{\tilde{g}} > m_{\tilde{q}}$.

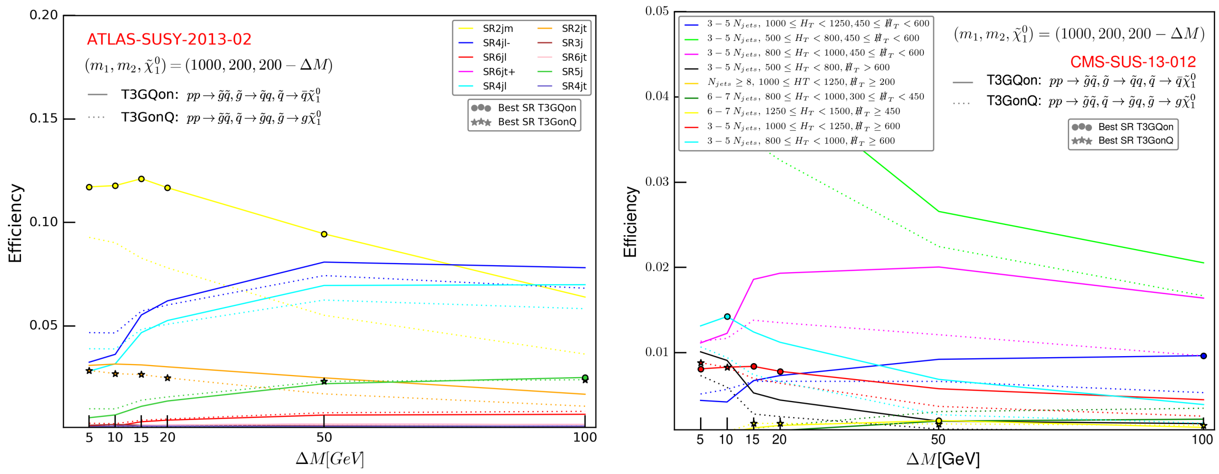

FIGURE 5.23: Efficiencies for ATLAS-SUSY-2013-02 (left) and CMS-SUS-13-012 (right). The solid lines correspond to the values for the *T3GQon*, while the dashed lines to the *T3GonQ* case. With the circle and star marks, the best SR for the *T3GQon* and for the *T3GonQ* are indicated respectively. The mass point considered is $(m_1, m_2, \tilde{\chi}_1^0) = (1000, 200, 200 - \Delta M(m_2, \tilde{\chi}_1^0))$ where the ΔM=(5, 10, 15, 20, 50, 100) GeV values are reported on the x-axis.

	SR 2jm					**SR 2jt**			
	T3GQon		*T3GonQ*			*T3GQon*		*T3GonQ*	
	Eff.	% Drop	Eff.	% Drop		Eff.	% Drop	Eff.	% Drop
$\not{E}_T > 160$	0.924	-7.55	0.901	-9.92	$\not{E}_T > 160$	0.924	-7.55	0.901	-9.92
$n_{Jets} > 1$	0.668	-27.73	0.702	-22.09	$n_{Jets} > 1$	0.668	-27.73	0.702	-22.09
$n_{Lep} = 0$	0.665	-0.51	0.697	-0.74	$n_{Lep} = 0$	0.665	-0.51	0.697	-0.74
$p_T(j_1) > 130$	0.654	-1.54	0.684	-1.84	$p_T(j_1) > 130$	0.654	-1.54	0.684	-1.84
$p_T(j_2) > 60$	0.505	-22.89	0.560	-18.16	$p_T(j_2) > 60$	0.505	-22.89	0.560	-18.16
$\Delta\phi(j_1, \not{E}_T) > 0.4$	0.504	-0.05	0.559	-0.10	$\Delta\phi(j_1, \not{E}_T) > 0.4$	0.504	-0.05	0.559	-0.10
$\Delta\phi(j_2, \not{E}_T) > 0.4$	0.460	-8.86	0.508	-9.15	$\Delta\phi(j_2, \not{E}_T) > 0.4$	0.460	-8.86	0.508	-9.15
$\not{E}_T/\sqrt{H_T} > 15$	0.290	-36.89	0.268	-47.33	$\not{E}_T/\sqrt{H_T} > 15$	0.290	-36.89	0.268	-47.33
$m_{eff} > 1200$	0.118	-59.39	0.090	-66.29	$m_{eff} > 1600$	0.032	-89.12	0.027	-89.92

TABLE 5.4: Cutflow comparison for the $(m_1, m_2, m_{\tilde{\chi}_1^0}) = (1000, 200, 190)$ [GeV] mass point for the ATLAS-SUSY-2013-02 analysis. The two SR $2jm$ and $2jt$ are selected as best SR (see Fig. 5.23 for ΔM = 10 GeV) by the *T3GQon* and *T3GonQ* models respectively. The absolute efficiency ('Eff.' column, defined as number of events surviving the cut divided by the number of generated events) and the corresponding % drop are reported after each cut.

SR $\mathbf{[3,5]\ n_j, 800 \le H_T < 1000, \not{H}_T > 600}$				
	T3GQon		*T3GonQ*	
	Eff.	% Drop	Eff.	% Drop
$n_{Lep} = 0$	1.000	0.00	1.000	0.00
$n_{Jets} > 2$	0.314	-68.61	0.401	-59.91
$H_T > 500$	0.251	-19.91	0.326	-18.65
$\not{H}_T > 200$	0.232	-7.63	0.283	-13.25
$min(\Delta\phi)$	0.182	-21.50	0.216	-23.49
$3 \le n_{Jets} \le 5$	0.176	-3.25	0.207	-4.34
$800 \le H_T \le 1000$	0.040	-77.57	0.039	-81.40
$\not{H}_T > 600$	0.014	-63.99	0.009	-75.48

SR $\mathbf{[3,5]\ n_j,\ 1000 \le H_T < 1250, \not{H}_T > 600}$				
	T3GQon		*T3GonQ*	
	Eff.	% Drop	Eff.	% Drop
$n_{Lep} = 0$	1.000	0.00	1.000	0.00
$n_{Jets} > 2$	0.314	-68.61	0.401	-59.91
$H_T > 500$	0.251	-19.91	0.326	-18.65
$\not{H}_T > 200$	0.232	-7.63	0.283	-13.25
$min(\Delta\phi)$	0.182	-21.50	0.216	-23.49
$3 \le n_{Jets} \le 5$	0.176	-3.25	0.207	-4.34
$1000 \le H_T \le 1250$	0.019	-89.24	0.022	-89.31
$\not{H}_T > 600$	0.008	-56.19	0.008	-62.54

TABLE 5.5: Cutflow comparison for the $(m_1, m_2, m_{\tilde{\chi}_1^0}) = (1000, 200, 190)$ [GeV] mass point for the CMS-SUS-13-012 analysis, analogous to Tab. 5.4. The two best SRs are selected according to Fig. 5.23.

5.4.2 T3GQon Constraints on the pMSSM

This final part of the Chapter will discuss the impact of the *TGQ* maps on the pMSSM coverage, together with the contribution from the signal combination with the *T2* and *T5* models.

5.4.2.1 EMs Production for T2, T5 and T3GQon

The usual set-up for homegrown EMs production was used. The complete set of simplified models results, together with the relative grid and mass planes used are described in Tab. 5.6. The analyses considered were the two multijets analyses ATLAS-SUSY-2013-02 and CMS-SUS-13-012. Although official EM results for the *T2* model were provided by the collaboration, the part of the parameter space where the mass gap between the squark and the LSP is below 50 GeV is not covered by the official results while, as described in the table, the recast maps reaches a mass difference as small as 5 GeV. It is true however that the experimental uncertainty in such compressed regions is typically high, but this will be considered on the same footing as all the recast related uncertainties. Finally, the mass hierarchy used for the production is $m_{\tilde{g}} > m_{\tilde{q}}$, meaning that the *T3GQon* model was chosen to constrain the "[[['jet']],[['jet],['jet']]]" signature. Note that the same problem related to the choice of the mass hierarchy applies to the $T5$ model: the "[[['jet']],[['jet']]]" signature can be obtained both with $\tilde{g} \to g\tilde{\chi}_1^0$ and $\tilde{q} \to q\tilde{\chi}_1^0$; for the maps production, again the former was chosen. All the maps here described were made available in the database of the version 1.2 of `SModelS` [3].

5.4.2.2 T3GQon Constraints on the pMSSM

Fig. 5.24 shows the distributions of points with the corresponding r-value in the gluino-squark mass plane, where the mass of the lightest squark is considered, divided by topologies *T2*, *T5* and *TGQ* (i.e. *T3GQon*). Only the Bino-like LSP dataset for the ATLAS-SUSY-2013-02 analyses is shown, since no substantial differences are found for the CMS analyses and/or the Higgsino-like LSP dataset. In addition, the r-value resulting form the combination of the above weights is shown. Points that are not excluded by the sum of the three results constitute the grey background. Note that in the individual Txname plots, dark blue points have r-value below unity when not constrained by that specific simplified model results, but they can be excluded by the total sum.

Txname	Mass Planes	Description
T2	-	$\Delta M(\tilde{q}, \tilde{\chi}_1^0)$ as low as 5 GeV
T5	x = (0.05 , 0.50, 0.95)	-
	$\Delta M(\tilde{g}, \tilde{q}) = 5$ GeV	-
	$\Delta M(\tilde{q}, \tilde{\chi}_1^0) = 5$ GeV	-
T3GQon	Fixed $m_{\tilde{g}}$ = 200,250,...,1200	$m_{\tilde{g}}$ in 50 GeV bins
	Fixed $m_{\tilde{g}}$ = 1300,1400,...,2000	$m_{\tilde{g}}$ in 100 GeV bins
		$m_{\tilde{q}}$ in 50 GeV bins (up to 1 TeV)
		$\Delta M(\tilde{q}, \tilde{\chi}_1^0)$ as low as 5 GeV

TABLE 5.6: Mass plane parametrization used for the EMs production of the *T2*, *T3GQon* and *T5*. The parameter x is defined so that $m_{\tilde{q}} = x \cdot m_g + (1-x) \cdot m_{\tilde{\chi}_1^0}$. For the *T3GQon* model, the gluino mass reaches the value of 2 TeV, with a binning of 50 GeV for $200 \leq m_{\tilde{g}} < 1200$, and a binning of 100 GeV for $1200 \leq m_{\tilde{g}} \leq 2000$ GeV. The squark masses have a 50 GeV binning, up to 1 TeV. For a better coverage of the parameter space in the case of small mass differences, additional mass planes parametrized with $\Delta M(\tilde{q}, \tilde{\chi}_1^0)$=(5,10,15) GeV were produced.

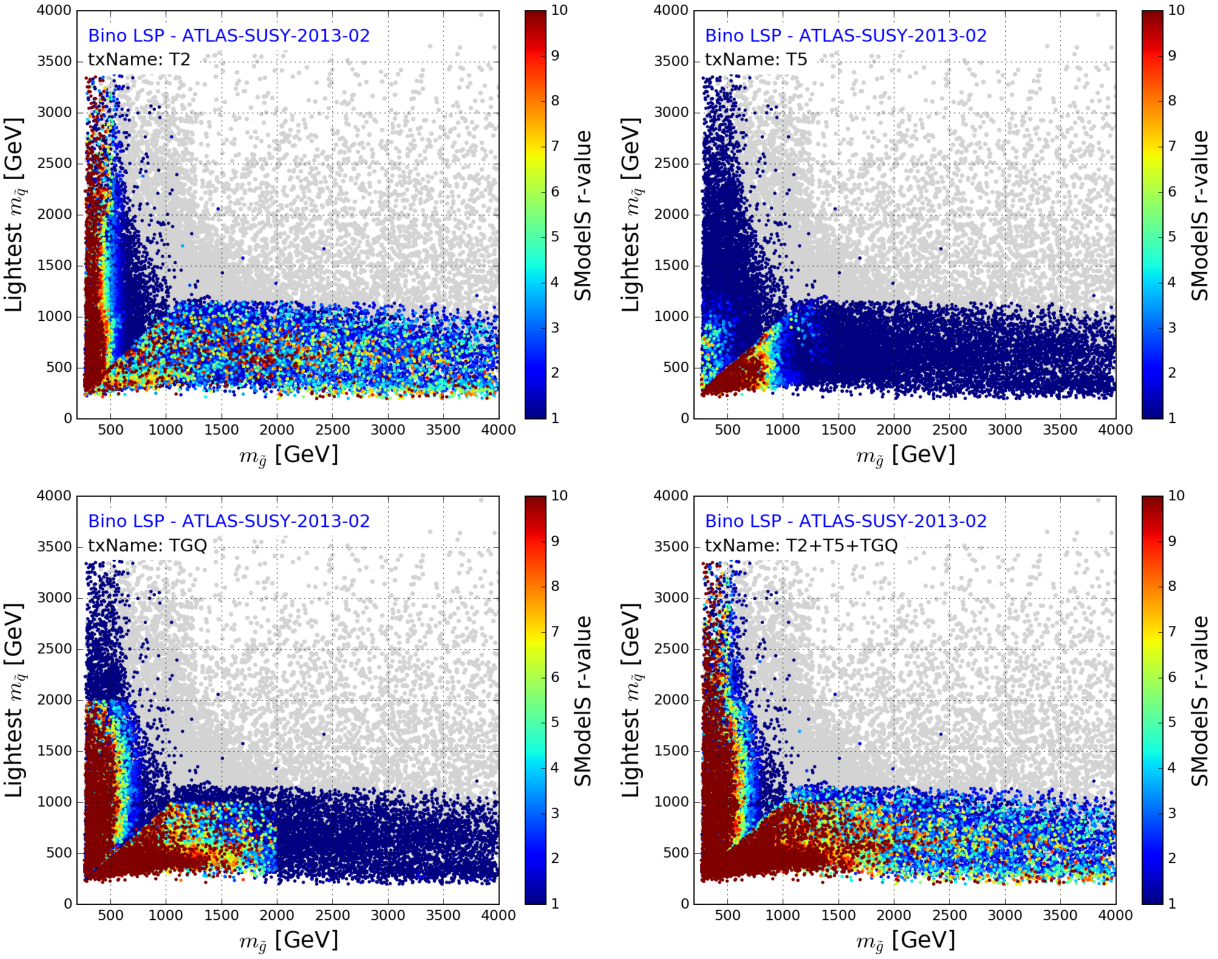

FIGURE 5.24: r-value scatter plot for the *T2*, *T5*, *T3GQon* and their combination for the ATLAS-SUSY-2013-02 analysis in the gluino-squark mass plane. For each Txname, only the points that can be excluded considering the contributions of all topologies are drawn using the bar color code; the points in grey cannot be excluded by the considered analysis. The dark blue point cannot be excluded by the Txname considered, but only by the combination with at least one of the remaining.

Number of Points	**Bino-like LSP**	**Higgsino-like LSP**
Total	38527	45345
Excluded by UL+EM	28761 (74 %)	32297 (71 %)

TABLE 5.7: Updated SModelS constraints for the Bino and Higgsino-like LSP after the addition of the newly implemented EMs results.

The plots are interesting for different reasons related to the production of the recast results. First, with the choice of this specific mass plane, it is easy to discriminate the type of SUSY production, for example as it was already shown in Fig. 5.14 for the *T2* UL results dividing between the region where the *T2* results were applied to proper squark production, and the region where instead the gluon loop decay was constrained by the limits derived for squarks. This is visible for the *T5* model, where however the contribution from the model $pp \to \tilde{q}\tilde{q}, \tilde{q} \to q\tilde{g}, \tilde{g} \to g\tilde{\chi}_1^0$ is more limited. Finally for *TGQ*, the distributions show the sharp separation between the two possible mass hierarchy, where a similar number of points appear basically for both the *T3GQon* and *T3GonQ* models. The edge of the distributions at $m_{\tilde{g}} = m_{\tilde{q}} = 2$ TeV is due to the grid of SLHA defined to produced the EMs results, for which the mass of the gluino was up to 2 TeV (see Tab. 5.6). Interestingly, the r-value for points at the border is still large. We see that in the low gluino-high squark the r-values are affected by the errors induced by using EMs obtained with a wrong mass hierarchy; in the high gluino-low squark mass region, which utilises the correct EMs with no further assumption, it is worthwhile to extend the maps to higher gluino mass to extend the coverage. The same consideration holds for the maximum light squark mass, which for the production was set up to 1 TeV. The detailed description of the mass planes is summarised in Tab. 5.6).

The complete coverage results are summarised in Tab. 5.7. The number of total points tested is slightly different from what was used in the publication[4], since a few tens of points that could not be matched to the *T2*, *T5* and *TGQ* results contained for this re-run of the `SModelS` analysis were not considered (i.e. *Decomposition output status = 0* in the output, see Appendix B). In any case, the important result is that with the addition of the newly homegrown EMs results, the coverage in the Bino and Higgsino-like case reaches up to 74 and 71 %, with an increase of +19% and +8% respectively. The major improvement appears to be in the Bino-like LSP case, as visible also in the gluino mass coverage distributions in Fig. 5.25, where the results are compared with the ones from the the previous study. In addition, it is interesting to see the individual contributions from the two multijet analyses used. Owing to the inclusive design of the SRs, the ATLAS analysis alone is able to exclude now more than 24,000 and 22,000 points of the Bino and Higgsino-like LSP datasets respectively, while the CMS analysis excludes only 75 of the points excluded by ATLAS-SUSY-2013-02. The reason for the weaker exclusion power of the CMS analysis was extensively discussed previously, however, I remind that the `MadAnalysis 5` recast code for ATLAS-SUSY-2013-02 introduces some over-exclusion, as seen in the *T2* validation. The next paragraph tries to address the uncertainties involved of the whole procedure.

5.4.2.3 Estimation of the Uncertainties

The `SModelS` output does not provide an uncertainty estimation on the r-value. It was explained that typically, if r >1, the point is considered to be excluded at 95% CL . While uncertainties regarding e.g. the theory cross section calculation of the entire recasting procedure cannot be currently handled by `SModelS` , it is straightforward to increase the r-value requirement to consider a point excluded. Note that recasting might as well under-estimate the values of the efficiencies, and

	Bino		**Higgsino**	
r > 1.0	21375	-	22593	-
r > 1.2	20287	-5%	21209	-6%
r > 1.5	18745	-12%	19286	-15 %
r > 2.0	16457	-23 %	16712	-26%

TABLE 5.8: Number of excluded points for different r-values requirements by the recast EM for the *T2*,*T5* and *TGQ(T3GQon)* models. Assuming a reasonable uncertainty of 50% from the theory prediction, the variation in the excluded number affects only a fraction of (10-15)% points.

similarly the impossibility of combining signal region leads to weaker limits.

As a concrete example, requiring that r >1.2, it is equivalent as allowing for a 20% uncertainty on the theory side, since the r-value is the ratio of the theory prediction (or theory cross section) over the experimental UL. It was shown in Sec. 5.4.1 that the `MadAnalysis 5` recast code for ATLAS-SUSY-2013-02 over-excludes the official ATLAS exclusion curve for the *T2qq* simplified model (see also Fig. 5.19). It is reasonable to think that such an effect propagates also to other simplified models, and it might thus induce over-exclusion for other SMS recast results.

It is of interest to quantify how much an uncertainty from the theory side can affect the overall exclusion in terms of number of points excluded. This is visualised in Fig. 5.26. The distributions show the total number of points excluded by the analysis ATLAS-SUSY-2013-02 for different requirements on of r $\geq$ (1.0, 1.2, 1.5, 2.0). This is equivalent to the inclusion of uncertainties by re-scaling the ($\sigma \times \epsilon$), or `SModelS` theory predictions, by (0, 20, 50, 100)%. I remind that all the previous plots showing excluded points assumed r >1 as standard exclusion criterion. In Tab. 5.8 the numbers of excluded points are explicitly reported. For r >1.2 the difference is around 5(6)% and 12(15)% for the Bino(Higgsino)-like LSP case. Note finally that the theory cross section used by `SModelS` is not exactly the theory cross section used by the ATLAS collaboration, but was calculated by `SModelS` as described in Sec. 5.3.1.

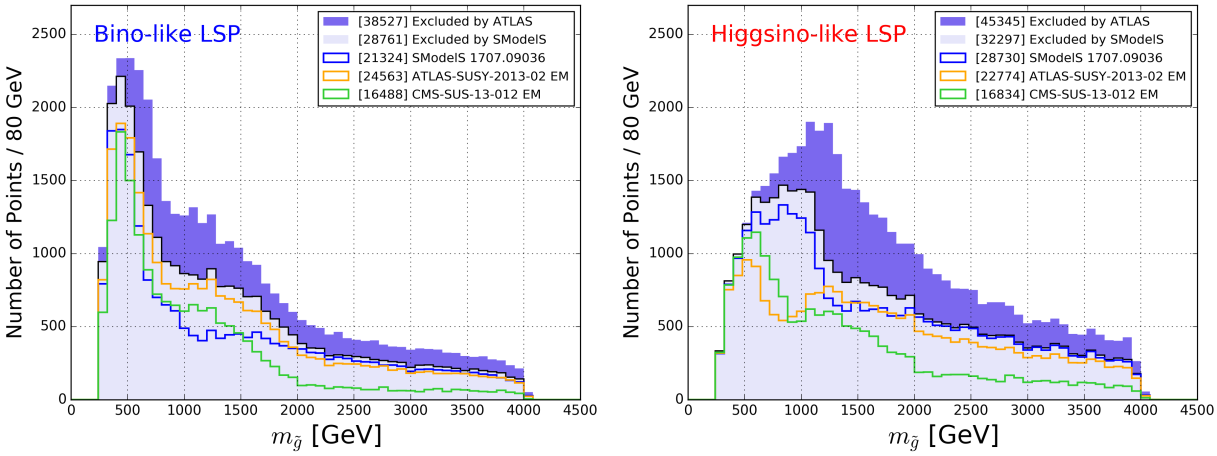

FIGURE 5.25: SModelS exclusion as a function of $m_{\tilde{g}}$ for the Bino(left) and Higgsino-like LSP (right). In slate blue the points officially excluded by ATLAS, in cyan the SModelS exclusion using the newly 'homegrown' maps for the *T2*, *T5* and *TGQ* (*T3GQon*) models. The blue line represents the point excluded by the version 1.1 of the database, as published in [4]. For comparison, also the exclusion provided by the ATLAS-SUSY-2013-02 (in orange) and CMS-SUSY-2013-012 (yellow) EM results are drawn.

The distribution of the r-values for the ATLAS and CMS analyses are plotted in Fig. 5.27. For each r-value bin, the number of points for a set of topologies (*T1+T2+T5+TGQ(T3GQon)*) or combinations of them are reported. Since the majority of points have large r-values, it is reasonably safe to consider the points effectively excluded by such analyses, even considering fluctuations in the efficiencies and/or cross sections. I remind finally that in the case of the CMS-SUS-13-012 analysis, the impossibility of fully using the constraining power coming from the combination of the different signal regions, makes the usage of this recast EMs results most likely conservative from the point of view of recast uncertainties. This becomes apparent also when looking at the different distribution in the cumulative bin $r \geq 10$, where the ATLAS analysis can exclude significantly more points with higher r-values. The side effect is that the full constraining power of the CMS analysis cannot be exploited by `SModelS` , and the total number of points excluded by this analysis adds up to only 75% of the points excluded by the ATLAS recast maps.

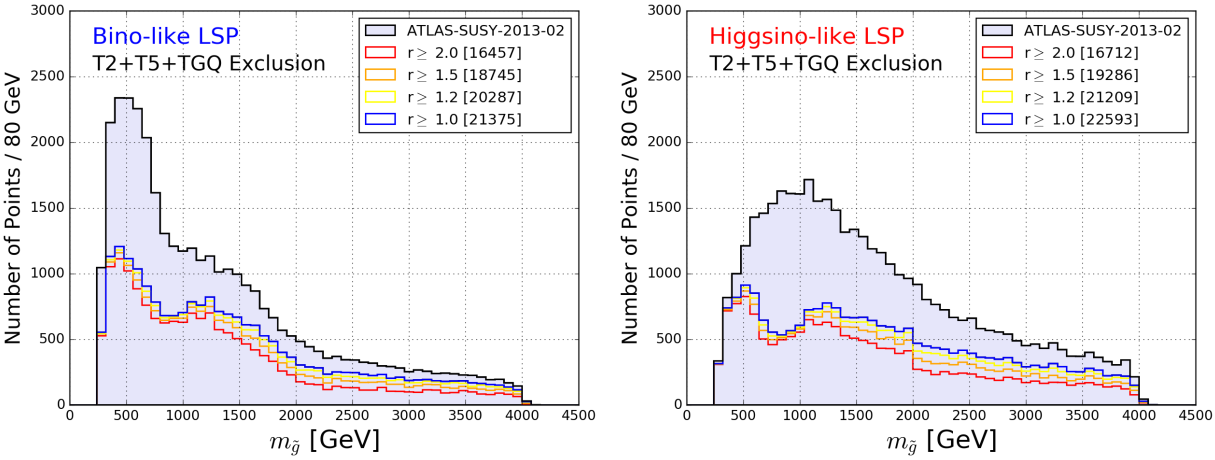

FIGURE 5.26: Distributions of the points excluded by ATLAS-SUSY-2013-02 for different the r-value, to emphasise the dependency of the exclusion with respect to theory prediction uncertainties. The blue distribution represents the points officially excluded by the analysis according to the ATLAS Collaboration, while different coloured lines show the distributions of points excluded by `SModelS` requiring that the r-value exceeds the limit indicated in the legend.

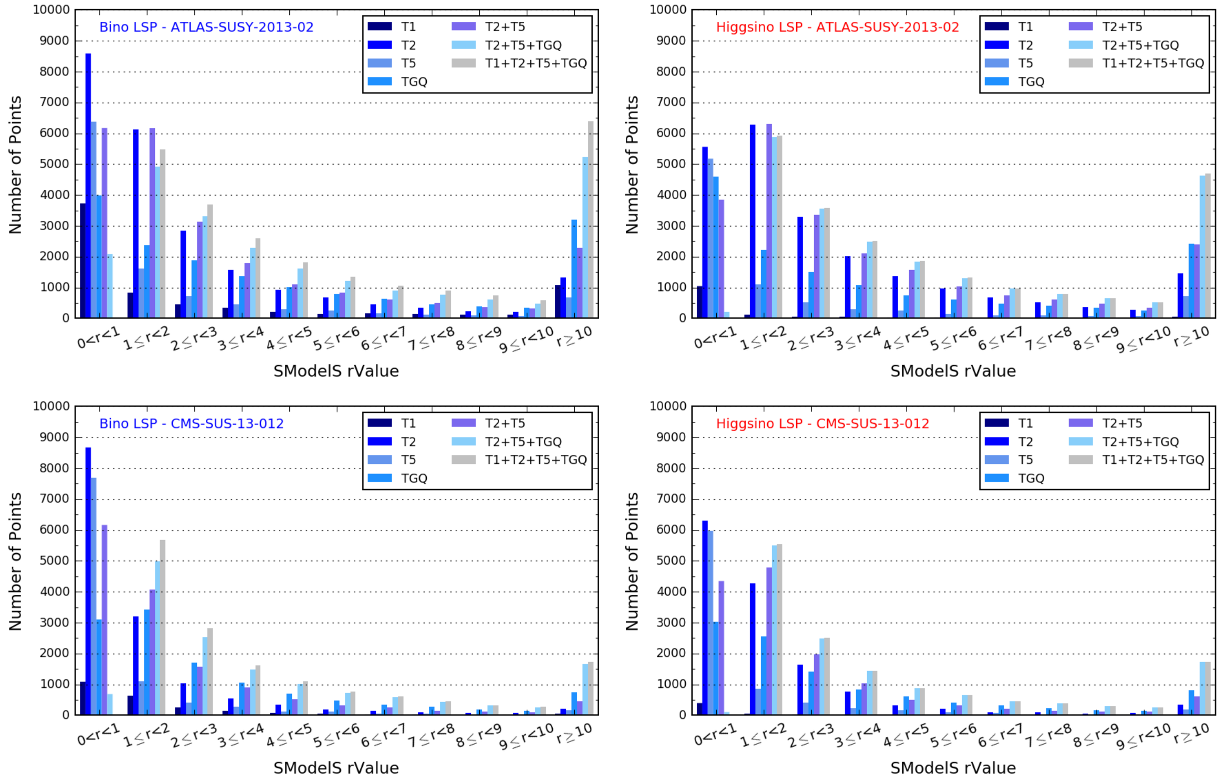

FIGURE 5.27: r-values distributions for the ATLAS (top) and CMS (bottom) for points excluded by the combination *T1+T2+T5+TGQ(T3GQon)*. Points falling in the first bin $0 < r < 1$ are excluded only by the total combination of weights. The results for the official *T1* EMs are also included, which are more constraining in the Bino-like LSP case as previously noted.

Summary

The analysis of the `SModelS` constraint compared with the results obtained by the ATLAS collaboration was the first case where the new features of v1.1 were tested against a concrete physics scenario. Of interest would be an analogous study with the results from the CMS collaboration, which however did not publish any public material regarding their pMSSM interpretation summary. Hopefully, for the next interpretation of Run 2 analyses, this will become possible.

The study was able to confirm the validity of the simplified model approach and of the capabilities of the `SModelS` tool itself. It was shown that, at least for energy that can be reached at present at the LHC, using simplified models results is an efficient way to constrain generic, complicated models. `SModelS` is currently the only tools that takes directly the SUSY simplified models results from the LHC experiments and applies them without the need of proper analysis recasting or Monte Carlo simulations. Furthermore, it was shown how EMs results produced from recast analyses, e.g. from the `Fastlim` collaborations or from ourselves, can also be implemented straightforwardly into the database. The extensive effort at the basis of this thesis work i.e. the production and inclusion of the homegrown recast results concretely increases the constraining power of the database. It was shown in fact how the implementation of the *T3GQon* maps, which were already found by `SModelS` to be the critical missing signature, improves the coverage of the pMSSM model. By iterating the procedure, more and more relevant signal topologies will be covered by implementing additional EMs results.

The multijets - all hadronic final states analyses described in this Chapter play an important role, since they are designed to be able to constrain a large number of simplified model for squark and gluino production, besides the fact that coloured particles at the LHC benefit from a high cross section. New analyses, specifically ATLAS-SUSY-2016-07[143] an CMS-SUS-16-033[76] are the Run 2 successors of the analyses used here. Both analyses are available in CheckMATE and/or `MadAnalysis 5` (see Section 4.1.4 for the validation of the recast of the CMS analysis), and can be already used to produce additional EMs. The detailed analysis of the constraints provided by many simplified models constitute a guiding principle for the production of the new results.

Finally, the results obtained here offer a feedback to the experimental Collaborations, that might adopt the *T5* and *T3GQ* to interpret their searches for SUSY.

Chapter 6

Parametrization of SUSY Simplified Models

Contents

The main objects of study of this rather technical Chapter are 1-step cascade decays models, or simplified models where the BSM particles produced in proton-proton collisions decay to the LSP via an intermediate BSM state. When considering completely symmetric cases, i.e. pair production of sparticles that decay in both branches with 100% in a certain pattern, three free mass parameters fully characterise the simplified model.

For the interpretation of searches with cascade topologies, the ATLAS and CMS collaborations typically consider two-dimensional ‘slices’ of the three-dimensional parameter space. That way, the final results can be presented in a more digestible way. Such slices are called *mass planes*, and the mathematical relations or constraints that set the values of the masses used to reduce the parameter space are referred to as *mass parametrizations*.

In the previous Chapter 4, it was described how the `SModelS` database was largely expanded with new simplified models results, both for direct decays, 1-step cascade decays and asymmetric topologies like the *T3GQon*, parametrizing the mass planes with different choices depending on the topology considered. The whole `SModelS` framework is based on the ability to interpolate between different mass planes to extract data for arbitrary mass spectra, as they appear in generic BSM models, without any mass restriction. However, even in the SMS approach when only the masses of the BSM states matter, it is not feasible to produce Monte Carlo samples that covers the entire mass parameter space when more than three new particles are involved.

It is of interest, especially for tools like `SModelS`, to test the underlying assumption that an interpolation between such mass planes is correct within reasonable uncertainty. The hypothesis is valid if the efficiencies or upper limits do not exhibit large fluctuations when the mass of the intermediate particle is varied, and a linear interpolation between the available results is a sufficiently good approximation.

Up to v1.0, only UL-type results were implemented in the `SModelS` database. With the inclusion of EMs results in version v1.1, together with the framework set up by the *EM Bakery*, it is possible to produce several mass planes and test the performance of the interpolation procedure, for example by extracting interpolated values and comparing with real recast data, in a systematic way.

This is the main topic of this Chapter, structured as follows: Section 6.1 introduces the problem of parametrizations and summarises the inherent critical aspects. Section 6.2 discusses the results of the validation test in different cases of parametrization choices, in particular for fully-hadronic searches for the *T5WW* simplified model. The final Section 6.3 shows concretely how the parameter space of the pMSSM-19 is constrained efficiently if a proper number of mass planes for the *T5WW* model is implemented in the `SModelS` database, and highlight how an interesting region of the parameter space is typically neglected by the official interpretation results.

6.1 Generalities on Mass Planes Parametrizations

I begin this Chapter by defining the object of the study, namely 1-step decay SUSY simplified models. This class of SMS includes models where the mother SUSY particle decays to intermediate SUSY particles, i.e. next-to LSP (NLSP), eventually decaying to the LSP. All of the following discussion will be restricted to symmetric models, where the topological structure of BSM mass arrays and SM particles in the vertices are identical for both branches (see 4.2.1). This class of simplified models can be completely described by the mass array *[Mother,Intermediate,LSP]* and by the SM particles from the two vertices. The mass parameter space of such simplified models, in its more general realisation, is then represented by a 3-dimensional volume. Examples of such models are, e.g. the gluino SMS *T5WW* and *T5bbbb*, the stop SMS *T6ZZtt*, the chargino SMS *TChipChimSlepSnu* etc (see Appendix A for a description of the models).

In general experimental results are provided by fixing one of the three mass parameters and cutting out one of the free parameters, thus reducing the complete 3-D representation to a 2-D slice or mass plane. This however implies the choice of arbitrary values for one of the masses, for example by imposing a specific mass relation between the remaining two. This is usually not justified by any physical motivations, at least for the case of the MSSM. Below I summarise the most frequent choices for mass planes parametrizations.

"x" parametrization

With "M" and "I" being the mother and intermediate SUSY particles respectively, the x parameter is defined as

$$x = \frac{m_I - m_M}{m_M - m_{LSP}} \qquad \longrightarrow \; m_I = x \cdot m_M + (1-x) \cdot m_{LSP} \tag{6.1}$$

This parametrization is the most frequently used by the ATLAS and CMS Collaborations to define mass planes. An example is shown in panel (a) of Fig. 6.1, where in this simplified model for chargino production decaying to sleptons, from the analysis ATLAS-SUSY-2013-11[50], the mass of the intermediate particle is set as the average between the mother and the LSP with x=0.50. Other common values found in the experimental papers are x=0.05, corresponding to small mass gaps between the intermediate and the LSP, and x=0.95, which reduces the gap between the mother and the intermediate.

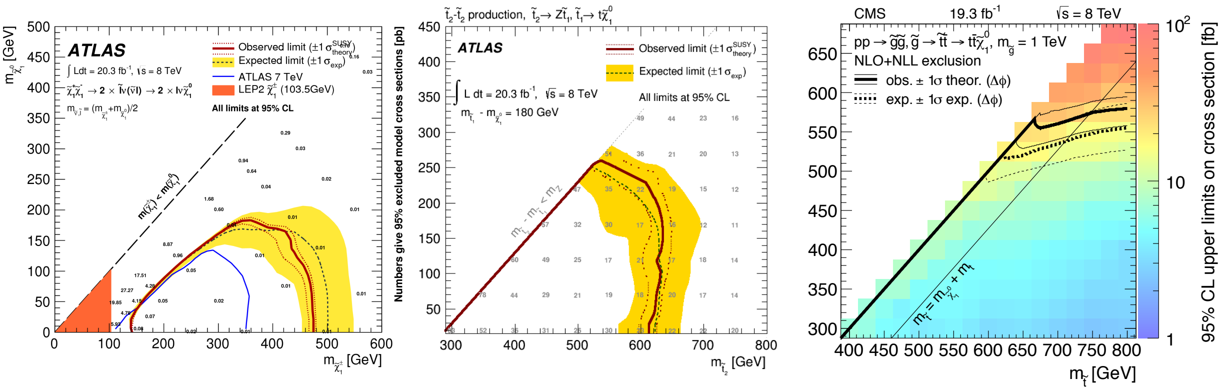

(a) (b) (c)

FIGURE 6.1: Example of parametrization of SUSY mass planes. (a): x=0.50 parametrization of the *TChipChimSlepSnu* model in ATLAS-SUSY-2013-11 ; (b): fixed mass gap intermediate-LSP parametrization of the *T6ZZtt* model for ATLAS-SUSY-2013-08 ; (c): fixed intermediate mass parametrization of the *T5tttt* model for CMS-SUS-13-007.

"Delta" parametrization

The mass gap between the mother-intermediate or the intermediate-LSP is fixed to a certain value. This is shown in panel (b) of Fig. 6.1, where in ATLAS-SUSY-2013-08[97] (*T6ZZtt* model) the gap of the intermediate light stop $\tilde{t}_1$ mass and the LSP is fixed to 180 GeV, to ensure that the stop decay to an on-shell top is kinematically allowed. This choice is frequently used by analyses searching for specific on-shell particles like the SM weak bosons, and top quarks.

Fixed mass value

The mass of a sparticle is set to a fixed value, like in CMS-SUS-13-007[108] shown in panel (c), where $m_{\tilde{t}_1} = 1$ TeV in the *T5tttt* model.

The choice of the parametrisation to be used depends largely on the specific signature of the search. In fact the mass gap between the sparticles influences the energy and mass of the produced SM particle that will be detected. If the mass gaps are small, part of the SM decay products might fall below experimental sensitivity due to small phase space available, that can also prevent particles to be produced on-shell.

The context of this discussion is the possibility for tools like `SModelS` to interpolate, for a given simplified model, between the results available for specific mass planes, and extract limits or efficiencies for generic mass combinations. One crucial aspect is the proper coverage of the full parameter space of a simplified model. Often the number of mass planes available in the official data is insufficient for interpolation, and indeed most frequently only the interpretation for only a single mass plane is available.

Another question concerns how well the interpolation procedure works, or better how much is the size of the uncertainty introduced when interpolating between different mass planes. Before v1.1, only UL results from the experimental collaborations were available in the `SModelS` database, hence it was not possible to validate the interpolation procedure against physics results. With the introduction of EM results, and the possibility to produce efficiencies for an arbitrary mass configuration, this eventually became possible. The above two questions will be treated in the following Sections, starting from the testing of the interpolation procedure. The last Section of this Chapter will show instead how the availability of multiple mass planes is crucial to efficiently constrain the pMSSM-19 with *T5WW* simplified model results.

6.2 Testing the Parametrization with a T5WW model

The main idea behind the validation of the interpolation procedure is the following. The 1-step cascade simplified model considered is the *T5WW*:

$$pp \to \tilde{g}\tilde{g}\ ,\ \tilde{g} \to q\bar{q}'\tilde{\chi}_1^{\pm}\ ,\ \tilde{\chi}_1^{\pm} \to W^{\pm}\tilde{\chi}_1^0$$

i.e. the pair produced gluinos decay via a chargino to the LSP. The experimental signature might be a fully hadronic final state with large jets multiplicity, or a single lepton/di-leptonic final state plus jets, depending on the decay modes of the W boson coming from the chargino.
The parametrization with x=(0.05, 0.50, 0.95), as frequently used by the LHC collaborations, was employed to produce EMs results, that were afterwards implemented in the `SModelS` database. The interpolation procedure allowed to extract efficiencies and limits for a set of arbitrary mass points. The same mass point finally were processed through to the full simulation and recast chain. This allowed to confront the interpolated values obtained from `SModelS` and the 'true' recast values of efficiencies and limits obtained from the full recast.

For a set of arbitrary mass points, the interpolated efficiencies are then confronted against the 'true' values obtained with a proper full recast.

An important feature of this model, and of all the cascade decays involving gauginos, is the presence of the W boson in the final state. The analyses considered are sensitive solely to the hadronic decay of the W boson since a veto on isolated leptons is applied, and only a fraction of the full SUSY signal is effectively picked up by the search. This has an impact when the mass splitting $\Delta M(\tilde{\chi}_1^{\pm},\tilde{\chi}_1^0)$ is small, when choosing e.g. a x=0.05 parametrization, as opposed to the case where $\Delta M(\tilde{g},\tilde{\chi}_1^0)$, e.g. for x=0.95.

This topology carries in fact an intrinsic asymmetry regarding the choice of the x parametrization. By naive considerations we expect 8 signal jets in the final state from, since 4 jets come from the gluino decay and 4 jets from hadronic decays of the Ws. However the effective number of jets, as measured in the samples after detector simulation, depends on other factors such as the hadronization and fragmentation processes, possible initial and final state radiation of extra partons, the detector acceptance along with the efficiencies of objects reconstruction and identification etc. Moreover the mass splitting between the sparticles influences the number of signal jets: when the chargino mass is very close to the gluino or to the LSP, the jets from the gluino and/or the $W^{(*)}$ boson might become too soft to be detected. This in turns will increase the efficiencies of SR with small n_{jets} requirement, and on the opposite lowering the efficiencies for SR requiring higher jets multiplicity. Note that this also possibly reduces the sensitivity of an analysis to a specific region of the mass space. This is the case of the ATLAS-SUSY-2013-04 analysis, since it requires a high jet multiplicity (at least 7 jets) with high transverse momentum, while for the CMS-SUS-13-012 analyses, different SRs cover events with both low and high jet multiplicity

For the above model, efficiency maps results for the analyses ATLAS-SUSY-2013-04[92] and CMS-SUS-13-012[49] for *T5WW*$^{(*)}$[1] were produced. The recast analyses implemented in `MadAnalysis 5` were used, and the code together with the validation notes can be retrieved at [144],[145] and [141],[75] respectively. They belong to the class of inclusive analyses searching for coloured SUSY

---

[1] For some mass points, the W boson will be produced off-shell.

particles, as defined in the previous Chapter. The Monte Carlo sample generation chain followed the chain described in Section 4.3. The primary targets for the comparison are the values of the efficiencies of the various SRs. However, as extensively discussed in the previous Sections, the choice of the signal region providing the best expected upper limits affects the final limit. The linear interpolation might lead to differences in the choice of the best SR, and thus in the upper limit.

The comparison is based on three benchmark points, for which $m_{\tilde{g}}$ and $m_{\tilde{\chi}_1^0}$ are chosen arbitrarily, while $m_{\tilde{\chi}_1^\pm}$ is calculated for different x parametrizations. The mass points are summarised in Table 6.1; the first two points lie in the region excluded at 95% C.L. by the ATLAS and CMS analysis, while the third point is not excluded by 8 TeV LHC search (speaking in terms of naive SMS exclusion).

$(m_{\tilde{g}}, m_{\tilde{\chi}_1^0})$		$x = 0.05$	$x = 0.25$	$x = 0.50$	$x = 0.75$	$x = 0.95$
$(700, 400)$	$m_{\tilde{\chi}_1^\pm} =$	415	475	550	625	685
$(1200, 200)$	$m_{\tilde{\chi}_1^\pm} =$	250	450	700	950	1150
$(1200, 700)$	$m_{\tilde{\chi}_1^\pm} =$	725	825	950	1075	1175

TABLE 6.1: Summary of the masses of the gluino, chargino and neutralino for the tested *T5WW* benchmark points (masses expressed in [GeV]).

6.2.1 Results for CMS-SUS-13-012

This analysis was used extensively to produce the recast EMs used for the pMSSM reinterpretation work. I briefly remind that 36 signal regions are defined, binned in the variables jets multiplicity n_{jets}, the hadronic transverse energy H_T and missing hadronic transverse energy $\not{H}_T$. As it will become evident, this is important to understand how the efficiencies behave with different parametrization of $m_{\tilde{\chi}_1^\pm}$. A more detailed description can be found in Appendix C. Note that the official results from the CMS collaborations are interpreted with a slightly different model, called *T5VV*, where the gluino can decay with equal BR to an intermediate chargino or heavy neutralino. In the last case, the neutralino decays to a $Z^{(*)}$ boson and the LSP. The model is not, strictly speaking, a simplified model, since the BR is not fixed to one decay mode only. In Appendix G it is demonstrated that the limits obtained for the *T5WW*, *T5ZZ* and *T5VV* models are indeed very similar for inclusive all-hadronic final states analyses.

Additionally, in Fig. 6.2 the kinematic distributions of the n_{jet}, H_T and $\not{H}_T$ variables for the benchmark point $(m_{\tilde{g}}, m_{\tilde{\chi}_1^0}) = (1200, 200)$ [GeV] are shown. In particular the n_{jet} distributions reflects the asymmetry of the topology regarding the fraction of leptonic decays of the W boson: the mass compression due to x=0.95 results in a lower jet multiplicity wrt the symmetric compression x=0.05. The distributions were obtained from the `MadAnalysis 5` recast of the CMS analysis, following the preselections cuts. Nevertheless the distributions are practically independent of the analysis chosen, since they generically represent the properties of the SUSY model tested, and similar results would be obtained for the ATLAS analysis.

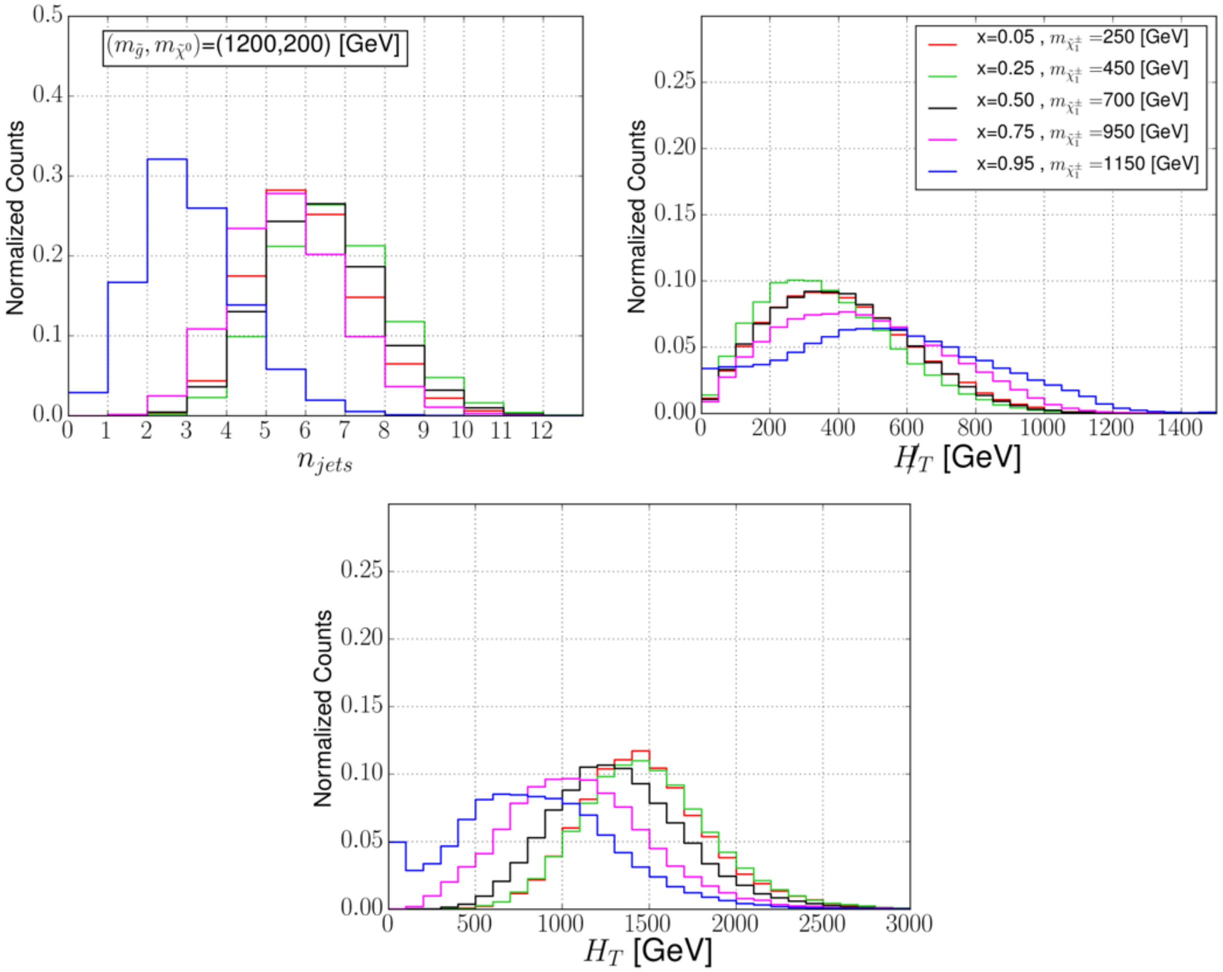

FIGURE 6.2: Kinematic distributions for the $N_{jets}, H_T, \not{H}_T$ variables for the benchmark point $(m_{\tilde{g}}, m_{\tilde{\chi}_1^0}) = (1200, 200)$ [GeV], obtained after the preselection and 'MET Cleaning' cut in the `MadAnalysis 5` implementation of the analysis. The chargino masses parametrized with various x are indicated in the legend. Note the peak at small n_{jet} values for $x = 0.95$, caused by the W boson branching fraction to leptons, resulting in a shift to lower values with respect of the $x = 0.05$ case, which gives between 5 and 6 jets on average.

6.2.1.1 On the Statistical Uncertainties

The efficiency values carry uncertainties related to the Monte Carlo samples statistics. Since at least 50k events were passed through `MadAnalysis 5` after detector simulation, statistical fluctuations should be considered under reasonable control, at least for high efficiency SRs (typically at $O(1\%)$). It is also true, however, that very often the most discriminating SUSY signals come from events populating the tails of the kinematic distributions, where large statistical fluctuations are expected due to limited statistics. This effect increases if exclusive bins are considered, like in this CMS analysis considered. It is however instructive to look at the statistical uncertainty of the efficiencies.

Fig. 6.3 shows as an example the SR $N_{jets} \geq 8, H_T \geq 1500, \not{H}_T \geq 200$ (the choice of this specific SR is guided by the considerations about the limit setting that will be discussed in the next section). The top panels show the efficiencies, in absolute units, for the $x = (0.05, 0.5, 0.95)$ parametrizations (form left to right); the bottom panels show the associated binomial uncertainty to the efficiency ϵ, calculated as:

$$\sigma = \sqrt{\epsilon(1-\epsilon)/N} \tag{6.2}$$

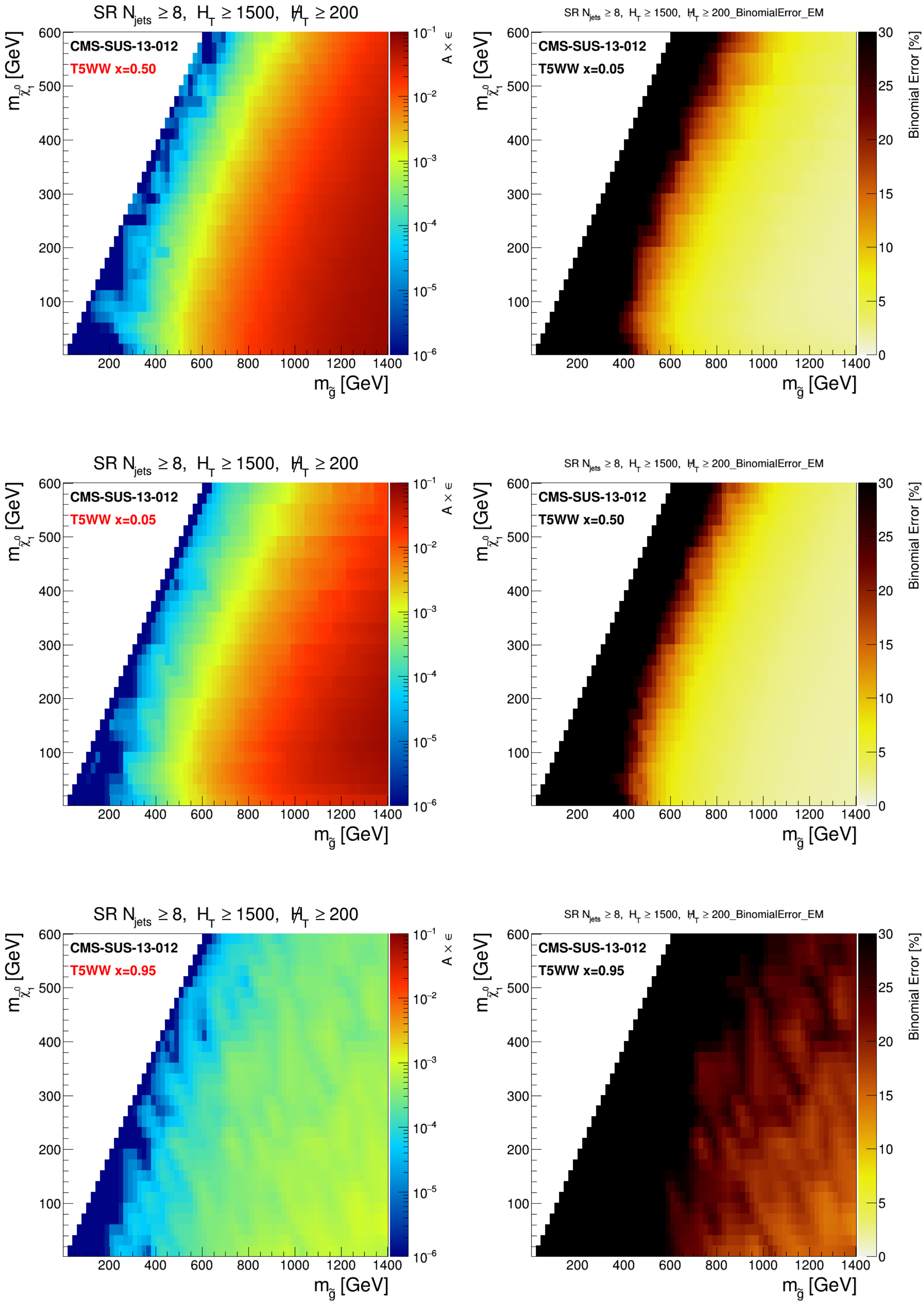

FIGURE 6.3: Efficiency, in absolute values, for the SR $N_{jets} \geq 8, H_T \geq 1500, \not{H}_T \geq 200$ and corresponding binomial error in % for the x =(0.05,0.50,0.95) parametrization. Nothe that in the case of x=0.95, in most of the plane the efficiency drops below 10^{-4}.

where N is the total number of Montecarlo events for each point.

For a large part of the region, where the efficiency assumes high values and the SR is fully sensitive to the signal, the statistical error is sufficiently small, around few %. On the opposite the efficiency is extremely low, the associated error exceeds 30%, as expected for mass points where only few events pass the selection cuts. The situation is quite severe if we focus on the $x = 0.95$ mass plane, where the loss of jets coming from the gluino drastically kills the signal. Unfortunately these considerations are strictly analysis dependent and cannot be generalised in terms of SRs and models. Nevertheless it helps give an estimation of the size of the uncertainty due to the limited sample statistics. Finally, it is to be reminded that the interpolation procedure is performed before the choice of the best SR.

6.2.1.2 Effect of the Interpolation on Limit Setting

In this Section the effect of the interpolation procedure on the limit setting is discussed. The most straightforward way to visualise this is shown in the top of Fig. 6.4. The exclusion curve for the mass plane parametrized with x=0.25 is shown in magenta for interpolated efficiencies, and in grey for recast values. The interpolation was performed between the x=(0.05, 0.50,0.95) mass planes implemented in the `SModelS` database. The dashed line represents the kinematic edge for on-shell W bosons to which the intermediate chargino decays. The part of the mass parameter space where the chargino decays via 3-body decays is not discussed here. The lines were extracted from the `SModelS` validation plots, as described in Section 4.2.

There are at least two regions where the effect of the interpolation impacts the limit setting. For the one centred around $(m_{\tilde{g}}, m_{\tilde{\chi}^0_1}) = (1000, 400)$ GeV, the interpolated limit over-excludes the true recast limit, although a little discrepancy is found, of order 50 GeV in neutralino mass. For the region around $(m_{\tilde{g}}, m_{\tilde{\chi}^0_1}) = (1200, 200)$ GeV, the interpolated limit results weaker, and the discrepancy is more prominent.

The source of the discrepancy can be attributed to the choice of different best SR, as indicated by the bottom panels of Fig. 6.4, that show that there is a large region where two competing SRs are selected differently in the recast and interpolated case. While for recast efficiency the $N_{jets} \geq 8, H_T \geq 1500, \not{H}_T \geq 200$ dominates over most of the plane, for the interpolated case this is mainly divided between $6 \leq N_{jets} \leq 8, 1250 \leq H_T \leq 1500, \not{H}_T \geq 450$ and $6 \leq N_{jets} \leq 8, 1000 \leq H_T \leq 1250, H_T \geq 450$. Ultimately, the reason for the different choice of the best SR depends on the values of the efficiencies and on the expected UL. This is further investigated in Fig. 6.5. On the top, the limits were calculated using alternatively the efficiency either for the $6 \leq N_{jets} \leq 8, 1250 \leq H_T \leq 1500, \not{H}_T \geq 450$ SR or for the $6 \leq N_{jets} \leq 8, 1000 \leq H_T \leq 1250, H_T \geq 450$ SR. This allows to disentangle the effect of the selection of the best SR on the global limit setting, since the discrepancy comes purely from the interpolation effects on the efficiencies (for a fixed SR). For the same parametrization the interpolated values underestimate (green lines) and overestimate (blue lines) the recast efficiency.
On the right, the ratio of recast over interpolated efficiency for the SR which drives the limits in the region of discrepancy for the recast case, i.e. $N_{jets} \geq 8, H_T \geq 1500, \not{H}_T \geq 200$. Recast values exceed more than 20% the interpolated ones in the region of interest, and up to a factor 2 for high gluino and neutralino masses.

I conclude this section with a final comment on the official results from the CMS analysis. Once again, the strength of this analysis is the combination of the 36 SRs, so the limits are in general

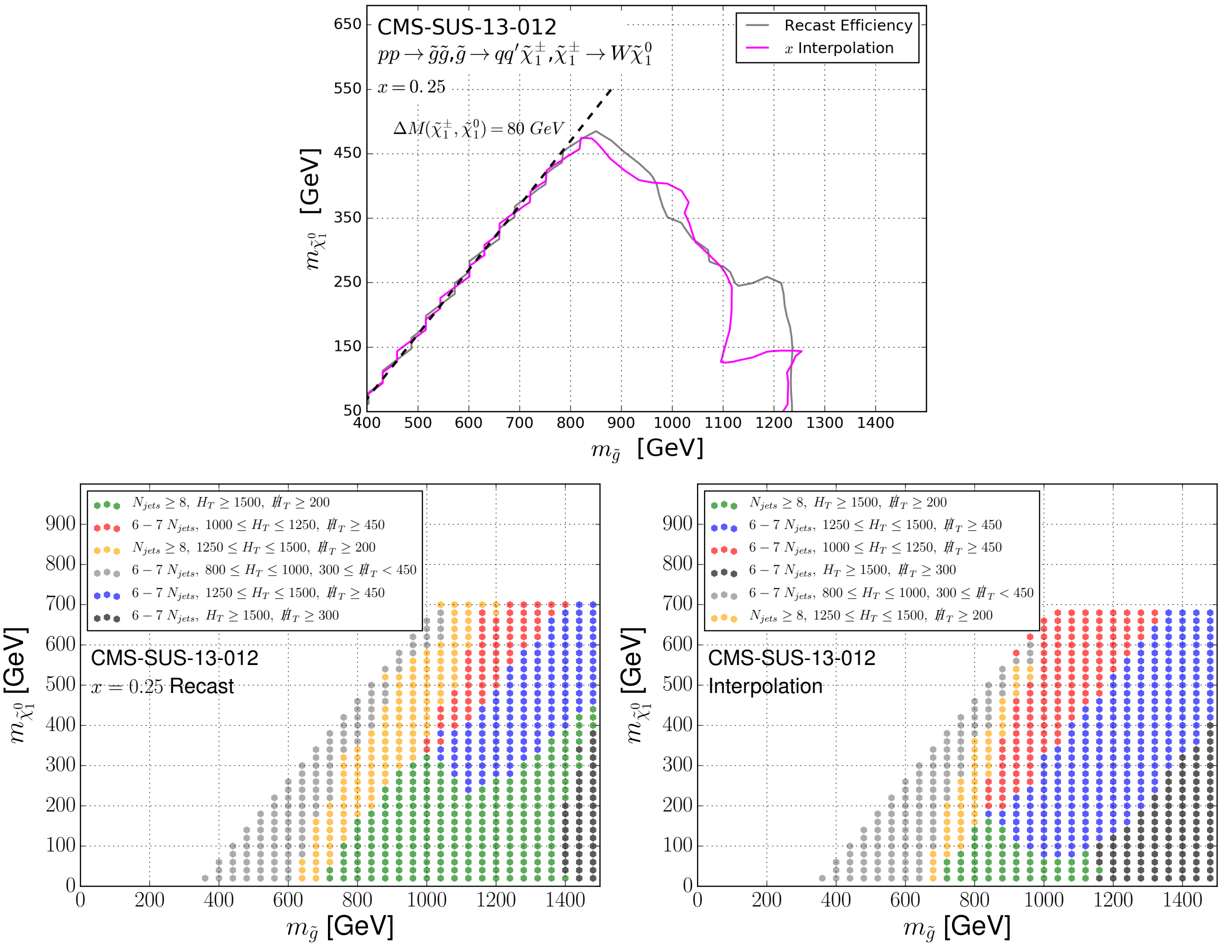

Figure 6.4: Top: exclusion curves obtained for the x=0.25 parametrization. The grey line shows the exclusion based on the recast values, while with magenta the exclusion line based on the interpolated values, obtained by interpolation between the $x = 0.05, 0.50, 0.95$ mass planes. The dashed black line corresponds to the kinematic edge allowing the chargino to decay to on-shell W bosons. Bottom: best SR maps for the recast (left) and interpolated values (right). For a vast region of the parameter space the SR $n_{jet} \geq 8$, $H_T \geq 1500$, $\not{H}_T \geq 200$ is chosen as best SR for the recast EM, contrarily to the choice of the SR $6 \leq n_{jet} \leq 8$, $1000 \leq H_T \leq 1250$, $\not{H}_T \geq 450$ for the interpolated results.

stronger than the ones obtained by considering one single leading SR at a time. This happens as well when using official CMS EM results, as it is shown in the validation plots available for the CMS-SUS-13-012 analysis on the official `SModelS` wiki page dedicated to validations. The limits obtained with `SModelS` with the best SR are always conservative, typically under-excluding CMS limits by up to $\sim$ 100 GeV for gluino simplified models. Any uncertainty introduced by recasting and interpolating is thus acceptable.

6.2.2 Results for ATLAS-SUSY-2013-04

Here the results for the ATLAS-SUSY-2103-04 analysis are presented. This analysis is designed to search for SUSY events producing large jets multiplicity and a large imbalance in the transverse energy, vetoing isolated leptons. The selection cuts defining the 13 SRs in the *multi-jet + flavour stream* analysis, as called in the official paper, are the following. Signal jets must have $\eta < 2$; they are divided in two categories depending on their momenta. For the looser selection $p_T > 50$ GeV, three SRs are defined for $n_{jets} = 8, 9$ or $n_{jets} \geq 10$. The tighter selection criterium requires $p_T > 80$ GeV, and considers $n_{jets} = 7$ or $n_{jets} \geq 8$. The binning in number of b-tagged jets is then applied,

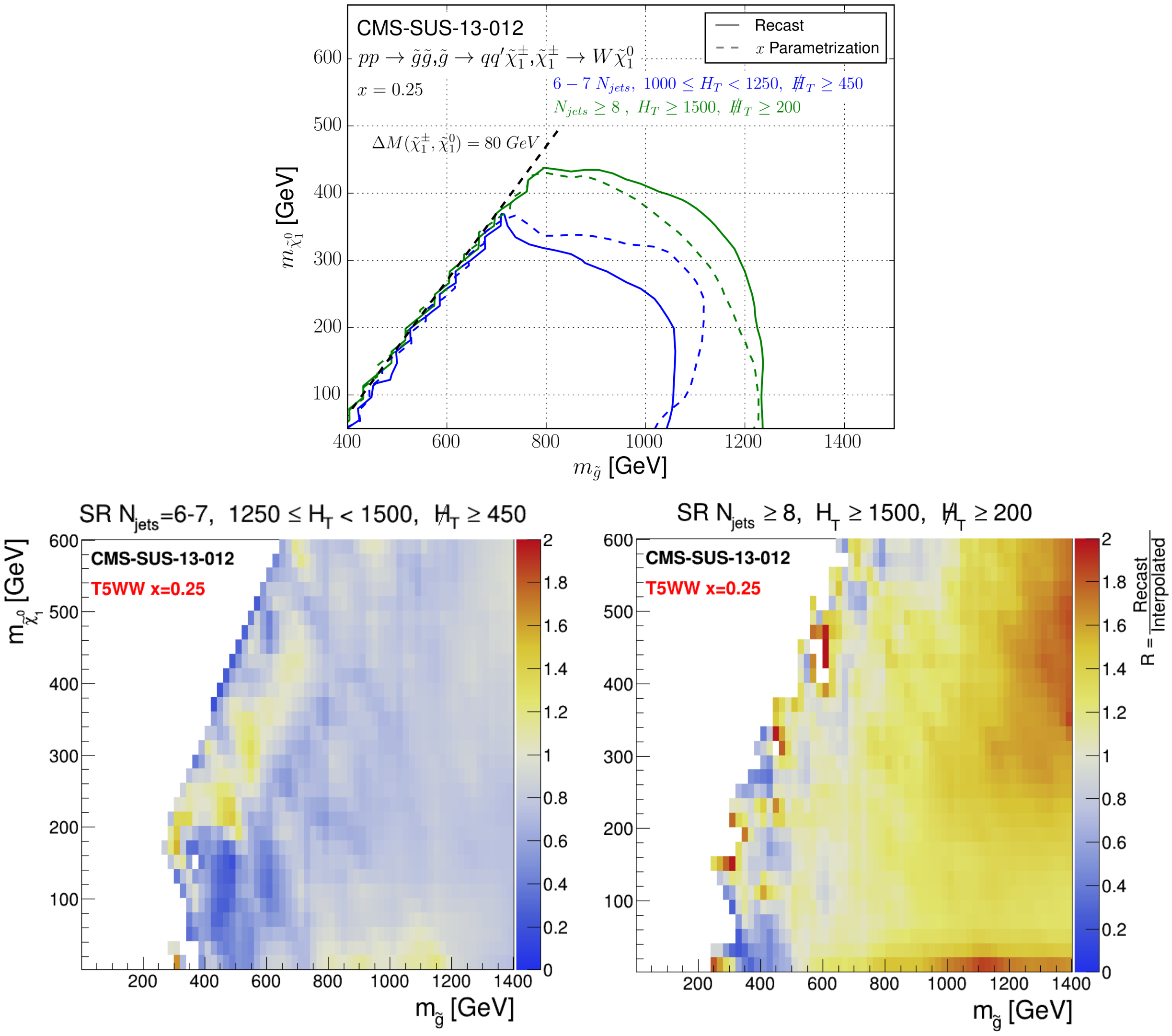

FIGURE 6.5: Top panel: exclusion curves for the two competing SRs $6 \leq N_{jets} \leq 8,\ 1000 \leq H_T \leq 1250,\ H_T \geq 450$ in blue and $N_{jets} \geq 8,\ H_T \geq 1500,\ \not{H}_T \geq 200$ in green and. For the first SR the interpolation procedure leads to an underestimation of the limits, while the opposite happens for the latter. Bottom panels: ratio of the recast/interpolated efficiencies for the two competing SRs. White patches are due to small values of at least one of the two efficiencies considered ($\leq 10^{-3}$ %) for which the ratio is not shown.

but for this work only the five $n_b = 0$ SRs are considered, since there are no SUSY signal b- jets. Finally the main kinematic variable used to discriminate SUSY events from the SM background is the ratio $\not{E}_T/\sqrt{H_T} > 4$ GeV $^{1/2}$, where H_T is the scalar sum of the jets p_T if $p_T > 40$ GeV and $\eta < 2.8$.

Among the various simplified models used for the interpretations of results, there are two mass planes for the *T5WW* model, the first with x=0.50 and the second by fixing $m_{\tilde{\chi}_1^0}$=60 GeV.

In the same fashion of the previous case, I start the discussion of the results with Fig. 6.6, that shows the efficiencies for three SRs, $N_{jets} = 8,\ p_T > 80,\ n_b = 0,\ N_{jets} = 8,\ p_T > 50,\ n_b = 0$ and $N_{jets} = 9,\ p_T > 80,\ n_b = 0$. For this analysis, the efficiencies behaves quite smoothly and on average small discrepancies can be found between the recast and interpolated values for $x = (0.25, 0.75)$. Higher efficiencies are obtained for values of the x between 0.25 and 0.50, due to the lower momentum of the jets coming from the gluino decay when the gluino-chargino mass gap decreases, as discussed in the introduction. The efficiencies in fact suffer from the tight cut on the signal jets ($p_t \geq$50 or $p_t \geq$80 GeV depending on the SR considered). Differently from the CMS strategy, the ATLAS collaboration prefers to design separate analyses targeting low jets multiplicity - i.e. ATLAS-SUSY-2013-02 $2-6\ jets\ +E_T^{miss}$, and higher jet multiplicity with ATLAS-SUSY-2013-04 $\geq 7\ jets\ +E_T^{miss}$.

Figure 6.7 shows the EMs for the two selected SRs with $n_{jets} = 7$, $p_T \geq 80$ and $n_{jets} \geq 10$, $p_T \geq 50$ GeV obtained using the parameters $x = (0.05, 0.50, 0.95)$ (left to right). Particularly evident is the difference between the two limiting cases x=0.05 and x=0.95, where the efficiency for the compressed gluino-chargino model is sensibly lower than the corresponding chargino-neutralino compression, as already highlighted in Section 6.2.1. This is due to the small sensitivity of the analysis to low jet multiplicity.

A comparison between the recast and interpolated value for the $x = 0.25$ parametrization is shown in Fig. 6.8, again showing the results for the limit setting and the difference in the choice of the best signal region. I omit here a detailed discussion of the reason of the discrepancy as done in the previous CMS analysis case, but the explanation lies in the fact that interpolation tends to favour lower values of the efficiency. In fact, all the $x = 0.25$ interpolated values for the efficiency underestimate the recast value.

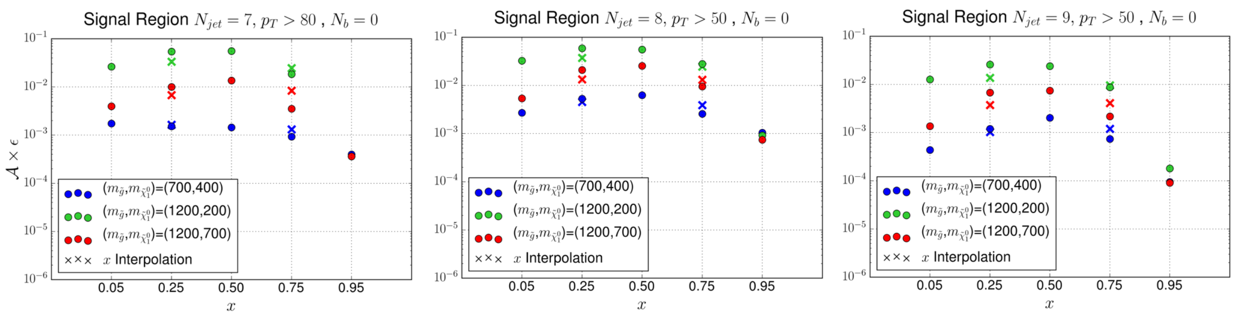

FIGURE 6.6: Efficiencies for the three mass points $(m_{\tilde{g}}, m_{\tilde{\chi}_1^0}) = (1200, 200), (1200, 700), (700, 400)$ [GeV] for three selected SRs. Similar behaviour is found for the other SR with $N_b = 0$ (not shown here).

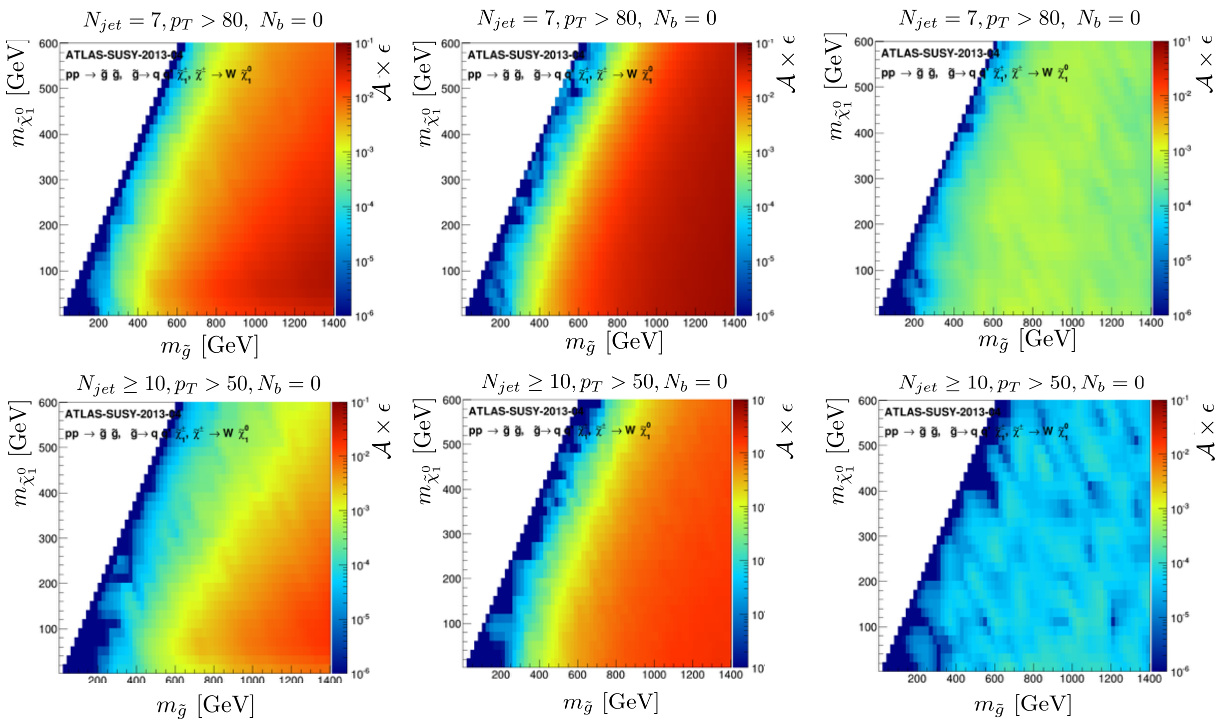

FIGURE 6.7: Temperature plots of the EMs for the SR $N_{jet} = 7, p_T > 80,\ N_b = 0$ (upper panels) and $N_{jet} \geq 10, p_T > 50, N_b = 0$ (lower panels) for the $x = 0.05, 0.50, 0.95$ parameters on the left, middle and right respectively. Note the small low efficiencies for x=0.95 parametrization.

6.3 T5WW in the pMSSM

The goal of this last Section is to show concretely how the 1-step cascade decay model *T5WW* can efficiently constrain the pMSSM if several mass planes are available, in particular parameter points where the mass gap between the $\tilde{\chi}_1^\pm$ and $\tilde{\chi}_1^0$ is small. This region of parameter space is often neglected by the experimental searches which most frequently require a large mass gap to ensure that the W boson in on-shell. Once again the following results were obtained considering the ATLAS pMSSM scan as described in Chapter 5, and specifically considering only the ATLAS-SUSY-2013-04 and CMS-SUSY-2013-012 EM results for the *T5WW* and *T5WW*$^{(*)}$ models. Two different mass planes parametrizations were used:

- x = (0.05, 0.50, 0.95) ;
- $\Delta M(\tilde{\chi}_1^\pm / \tilde{\chi}_2^0 , \tilde{\chi}_1^0$)= (10,75) GeV .

With this choice, the coverage of the mass parameter space extends also into the interesting region suggested above, owing to the x=0.05 and the two ΔM parametrizations. Moreover the interpolation spans over a sufficiently small mass difference, and no large fluctuations in the efficiencies are expected. The official CMS interpretations uses the x=0.50 parametrization of the *T5VV* model (CMS-SUS-13-012), while x=0.50 and $m_{\tilde{\chi}_1^\pm}$=60 GeV are used in the ATLAS analysis. Official results are however provided for only one mass plane, and not implemented in `SModelS` database.

In Fig. 6.9 the distribution of points in the gluino-neutralino mass plane is shown, with the colour code quantifying the `SModelS` r-value. The triangles and circles are used to identify the analysis providing the best exclusion, respectively for ATLAS and CMS. Red coloured points are excluded by *T5WW* or *T5WW*$^{(*)}$ results alone. It is then interesting to study the anatomy of points which are most constrained by this kind of simplified model results, looking for example at the branching

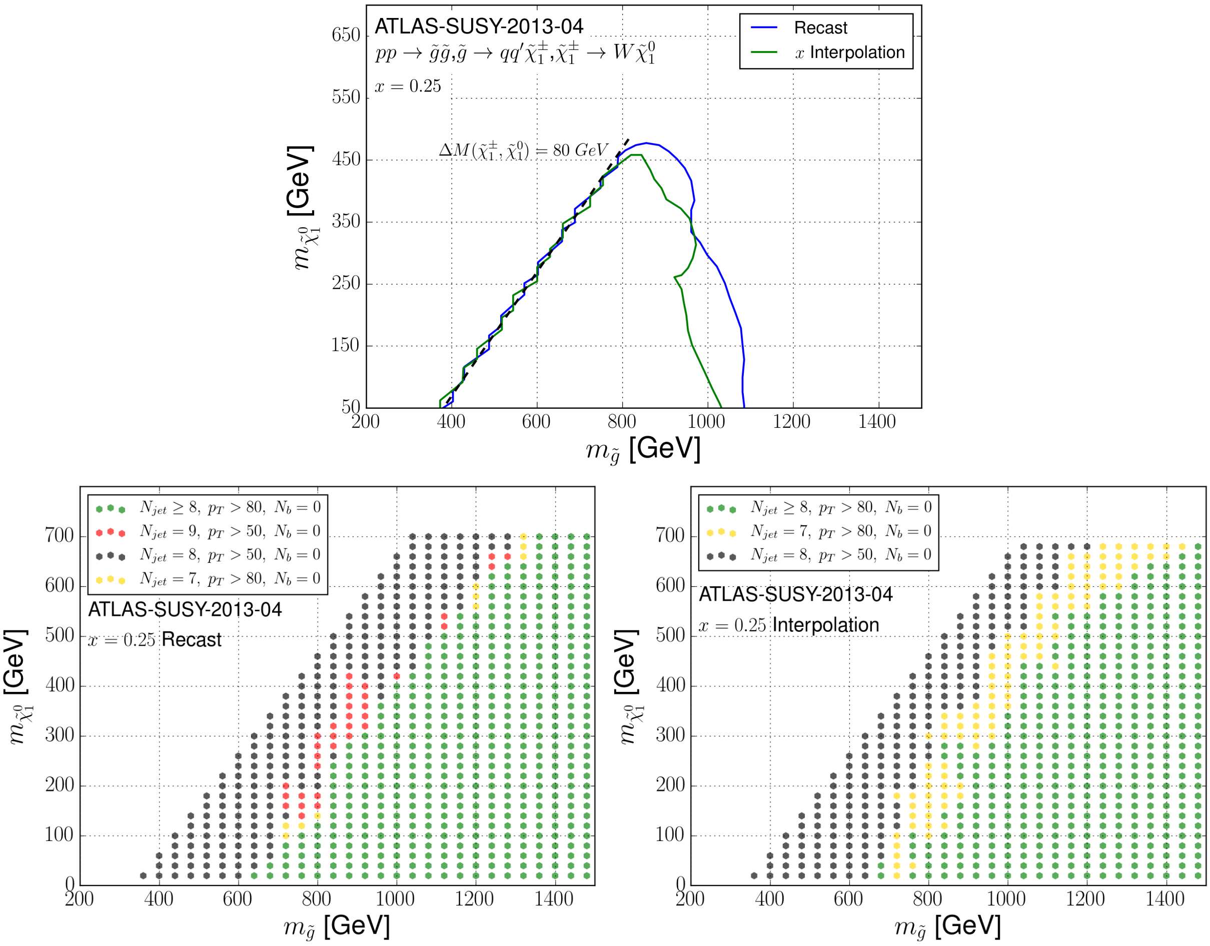

FIGURE 6.8: Top panel: exclusion curve and best SR maps of the ATLAS-SUSY-2013-04 analysis, for the recast and interpolated x=0.25 parametrization. Bottom left and right panels: best SR maps for recast and interpolated values.

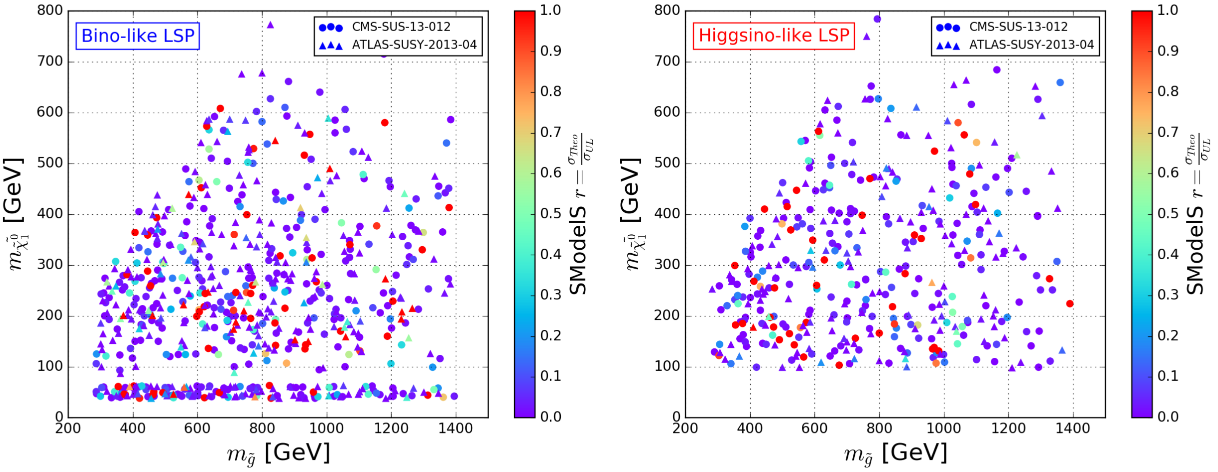

FIGURE 6.9: Distributions of points constrained by the $T5WW^{(*)}$ EMs results for the ATLAS-SUSY-2013-04 and CMS-SUS-13-012 analyses. The circle and triangle marks show the best constraining analysis, while the color code corresponds to `SModelS` r-value. Left: Bino-like LSP set of points, right: Higgsino-like LSP.

ratio in Fig. 6.10. Both the fractions to $\tilde{\chi}_1^{\pm}$ and $\tilde{\chi}_2^0$ are shown, which for some points exceeds the 70% value. The complementary decay of the gluino via both gauginos is important in the context of small mass gap between the gauginos and the LSP. In fact, in the simplified model and consequently for `SModelS`, if the mass gap $\Delta M(\tilde{\chi}_1^{\pm}\,/\tilde{\chi}_2^0\,, \tilde{\chi}_1^0\,)$ is lower than the mass of the W boson, the models *T5WW**, *T5ZZ** and *T5WZ** (mixed decay to chargino/neutralino with 100 % in each branch) are identified by the same constraint, that in the case of fully hadronic final state reads *[[['jet','jet']],[['jet','jet']]]* in `SModelS` bracket notation. This means the *T5WW** EMs results are effectively the combination of any model where the intermediate gaugino decays via off-shell bosons (W, Z or Higgs) to a pair of jets and the LSP. The T5ZZ constraints, with the on-shell Z boson, are not considered here, but the efficiency maps for the *T5ZZ* model, parametrized in the same fashion as the *T5WW* , were produced and included in the database. Note that, differently from the off-shell case where there is an automatic combination of the *T5WW**, *T5ZZ** and *T5VV** models, for the on-shell vector boson models the efficiency maps for each separate case must be produced and included in the database. The asymmetric decay *T5WZ* is not implemented in the current database, so only the *T5WW* and *T5ZZ* results can be combined for EMs results.

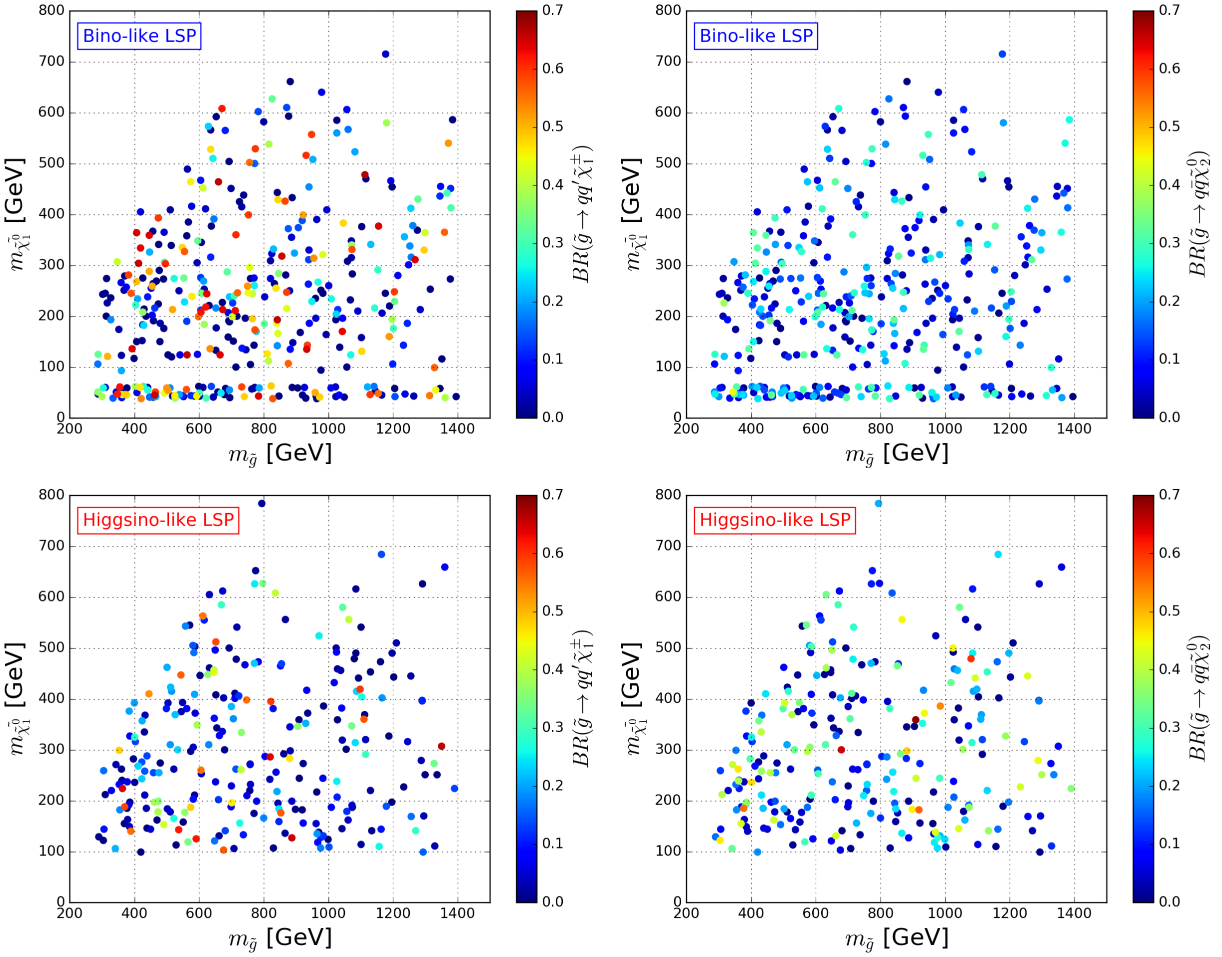

FIGURE 6.10: Branching ratios $\tilde{g} \to qq'\tilde{\chi}_1^{\pm}$ and $\tilde{g} \to q\bar{q}\tilde{\chi}_2^0$ for the Bino-like LSP (top row) and Higgsino-like LSP (bottom row). A fraction of points have BR exceeding 70 % to charginos or neutralinos, hence the importance of the $T5WW^{(*)}$ model.

This can be understood by looking at Fig. 6.11 that shows the same points but as a function of the mass difference between the gluino and the intermediate gaugino (x-axis) and between the gaugino-LSP (y-axis). This representation is useful to plot the dashed lines corresponding to the mass planes parametrizations used for the production of the results. For both Bino and Higgsino-like LSP cases, the majority of the points with large r-value have a small NLSP-LSP gap, below the mass of the W boson. The situation is more pronounced in the Higgsino-like LSP case, where basically no decay of the $\tilde{\chi}_1^{\pm}$ or $\tilde{\chi}_2^0$ to the LSP via an on-shell vector boson in allowed.

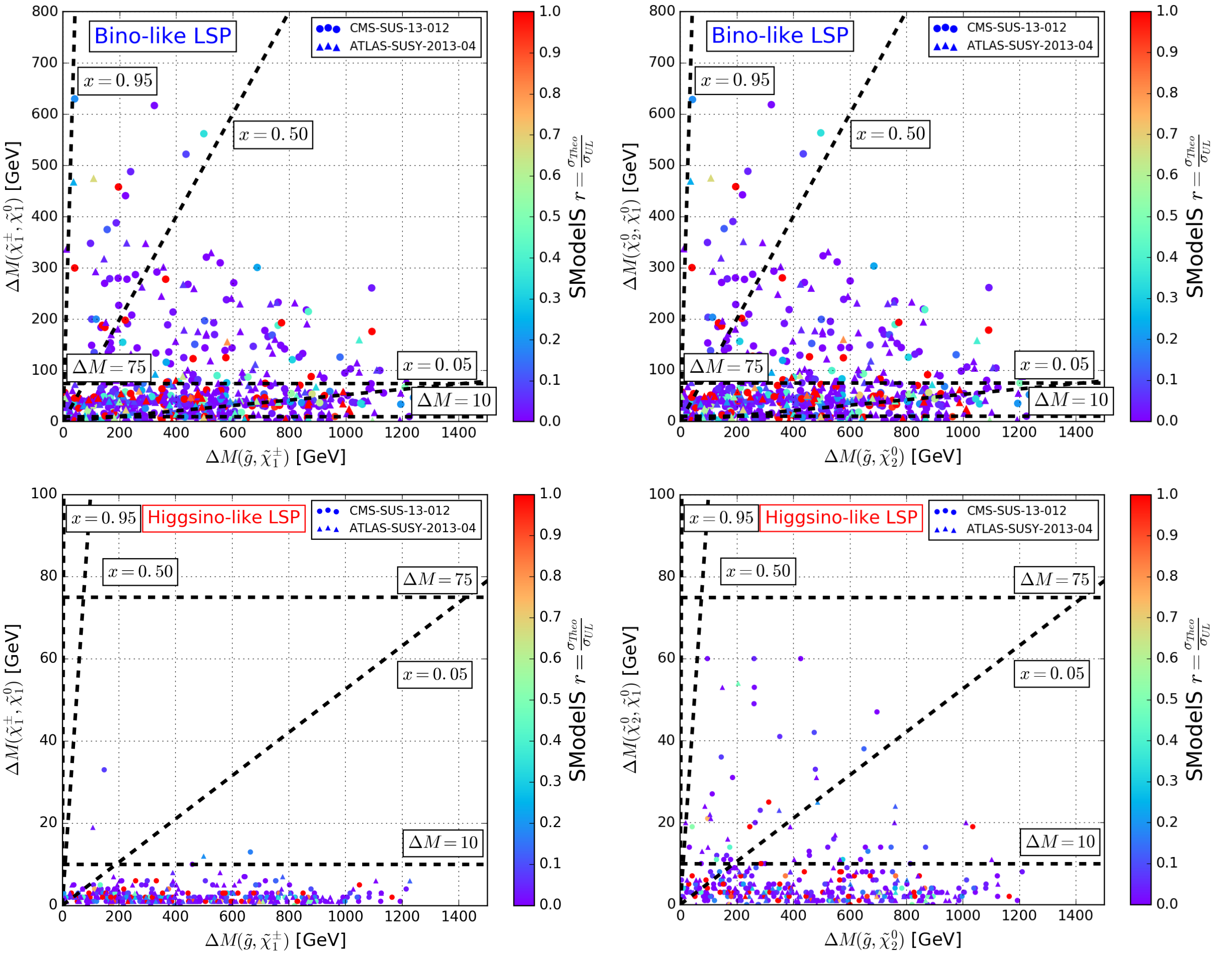

FIGURE 6.11: Distributions of points constrained by the *T5WW*$^{(*)}$ EMs as a function of the mass difference $\Delta M(\tilde{g}, \tilde{\chi}_1^{\pm})$ or $\Delta M(\tilde{g}, \tilde{\chi}_2^0)$ and $\Delta M(\tilde{\chi}_1^{\pm}, \tilde{\chi}_1^0)$ or $\Delta M(\tilde{\chi}_2^0, \tilde{\chi}_1^0)$ (y-axis). The dashed black lines show the mass planes implemented in `SModelS` database, parametrized with $x = (0.05, 0.50, 0.95)$ and $\Delta M(\tilde{\chi}_1^{\pm}/\tilde{\chi}_2^0, \tilde{\chi}_1^0) = (10, 75)$ GeV. The Higgsino-LSP focusses on the small gaugino-LSP mass gap, up to 100 GeV mass difference.

This is summarised by Fig. 6.12, which represents the distribution of the mass splitting between NLSP-LSP. Note finally that the gluinos, according to different mass spectra, can decay as well to $\tilde{\chi}_2^{\pm}$ and heavier neutralinos, for which the decay to on-shell bosons to the LSP is allowed. This is the explanation for which, in Fig. 6.11, several points can be constrained even if they lie outside the region allowed for interpolation, i.e. the constraints do not come directly from the decays of the gluinos to $\tilde{\chi}_1^{\pm}$ or $\tilde{\chi}_2^0$. In particular in the Bino-LSP case, 50% of the points have $\Delta M(\tilde{\chi}_3^0, \tilde{\chi}_1^0) < 80$ GeV. Since mass compression was also allowed in the `parameters.ini` card, other more complex models could be reduced to this specific topology.

Finally, the mass spectrum obtained with `PySLHA`[146] and the main decay modes of the SLHA point *274548389* from the Bino-like LSP dataset is shown in Fig. 6.13. It is an illustrative example to show concretely the importance of the inclusion of the *T5WW* model in the database. The complete `SModelS` results, obtained by using the full database released with the publication of v1.1, are summarised in Tab. 6.2. The point can be excluded with r = 1.06 by the CMS-SUS-13-012 EM result thanks to the *T5WW** model, which contributes more than the 94 % to the total weight. The other two EM results providing constraints are the *T1* and *T1bbbb*, which owe their constraining power to the strong coupling of the gluino with the off-shell squarks and sbottoms,

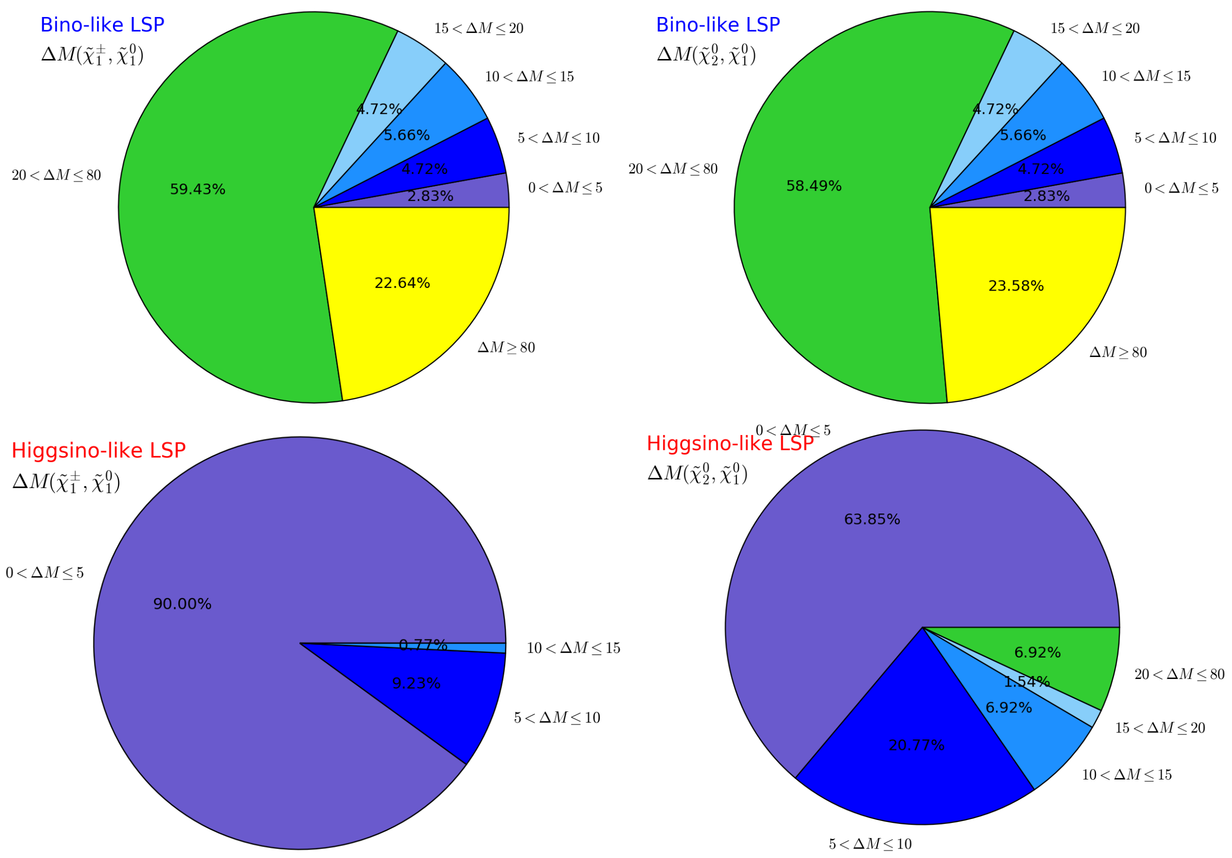

FIGURE 6.12: Mass splitting $\Delta M(\tilde{\chi}_1^\pm, \tilde{\chi}_1^0)$ and $\Delta M(\tilde{\chi}_2^0, \tilde{\chi}_1^0)$ for the same points int he plots above.

despite the heavy > 1.5 TeV mass. The other result considered, the $T5WW^*$ UL from ATLAS-SUSY-2013-02, cannot exclude the point.

$\sigma(pp \to \tilde{g}\tilde{g})$	Txname	weight	r$_{obs}$	r_{exp}
CMS-SUS-13-012 (SR:$6 - 7jets, 800 \leq H_T < 1000, 300 \leq \not{H}_T < 450$)				
1.03 [pb]	T5WW*	1.27	1.04	1.38
	T1bbbb	0.002	0.003	0.002
	T1	0.013	0.011	0.014
ATLAS-SUSY-2013-02 (UL)				
	T5WW*	-	-	0.87

TABLE 6.2: Summary of `SModelS` results for the point *274548389* from the Bino-like LSP dataset. Only the two most constraining analyses, i.e. CMS-SUS-13-012 (EM) and ATLAS-SUSY-2013-04 (UL) are shown.

Summary

The goal of this Chapter was to give an estimate of the uncertainty introduced by the interpolation procedure between different mass planes parametrizations. The case taken in consideration were the results for the *T5WW* model, which is one of the most popular models chosen by the ATLAS and CMS collaborations for the interpretation of their searches for SUSY events with large hadronic

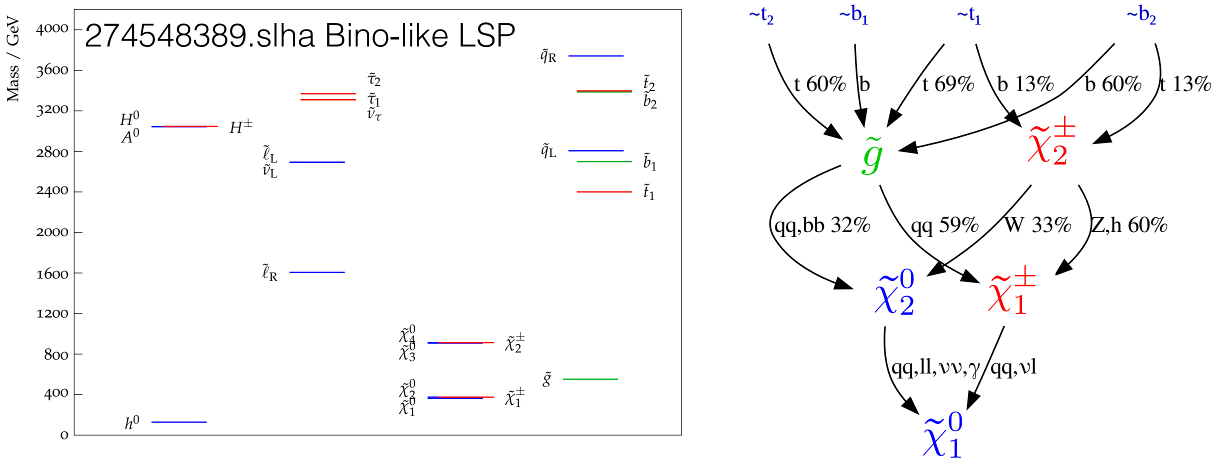

FIGURE 6.13: Mass spectrum (left) and main decay modes (right) for the representative point *274548389* from the Bino-like LSP dataset. Note that in addition to the decay $\tilde{g} \to q\bar{q}\tilde{\chi}_2$, also $\tilde{g} \to b\bar{b}\tilde{\chi}_2$ is important. This simplified model is currently missing in the database.

activities, like the ATLAS-SUSY-2013-04 and CMS-SUS-13-012 analyses.

Overall, the results of the interpolation are in acceptable agreement with the more accurate results obtained with a proper recast. This is very important, since on the one hand the possibility of interpolating between several mass planes is crucial for the `SModelS` workflow, and it allows to directly use directly the experimental results. On the other hand, thanks to the possibility of creating customised EM results, it serves as a guideline for the creation of future homegrown results. Even though one can in principle produce as many mass planes as desired, it is important to remember that this has a cost in terms of computing resources, and in terms of database size. So it is certainly advantageous to make use of the interpolation procedure whenever sufficiently accurate.

In particular it was highlighted that the standard $x = (0.05,\ 0.50,\ 0.95)$ parametrizations should be extended by adding a few more additional mass planes, e.g. planes at x=(0.25,0.75) so that the interpolation is performed on a denser grid of points. But more important it was drawn attention to a region of parameter space that is often neglected in the official simplified model interpretations, where the intermediate gaugino-LSP mass gap is small. By introducing additional mass planes that cover this region, it is possible to exploit efficiently the constraining power of the *T5WW*/T5ZZ*/T5WZ** simplified models. It was indeed shown that only thanks to this kind of simplified model results many points can be constrained by `SModelS`, which would otherwise escape the LHC Run 1 limits.

One final remark concerns the possible generalisation of the study performed here. Analogously to the *T5WW* model, models such as the *T6bbWW/T6WWbb*, *T6bbZZ/T6ZZbb* etc. can be used for the reinterpretation of generic multijet analyses, and due to the presence of the W/Z boson in the final state, they should exhibit similar features with respect to the interpolation procedure.

Chapter 7

A Comprehensive Tool for DM Studies: `MadDM v.3.0`

Contents

Many experimental searches for DM signals have been performed, exploiting different experimental techniques designed to cover the rich DM phenomenology. If the dark sector interacts weakly with the SM particles, not only can we hope to produce DM particles at colliders like the LHC, but we can also think of processes where the DM annihilates into SM particles or scatters elastically against heavy nuclei. The right diagram in Fig. 7 is a very popular diagram summarising the principles of DM particle detections and how we can catch signals of the presence of DM particles with three types of experiments:

- production of DM particles at colliders like the LHC ;
- DM annihilation into SM particles, or '*indirect detection*;
- DM scattering onto SM particles, or '*direct detection*'.

Typically, the details of the interaction are left unresolved, according the established fashion of using simplified models. This implies that, for example in the case of indirect detection, the kinematic properties of the SM particles produced do not strongly depend on the type of interaction.

The experimental techniques and challenges of DM searches at the LHC have been extensively treated in the previous Chapters; the current Chapter focusses on the searches based on the indirect detection of DM. To make use of the large quantity of limits from DM experiments, it is very useful to develop tools that simplify both the theoretical and experimental aspects of phenomenological DM studies. The latest `MadDM v.3.0` aims at providing a comprehensive and flexible

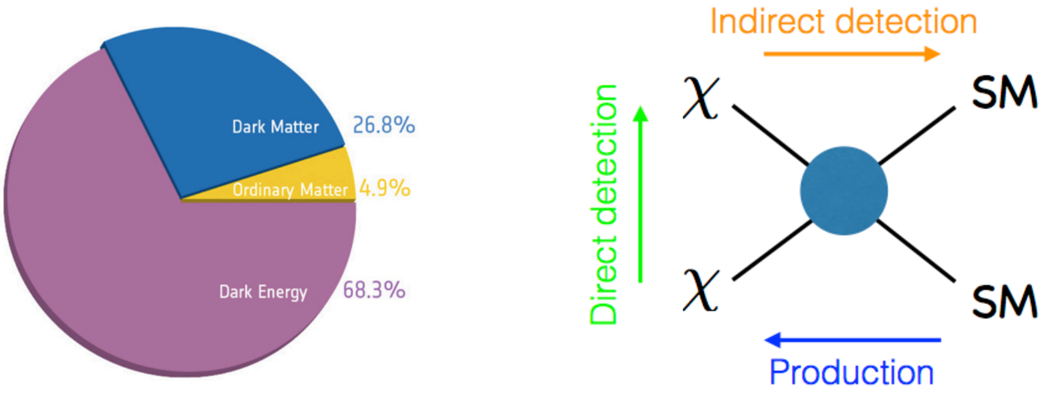

FIGURE 7.1: Contribution of baryonic matter, DM and dark energy from the latest Planck Collaboration's measurements (left) for the ΛCDM model; schematic principles of DM detection for direct, indirect and collider searches (right).

framework for phenomenological studies of general DM models, introducing a dedicated module for the study of DM indirect detection.

The Chapter is structured as follows. The physics at the basis of the DM phenomenology, with emphasis on the quantities relevant for DM indirect detection are presented in Sections 7.1 and 7.2. The `MadDM v.3.0` tool is introduced in Section 7.3, with a special focus on the indirect detection module. This module constitutes the major new feature of v.3.0, allowing the user to obtain theory predictions for the DM annihilation cross sections and fluxes of cosmic rays (CR), and confront directly with the limits obtained by the Fermi-LAT experiment. The idea behind `MadDM v.3.0` is the flexibility of usage: two main running modes were implemented, allowing the user to choose between a 'fast' and a 'precision' running mode. The main contributions to this project are: the implementation of the annihilation spectra, in particular the interface with the existing tabulated spectra, and the validation with Monte Carlo samples; the module for the comparison of the theory predictions with the experimental limits; the module for the propagation of CR, such as neutrinos and positrons; the creation of the user interface and of the output files, in the case of the 'fast' or 'precision' running mode, for single points or scan modes. The last Section (Sec. 7.4) is a brief user's guide, describing how to launch a `MadDM v.3.0` analysis and how to interpret the results.

7.1 A Universe filled with Dark Matter

There are strong indications for our universe to be composed of a form of matter which does not possess electric and color charge, making up to 84% of the total matter density, and almost 27% of the total energy content of the universe (see the latest measurements from the Planck Collaboration [13]). The problem of dark energy is maybe an even bigger puzzle than the nature of dark matter; while it is not gonna be treated in this work, I briefly remind that it causes the universe to expand, nowadays, at an accelerated rate.

Coming back to DM, there exist also models of DM possessing fractional electrical charge, called 'millicharged' particles which might constitute a viable DM candidate, see e.g. [147]. For the rest of the discussion only charge neutral DM particle candidate will be considered, for which the only possible interaction with the SM is via the electroweak force. The gravitational interaction with ordinary matter is also fundamental, since indeed the only evidences of the existence of DM particles are purely of gravitational kind. In any case, any gravitational effect between fundamental particle is negligible compared to the other interactions. The only feasible interaction between DM and the SM particles is the weak force (or possibly a new type of force with even weaker coupling), since electromagnetic or strong coupling are tightly constrained by astrophysical observation, or rather non-observation of signal of DM interaction with the SM of self-interaction.

The presence of a large quantity of DM affects many astrophysical and cosmological observables. The global properties of the universe are explained in the context of the ΛCDM model, where Λ is the cosmological constant introduced by Einstein's formulation of general relativity, and *CDM* stands for cold dark matter. Cold DM candidates are no more relativistic at time of their decoupling from the other particles, while warm or hot DM candidates are still mildly or highly relativistic. All the current astrophysical observations, in particular regarding the large scale structure, tend to prefer the CDM scenario and a bottom-up evolution of the universe: small gravitationally bound objects of the size of our Milky Way's globular clusters (M $\approx 10^5 M_\odot$, $M_\odot$ =1 solar mass) will merge and accrete their mass during the evolution of the universe to form the galaxies and clusters observed today. Fig. 7 (right) shows the percentage of each component of the universe, divided into baryonic matter (that includes ordinary matter forming the various structure of the universe, the interstellar and intergalactic medium, stars etc.), a DM component, and a dark energy component, responsible for the accelerated expansion of the universe.

It is natural to consider the ΛCDM as the companion of the Standard Model of particle physics in the context of cosmology. One of its building block is certainly the theory of Big-Bang, which predicts that the universe, after a phase of extremely rapid expansion, slowly cools down permitting the growth of regions with peaks of matter density that nowadays form the galaxies and all the other astrophysical objects. Our universe begins in a form of 'soup' of ultra-relativistic particles all coupled together by a hypothetical force unifying the strong, the weak and the electromagnetic forces (and even gravitational at Planck scale, see Section 2.2.2.2).
Due to the expansion of the universe, the various components cease to be in thermal equilibrium. This happens with regular components of matters, e.g. the photons decouples from electrons and other charged particles giving rise to the Cosmic Microwave Background (CMB) spectrum, but also possibly with BSM components, such as DM particles. A fundamental parameter is the DM relic density, or the observed density of DM particles that we presently see in the universe. This important parameter will be discussed in detail in Section 7.1.1. I finish this introduction by listing the most compelling evidences for the presence of DM.

Stars and Galaxies dynamics The first observation of an astrophysical anomaly was due to Zwiky in 1933[148], who found that the average velocity of around a thousand galaxies inside the Coma cluster were exceeding the standard Newtonian predictions for a virialised bound system. He was able to estimate that around 90% of the matter responsible for the gravitational potential was non-luminous, and that he called 'dunkle Materie'. In the late '60s, thanks to advanced spectroscopical observations of stellar dynamics in spiral galaxies, it was found that most of the stellar rotation curves were not dropping according to classical Newton's and Kepler's laws predicting $v(r) \propto r^{-1/2}$, but were rather flat at increasing distances from the center. This meant again that the distribution of the luminous matter was not following closely the distribution of the matter gravitationally bounding the system, and a sort of obscure halo was surrounding the visible objects.

For completeness, there exist theories where DM is not formed by exotic particles, but rather an incomplete formulation of the theory of gravity. This is the case of the Modified Newtonian Dynamics[149] (MOND), which introduces a new fundamental constant to be considered when applying the second Newton's law of dynamics. This theory can partially explain the flattening of the rotation curves, but it is unable to explain the thermal evolution of the universe and in general other properties or measurements.

Cosmic Microwave Background One of the biggest achievement of the Big-bang theory is the prediction, followed by successful observations, of a background of low energy photons permeating uniformly the entire universe. With a wavelength of 1.9 mm, they constitute the so called cosmic microwave background (CMB). The COBE[150], WMAP[151] and most accurately the Planck[13] experiments have studied the variation of the CMB temperature across the sky, finding that anisotropies of the temperature wrt the average value of 2,725 K at present time, does not exceed a 10^{-5} level. The CMB is perfectly explained in the context of the ΛCDM cosmology; it was originated at time of photon-matter decoupling, when the cross section scattering of photon and matter dropped due to the expansion of the universe, and photons were then freely streaming.

Gravitational Lensing Due to the presence of matter and energy densities, the space-time bends according to Einstein's law of general relativity. When a massive object such as a DM halo is placed between an observer and a bright object, it acts as a lens, bending the light to form peculiar luminous arches. This is frequently seen in the pictures of the deep universe taken by the Hubble satellite, where the light from background galaxies appears flexed and distorted into semi- or complete arches.

One of the smoking guns of the presence of DM halos was the observation of the 'bullet cluster'[151]. The system consists in a small cluster moving away from a bigger companion; the total mass and the mass distribution was estimated thanks to the observation of gravitational lensing of background objects and simulations. By comparison with the optical observation of stars and the x-ray observation of the cluster hot gas, it was determined that the center of masses of the luminous and non-luminous matter were highly offset: the two DM halos passed through each other, while the baryonic matter was still interacting and emitting highly energetic photons. This permitted also to estimate the upper limit on the DM self-interaction cross section. It also gave strong support to the particle DM theory, since these observations cannot be accommodated in MOND scenarios.

7.1.1 The WIMP Paradigm and the DM Freeze-out

According to the ΛCDM model the universe depends on its energy content, from an initial state where all the particles are in thermal equilibrium. Then, since it expands, the thermal equilibrium between the different components is broken, similarly for what discussed for the CMB. By identifying the DM candidate with an hypothetical particle χ of mass m_χ, it is possible to trace the density evolution by solving the Boltzmann equation:

$$\frac{dn_\chi}{dt} + 3H(T)n_\chi = \langle\sigma v\rangle(n_\chi^2 - n_{\chi,eq}), \tag{7.1}$$

where H(T) is the Hubble parameter, T the temperature of the thermal bath, and n_χ is the DM density defined as

$$n_\chi(T) = \int \frac{d^3p}{(2\pi)^3} f_\chi(p,T). \tag{7.2}$$

The quantity $\langle\sigma v\rangle$ is the thermally averaged DM annihilation cross section, that includes 2-body annihilation processes into SM particles: $\sigma \equiv \sigma(\chi\chi \to SM\ SM)$. For the function $f_\chi(p,T)$, typically a Maxwell-Boltzmann distribution is chosen, resulting in a DM density at thermal equilibrium:

$$n_{\chi,eq} = g_\chi \frac{m_\chi^2 T}{2\pi} K_2(m_\chi T). \tag{7.3}$$

The number density depends on the number of internal degrees of freedom g_χ of the DM candidate; K_2 is the type-2 modified Bessel function. The DM relic density, defined as the ratio of the energy density associated with DM particles and the critical density of the universe (today 10^{-5} GeV/cm^3)

can be calculated by integrating

$$\Omega_{DM}h^2 \equiv \frac{\rho_{DM}}{\rho_{cr}} \approx 8.76 \times 10^{-11} GeV^{-2} \left[\int_{T_0}^{T_f} g_*(T)^{1/2}\langle\sigma v\rangle dT\right]^{-1} \tag{7.4}$$

between the freeze-out temperature T_f and the current temperature of the universe T_0.

The results depend on the total number of degrees of freedom of the relativistic species in thermal equilibrium g_*, function of the temperature of the thermal bath. Figure 7.2 shows the evolution of the number density as a function of the temperature of the universe (scaled by the DM mass m_χ). The expansion of the universe, governed by the Hubble parameter H, decreases the interaction rate $\Gamma_\chi \equiv \langle\sigma v\rangle n_{\chi,eq}$ between the DM particles. When $H \geq \Gamma_\chi$, called DM "freeze-out", the DM number density becomes practically constant and takes the name of cold DM thermal relic density, or relic density for short.

Note that the annihilation cross section fixes the normalisation and absolute value of the relic density, and different DM theoretical models must be able to correctly predict the value of the relic density as constrained by various observations. This is particularly important since it gives a theoretical motivation for searching for DM and in general new physics at the TeV scale, i.e. around or slightly above the electroweak symmetry breaking scale and at energies which are reachable at the LHC. The latest measurement from the Planck Collaboration [13] reports a relic density of

$$\Omega_{DM}h^2 = 0.1197 \pm 0.0022^{1} \tag{7.5}$$

which can be obtained by a cross section of order $\langle\sigma v\rangle \sim 10^{-26}$ cm^3 s^{-1} . When considering a DM mass around the electroweak scale, e.g. $m_\chi = 200$ GeV , a typical freeze-out temperature of order $T \sim m_\chi/20$, and a weak cross section that scales as $\sigma \sim G_F^2 T^2$ (where G_F is the Fermi coupling constant), the predicted relic density approximates the measured value.

DM particles that are able to explain the observed relic density thanks to the weak force are called 'WIMP', acronym for weakly interactive massive particles. Note that the names is frequently used

---

[1] Planck TT+lowP analysis

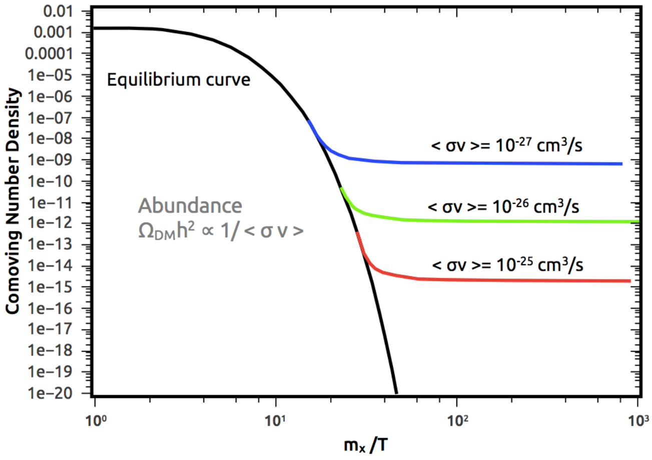

FIGURE 7.2: Comoving number density of DM as a function of the temperature of the universe T and the annihilation cross section $\langle\sigma v\rangle$. After a certain temperature, the density number is "frozen" and the total number density of DM remains constant up to the present age. The $\langle\sigma v\rangle$ gives the normalisation of the curve and fixes the absolute value. Taken from [152].

also to identify a wider class of particles that interact with sub-weak interaction with the SM, not necessarily through the 'standard' weak-interaction. Theorists friendly call the fact that WIMPs with mass at around the weak scale seem astrophysically favoured as the 'WIMP miracle', since this scenario miraculously offer a very rich phenomenology that can be looked for with several types of experiments, at the current accessible energies and experimental sensitivity. This motivation is also at the basis of the searches for DM (or R-parity conserving SUSY) production at the LHC, as detailed in the previous Chapters. Next, the motivations and the principles of WIMPs direct and indirect detection experiments are introduced.

7.2 Principles of Direct and Indirect Dark Matter Detection

According to the ΛCDM model, the formation and evolution of cosmic structures is driven by the initial formation of gravitationally bound DM halos. This halos of particle DM still surround the observed galaxies and galaxy clusters. A priori, the shape of those halos is not known, nor it has to have a universal shape in all the different astrophysical environments. Popular choices for DM profiles are e.g. Navarro-Frank-White (NFW[153]), the Einasto, the Isothermal and the Moore[154] profiles (these four implemented in the 'fast' method for extracting positrons fluxes at Earth in `MadDM v.3.0` , see Section 7.3.1.4) and others.

All the models predict a flattening of the galaxy rotation curves for large radii, while the dynamics in the inner part is quite different. In particular, there are both theoretical and experimental motivations that allow the central parts of the halos to exhibit a peak of density (or cuspy profile), a constant value, or even population of sub-halos. The variety of models allowed is due to the high uncertainty in making observation towards the inner part of our galaxy.

As an example, the Isothermal, NFW and Moore profiles for ρ_{DM} can be expressed by the law:

$$\rho(r)_{DM} = \left(\rho_{\odot} \frac{R_{\odot}}{R}\right)^{\gamma} \left(\frac{1+(R_{\odot}/a)^{\alpha}}{1+(r/a)^{\alpha}}\right)^{(\beta-\alpha)/\gamma}$$

Profile	α	β	γ
Isothermal	2	2	0
NFW	1	3	1
Moore	1.5	3	1.5

where a is a fit parameters related to the halo scale,$R_{\odot} = 8.5$ kilo Parsec is the distance of the Sun from the galactic center, and $\rho_{\odot}$ ≈0.3 [GeV cm^{-}3] is the local DM density .

The various profiles exhibit different densities at different radii form the center of the objects (e.g. the Milky Way, other galaxies, globular clusters etc.) so that the total DM mass contained within a certain radius depends on the profile considered, that in turns influences the kinematics of stars and properties of other observables, e.g. the expected rate of DM annihilation events in different part of the halo. I turn now the discussion to the main theoretical and experimental features of direct and indirect DM searches.

7.2.1 Direct Detection

Direct detection experiments are designed to collect possible signals of nuclei recoil against the collision with DM particles (for a review see e.g. [155]). The recoil rate can be calculated as:

$$\frac{dR}{dE}(E,t) = \frac{\rho_0}{m_\chi m_A} \int v \cdot f(\mathbf{v},t) \cdot \frac{\sigma}{dE}(E,v) d^3 v \tag{7.6}$$

where the quantities ρ_0 and $f(v,t)$ are the local DM density and its velocity wrt the frame of the detector, and the time dependency encapsulates the dependency on the orbital revolution of the Earth around the Sun. From the particle physics point of view, the important quantity is the differential cross section $\sigma(E,v)/dE$; this can be computed by neglecting or considering the spin of the nucleon.

Spin-independent cross sections assume an equal contribution to the total WIMP-nucleon cross section form neutrons and protons:

$$\sigma_{SI} = \frac{4}{\pi}\mu_A^2 \cdot [Z \cdot f_p + (A-Z)\cdot f_n]^2 \tag{7.7}$$

where $\mu_A = \frac{m_\chi m_A}{m_\chi + m_A}$ is the reduced mass of the WIMP-nucleus , Z is the number of protons, A the total number of nucleons. The form factors for protons and neutrons are denoted with f_p and f_n respectively. Due to the coherent scattering off all the nuclei, a strong scattering enhancement is expected for heavy nuclei.

Figure 7.3 shows the results from the XENON1T[156] experiment for spin-independent cross section upper limits, currently implemented in the `ExpConstraint` class. In late Spring 2018, the experiment published an update with more stringent limits in [157], that will be included in the next release of `MadDM v.3.0` .

Spin-dependent cross sections consider only unpaired nucleons, so that only detector material with an odd number of protons or neutrons must be used in order to be sensitive to the spin structure. These processes probe in fact the spin content of the quarks inside the nucleons. The

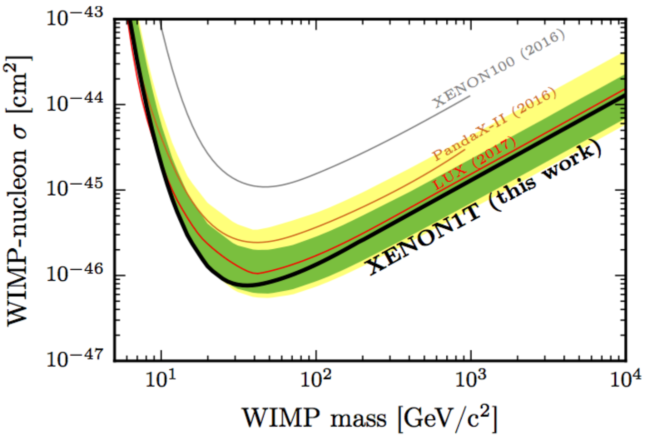

FIGURE 7.3: XENON1T limits for spin-independent WIMP-nucleon scattering implemented in `MadDM v.3.0 ExpConstraint|` class.

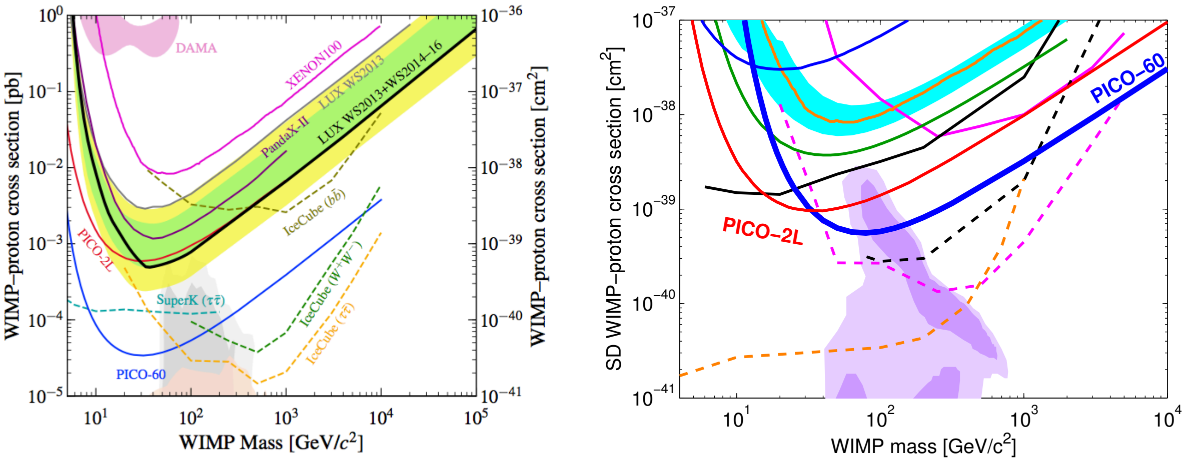

FIGURE 7.4: Pico60 limits for WIMP-proton scattering (left) and LUX limits (right) for the WIMP-neutron scattering (bottom), implemented in `MadDM v.3.0 ExpConstraint| class`.

cross sections can be calculated as:

$$\sigma_{SD} = \frac{16}{\pi}\mu_A^2 \cdot \frac{J_A + 1}{J_A}(f_p' + f_n')^2 \tag{7.8}$$

where J_A is the spin of the nucleon. Direct detection predictions for spin independent and dependent scattering were the main feature of `MadDM v.2`[158], hence they will be not treated in details in this work.

The upper limits for DM-neutron scattering from the LUX experiment [159] and for DM-proton scattering from Pico60[160] were implemented in the `ExpConstraint` class; the limits for the above experiments are shown in Fig. 7.4.

7.2.2 Indirect Detection

Indirect detection experiments search for signatures of annihilation of DM into SM particles. The ideal astrophysical environments to look for such processes are dwarf spheroidal galaxies (dSphs for brevity) and the Milky Way galactic center. For example, dSphs are known to be the astrophysical objects with the highest DM density. These are compact galaxies that belong to the local group, showing no significant sign of recent star formation; this makes them very difficult to observe given the low luminosity of the old star population. One of the most famous Milky Way satellite is *Segue1*, frequently dubbed as 'The Darkest Galaxy'. Commonly the *mass-to-light,* M/L quantity is used to characterise objects with a significant presence of DM: it is defined as the ratio of the total mass of an object divided by its luminosity, and normalised by the value measured for the Sun. Segue 1 is the object with the largest M/L[161], reaching up to 3.400 in some photometric bands. A high M/L value is found also in the other dSphs, making these objects ideal to search for DM annihilation. Together with Coma Berenices, it is the dSph with the highest J-factor: $10^{19.4} GeV^2 \mathrm{cm}^{-5}$. Besides the large quantity of DM, dSphs are ideal observational targets since they are in the vicinity of the Milky Way, and astrophysical objects producing non-thermal γ-rays are absent. Similar argument holds in favour of observing towards the center of the Milky Way, since a peak in the density of DM is expected, and taking advantage of a J-factor increased by $O(10^2)$. However is carries also a non-thermally produced background [162].

DM indirect detection experiments tries to catch signals of DM annihilation by measuring the fluxes of cosmic rays (CRs) arriving at Earth, both with experiments outside the atmosphere and on the ground. In this thesis and in `MadDM v.3.0` , CRs include high energy photons, positrons, antiprotons, electrons and neutrinos of the three flavours. Measured excesses in the fluxes of CRs, in the form of sharp lines or bumps in the energy spectra of such particles, might be addressed to DM annihilation in addition to the known astrophysical processes.

In general, the CR flux detected ad Earth is expressed as:

$$\frac{\mathrm{d}\Phi}{\mathrm{d}E_{CR,n}}(E_{CR,n},\psi) = \frac{1}{2m_\chi^2}\sum_i \langle\sigma v\rangle_i \frac{\mathrm{d}N^i_{CR,n}}{\mathrm{d}E_{CR,n}}\,\frac{1}{4\pi}\underbrace{\int_\psi \frac{\mathrm{d}\Omega}{\Delta\psi}\int_{\mathrm{los}}\rho_\chi^2(\psi,l)\,\mathrm{d}l}_{J\ \text{factor}}\ . \tag{7.9}$$

For each neutral CR species, the energy-differential flux depends on the sum over the DM annihilation into each possible SM channel "i". Note that CRs originate from the decay, showering, hadronization, electroweak emission etc. of the SM particles into which the DM particles annihilates, and not only from direct DM annihilation. The energy spectrum dN^1/dE^i gives the differential number of particle with respect to the energy, at the source. The rightmost term constitutes the astrophysical J factor, which essentially quantify the total amount of DM contained in the object observed: it is the integral performed along the line of sight of the squared of the DM density ρ_χ, averaged over an opening solid angle ψ. Each dSph galaxy, as well as the Milky Way center, has its own measured J-factor, which is typically inferred from the study of stellar kinematics from spectrographic measurements. The numerical factor $1/4\pi$ is valid assuming that the nature of the DM candidate is of Majorana type, i.e. the DM is its own antiparticle; for Dirac DM, an additional $1/2$ factor must be applied.

By solving equation 7.9 it is possible to predict the flux of neutral CR,n for specific DM models, and compare with the experimental measures. However, further complications arise when considering charged CRs, since the propagation of such particle within the Milky Way strongly depend on the details of the galactic propagation models as well as other effects to be considered such as the solar modulation. In general, photons and neutrinos can be used to trace extragalactic source since their propagation is essentially straight (up to gravitational effects like lensing), and their flux at detection can be easily computed with equation 7.9 up to the J-factor. This is not possible with charged CRs that must be properly propagated inside the galaxy (see Section 7.3.1.4).

7.3 The New `MadDM v.3.0`

As it was shown above, DM has a rich phenomenology and many results are now available from colliders, direct and indirect types of experiment, in addition to fundamental astrophysical observation. One of the tools than incorporates both the ability of making theoretical predictions and automatically confronting them with the latest experimental limits on various observables is `MadDM`. Tools of this kind are extremely useful to make comprehensive DM studies, aiming at constraining the parameter space of existing DM models with the current experimental bounds; available tools are e.g. MicrOMEGAS[163], DarkSUSY[164] and the DarkBit[165] module from the GAMBIT tool.

The previous `v.1`[166] and `v.2`[158] MadDM versions focused on the calculation of relic density, and direct detection predictions for generic DM models. I omit here specific details about the code implementation of the previous versions, to give more space to presenting the new features of version `v.3.0`, summarised in Fig. 7.5. `MadDM v.3.0` is now a standard `MadGraph5_aMC@NLO v.2.6.2` plugin, and can be installed directly inside the framework; this allows to inherit and fully exploits the capabilities of the `MadGraph5_aMC@NLO v.2.6.2` platform (from here referred to

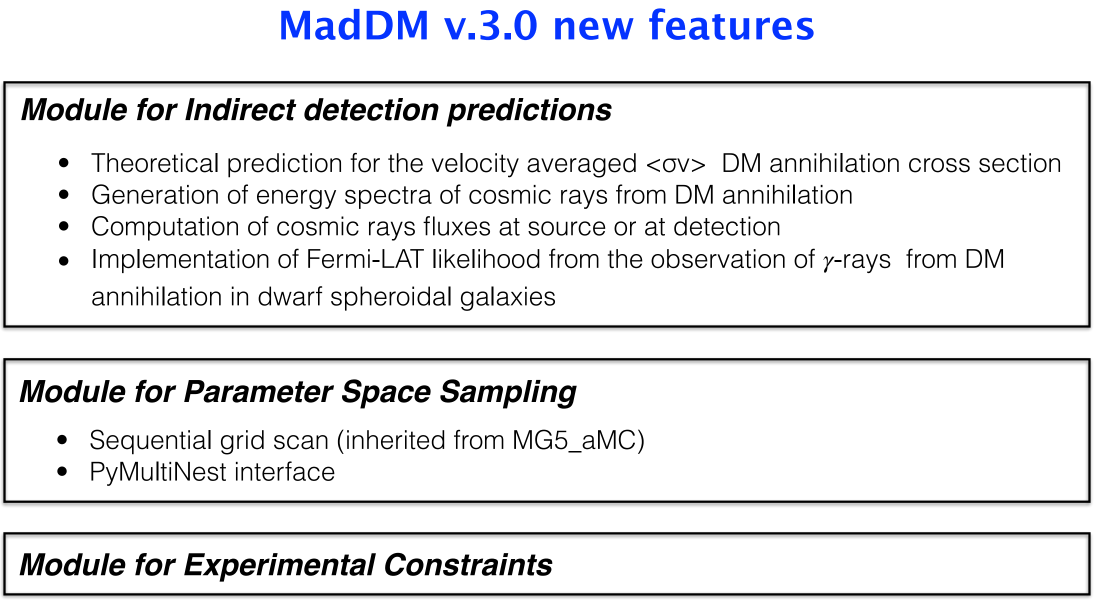

MadDM v.3.0 new features

Module for Indirect detection predictions

- Theoretical prediction for the velocity averaged <σv> DM annihilation cross section
- Generation of energy spectra of cosmic rays from DM annihilation
- Computation of cosmic rays fluxes at source or at detection
- Implementation of Fermi-LAT likelihood from the observation of γ-rays from DM annihilation in dwarf spheroidal galaxies

Module for Parameter Space Sampling

- Sequential grid scan (inherited from MG5_aMC)
- PyMultiNest interface

Module for Experimental Constraints

FIGURE 7.5: Summary of the new features introduced in `MadDM v.3.0`.

as `MG5_aMC`) to calculate matrix elements for the relevant DM processes, as well as the features for scanning the parameter space of the DM model tested. Arbitrary DM models can be tested, providing their UFO[68] implementation.

The biggest improvement introduced by this version concerns the *indirect detection* module, that extends its capabilities to this additional type of DM phenomenology predictions and corresponding experimental constraints. In particular the major contribution of this thesis was the implementation, validation and testing of the infrastructure for the calculation of DM annihilation rates with the latest bound from the Fermi-LAT Collaboration. When developing the code a special attention was given to allow the user to opt for different running modes. Since typically the parameters of DM models cover large multi-dimensional spaces, it is very advantageous to allow for a rapid calculation of results, in order to highlight interesting regions that can be later studied with increased accuracy. A the same time, for specific model points, one could be interested in high precision calculation, allowing for long running time. Hence, two modes were implemented in `MadDM v.3.0`, called *'fast'* and *'precision'* methods. The main difference in the two methods concerns the:

- computation of the annihilation cross section $\langle \sigma v \rangle$;
- generation of the energy spectra of the cosmic rays.

These differences will be explained when relevant in the following discussion, which will focus on the presentation of the indirect detection module.

7.3.1 Indirect detection module

The indirect detection module provides the theory prediction the value of the current constraints from the Fermi-LAT experiment, obtained from the observation of γ-rays flux from dwarf spheroidal galaxies. The needed physical quantities are the annihilation cross section, the CRs energy spectra at source and finally the spectra at detection. As a first step, `MadDM v.3.0` calculates the annihilation cross section for the relevant processes (see. Section 7.3.1.1). If not specified by the user, all the 2-body annihilation channels i.e. $\chi\chi \to$ 2-body will be considered, both with SM and BSM particles. Otherwise the user can specify a generic n-body final state; an interesting case is for example described in [5](Section 5.3), showing that, for the interesting case of extra photon emission via internal bremsstrahlung, the computation of the 3-body annihilation cross section and spectra can be automatically performed by `MG5_aMC` .

Then, the energy spectra of the γ-rays are extracted (Section 7.3.1.2) and used to calculate the Fermi-LAT limits (Section 7.3.1.3). Finally, the charged CRs can be propagated to Earth using the external tool `DRAGON` (Diffusion of Cosmic Rays in Galaxy modelling) [167], or positrons fluxes for a set of fixed parameters can be extracted and provided to the user in the 'fast' mode. For the neutral components the differential and integrated fluxes are calculated by `MadDM v.3.0` and provided, using the Draco dSph J-factor.

7.3.1.1 Theory Predictions for $\langle \sigma v \rangle$

There are three distinct methods to compute the annihilation cross sections in `MadDM v.3.0` :

1. Inclusive ('fast')
2. Madevent ('precision')
3. Reshuffling ('precision' default choice)

As seen in the case of the relic density computation, in general the annihilation cross section depends on the velocity distributions of the DM particles. At present time, $\langle \sigma v \rangle$ can be computed (see e.g.[168, 169] for the complete derivation):

$$\langle \sigma v \rangle = \int \mathrm{d}^3 \boldsymbol{v}_1 \mathrm{d}^3 \boldsymbol{v}_2 P_{\boldsymbol{r}}(\boldsymbol{v}_1) P_{\boldsymbol{r}}(\boldsymbol{v}_2)\, \sigma v_{\mathrm{rel}} \;\equiv \int \mathrm{d}v_{\mathrm{rel}}\, \tilde{P}_{\boldsymbol{r},\mathrm{rel}}(v_{\mathrm{rel}})\, \sigma v_{\mathrm{rel}} \ . \tag{7.10}$$

In the leftmost term of the equation, $\boldsymbol{v}_i$ are the velocities of the two annihilating DM particles, according to velocity distribution $P_{\boldsymbol{r}}(\boldsymbol{v}_i)$ that depends on the position $\boldsymbol{r}$. The right term represents a more convenient way of calculating this quantity, where the quantity:

$$\tilde{P}_{\boldsymbol{r},\mathrm{rel}}(v_{\mathrm{rel}}) \equiv 4\pi v_{\mathrm{rel}}^2 \int \mathrm{d}^3 v_{\mathrm{CM}} P_{\boldsymbol{r}}(\boldsymbol{v}_{\mathrm{CM}} + \boldsymbol{v}_{\mathrm{rel}}/2) P_{\boldsymbol{r}}(\boldsymbol{v}_{\mathrm{CM}} - \boldsymbol{v}_{\mathrm{rel}}/2) \, , \tag{7.11}$$

is expressed as function of the velocity in the center-of-mass frame $\boldsymbol{v}_{\mathrm{CM}} \equiv (\boldsymbol{v}_1 + \boldsymbol{v}_2)/2$, and $\boldsymbol{v}_{\mathrm{rel}} \equiv \boldsymbol{v}_1 - \boldsymbol{v}_2$. Typically and likewise done in `MadDM v.3.0` , one assumes a Maxwell-Boltzman distribution with most probable velocity $\sqrt{2} v_0$, so that the distribution of the relative velocity can be expressed as:

$$\tilde{P}_{\boldsymbol{r},\mathrm{rel}}(v_{\mathrm{rel}}) = \sqrt{\frac{2}{\pi}} \frac{v_{\mathrm{rel}}^2}{v_0^3} \exp\left(-\frac{v_{\mathrm{rel}}^2}{2 v_0^2} \right) \, . \tag{7.12}$$

In partial wave analysis, the cross section can be generally expanded as $\langle \sigma v \rangle = a + b v_{rel}^2 + ...$, where the first (independent on v) and second are the s- and p-wave terms of the expansion. When these two terms are the dominant contributions, it is possible to calculate the velocity averaging by calculating σv_{rel} at $v_{rel} = \sqrt{3} v_0$.

The differences in the three available methods of calculating $\langle \sigma v \rangle$ are analysed here briefly.

Inclusive method This method, used in the 'fast' running mode, allows only 2-body DM annihilations (both SM and BSM), with cross section matrix elements evaluated at leading order; the phase-space integration is performed only on the angular separation of the two final state particles. The $\langle \sigma v \rangle$ is finally evaluated considering a Dirac delta function peaked at v_{rel}, which the user can select in the `maddm_card.dat` in input. Although very fast (few seconds), it agrees within 10-20% difference with the other two, more accurate methods. This method does not involve Monte Carlo events production, so the energy spectra of the annihilation into SM particles are extracted from a dedicated module containing pre-compiled tables (see Section 7.3.1.2). Energy spectra for BSM states decays are not available from this method.

Madevent method This method used the functionalities inherited by `MG5_aMC` , and evaluates all the relevant matrix elements (up to NLO depending on the processes considered) and performs the full phase-space integration. Any generic n-body annihilation process is allowed. The event generation is performed by considering two colliding DM particles with a CM energy $\sqrt{s} = 2m_\chi\big(1 + 1/8\, v_{\text{rel}}^2\big)$ with $v_{\text{rel}} = \sqrt{3}v_0$. Again, the cross section is then evaluated at a velocity v_{rel}. An important feature of this method is the creation of LHE events files, which will be passed to `Pythia 8` for showering and other relevant processes to create the CR spectra. This also allows to extract the CR energy spectra from the decay of BSM particles.

Reshuffling method This method is based on the previous Madevent, with an additional reshuffling of the kinematics of the particles generated in the events by using a full Maxwell-Boltzmann distribution around v_0. Accordingly, the events cross section are reweighed. The new kinematic distributions of the particles might alter significantly the cross section of certain processes, especially in the case of thresholds effect: a fraction of the newly reweighed events might in fact allow for processes which were previously kinematically suppressed.

7.3.1.2 Cosmic Rays Energy Spectra

As explained in 7.2.2, the cross section upper limits for indirect detection are interpreted with generic simplified models assuming DM annihilation into SM channels with 100% BR. In this approximation, details regarding the exact interaction at the basis of the annihilation process are neglected. We expect no strong dependency on the exact kinematics of the process that might effect the resulting energy spectra, and the only important variable left is the DM mass m_χ. Once this is fixed, the CR energy spectra will be approximately the same for any DM model tested. In this Section the energy spectra are considered at source, i.e. where the DM annihilation process takes place, for example inside a dSph galaxy or in the galactic center.

It is possible and very convenient, for the sake of saving computation time, to consider a set of energy spectra for the different CR, relative to different DM candidate mass. Once these spectra are produced, they can be stored to be rapidly accessed to extract the spectra. This was done by a group of phenomenologists, that made available a set of energy spectra for different CR and different annihilation channels [170, 171, 172]. This philosophy is not conceptually different from the use of EMs to reconstruct full SUSY signals.

The energy spectra were produced using `Pythia 8` , simulating two DM particles collisions producing a generic heavy resonance of mass double the mass of the DM particles. The resonance than decays into the desired SM channels (only 2-body annihilation was considered). Energy spectra for CR $= \gamma, \nu_e, \nu_\mu, \nu_\tau, e^+, \bar{p}$, originating from the decay, hadronization etc. of the initial SM particles are then extracted. The results for a set of DM mass values are then provided in form of text tables, which have been converted to a python dictionary (and stored in a numpy file) and implemented in `MadDM v.3.0` . Throughout this thesis and in `MadDM v.3.0` , we refer to these as `PPPC4DMID` tables. This is the method employed by ‘fast’ running mode to extract the energy spectra. Figures 7.6

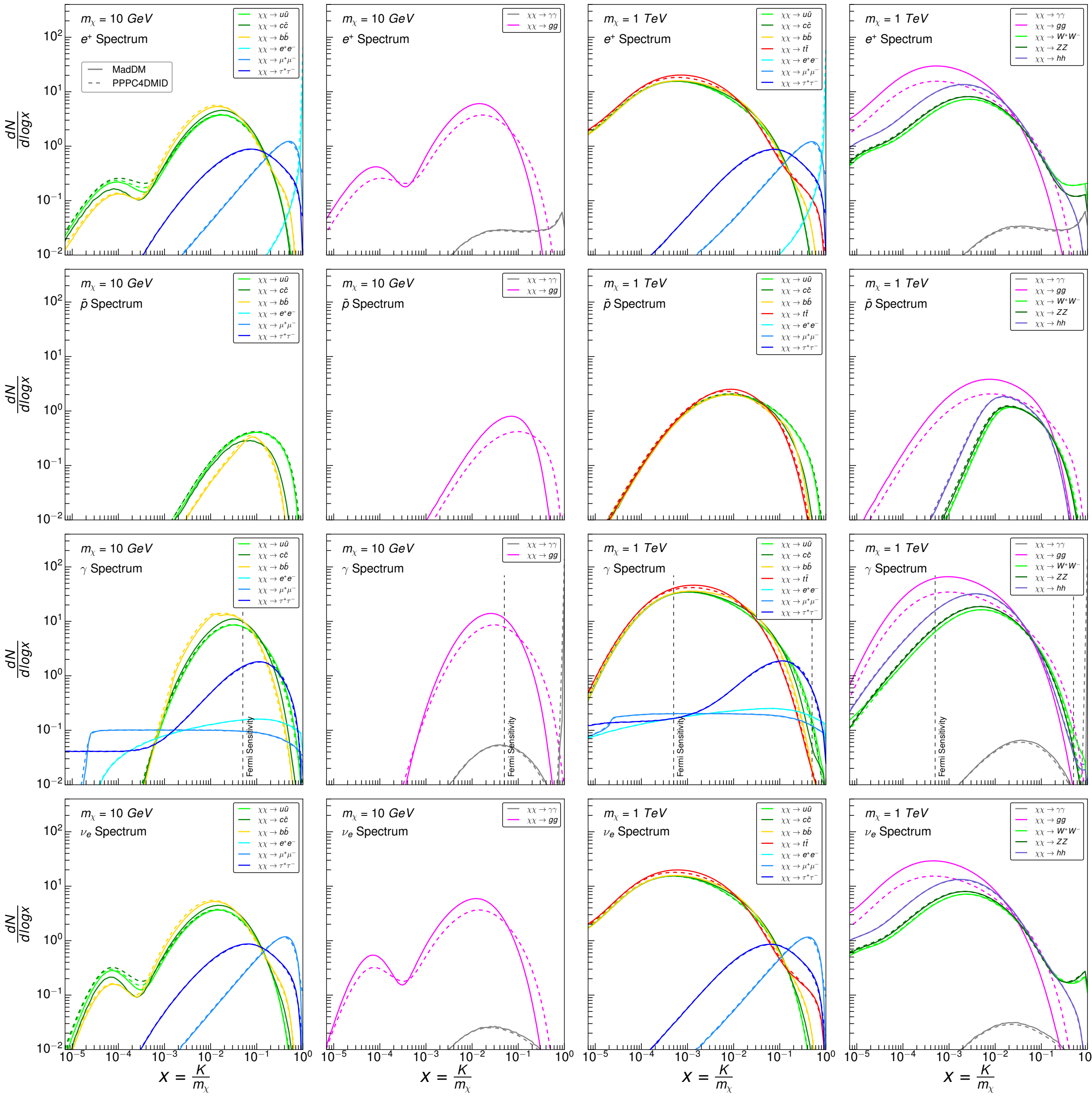

FIGURE 7.6: Energy spectra (dN/dlogx) at source as a function of x=E_{kin}/m_χ, for m_χ = (10 GeV, 1 TeV). Only the kinematically available annihilation channels are shown; the plots show Fermions and Bosons separately. The spectra are given for positrons, antiprotons, gamma rays, and electron neutrinos. Note that for gammas, the sensitivity bounds for the Fermi-LAT experiment (500 MeV, 500 GeV) are shown as a reference.

and 7.7 show the comparison and validation of the spectra from the `PPPC4DMID` tables, and spectra obtained by using the full event generation `MG5_aMC` + `Pythia 8` , for four different DM masses (10 GeV and 1 TeV, 100 GeV and 10 TeV respectively). The spectra are plotted as a function of the ratio of the kinetic energy of the DM particle and its mass, and the differential of the number count wrt the logarithm of this ratio. The available 2-body annihilation channels are:

$$\chi\chi \quad \rightarrow \quad gg, q\bar{q}, c\bar{c}, b\bar{b}, t\bar{t}, e^+e^-, \mu^+\mu^-, \tau^+\tau^-, ZZ, W^+W^-, hh\,, \tag{7.13}$$

where the light quarks are grouped into the generic particle $q = (u, d, s)$ with the exception of the charm quark. In general there is a very good agreement between `PPPC4DMID` and `MadDM v.3.0` spectra, while a small discrepancy can be seen for the "c" quarks and for gluons. However these are not dramatically different, and this can be addressed to different implementation of the effective coupling between DM and gluons as implemented by the group.

The spectra shown in Fig. 7.6 deserve a special mention. The difference wrt the previous case is that when showering, `Pythia 8` is allowed to consider the emission of real on-shell electroweak (EW) boson (see [173] for details). The default setting in `MadDM v.3.0` has an active weak emission (`TimeShower:weakShower=on` in the input card). This is important when considering the spectra (and consequently the expected fluxes at Earth) of some CR which might be enhanced by the decay of the real EW bosons emitted; the difference in the spectra with and without EW corrections from the `PPPC4DMID` collaboration is shown in Appendix H. Note that for the spectra produced with the 'precision' method, a very large number of Monte Carlo events were generated, in the range $5 \times 10^{5-6}$, in order to populate properly each energy bin.

In the 'fast' mode, the energy spectra for each CR is thus extracted for each annihilation channel and then summed up to evaluate the total energy spectrum for each CR:

$$\frac{\mathrm{d}N_i}{\mathrm{d}\log x} \equiv \sum_{\mathrm{SM}} \langle \sigma v \rangle_{SM} \frac{\mathrm{d}N_i^{\mathrm{SM}}}{\mathrm{d}\log x}\ . \tag{7.14}$$

In equation 7.14, each energy spectrum originating from a specific annihilation channel "i" is scaled by its own annihilation cross section. Figure 7.8 compares the total γ-rays obtained with the 'fast' and 'precision' running modes, in the case of a spin-1 mediator simplified DM model, for a DM mass of 500 GeV.

7.3.1.3 Implementation of the Fermi-LAT Limits

Among the scientific scopes of the Fermi experiment, there is the observation of dSphs aiming at catching excesses in the γ-ray flux as explained in the introduction. The main instrument, the LAT- large area telescope, is able to detect single gamma ray emission from astrophysical sources [2]. By estimating the γ-ray background, the Fermi collaboration is able to set limits on the DM $\langle \sigma v \rangle$, that if present, would result in an excess in the count rate.

In their latest results, the Fermi-LAT collaboration[174] extracted limits on the annihilation cross section by using the data collected during 6 years of observations. The sample used in the analysis includes 28 kinematically confirmed dwarfs, plus additional 17 systems of stars which exhibit photometric properties compatible with dSphs, labelled 'candidate' dSphs. The data showed no significant excess in the γ-ray flux, with the exception of a local $\approx 2\sigma$ deviation appearing in the

---

[2] The other instrument, the GBM - gamma ray burst monitor, aims at detecting transient events such as gamma ray bursts and solar flares.

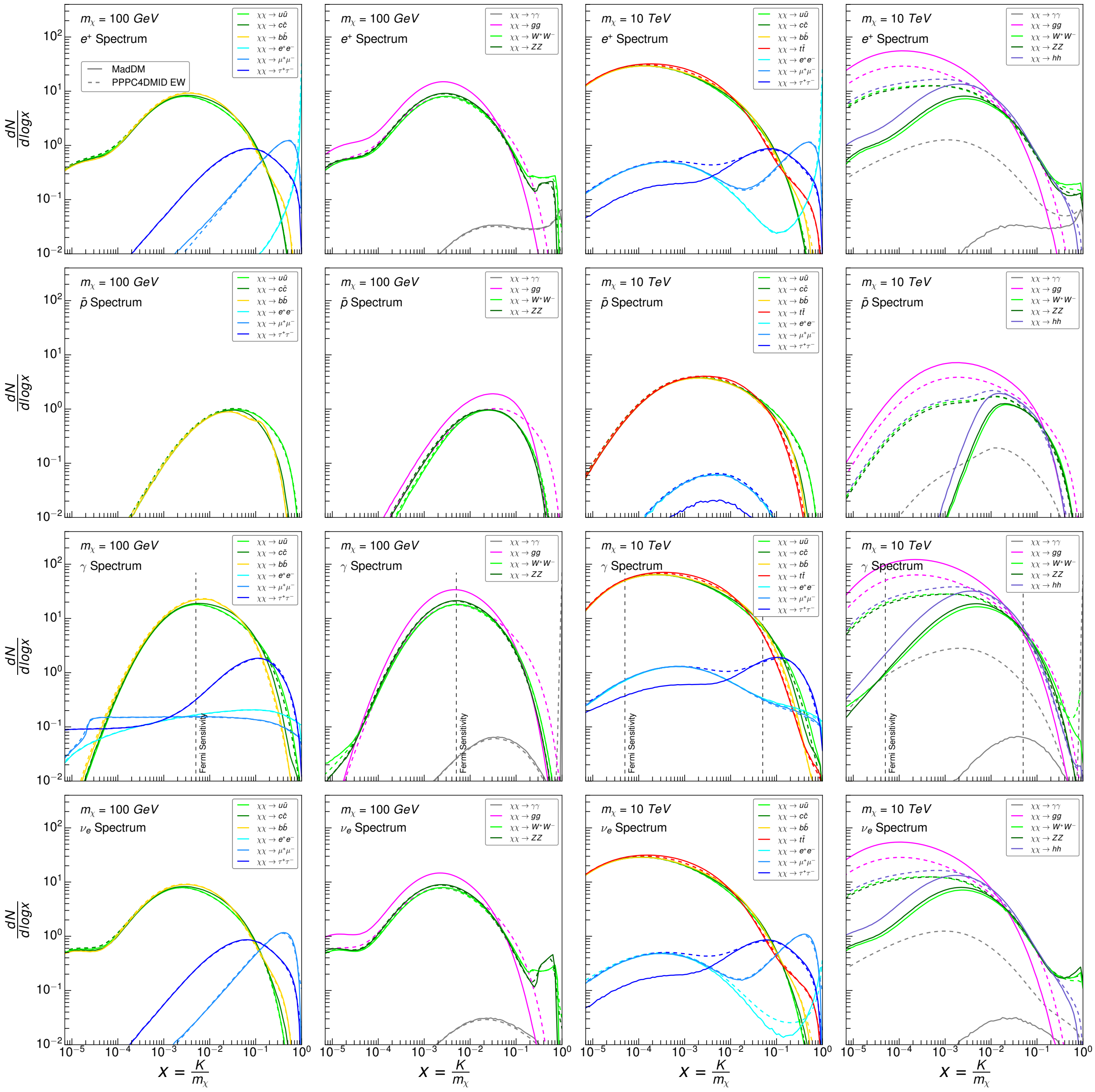

FIGURE 7.7: Same as Fig.7.6 but for spectra produced with `Pythia 8` electroweak showering, for x=E_{kin}/m_χ, for m_χ = (100 GeV, 10 TeV). As expected, the EW corrections show a significant effect only for large m_χ.

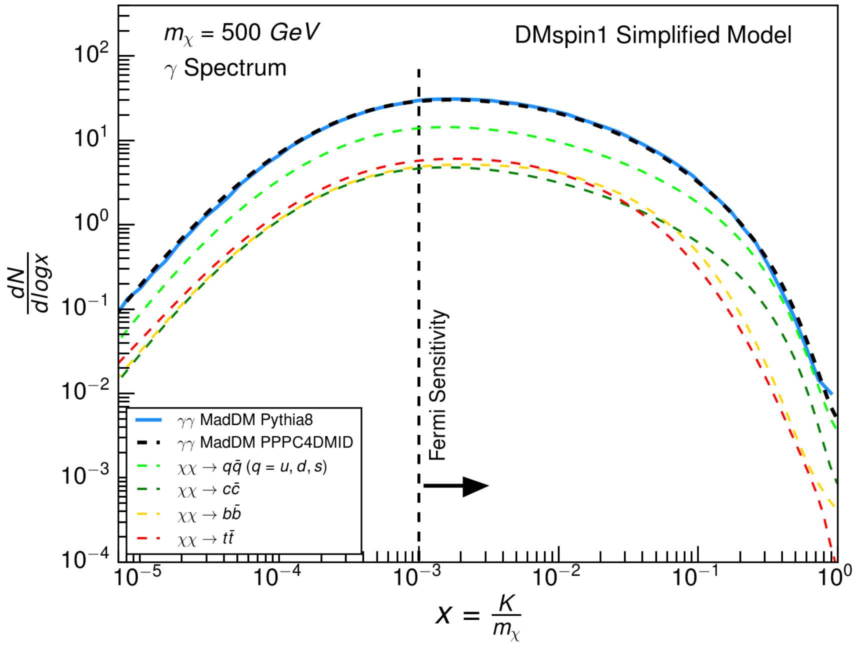

Figure 7.8: Validation of the combination procedure for the γ-ray energy spectra for the different annihilation channel for a spin-1 mediator DM simplified model, for $m_{DM} = 500$ GeV. The Mediator couples democratically to all quark flavours. The coloured dashed lines correspond to the spectra extracted from the PPPC4DMID tables; the black dashed lines is the total spectrum obtained by combining the spectra using eq. 7.14, in agreement with the spectra generated with the ‘precision’ method (solid light blue line).

observation of a few dSphs, which however disappears when combining all the datasets leading to a global significance $< 1\sigma$.

Published limits are interpreted with DM simplified model in the $\chi\chi \to b\bar{b}/\tau^+\tau^-$ channels assuming 100% BR, both for each individual dSph and and for the combined dataset. The likelihood profiles as well as a code template to extract the limits using single dSphs are available at [175]. Specifically the likelihood is given for each of 25 energy bins covering the Fermi-LAT detector sensitivity (between 500 MeV and 500 GeV), for a putative energy flux coming from the observed dSph. The data provided by the collaboration includes also the appropriate J-factors used for the calculation of the predicted DM annihilation γ-ray fluxes, that were taken from [176]. The simplified code distributed with the data was adapted to and implemented in MadDM v.3.0 in a more general framework, that allows also to stack the likelihood profiles of a chosen set of dSphs. Additionally, uncertainties on the J-factors were included by considering J-factors as a nuisance parameter, and subsequently profiling over them. p-values and stacked likelihood for the point tested that can be used for statistical analysis, like e.g. by the module to guide the sampling procedure, are also provided. Finally, the 95% CL upper limit on the thermally averaged annihilation cross section, for a given energy spectrum is computed, and it can be compared against the theory prediction to constrain the model point. If $\langle\sigma v\rangle_{Theo} > \langle\sigma v\rangle_{ul}$, the model tested is considered excluded by the Fermi-LAT experiment.

In Fig. 7.9 the validation of the Fermi-LAT limits implementation is shown: the official experimental results are confronted with the values $\langle\sigma v\rangle$ calculated by MadDM v.3.0 for a selection of dSph. By default, MadDM v.3.0 stacks the likelihood of the six dSphs with the highest J-factors, that provide the best constraints. The set includes Segue I(19.4), Ursa Major II (19.4), Coma Berenices(19.0), Reticulum II(18.9), Draco(18.8) and Ursa Minor(18.8), where the number

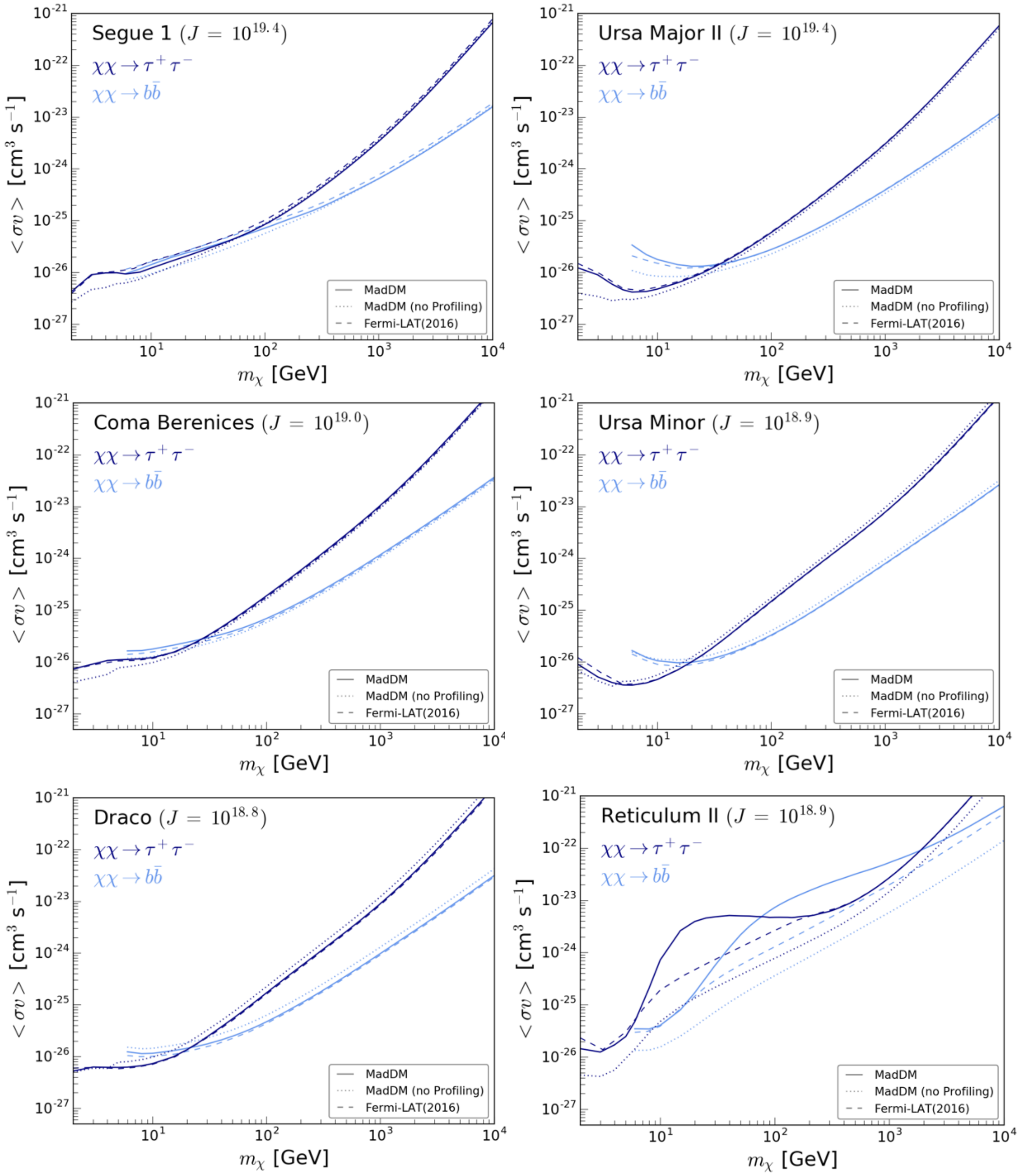

FIGURE 7.9: Validation of the Fermi-LAT $\langle \sigma v \rangle$ cross section in `MadDM v.3.0` for the six dwarf spheroidal galaxies with the highest J-factors for the $b\bar{b}$ and $\tau^+\tau^-$ channels with 100% BR. The dashed line is the official Fermi-LAT limit; the solid and dotted lines represent the `MadDM v.3.0` limits with and without the profiling on the J-factor.

in brackets is the log_{10}(J-factor). It was verified that including the data of the remaining dSphs does not improve significantly the limits, hence they are disregarded to save computing time.

According to the running method, the Fermi-LAT limits are used to constrain the model tested in different ways. The first one makes use of the limits included in the `ExpConstraints` class. For each SM channel listed in 7.3.1.2, the γ-ray spectra were used to compute the Fermi-LAT limits stacking the best six dSphs; the limits were then stored in the `ExpConstraints` class, and are provided to

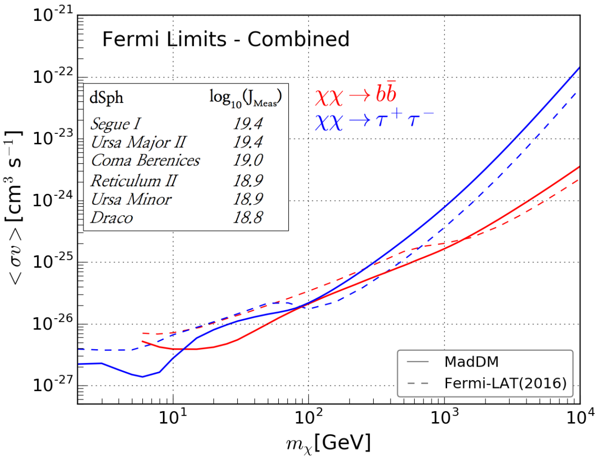

FIGURE 7.10: Validation of the Fermi-LAT $\langle \sigma v \rangle$ cross section in for the six dSphs with the highest J-factors for the $b\bar{b}$ and $\tau^+\tau^-$ channels with 100% BR. The dashed line is the official Fermi-LAT limit; solid and dotted lines represent the `MadDM v.3.0` limits with and without the profiling on the J-factor.

the user in the `MadDM v.3.0` output as will be described in Section 7.4. The limits for the stacked analysis are shown in Figures 7.10, showing the limits for the SM channels $\chi\chi \to b\bar{b}/\tau^+\tau^-$ assuming 100% BR, and 7.11, which shows the limit extracted for the remaining channels not provided by the Fermi collaboration.

The peculiar behaviour of the limits for low DM mass is explained by the presence of the Reticulum II dSphs which exhibits an observed excess in the γ-ray rays counts with a local significance of 2σ, found also in other works e.g.[177, 178]. The distortion in the limit can be see also in Fig. 7.9 where the limits for this individual dwarf are shown. Note that due to the excess of Reticulum II and of three other dSphs used by the Fermi collaboration, the limits in [174] are weaker in the low DM mass region wrt the previous results in [162] by approximately a factor 1.5 in the $b\bar{b}$ and $\tau^+\tau^-$ channel.

In both the ‘fast’ and ‘precision’ methods, the code will compare each separate SM channel theory prediction with the corresponding limits. Furthermore, on-the-flight computation of the $\langle \sigma v \rangle$ is performed using the total γ-ray spectrum from 2-body annihilations into SM channels obtained with equation 7.14 in the ‘fast’ mode, while in the ‘precision’ mode the spectrum obtained with event generation, including the production and decay of any $\chi\chi \to$ n-body is used in input. This last method gives is most accurate computation of the best Fermi-LAT limit. Note that in general, whenever SM channels have dominant theory prediction for $\langle \sigma v \rangle$, it is equivalent to use the limits from the `ExpConstraints` class and to produce them with the ‘precision’ method, since the energy spectra would be equivalent as well as the procedure to calculate the limits. However one needs to remind that the spectra included in the `PPPC4DMID` tables were generated with a large Monte Carlo statistics, so if the ‘precision’ method is run with a small number of events, small differences in the limits computed with the two methods are be expected due to statistical fluctuations. On the opposite, if the annihilation cross section of the model is dominated by BSM particles (then decaying to SM), using the ‘precision’ mode can provide better the upper limits.

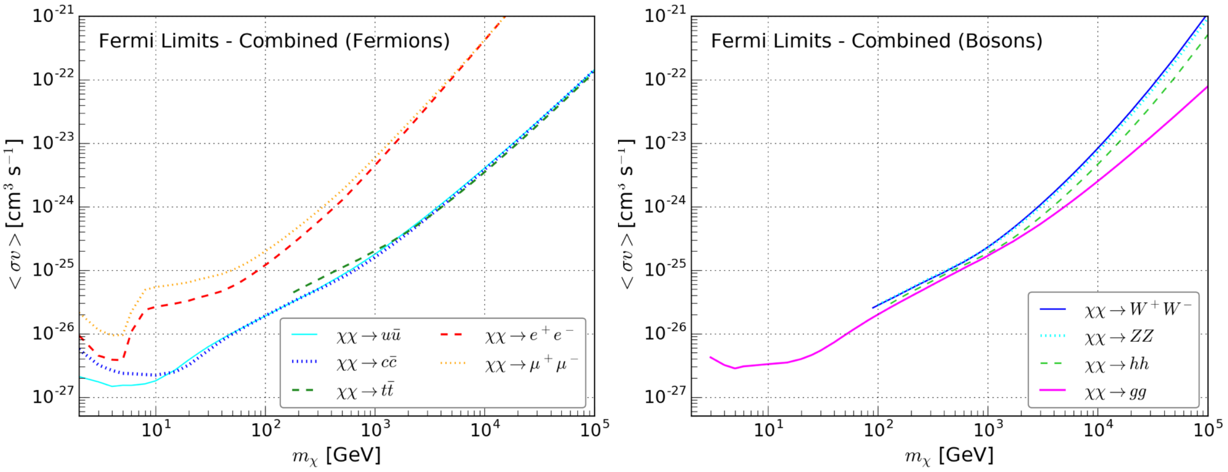

FIGURE 7.11: Exclusion limits for DM simplified models annihilating with 100% BR to Bosons (left) and Fermions (right), obtained with `MadDM v.3.0` , considering the dSphs with the 6 largest J-factors. These limits complements the ones provided for the $b\bar{b}$ and $\tau^+\tau^-$ channels provided by the Fermi-LAT Collaboration.

7.3.1.4 Cosmic Rays Propagation

From equation 7.9 one can easily compute the expected flux of particle at detection, by properly taking into account the astrophysical J-factor, for neutral particles i.e. $\gamma, \nu_e, \nu_\mu, \nu_\tau$. Since experiments for neutrino detection are sensitive to the flavour considered, oscillations must be properly performed in order to guarantee a correct prediction for the flux at Earth to compare with any experimental sensitivity, e.g. for the IceCube telescope. In `MadDM v.3.0` only neutrinos oscillation are evaluated in the long baseline limit, which is a good approximation for neutrinos coming from extragalactic sources. This induces a democratic flavour mixing with equal ratio $\nu_e : \nu_\mu : \nu_\tau = 1 : 1 : 1$ at Earth.

For example for the case of electron neutrinos, the energy spectrum at Earth is given by:

$$\left.\frac{\mathrm{d}N_{\nu_e}}{\mathrm{d}\log x}\right|_{\mathrm{E}} = \frac{\mathrm{d}N_{\nu_e}}{\mathrm{d}\log x}\left[1 - P(\nu_e \to \nu_\mu) - P(\nu_e \to \nu_u)\right] + \frac{\mathrm{d}N_{\nu_\mu}}{\mathrm{d}\log x} P(\nu_e \to \nu_\mu) + \frac{\mathrm{d}N_{\nu_\tau}}{\mathrm{d}\log x} P(\nu_e \to \nu_\tau), \quad (7.15)$$

where $P(\nu_\alpha \to \nu_\beta)$ is the oscillation probability between flavour α and β. These probabilities are given by the 3× 3 unitary matrix

$$U_{\alpha,i} = \begin{pmatrix} 0.82 & 0.55 & 0.15 \\ 0.37 & 0.57 & 0.71 \\ 0.40 & 0.59 & 0.68 \end{pmatrix}, \quad (7.16)$$

and the oscillation probability are:

$$P(\nu_\alpha \to \nu_\beta) = \sum_i \left|U_{\beta i}\right|^2 \left|U_{\alpha i}\right|^2 + \sum_{i<j} 2\Re\left[U_{\beta j}U^*_{\alpha j}U^*_{\beta i}U_{\alpha i}\, \mathrm{e}^{\mathrm{i}(m_j^2 - m_i^2)L/(2E_\nu)}\right]. \quad (7.17)$$

(greek letters refer to flavour indices and latin letters to mass eigenstates). The rightmost term does not contribute in the approximation $L/E_\nu \gg 2\pi$ as it holds for extragalactic sources. Note that the present discussion is valid for vacuum oscillations, so `MadDM v.3.0` predictions should not be used for neutrinos coming from the Sun and traveling through Earth, since all the matter effects are neglected. The results from `MadDM v.3.0` are obtained by first properly oscillating the energy spectrum for each neutrino flavour into the other two, and then summing up the contribution of each flavour. Results are then scaled using the Draco dSph galaxy as normalisation.

The propagation of the charged cosmic rays, i.e. positrons and antiprotons, strongly depends on the astrophysical input to model the Milky Way [3] These include energy loss of the particles due to e.g. synchrotron radiation and inverse Compton scattering on background photons.
`MadDM v.3.0` offers two way of extracting the propagated fluxes of CR at Earth. In the 'fast' method, similarly to what discussed for the energy spectra at source, `PPPC4DMID` tables for positrons available at [170] were converted to a python dictionary implemented in `MadDM v.3.0` . The positron fluxes were obtained again for several DM mass values that will be linearly interpolated to extract the flux for the desired m_χ, as well as several combination of the following three astrophysical parameters:

- **halo profile**: Einasto, Isothermal, NFW, Moore;
- **propagation model**: MIN, MED, MAX;
- **galactic magnetic field**: MF1, MF2, MF3.

On the `PPPC4DMID` website[170] more details regarding how the tables were produced and on the precise values used for the parameters above can be found. Finally, in Fig. 7.12 the positron flux extracted from the tables of selected annihilation channels, for $m_\chi = 1$ TeV are shown, highlighting the differences for two different halo profiles (Einasto and NFW), propagation and magnetic field models.

7.4 Running `MadDM` and Results

After discussing all the most important features of the new version, I show concisely the results of a standard `MadDM v.3.0` session, referring the reader to the official manual for an extended explanation.
By the following commands:

```
import model DMsimp_s_spin0_MD
define darkmatter ~xd
generate relic_density
add direct_detection
add indirect_detection
output test_y0y0_scalar
launch test_y0y0_scalar
indirect=flux_earth
set sigmav_method madevent
set indirect_flux_source pythia8
set nevents 100000
set MXd 200
set MY0 100
```

the user asks for theory predictions for the relic density calculation, direct and indirect detections as well as and limits when available. The model used is a spin-0 mediator simplified model, where the DM candidate is labelled as ' xd'. The mass 'MXd' of the DM candidate and the mass 'MY0' of the mediator are set to 200 and 100 GeV respectively. This run used the 'precision' method, using Madevent for the calculation of the annihilation cross section, followed by `Pythia 8` for the generation of the CR energy spectrum. The results, reported here the versions printed on the screen,

---

[3] Charged CR are confined to be of galactic origin due to the effect of average magnetic field of the Milky Way, of the order of few to tens of micro Gauss.

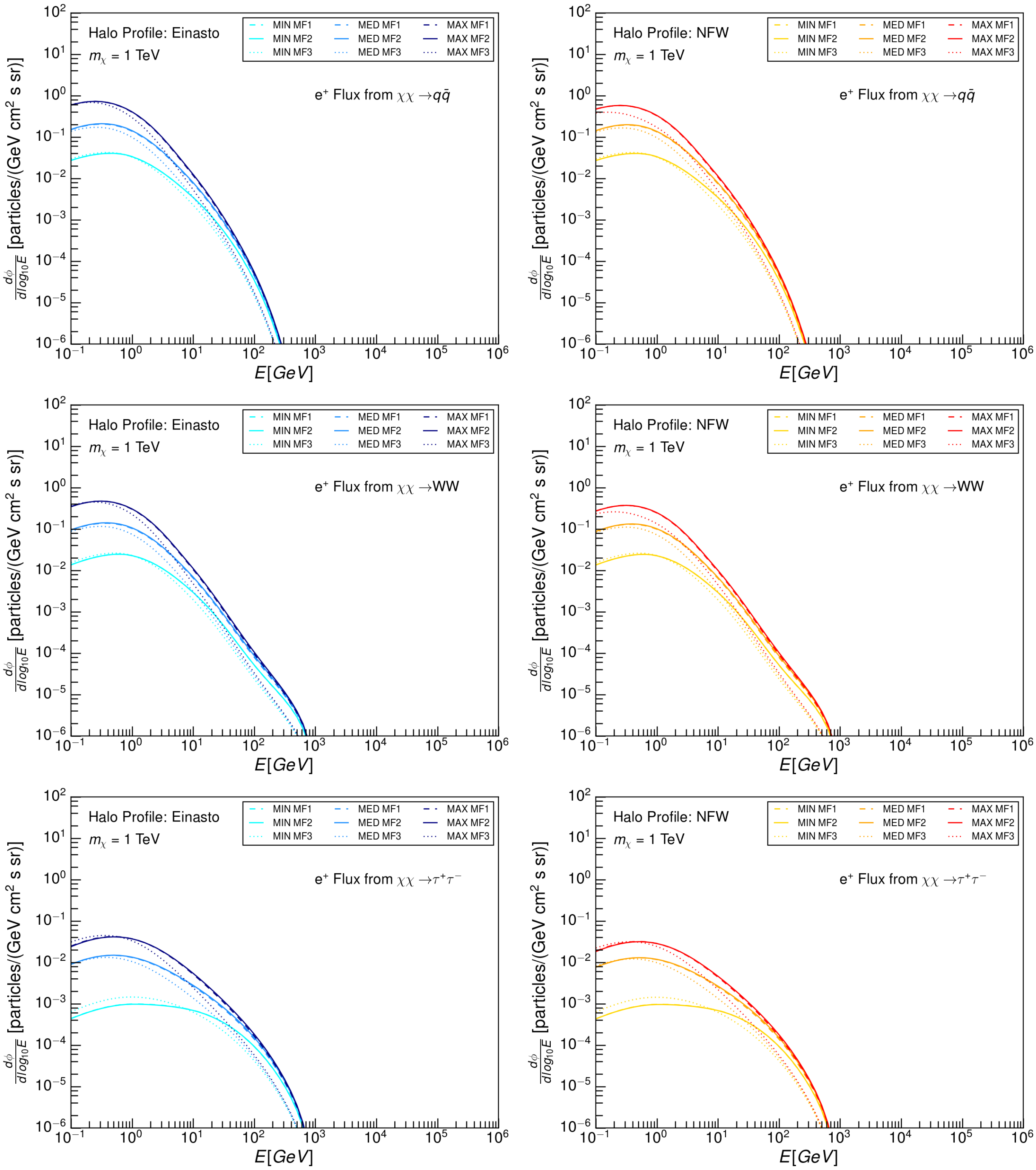

FIGURE 7.12: Positron fluxes, extracted from the `PPPC4DMID` tables, for the $\chi\chi \rightarrow q\bar{q}/\tau^+\tau^-/WW$ where $q = (u, d, s)$ annihilation channels for the Einasto halo profile (left column) and Navarro-Frenk-White (right column), and a DM candidate of 1 TeV mass. The different shade colours represent the different propagation models, while the solid, dashed and dotted lines show the different magnetic field model.

are shown in Fig.res:relic,7.14 and 7.15 for the relic, direct and indirect detection respectively.

The relic density block 7.13 shows the value of the calculated relic density Ωh^2 , the value $x = m_\chi/T$ at freeze-out (see Section 7.2), the annihilation cross section calculated at freeze-out $\langle\sigma v\rangle(xf)$ [GeV^2], and the ratio $\xi = (\Omega h^2)_{\text{theo}}/(\Omega h^2)_{\text{Planck}}$.

The ξ parameter is important when considering models which leads to under-abundant DM wrt the Planck observed value. According to the value predicted for the model tested, there are two possible distinct scenarios, labelled 'thermal' and 'all DM'. For the former, the value of ξ is equivalent to the definition above; for the latter, `MadDM v.3.0` sets $\xi = 1$. The value of ξ is used to rescale the theory predictions to be compared with the experimental upper limits in the following ways:

- **'All DM'** - the DM candidate of the tested model is considered to be the only existing form of DM making up all of the relic density as measured by Planck, irrespectively of the value calculated by `MadDM` . The value of the local DM density, that enters the calculation of detection rates and fluxes, is by construction the one measured by Planck, so the 'All DM' theory predictions need no rescaling for the comparison with the upper limits;

- **'Thermal'** - the DM candidate is the responsible of the relic density after 'the thermal freeze-out' in a standard cosmological model. This implies that if the relic density evaluated is less than the Planck measured value (0.1197, see equation 7.5), other DM species must also be present and contribute to the total relic density. Accordingly, the theory prediction for the direct and indirect detection must be rescaled by a factor ξ and ξ^2 respectively, where by definition $\xi < 1$.

The specific model point tested here leads to under-abundant relic density $\Omega h^2_{Th.} = 0.0193$ for which $\xi = 0.161$; hence, when presenting the results for direct and indirect detections, the two predictions for the scenarios 'All DM' and 'Thermal' will be shown. Whenever available, `MadDM v.3.0` conveniently reports the values of the experiment limits or measurements, printing on screen if the model is allowed, excluded or such the comparison cannot be performed. In this case, the model is allowed wrt the relic density, since it does not exceed Planck measured value.

The block 7.14 is relative to the results for direct detection; it reports the scattering cross sections for spin-independent and spin-dependent (for protons and neutrons), as well as the experimental upper limits from the XENON1T, Pico60 and LUX experiments. Accordingly, each theory prediction is compared with the limits, and if $\sigma_{Theo} > \sigma_{ul}(\sigma_{Theo} \leq \sigma_{ul})$, a point is considered excluded(allowed). Since both the theory values and upper limits are provided, the user has all the needed information to determine if the model should be considered excluded, and eventually perform his own statistical analysis.

Finally, block 7.15 summarises the cross section annihilations and Fermi-LAT limits. Since the 'precision' running mode was selected, also BSM 2-body channels are available, in this case $\chi\chi \rightarrow y0y0$ which has indeed the largest annihilation cross section $\sigma(\chi\chi \rightarrow y0y0 = 7.91 \times 10^{-35}$ cm^3 /s , followed by the $t\bar{t}$ channel $\sigma(\chi\chi \rightarrow t\bar{t} = 4.94 \times 10^{-36}$ cm^3 /s . For SM channels, Fermi-LAT limits are reported, since they are included in the `ExpConstraint` class. For the BSM channel this information

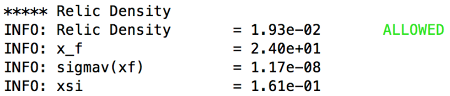

```
***** Relic Density
INFO: Relic Density          = 1.93e-02        ALLOWED
INFO: x_f                    = 2.40e+01
INFO: sigmav(xf)             = 1.17e-08
INFO: xsi                    = 1.61e-01
```

FIGURE 7.13: Results for the relic density computation.

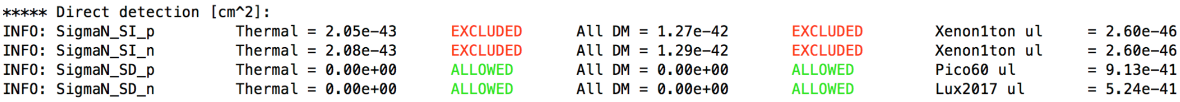

```
***** Direct detection [cm^2]:
INFO: SigmaN_SI_p        Thermal = 2.05e-43      EXCLUDED        All DM = 1.27e-42       EXCLUDED        Xenon1ton ul        = 2.60e-46
INFO: SigmaN_SI_n        Thermal = 2.08e-43      EXCLUDED        All DM = 1.29e-42       EXCLUDED        Xenon1ton ul        = 2.60e-46
INFO: SigmaN_SD_p        Thermal = 0.00e+00      ALLOWED         All DM = 0.00e+00       ALLOWED         Pico60 ul           = 9.13e-41
INFO: SigmaN_SD_n        Thermal = 0.00e+00      ALLOWED         All DM = 0.00e+00       ALLOWED         Lux2017 ul          = 5.24e-41
```

FIGURE 7.14: Results for the direct detection computation.

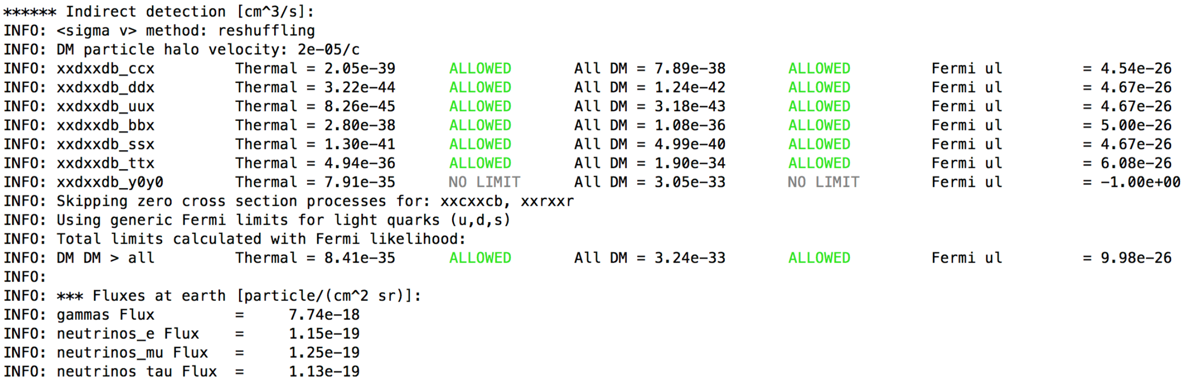

```
****** Indirect detection [cm^3/s]:
INFO: <sigma v> method: reshuffling
INFO: DM particle halo velocity: 2e-05/c
INFO: xxdxxdb_ccx         Thermal = 2.05e-39      ALLOWED       All DM = 7.89e-38       ALLOWED         Fermi ul         = 4.54e-26
INFO: xxdxxdb_ddx         Thermal = 3.22e-44      ALLOWED       All DM = 1.24e-42       ALLOWED         Fermi ul         = 4.67e-26
INFO: xxdxxdb_uux         Thermal = 8.26e-45      ALLOWED       All DM = 3.18e-43       ALLOWED         Fermi ul         = 4.67e-26
INFO: xxdxxdb_bbx         Thermal = 2.80e-38      ALLOWED       All DM = 1.08e-36       ALLOWED         Fermi ul         = 5.00e-26
INFO: xxdxxdb_ssx         Thermal = 1.30e-41      ALLOWED       All DM = 4.99e-40       ALLOWED         Fermi ul         = 4.67e-26
INFO: xxdxxdb_ttx         Thermal = 4.94e-36      ALLOWED       All DM = 1.90e-34       ALLOWED         Fermi ul         = 6.08e-26
INFO: xxdxxdb_y0y0        Thermal = 7.91e-35      NO LIMIT      All DM = 3.05e-33       NO LIMIT        Fermi ul         = -1.00e+00
INFO: Skipping zero cross section processes for: xxcxxcb, xxrxxr
INFO: Using generic Fermi limits for light quarks (u,d,s)
INFO: Total limits calculated with Fermi likelihood:
INFO: DM DM > all         Thermal = 8.41e-35      ALLOWED       All DM = 3.24e-33       ALLOWED         Fermi ul         = 9.98e-26
INFO:
INFO: *** Fluxes at earth [particle/(cm^2 sr)]:
INFO: gammas Flux         =     7.74e-18
INFO: neutrinos_e Flux    =     1.15e-19
INFO: neutrinos_mu Flux   =     1.25e-19
INFO: neutrinos tau Flux  =     1.13e-19
```

FIGURE 7.15: Results for the indirect detection computation.

is not available, as suggested by the 'no limit' message. The Fermi-LAT limit obtained by considering the global γ-ray spectrum from SM and BSM particle is 9.98×10^{-26}, which improves the best SM limits coming from $t\bar{t}$ annihilation. Finally the total integrated flux at detection of the neutral components of CRs is provided. The values are calculated using the Draco dSph J-factor, so if the user is interested in other dwarfs, a rescaling by the ratio of the two J-factors should be performed.

As an important remark, I remind that this is the output printed on screen of a single run with `MadDM` ,that gives the user a friendly and easy way to perform simple and quick checks on his/her DM model, and not for intensive scans. When the single-point running mode is used, all the intermediate files are stored in the `output` directory inside the user's project folder (in the case above, called *test_ y0y0_ scalar'*); these include the `maddm_card.dat` which includes all the switches regarding the parameters available for the user, the LHE file produced by `MG5_aMC` , the spectra at source for all the six species of CRs produced by `Pythia 8` , and the differential fluxes in bins of energies at Earth for the neutral CRs . If `DRAGON` is run (only if the user choose a DM halo velocity 10^{-3} compatible with the Milky Way center, the propagated spectra for antiprotons and positrons will be found inside the default `DRAGON` directory. When the `PPPC4DMID` method is chosen either for spectra at source or for propagated positrons, the spectra and fluxes extracted from the tables are as well written inside the *output* directory.

Summary

To conclude this concise presentation of `MadDM v.3.0`, I summarise here the most important features of the new version as well as the philosophy that was assumed in implementing the new functionalities.

Overall, `MadDM v.3.0` fits in the category of tools that try to make the most out of the numerous and varied experimental results for DM searches. One of the unique features is that it directly inherits all the abilities of the `MG5_aMC` platform for the generation of Monte Carlo events, for example needed for the generation of the energy spectra of the CR for indirect detection and the calculation of annihilation cross sections for completely generic processes. This can be done 'out-of-the-box' for any model implemented according to the `UFO` format.
Noticeable is the level of accuracy provided by the 'reshuffling' method for the computation of the $\langle\sigma v\rangle$, which makes `MadDM v.3.0` the only tool on the market able to perform such a precise calculation.

The other key aspect is the usability of the code, not only regarding the easiness of usage, but also its flexibility. In particular the available 'fast' and 'precision' methods were intended to suit the needs of the user for great speed e.g. when performing scan of large portion of a model parameter space (but with reasonable accuracy), or great level of accuracy. Details of the output in scan mode are given in Appendix I.

The whole new module for the indirect detection represents the major new feature of `v.3.0`. While there exist other tools that allow to compute the rate for the detection or the energy spectra (e.g. microMEGAs[179]), `MadDM v.3.0` provides the direct comparison of the theory predictions with the latest experimental constraints. This is a step forward to make `MadDM` a comprehensive tool for the phenomenology of generic DM models.

Chapter 8

Conclusions

All the tools described this thesis work are connected together by one simple motivation: building an interface between the world of theory and the world of experiment. `SModelS`, `MadAnalysis 5` and `MadDM v.3.0` represent not only examples of what is already available and already being used for phenomenological study of BSM theories, but they are also representative of different approaches to handle the complexity of the theories tested and the limitation imposed by available computing resources.

The first possible way, employing the full chain of Monte Carlo sample generations, detector simulations and analyses recasting is lengthy yet very powerful, since it can be applied to any generic BSM theory. As an example, I described the implementation of the CMS-SUS-16-033 search for SUSY events in the `MadAnalysis 5` package. The importance of the validating the implementation, which is a complicated process that sometimes leads to unsatisfactory results, was particularly highlighted. The extension of the `MadAnalysis 5` physics analyses database is crucial to grant a proper coverage of the many signatures of BSM theories. In particular the CMS analysis implemented was the first searching for SUSY in the all-hadronic final state at 13 TeV centre-of-mass energy, using the available total integrated luminosity of 35.9 fb^{-1}.

On the other side, we have the simplified model framework, used for example for the interpretation of searches for SUSY at the LHC, or for the searches for excesses in the CR fluxes from DM annihilation into SM channels. Also searches for production of DM at the LHC use a special class of simplified models for the interpretations of results, introducing the masses of the DM candidate and of the particles that mediate the interaction between the SM and DM as free parameters, as well as the values of the coupling constants. Simplified model results for SUSY searches can be used systematically by `SModelS` and `MadDM` to constrain generic theories. Although the needed computing times sensibly decreases as compared to the full recast approach, there are uncertainties introduced by this simplified approach. In this thesis, two main aspects were analysed in detail. The first regards how well simplified models are able to reproduce the results obtained with a full recast, studied in the context of the pMSSM. The second concerns how much the interpolation procedure can be trusted, in particular depending on the design of the specific analysis and simplified model used for the interpretation. This work then offers an additional evidence of how useful and valid the simplified model approach is.

In this respect, the `MadDM` tools lies exactly in between the two philosophies. With the DM indirect detection module recently introduced, it offers the user the possibility of either calculating accurate theory predictions by producing Monte Carlo events and calculate precise upper limits using Fermi-LAT likelihoods, or reading the limits from a database of available annihilation channels. In this respect, a lot of the effort was dedicated to develop a friendly and understandable interface, both at run time and at the time of the analysis of the output.

I mention here other two approaches used to constrain BSM theories, used by e.g. Gambit[180] and ScyNet[181]. The Gambit tool is a so called "global fits package", which makes use of an extensive number of measurements from several types of experiments (previous colliders like the Large Electron-Positron at CERN, the LHC Run 1 and Run 2, direct detection, indirect detection etc.) to extract the global likelihood for the regions of the parameter space of various testable theories. ScyNet instead makes use of machine learning techniques to extract likelihoods in the context of a subset of the MSSM; in case of more general models the network is trained on model independent signatures and observables such as the jet multiplicity, momenta of particles and missing energy.

Appendix A

Txnames Description

List of simplified models mapped to the `SModelS` constraints, relevant for this work, with the corresponding Txname. The complete list, together with the analysis using the specified model for the interpretation of results, can be found at `http://smodels.hephy.at/wiki/SmsDictionary`.

Gluino Simplified Models T1xx , T5xx

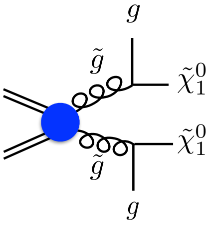

T2gg: [[['jet']],[['jet']]]

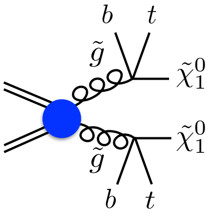

T1btbt:[[['b','t']],[['b','t']]]

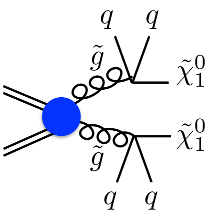

T1:[[['jet','jet']],[['jet','jet']]]

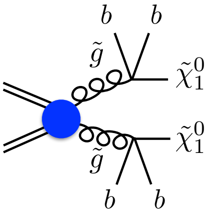

T1bbbb:[[['b','b']],[['b','b']]]

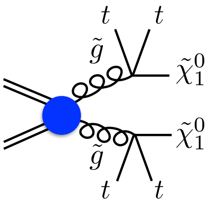

T1tttt:[[['t','t']],[['t','t']]]

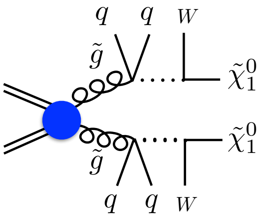

T5WW:[[['jet','jet']],['W']],[['jet','jet']],['W']]]

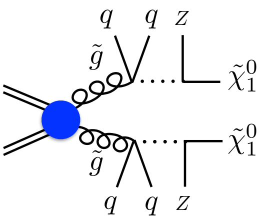

T5ZZ:[[['jet','jet']],['Z']],[['jet','jet']],['Z']]]

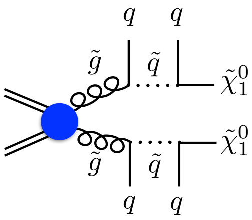

T5:[[['jet']],['jet']],[['jet']],['jet']]]

Squarks Simplified Models T2xx , T6xx

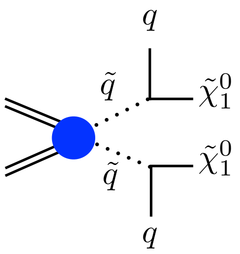

T2qq: [[[‘jet’]],[[‘jet’]]]

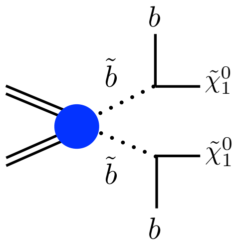

T2bb: [[[‘b’]],[[‘b’]]]

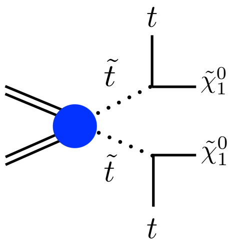

T2tt: [[[‘t’]],[[‘t’]]]

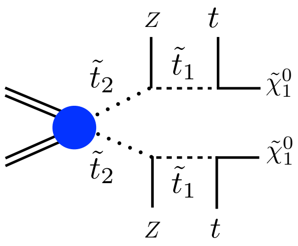

T6ZZtt: [[[‘Z’,’t’]],[[‘Z’,’t’]]]

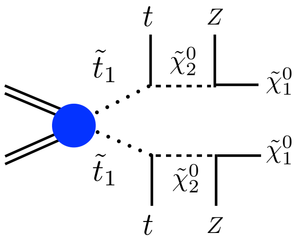

T6ttZZ: [[[‘t’,‘Z’]],[[‘t’,‘Z’]]]

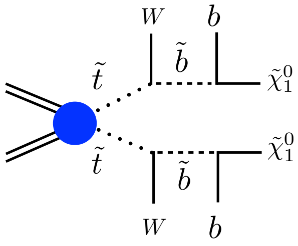

T6WWbb: [[[‘W’,’b’]],[[‘W’,’b’]]]

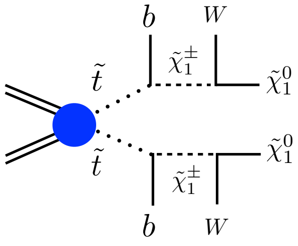

T6bbWW: [[[‘b’,’W’]],[[‘b’,’W’]]]

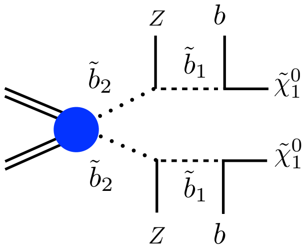

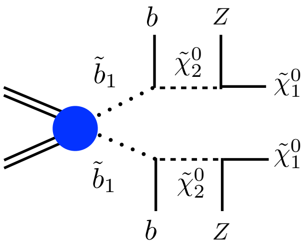

T6ZZbb: [[[‘Z’,‘b’]],[[‘Z’,‘b’]]] T6bbZZ: [[[‘b’,‘Z’]],[[‘b’,‘Z’]]]

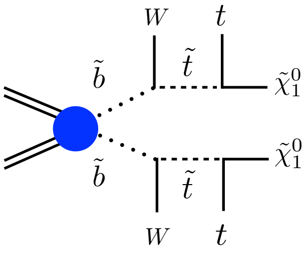

T6WWtt: [[[‘W’,‘t’]],[[‘W’,‘t’]]]

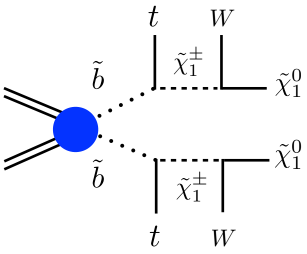

T6ttWW: [[[‘t’,’W’]],[[‘t’,’W’]]]

Gluino-Squark T3GQ

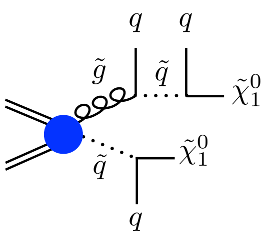

T3GQon: [[[‘jet’]],[‘jet’]], [[‘jet’]]]

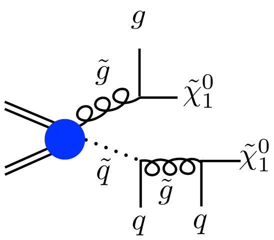

T3GonQ: [[[‘jet’]],[[‘jet’], [‘jet’]]]

Gauginos and Slepton Simplified Models

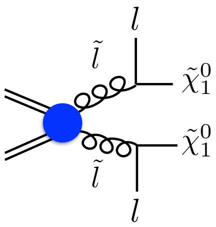

TSlepSlep: [[[‘l’]],[[‘l’]]] (l=e,μ)

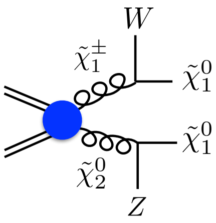

TChiWZ: [[[‘W’]],[[‘Z’]]]

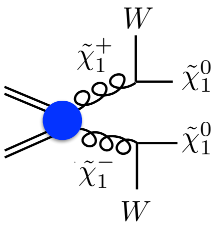

TChiWW: [[[‘W’]],[[‘W’]]]

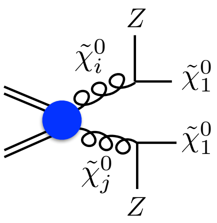

TChiZZ: [[[‘Z’]],[[‘Z’]]]

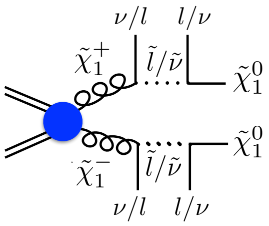

TChipChimSlepSnu:[[[‘l/v’]],[‘v/l’]],[[‘l/v’]],[‘v/l’]]]

Appendix B

Testing a Point with SModelS

Here a `SModelS` run example is presented, providing details regarding instructions, a brief description of the most important input parameters, and a quick look at the output. As a test point, the SLHA file *100559821* from the Bino-like LSP set from the ATLAS pMSSM study (see Chapter5) is considered. The complete reference and documentation can be found in [83],[2] and in the online manual [182].

The python script *runSModelS.py* provides a series of utilities to check the input file, to run the decomposition and to write the output in a few possible formats. The file `parameters.ini` allows to choose most of the relevant input parameters, such as the `sigmacut` allowing only elements with weight above a certain threshold, or the possibility of (de)activating the invisible and mass compressions. In v1.1 the following new functionalities were introduced: the possibility of processing an entire directory of SLHA or LHE files, and of parallelising the run using a desired number of CPUs.

`SModelS` can be conveniently used by running:

```
runSModelS.py [-h] -f FILENAME [-p PARAMETERFILE] [-o OUTPUTDIR] [-v VERBOSE] [-T TIMEOUT]
```

where:

- FILENAME is the name of the file (SLHA or LHE) or the directory containing the file(s);
- PARAMETERFILE is the `parameters.ini` file containing the relevant parameters;
- OUTPUTDIR is the name of the directory that will be created containing the results;
- VERBOSE sets the desired level of screen output;
- TIMEOUT sets the maximum time allowed for the decomposition, after which the point is skipped.

As a concrete example, by running the command:

```
python runSModelS.py -p parameters.ini -f 100559821.slha
```

`SModelS` will read the configuration specified in the `parameters.ini` file, and test the selected SLHA file. In particular, the options:

```
#Select running mode
[options]
checkInput = True ;Set True to check the input file for possible errors
doInvisible = True ;Set True if invisible compression should be performed
doCompress = True ; Set True if mass compression should be performed
testCoverage = True ;Set True if topologies not covered by experiments (missing topologies) ...
#Select input parameters
[parameters]
```

```
sigmacut = 0.03 ;Give minimum cross section value [fb] considered in SLHA decomposition
minmassgap = 5.
[printer]
outputType = summary,stdout,python ;
[python-printer]
addTxWeights = True ;
```

will activate the module for the the missing topologies, and will write the results in a text file(*summary*), on the screen (*stdout*), and in a python file in the form of a dictionary (*python*). The other selected parameters will activate both the invisible and mass compression, performed when the mass gap between two Z_2-odd states is below 5 GeV (see Section4.2.1). Elements with weight below 0.03 fb will not be considered.
Focusing on the text output *100559821.slha.smodels*, the top block

```
Input status: 1
Decomposition output status: 1 #decomposition was successful
# Input File: 100559821.slha
# maxcond = 0.2
# minmassgap = 5.
# ncpus = 6
# sigmacut = 0.03
# Database version: xxx
```

provides the basic information about the run. The *Decomposition output status: 1* states that the point was successfully decomposed and that the point can be constrained by at least one of the results in the database[1] Since the decomposition was successful, it was possible to constrain the elements with the results implemented in the database. An extract of the complete results list is the following:

```
================================================================================
#Analysis  Sqrts  Cond_Violation  Theory_Value(fb)  Exp_limit(fb)  r  r_expected

 ATLAS-SUSY-2013-02  8.00E+00    0.0  2.231E+00  1.818E+00  1.227E+00  1.475E+00
 Signal Region:  SR2jt
 Txnames:  T1, T2, T3GQon, T5
--------------------------------------------------------------------------------
     CMS-SUS-13-019  8.00E+00    0.0  2.497E+00  3.244E+00  7.697E-01  N/A
 Signal Region:  (UL)
 Txnames:  T2
--------------------------------------------------------------------------------
     CMS-SUS-13-012  8.00E+00    0.0  6.121E-01  1.210E+00  5.059E-01  8.239E-01
 Signal Region:  3NJet6_1000HT1250_600MHTinf
 Txnames:  T2, T2bb, T3GQon, T5
 --------------------------------------------------------------------------------
 [ ... ]
================================================================================
The highest r value is = 1.22736896744

Total missing topology cross section (fb):  7.727E+01
Total cross section where we are outside the mass grid (fb):  6.081E+00
Total cross section in long cascade decays (fb):  2.297E+01
```

---

[1] Other possible values of the *Decomposition output status* :

- -1: "could not run the decomposition",
- -3: "no cross sections above sigmacut found",
- -4: "database not found",
- -2: "bad input file, did not run decomposition",
- 0: "no matching experimental results",

```
Total cross section in decays with asymmetric branches (fb):  5.421E+01

Full information on unconstrained cross sections
================================================================================
Missing topologies with the highest cross sections (up to 10):
Sqrts (TeV)   Weight (fb)       Element description
  8.0  1.756E+01    #                            [[],[[jet,jet]]]
  [ ... ]
================================================================================
Contributions outside the mass grid (up to 10):
Sqrts (TeV)   Weight (fb)       Element description
  8.0  3.946E+00    #                     [[[jet]],[[jet],[jet]]]
  [ ... ]
================================================================================
Missing topos: long cascade decays (up to 10 entries), sqrts = 8 TeV:
Mother1 Mother2 Weight (fb) # allMothers
2000001 2000002  7.588E+00 # [[2000001, 2000002]]
[ ... ]
================================================================================
Missing topos: asymmetric branches (w/o long cascades, up to 10), sqrts = 8 TeV
Mother1 Mother2 Weight (fb) # allMothers
1000022 1000024  1.665E+01 # [[1000022, 1000024]]
[ ... ]
```

The file reports the full set of experimental results that provide constraints for the elements in the decomposition, starting with the most constraining (highest r-value). The result shows the name of the analysis with its centre-of-mass. Only the three most constraining results are shown for brevity. The most constraining result is provided by the combination of the EMs for the list of Txnames *T1+T2+T5+T3GQon* of the ATLAS-SUSY-2013-02 analysis, being the only result providing an observed r-value=1.2 $>$ 1. The output shows also the expected and observed upper limits for the best signal region SR2jt, and the value of the theory prediction (or total $w = \sigma \times BR$). The UL from the analysis CMS-SUS-13-019 delivers the second best limit; the expected limit is not available from the CMS collaboration, and being an UL result, no SR is defined. UL for different simplified models cannot be combined together, so for UL results the list of Txnames include only one model at a time.

The following block gives details about the unconstrained signal. We see that the total missing cross section (77.2 fb) is further classified according to the contributions of elements with long cascade decay (22.9 fb or 28.5 % to the total) and asymmetric topologies (54.2 fb or 71.5 %). This is in agreement with what is discussed in Section5 regarding the importance of asymmetric branches versus long cascade decays, which are however relevant for this model but sub-dominant. The missing topology with the highest weight is identified as the constraint [[[]],[jet,jet]]]. The origin of this element can be understood by looking at the last column, which reports the *pdgid* numbers of the mother particles of the two asymmetric branches, following the convention of Monte Carlo generators. In this case, we identify a $(\tilde{\chi}_1^0, \tilde{\chi}_1^\pm)$ production, with the chargino being Higgsino-like as can be see in the SLHA.

Finally, the 100559821.slha.py file contains additional information, such as the weight $w = \sigma \times BR$ of each Txname constrained by a specific experimental analysis. For the analysis excluding the point, the python dictionary reads:

```
'AnalysisSqrts (TeV)': 8.0,
'dataType': 'efficiencyMap',
'Mass (GeV)': None,
'maxcond': 0.0,
```

```
‘expected upper limit (fb)’: 1.5124,
‘upper limit (fb)’: 1.8181,
‘AnalysisID’: ‘ATLAS-SUSY-2013-02’,
‘efficiency’: 0.26221876406964295,
‘theory prediction (fb)’: 2.231479519695691,
‘lumi (fb-1)’: 20.3,
‘TxNames’: [‘T1’, ‘T2’, ‘T3GQon’, ‘T5’],
‘DataSetID’: ’SR2jt’}
{‘TxNames weights (fb)’:  {‘T5’: 0.13403074173565857,
                           ‘T2’: 1.3560891401672666,
                           ‘T3GQon’: 0.7400910147773285,
                           ‘T1’: 0.0012686230154375165},
```

While the key *theory prediction (fb)* provides the value of the total prediction, the contribution of each individual topology can be retrieved from the *TxNames weights (fb)* list. The observed r-value can be calculated by dividing the total prediction by the observed UL, and similarly the r-value of each single topology by considering only its proper weight. One can recognize that this point can be excluded only exclusively thanks to the combination of the *T2+T3GQon* results, since the sum of any other combination is below unity.

Appendix C

Inclusive SUSY Searches

Here the main properties of the inclusive searches for SUSY, ATLAS-SUSY-2013-02[91] and CMS-SUS-13-012[49] used for the EMs recast are discussed. Both analyses used data of proton proton collisions at $\sqrt{s} = 8$ TeV (LHC Run1), and target possible SUSY events exhibiting large jets multiplicity, large missing transverse energy and no isolated leptons.

CMS-SUS-13-012

This search looks for events with no isolated leptons, high hadronic activity and large missing energy $\not{E}_T$. The data used adds up to 19.5 fb^{-1} integrated luminosity. Its strength lies in the combination of 36 signal regions, divided into bins of:

- jets multiplicity n_{jets} where the intervals $3 \leq n_{jets} \leq 5$, $6 \leq n_{jets} \leq 7$ and $n_{jets} \geq 8$ are used;
- the hadronic transverse energy H_T defined as the scalar sum sum of the signal jets;
- missing hadronic transverse energy $\not{H}_T$, defined as the vectorial sum of thep_T of the signal jets.

The signal jets used to evaluate H_T must satisfy the requirements p_T>20 GeV and η<2.5, while for the $\not{H}_T$ the criteria are p_T>30 GeV and the more relaxed η<5. The final limit computation is performed by combination of the 36 signal regions considering the proper statistical correlation, the analysis is able to set upper limits on the production cross sections of several SUSY scenarios. The lowest signal jet multiplicity required is $n_{jets} = 3$.

ATLAS-SUSY-2013-02

This analyses supersedes the preliminary results of ATLAS-CONF-2013-047 introduced in 5.3.4. The dataset used for the analysis adds up to a total integrated luminosity of 20.3 fb^{-1}. The signal jets must satisfy p_T >20 GeV and $| < |4.5$. The two main kinematic variables used to discriminate interesting events form the SM backgrounds are the effective mass m_{eff}:

$$m_{eff} = \sum_j |\mathbf{p_T}^j| + |\not{E}_T^{miss}| \tag{C.1}$$

and the scalar hadronic transverse energy H_T, scalar sum of the transverse momenta of jets if p_T >40 GeV.

The analysis defines a total of 15 inclusive signal regions, with increasing minimum jet-multiplicity requirement (2 to 6). Depending on the requirement on jets, SRs are labelled as very loose, 'lose', 'medium', 'tight' and very tight. This is the main difference in the strategy wrt the CMS analysis described above. Events with isolated leptons or muons are discarded if p_T>10 GeV.

The rejection of the QCD background is obtained by requiring that either $E_T^{miss}/\sqrt{H_T}$ or E_T^{miss}/m_{eff} exceed a certain threshold, different in each SR. In particular the hadronic transverse energy H_T is more effective in background discrimination for low multiplicity events. varying requirement are set also on the p_T of the leading n-th jet (according to the minimum number of jets in each SR), and on the azimuthal angular separation between the jet p_T and the missing energy energy $\Delta\phi(p_T, E_T^{miss})$.

Finally, dedicated signal regions reconstructing possible W bosons candidates are defined, useful to increase the sensitivity for model of gluinos and squarks decaying to intermediate charginos (the implementation of such complicated algorithm was not possible in `MadAnalysis 5` , and the corresponding recasting code does not include those regions).

Appendix D

Complete List of UL Results

The following Tables summarise the exclusion provided by the official UL results from the ATLAS and CMS collaborations, using v.1.1 of the `SModelS` database that includes all the available results from the LHC Run1.

The *T2* model gives overall the most constraining and powerful simplified model results contained in the database, for both the Bino and Higgsino-like LSP scenarios. In particular, out of a total of 16957 and 25024 Bino and Higgsino-like LSP points excluded by UL results (Tab.5.2), the CMS analysis can exclude 9979(58%) and 17799(71%) points using the *T2* result alone.

For the Bino-like LSP, the second most important model is represented by the *T1* model, whereas for the Higgsino case the *T1bbbb* becomes more important.

Bino-like LSP

Analysis	**T1**	**T1bbbb**	**T1tttt**	**T1tttoff**	**T2**	**T2bb**	**T2tt**	**T2ttoff**	**T2bbWWoff**	**TGQ**	**T5tctc**	**T5WW**	**T5WWoff**	**T6ZZtt**	**T6bbWW**	**T6bbWWoff**	**T6WW**	**TChiWZ**	**TChiWH**	**TChiWW**	**TSlepSlep**	**TChiChipmStauL**	**TChipChimStauSnu**	**TChiChipmSlepL**	**TChiChipmStauL**	**TChipChimSlepSnu**
ATLAS-SUSY-2013-02	3525	-	-	-	9955	-	-	-	-	0	4	3	14	-	-	-	14	-	-	-	-	-	-	-	-	-
ATLAS-SUSY-2013-04	-	-	3	-	-	-	-	-	-	-	-	-	-	-	-	-	-	-	-	-	-	-	-	-	-	-
ATLAS-SUSY-2013-05	-	-	-	-	-	488	-	-	-	-	-	-	-	-	0	2	-	-	-	-	-	-	-	-	-	-
ATLAS-SUSY-2013-08	-	-	-	-	-	-	-	-	-	-	-	-	-	0	-	-	-	-	-	-	-	-	-	-	-	-
ATLAS-SUSY-2013-09	-	-	3	-	-	-	-	-	-	-	-	-	-	-	-	-	-	-	-	-	-	-	-	-	-	-
ATLAS-SUSY-2013-11	-	-	-	-	-	-	-	-	-	-	-	-	-	-	-	-	-	0	-	0	282	-	-	-	-	0
ATLAS-SUSY-2013-12	-	-	-	-	-	-	-	-	-	-	-	-	-	-	-	-	-	21	0	-	-	0	-	1	0	-
ATLAS-SUSY-2013-14	-	-	-	-	-	-	-	-	-	-	-	-	-	-	-	-	-	-	-	-	-	0	0	-	0	-
ATLAS-SUSY-2013-15	-	-	-	-	-	-	32	0	-	-	-	-	-	-	0	0	-	-	-	-	-	-	-	-	-	-
ATLAS-SUSY-2013-16	-	-	-	-	-	-	40	-	-	-	-	-	-	-	-	-	-	-	-	-	-	-	-	-	-	-
ATLAS-SUSY-2013-18	-	278	7	-	-	-	-	-	-	-	-	-	-	-	-	-	-	-	-	-	-	-	-	-	-	-
ATLAS-SUSY-2013-19	-	-	-	-	-	-	5	0	-	-	-	-	-	-	0	0	-	-	-	-	-	-	-	-	-	-
ATLAS-SUSY-2013-23	-	-	-	-	-	-	-	-	-	-	-	-	-	-	-	-	-	-	0	-	-	-	-	-	-	-

Table D.1: Number of points from the Bino-like LSP dataset excluded by the ATLAS 8 TeV analyses implemented in the `SModelS` database v.1.1 (official UL results). If the search is not interpreted using the simplified model indicated, a dash is used.

Higgsino-like LSP

Analysis	**T1**	**T1bbbb**	**T1tttt**	**T1tttoff**	**T2**	**T2bb**	**T2tt**	**T2ttoff**	**T2bbWWoff**	**TGQ**	**T5tctc**	**T5WW**	**T5WWoff**	**T6ZZtt**	**T6bbWW**	**T6bbWWoff**	**T6WW**	**TChiWZ**	**TChiWH**	**TChiWW**	**TSlepSlep**	**TChiChipmStauL**	**TChipChimStauSnu**	**TChiChipmSlepL**	**TChiChipmStauL**	**TChipChimSlepSnu**
ATLAS-SUSY-2013-02	290	-	-	-	16364	-	-	-	-	0	0	0	0	-	-	-	7	-	-	-	-	-	-	-	-	-
ATLAS-SUSY-2013-04	-	-	30	-	-	-	-	-	-	-	-	-	-	-	-	-	-	-	-	-	-	-	-	-	-	-
ATLAS-SUSY-2013-05	-	-	-	-	-	560	-	-	-	-	-	-	-	-	0	1	-	-	-	-	-	-	-	-	-	-
ATLAS-SUSY-2013-08	-	-	-	-	-	-	-	-	-	-	-	-	-	0	-	-	-	-	-	-	-	-	-	-	-	-
ATLAS-SUSY-2013-09	-	-	47	-	-	-	-	-	-	-	-	-	-	-	-	-	-	-	-	-	-	-	-	-	-	-
ATLAS-SUSY-2013-11	-	-	-	-	-	-	-	-	-	-	-	-	-	-	-	-	-	0	-	0	115	-	-	-	-	0
ATLAS-SUSY-2013-12	-	-	-	-	-	-	-	-	-	-	-	-	-	-	-	-	-	0	0	-	-	0	-	0	0	-
ATLAS-SUSY-2013-14	-	-	-	-	-	-	-	-	-	-	-	-	-	-	-	-	-	-	-	-	-	0	0	-	0	-
ATLAS-SUSY-2013-15	-	-	-	-	-	-	281	0	-	-	-	-	-	-	0	0	-	-	-	-	-	-	-	-	-	-
ATLAS-SUSY-2013-16	-	-	-	-	-	-	313	-	-	-	-	-	-	-	-	-	-	-	-	-	-	-	-	-	-	-
ATLAS-SUSY-2013-18	-	2270	518	-	-	-	-	-	-	-	-	-	-	-	-	-	-	-	-	-	-	-	-	-	-	-
ATLAS-SUSY-2013-19	-	-	-	-	-	-	68	0	-	-	-	-	-	-	0	0	-	-	-	-	-	-	-	-	-	-
ATLAS-SUSY-2013-23	-	-	-	-	-	-	-	-	-	-	-	-	-	-	-	-	-	-	0	-	-	-	-	-	-	-

Table D.2: Number of points from the Higgsino-like LSP dataset excluded by the ATLAS 8 TeV analyses implemented in the `SModelS` database v.1.1 (official UL results). If the search is not interpreted using the simplified model indicated, a dash is used.

Bino-like LSP

ANALYSIS	T1	**T1bbbb**	**T1tttt**	**T1ttttoff**	**T2**	**T2bb**	**T2tt**	**T2ttoff**	**T2bbWWoff**	**T5tttt**	**T6bbWW**	**T6bbWWoff**	**TChiWZ**	**TChiWH**	**TSlepSlep**	**TChipChimSlepStau**	**TChipChimSlepL**
CMS-SUS-12-024	-	0	1	0	-	-	-	-	-	-	-	-	-	-	-	-	-
CMS-SUS-12-028	1064	379	0	-	4139	308	0	-	-	-	-	-	-	-	-	-	-
CMS-PAS-SUS-13-015	-	-	-	-	-	-	0	0	-	-	-	-	-	-	-	-	-
CMS-PAS-SUS-13-016	-	-	1	0	-	-	-	-	-	-	-	-	-	-	-	-	-
CMS-PAS-SUS-13-018	-	-	-	-	-	852	-	-	-	-	-	-	-	-	-	-	-
CMS-PAS-SUS-13-023	-	-	-	-	-	-	155	0	-	-	0	0	-	-	-	-	-
CMS-SUS-13-002	-	-	3	-	-	-	-	-	-	-	-	-	-	-	-	-	-
CMS-SUS-13-004	-	354	3	0	-	-	96	0	-	-	-	-	-	-	-	-	-
CMS-SUS-13-006	-	-	-	-	-	-	-	-	-	-	-	-	0	0	46	0	0
CMS-SUS-13-007	-	-	7	0	-	-	-	-	-	2	-	-	-	-	-	-	-
CMS-SUS-13-011	-	-	-	-	-	-	45	0	-	-	10	0	-	-	-	-	-
CMS-SUS-13-012	2172	-	3	0	4381	-	-	-	-	-	-	-	-	-	-	-	-
CMS-SUS-13-013	-	-	-	-	-	-	0	0	-	-	0	0	-	-	-	-	-
CMS-SUS-13-019	2101	535	3	0	9979	529	7	0	-	-	-	-	-	-	-	-	-
CMS-SUS-14-010	-	-	8	0	-	-	-	-	-	-	-	-	-	-	-	-	-
CMS-SUS-14-021	-	-	-	-	-	-	-	0	0	-	-	-	-	-	-	-	-

TABLE D.3: Number of points from the Bino-like LSP dataset excluded by the CMS 8 TeV analyses implemented in the `SModelS` database v.1.1 (official UL results). If the search is not interpreted using the simplified model indicated, a dash is used.

Higgsino-like LSP

ANALYSIS	T1	**T1bbbb**	**T1tttt**	**T1ttttoff**	**T2**	**T2bb**	**T2tt**	**T2ttoff**	**T2bbWW**	**T5tttt**	**T6bbWW**	**T6bbWWoff**	**TChiWZ**	**TChiWH**	**TSlepSlep**	**TChipChimSlepStau**	**TChipChimSlepL**
CMS-SUS-12-024	-	0	0	0	-	-	-	-	-	-	-	-	-	-	-	-	-
CMS-SUS-12-028	200	2445	0	-	9299	179	0	-	-	-	-	-	-	-	-	-	-
CMS-PAS-SUS-13-015	-	-	-	-	-	-	0	0	-	-	-	-	-	-	-	-	-
CMS-PAS-SUS-13-016	-	-	0	0	-	-	-	-	-	-	-	-	-	-	-	-	-
CMS-PAS-SUS-13-018	-	-	-	-	-	1130	-	-	-	-	-	-	-	-	-	-	-
CMS-PAS-SUS-13-023	-	-	-	-	-	-	728	0	-	-	0	0	-	-	-	-	-
CMS-SUS-13-002	-	-	8	-	-	-	-	-	-	-	-	-	-	-	-	-	-
CMS-SUS-13-004	-	2518	0	0	-	-	556	0	-	-	-	-	-	-	-	-	-
CMS-SUS-13-006	-	-	-	-	-	-	-	-	-	-	-	-	0	0	1	0	0
CMS-SUS-13-007	-	-	358	0	-	-	-	-	-	6	-	-	-	-	-	-	-
CMS-SUS-13-011	-	-	-	-	-	-	311	0	-	-	0	0	-	-	-	-	-
CMS-SUS-13-012	242	-	1	0	9739	-	-	-	-	-	-	-	-	-	-	-	-
CMS-SUS-13-013	-	-	-	-	-	-	0	0	-	-	0	0	-	-	-	-	-
CMS-SUS-13-019	236	3313	13	0	17799	655	23	0	-	-	-	-	-	-	-	-	-
CMS-SUS-14-010	-	-	478	0	-	-	-	-	-	-	-	-	-	-	-	-	-
CMS-SUS-14-021	-	-	-	-	-	-	-	0	0	-	-	-	-	-	-	-	-

TABLE D.4: Number of points from the Higgsino-like LSP dataset excluded by the CMS 8 TeV analyses implemented in the `SModelS` database v.1.1 (official UL results). If the search is not interpreted using the simplified model indicated, a dash is used.

Appendix E

T3GQon vs T3GonQ UL Comparison

Comparison of the UL (expected and observed) for the T3GQon and T3GonQ for the mass point $(m_1, m_2, m_{\tilde{\chi}_1^0}) = (1000, 200, 190)$ [GeV], in the case of the ATLAS-SUSY-2013-02 and CMS-SUS-13-012 analyses. In bold font the observed limits calculated by `SModelS` are shown.

ATLAS-SUSY-2013-02			**T3GonQ**			**T3GQon**		
Signal Region	UL_{exp}	UL_{obs}	ϵ	UL_{exp}/ϵ	UL_{obs}/ϵ	ϵ	UL_{exp}/ϵ	UL_{obs}/ϵ
2jm	5.552	4.242	0.118	47.1	**36.0**	0.090	61.5	47.0
2jt	1.512	1.818	0.032	47.9	57.5	0.027	56.1	**67.4**
3j	0.332	0.433	0.002	139.4	182.2	0.002	186.4	243.6
4jl	5.435	4.749	0.032	171.4	149.8	0.039	139.7	122.1
4jl-	11.561	13.292	0.036	318.7	366.4	0.047	248.0	285.2
4jt	0.240	0.149	0.002	146.1	90.8	0.001	178.1	110.8
5j	1.714	1.543	0.007	245.1	220.7	0.010	172.9	155.6
6jl	1.531	1.923	0.002	965.5	1212.5	0.003	555.5	697.7
6jt	0.333	0.332	0.001	472.8	470.4	0.001	327.8	326.2
6jt+	0.302	0.399	0.001	428.6	566.3	0.001	297.2	392.7

CMS-SUS-13-02			**T3GonQ**			**T3GQon**		
Signal Region	UL_{exp}	UL_{obs}	ϵ	UL_{exp}/ϵ	UL_{obs}/ϵ	ϵ	UL_{exp}/ϵ	UL_{obs}/ϵ
$n_j[3,5]$,$H_T[500,800]$,$\not{H}_T[300,450]$	27.2	28.1	0.045	599.4	619.2	0.063	430.0	444.2
$n_j[3,5]$,$H_T[500,800]$,$\not{H}_T[450,600]$	6.9	8.3	0.038	179.6	214.7	0.039	179.9	215.1
$n_j[3,5]$,$H_T[500,800]$,$\not{H}_T \geq 600$	1.4	1.6	0.009	153.7	175.7	0.006	234.8	268.4
$n_j[3,5]$,$H_T[800,1000]$,$\not{H}_T[300,450]$	4.4	3.7	0.009	465.8	383.3	0.012	385.4	317.1
$n_j[3,5]$,$H_T[800,1000]$,$\not{H}_T[450,600]$	1.8	2.5	0.012	153.1	207.7	0.012	160.8	218.1
$n_j[3,5]$,$H_T[800,1000]$,$\not{H}_T \geq 600$	1.2	1.2	0.014	87.7	**82.8**	0.009	132.4	124.9
$n_j[3,5]$,$H_T[1000,1250]$,$\not{H}_T[300,450]$	2.3	2.1	0.004	543.8	482.1	0.006	409.9	363.4
$n_j[3,5]$,$H_T[1000,1250]$,$\not{H}_T[450,600]$	0.9	0.9	0.004	210.6	230.0	0.006	156.1	170.4
$n_j[3,5]$,$H_T[1000,1250]$,$\not{H}_T \geq 600$	0.7	1.2	0.008	89.3	145.5	0.008	89.6	**145.9**
$n_j[3,5]$,$H_T[1250,1500]$,$\not{H}_T[300,450]$	1.2	1.0	0.001	873.4	769.8	0.002	569.5	501.9
$n_j[3,5]$,$H_T[1250,1500]$,$\not{H}_T \geq 450$	0.6	0.9	0.004	144.1	207.2	0.005	129.4	186.0
$n_j[3,5]$,$H_T \geq 1500$,$\not{H}_T \geq 300$	0.8	1.3	0.002	391.3	601.6	0.004	217.8	334.9
$n_j[6,7]$,$H_T[500,800]$,$\not{H}_T \geq 450$	0.15	0.697	0.0003	586.4	2637.2	0.0003	566.3	2546.5
$n_j[6,7]$,$H_T[800,1000]$,$\not{H}_T \geq 450$	0.42	0.333	0.0007	580.2	453.5	0.0009	484.3	378.5
$n_j[6,7]$,$H_T[1000,1250]$,$\not{H}_T \geq 450$	0.26	0.377	0.0007	360.9	513.5	0.001	265.8	378.1
$n_j[6,7]$,$H_T[1250,1500]$,$\not{H}_T \geq 450$	0.15	0.274	0.0006	262.1	466.5	0.001	207.3	368.8
$n_j[6,7]$,$H_T \geq 1500$,$\not{H}_T \geq 300$	0.46	0.284	0.0008	559.4	345.4	0.0008	588.3	363.2

Appendix F

Parametrization of the TChipChimSLepSnu Model

In this Appendix the parametrization of the *TChipChimSlepSnu* model is discussed. It corresponds to an electroweak production of charginos, that decay to the LSP via intermediate sleptons or sneutrinos, with 50 % probability:

$$pp \to \tilde{\chi}_1^+\tilde{\chi}_1^- \quad \tilde{\chi}_1^\pm \to l^\pm\tilde{\nu}_l/\nu_l\tilde{l}^\pm, \tilde{\nu}_l \to \nu_l\tilde{\chi}_1^0 \ /\tilde{l}^\pm \to l^\pm\tilde{\chi}_1^0.$$

This produces di-leptonic opposite-sign events and missing $\not{E}_T^{miss}$, coming from both SM neutrinos and neutralinos. In this case the missing transverse energy originates from the LSP and also from the two SM neutrinos appearing in the decay chain. As opposite to the *T5WW* model considered in the discussion in Chapter 6, this model has a symmetric structure of the SM particles in the vertices, and for this reason a somewhat symmetric behaviour of the efficiencies wrt to the x=0.50 parametrization is expected. Concretely this means that efficiencies for the values x=0.25 and x=0.50 should be comparable, for all the SRs. Small differences might come from the initial boost of the pair produced charginos.

Similarly to what was done for the hadronic model, the results for the efficiencies and limits of the analysis ATLAS-SUSY-2013-11[50] are presented, using the available implementation in `MadAnalysis 5` (code available at [183] and validation note at [184]). This analysis is designed to search for electroweak production of sparticles (sleptons and electroweakinos) in the di-leptonic channel. The key kinematic variables of the analysis are the invariant mass of the dilepton system m_{ll}, and the 'stranverse mass' m_{T_2}. This quantity is defined as:

$$m_{T2} = min_{\mathbf{q}_T}[max(m_T(\mathbf{p}_T^{l_1}, \mathbf{q}_T), m_T(\mathbf{p}_T^{l_2}, \mathbf{p}_T^{miss} - \mathbf{q}_T))] \tag{F.1}$$

and

$$m_T(\mathbf{p}_T, \mathbf{q}_T) = \sqrt{2(p_T q_T - \mathbf{p}_T \cdot \mathbf{q}_T)}. \tag{F.2}$$

while $\mathbf{p}_T^{l_1}$ and $\mathbf{p}_T^{l_2}$ are the transverse momenta of the two signal leptons, and the vector $\mathbf{q}_T$ minimizes the transverse mass m_T.

The signal regions target either events with opposite sign 'same flavour' (SF) leptons, i.e. electrons or muons pairs, or events with opposite sign 'different flavour' (DF) leptons pairs. In total, seven signal regions are defined. The first three referred to as 'SR-m_{T_2}' are defined to be sensitive to direct slepton production; the next three 'SR-WW' are designed to be sensitive to charginos that decay to W-bosons ($pp \to \tilde{\chi}_1^+\tilde{\chi}_1^-, \tilde{\chi}_1^\pm \to W^\pm\tilde{\chi}_0^1$). The final region 'SR-Zjets' targets chargino-neutralino pair production, which decay to W and Z bosons respectively ($pp \to \tilde{\chi}_1^\pm\tilde{\chi}_2^0, \tilde{\chi}_1^\pm \to W^\pm\tilde{\chi}_0^1, \tilde{\chi}_2^0 \to Z\tilde{\chi}_0^1$). This last SR will not be discussed in this work. The total integrated luminosity of the data analysed

$(m_{\tilde{g}}, m_{\tilde{\chi}_1^0})$			$x = 0.05$	$x = 0.25$	$x = 0.50$	$x = 0.75$	$x = 0.95$
$(240, 100)$	$m_{\tilde{l}/\tilde{\nu}}$	$=$	107	135	170	205	233
$(420, 60)$	$m_{\tilde{l}/\tilde{\nu}}$	$=$	78	150	240	330	402
$(420, 200)$	$m_{\tilde{l}/\tilde{\nu}}$	$=$	211	255	310	365	409

TABLE F.1: $m_{\tilde{l}/\tilde{\nu}}$ values for the three benchmark points $(m_{\tilde{\chi}_1^{\pm}}, m_{\tilde{\chi}_1^0})$ [GeV], obtained with the five different values of the x parameter.

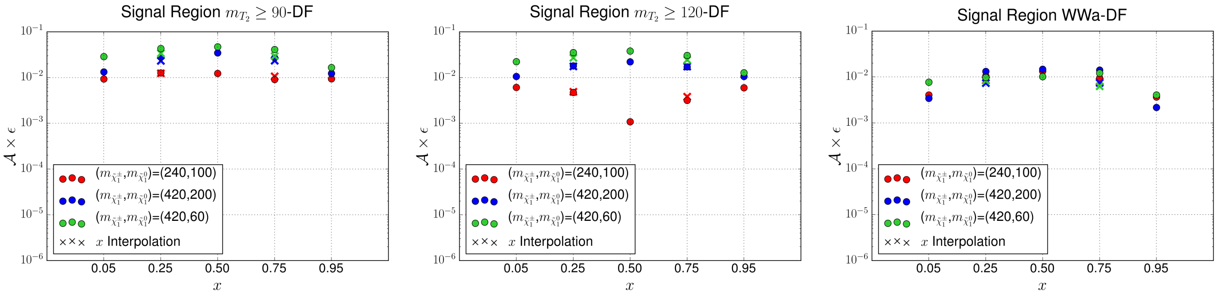

FIGURE F.1: Efficiency for the three mass points $(m_{\tilde{\chi}_1^{\pm}}, m_{\tilde{\chi}_1^0}) = (240{,}100),(420{,}60),(420{,}200)$ [GeV] for the selected $m_{T2} \geq 90$, $m_{T2} \geq 120$ and WWa SRs. The x parameter indicated on the x-axis is used to calculate the mass of the intermediate slepton/neutrino, as described in Tab. F.1. The full circles represent the recast values of the efficiencies, the crosses the values obtained with the `SModelS` interpolation between three mass planes parametrized with $x = (0.05, 0.50, 0.95)$.

is 20.3 fb^{-1}.

The comparison between interpolated and true recast efficiency values is shown in Fig F.1 for SRs labeled m_{T_2} and WW respectively, for different flavour leptons (events containing exactly one isolated electron and one isolated muon oppositely charged). Despite the latter being specifically designed to target the *TChiWW* SMS, they prove sensitive also in the cascade decays with intermediate sleptons/sneutrinos. The masses of the benchmark points are defined in Tab. F.1. The mass points $(240, 100)$ and $(420, 60)$ are excluded by the analysis when using the $x = 0.50$ parametrization of the intermediate particle, while the third point is not excluded with such parametrization. The efficiency values show a clear symmetry with respect to the $x = 0.50$ parameter, as intuitively discussed from considerations on the topology structure of the *TChipChimSlepSnu* model. This is reflected also in Fig. F.2 with the exclusion curves for the interpolated and recast efficiency values for the parameters $x = 0.25$ and $x = 0.75$ respectively. Not only the agreement seems in general better with respect to the hadronic model, but the comparison makes also evident that there is little difference in the exclusion and thus in the efficiency, and in the selection of the best SRs.

Overall the agreement between the recast and interpolated exclusion curves does not exceed 40 GeV in chargino mass, and the interpolated excluded values are more conservative than the recast ones, at least in the high chargino mass region.

Lastly the comparison between the exclusion curves obtained with the complete set of parameters $x = (0.05, 0.25, 0.5, 0.75, 0.95)$ is shown in Fig. F.3

Note that, as shown in the left plot, the highest reach in the chargino mass exclusion is obtained with the x=0.50 parametrization. However the analysis looses sensitivity for higher LSP mass in

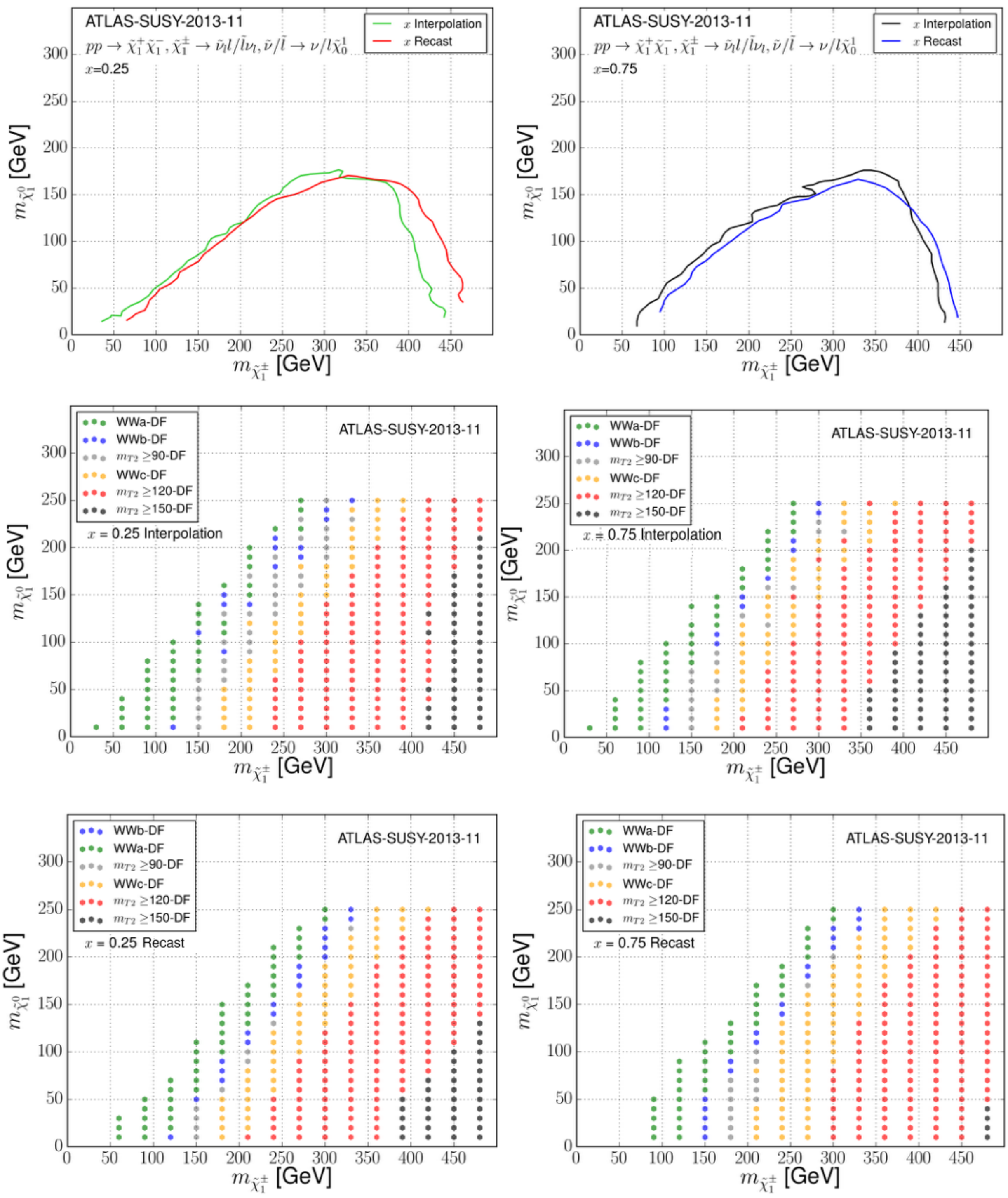

FIGURE F.2: Exclusion curves (top row) and Best SRs plots for the $x = 0.25$ parametrisation (left column) and $x = 0.75$ (right column). The middle panels show the Best SRs for the interpolated values, while the bottom panels refer to recast values.

the region $m_{\tilde{\chi}_1^\pm} \leq 300$ GeV, where the parametrizations x=(0.05,0.95) can constrain LSPs about 40 GeV heavier. As expected the curves for x=(0.25,0.75) are essentially equivalent up to $m_{\tilde{\chi}_1^\pm} \approx$ 350 GeV, where the x=0.05 is more sensitive in the high chargino mass region.

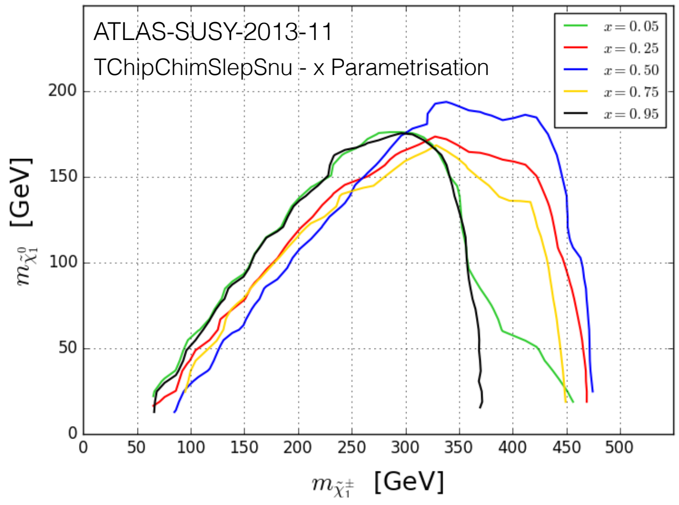

FIGURE F.3: Exclusion curves for the set of $x = (0.05, 0.25, 0.50, 0.75, 0.95)$ parameters.

Appendix G

Comparing the *T5WW*, *T5ZZ* and *T5VV* Models

As noted in Section 6.2.1, it is common for the CMS collaboration to interpret SUSY searches in the all-hadronic final state with a semi-simplified model $T5VV$:

$$pp \rightarrow \tilde{g}\tilde{g}\ , \tilde{g} \rightarrow qq'\chi_1^{\pm}/q\bar{q}\chi_2^0\ , \chi_1^{\pm} \rightarrow W^{(*)}\chi_1^0/\chi_2^0 \rightarrow Z^{(*)}\chi_1^0.$$

The gluino is allowed to decay to quarks and intermediate gauginos $\chi_1^{\pm}$ or χ_2^0 with equal probability. The analysis efficiency then corresponds to the effective combination of three distinct topologies, i.e. a model where both gluinos decay to a charginos (i.e. the $T5WW$ model), a model where both gluinos decay to neutralinos (i.e. the *T5ZZ* model), and a $T5WZ$ model where one gluino decays to a chargino and the other to a neutralino. It is however not clear if such $T5VV$ can be safely applied also in the case of pure $T5WW$ or *T5ZZ*, and I investigate this here. This test is useful for the implementation of such types of analyses in the `SModelS` database, since aslo results at $\sqrt{s}$=13 TeV are often interpreted with the same model, e.g. [76] .

In the top left panel of Fig. G.1 the exclusions curves and the best SR maps for the CMS-SUS-13-012 analysis are shown, and no significant difference can be noted. The curves are in fact compatible within 30 GeV mass difference in gluino or neutralino mass. Also the best SR maps (middle panels) are very similar, and localised differences for some points tested are expected due to Monte Carlo related uncertainties. The *T5ZZ* model seems to give slightly better limits, probably helped by the small difference in the branching fractions $BR(W \rightarrow \ hadrons = 67.41 \ \pm 0.27)\%$ and $BR(Z \rightarrow \ hadrons = 69.91 \ \pm 0.06)\%$. This analysis in fact does not reconstruct $b-jets$ so all the hadronic signal falls into the same SR.

Small differences are expected for analysis such as the ATLAS-SUSY-2013-04, since it divides SR according to $n_b = 0, 1, 2$ bins, with the addition of one inclusive SR with very high jet multiplicity and blind to b-jets multiplicity. The exclusion for the *T5ZZ* model is slightly lower with respect to the $T5WW$ and $T5VV$ model. Most likely this difference can be addressed to fewer events in the $n_b = 0$ best SR, since events where the decay $Z \rightarrow b\bar{b}$ takes place fall in other SRs with $n_b > 0$.

Finally, in Figure G.2 the distributions of the main kinematic variables H_T ,$\not{H}_T$and $n_{jet}$are shown for two selected points $(m_{\tilde{g}}, m_{\tilde{\chi}_2^0/\tilde{\chi}_1^{\pm}}, m_{\tilde{\chi}_1^0}) = (840, 570, 300)$ GeV and $(m_{\tilde{g}}, m_{\tilde{\chi}_2^0/\tilde{\chi}_1^{\pm}}, m_{\tilde{\chi}_1^0}) = (1080, 615, 150)$ GeV. The comparison confirms that such distributions are essentially the same for the three models tested, and any search based those is expected to provide similar efficiencies and limits for the three models.

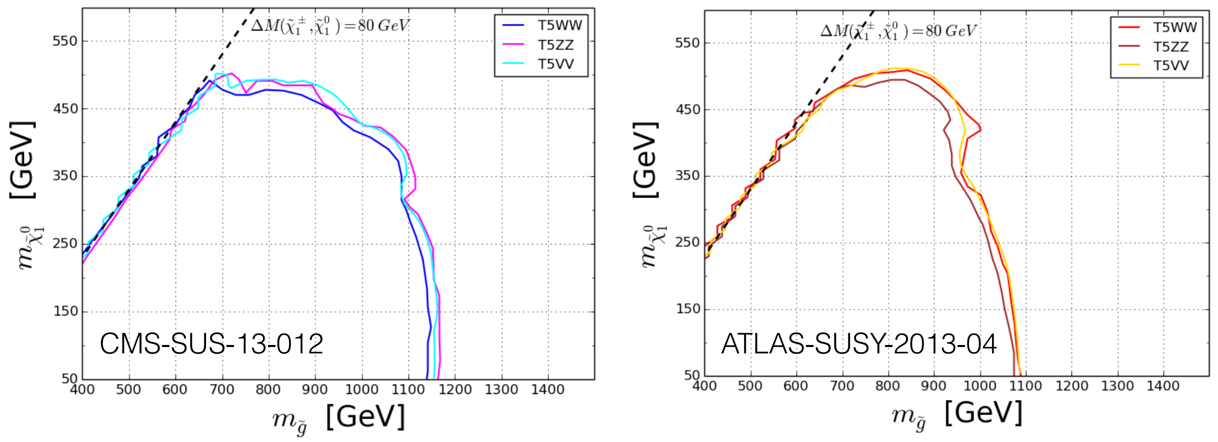

FIGURE G.1: Comparison of the exclusion curves for the *T5WW*, *T5ZZ* and *T5VV* SMS, parametrized with $x = 0.50$. Left panel: CMS-SUS-13-012, right panel: ATLAS-SUSY-2013-04.

It can be concluded that, for multijet final state searches, the two models have very similar characteristics, and the UL computation leads to comparable exclusion for the three models, with less than 30 *GeV* difference in the gluino mass reach of the exclusion.

These considerations apply also to general inclusive all-hadronic final state analyses blind to b-tagged jets, for models such as *T6bbWW*/*T6bbZZ*/*T6bbVV*, or any 1-step cascade model that include an intermediate chargino/neutralino.

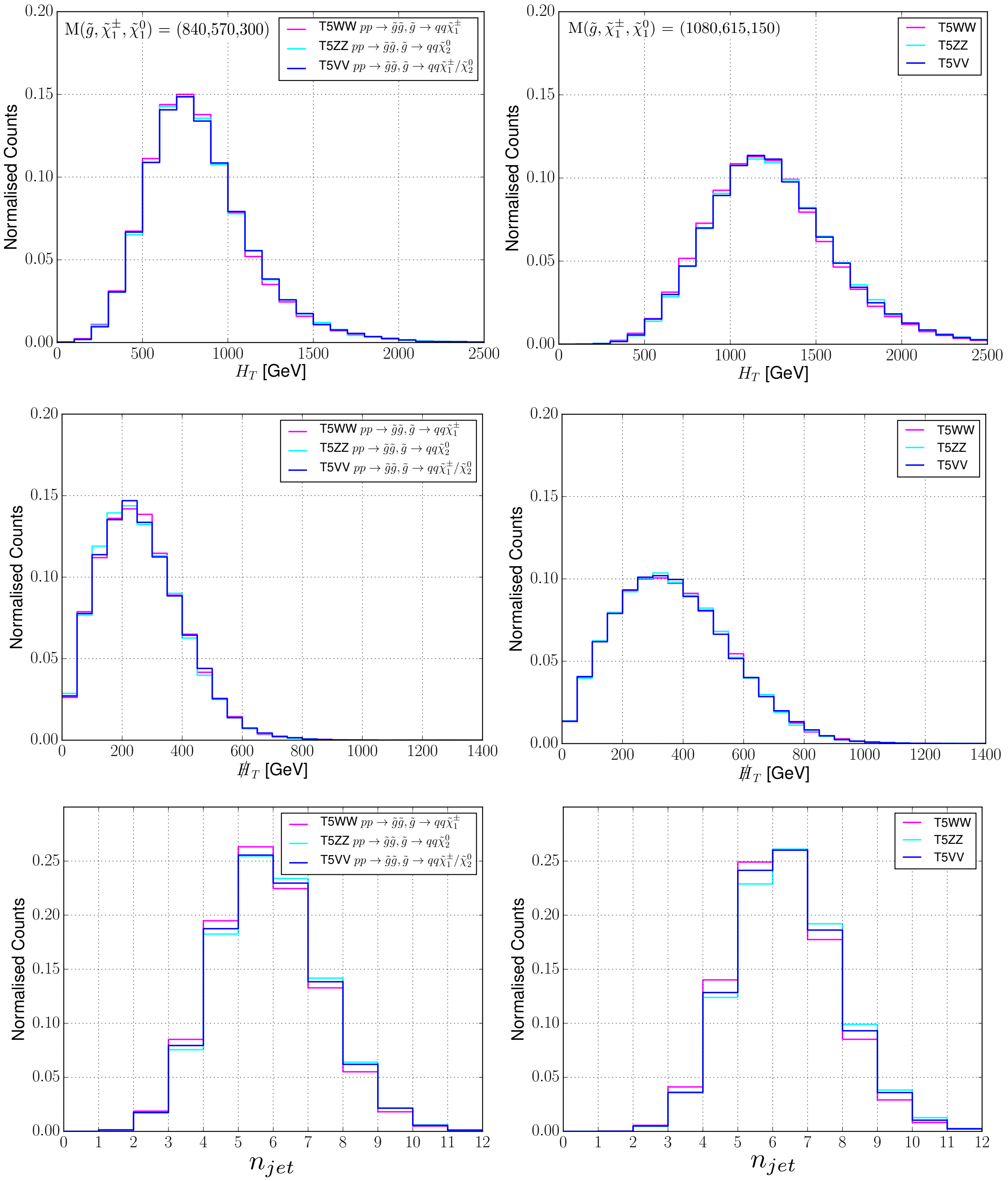

FIGURE G.2: From top to bottom: H_T, $\not{H}_T$and n_{jet} distributions for the *T5WW*, *T5ZZ* and *T5VV* models for CMS-SUS-13-012. Left column shows the mass point $(m_{\tilde{g}}, m_{\tilde{\chi}_2^0/\tilde{\chi}_1^{\pm}}, m_{\tilde{\chi}_1^0}) = (840, 570, 300)$, and the right column shows the point $(m_{\tilde{g}}, m_{\tilde{\chi}_2^0/\tilde{\chi}_1^{\pm}}, m_{\tilde{\chi}_1^0}) = (1080, 615, 150) GeV$.

Appendix H

Electroweak Corrections on CR Spectra

The following plots compare the spectra obtained with and without the electroweak corrections (emission of real on-shell W and Z bosons) in `Pythia 8` partly implemented by the PPPC4DMID collaboration, for different DM mass m_χ= (1,10,50,100) TeV. As can be seen, the contribution of the EW bosons alters significantly the spectra, that increase up to one order of magnitude in the case of emission from charged leptons.

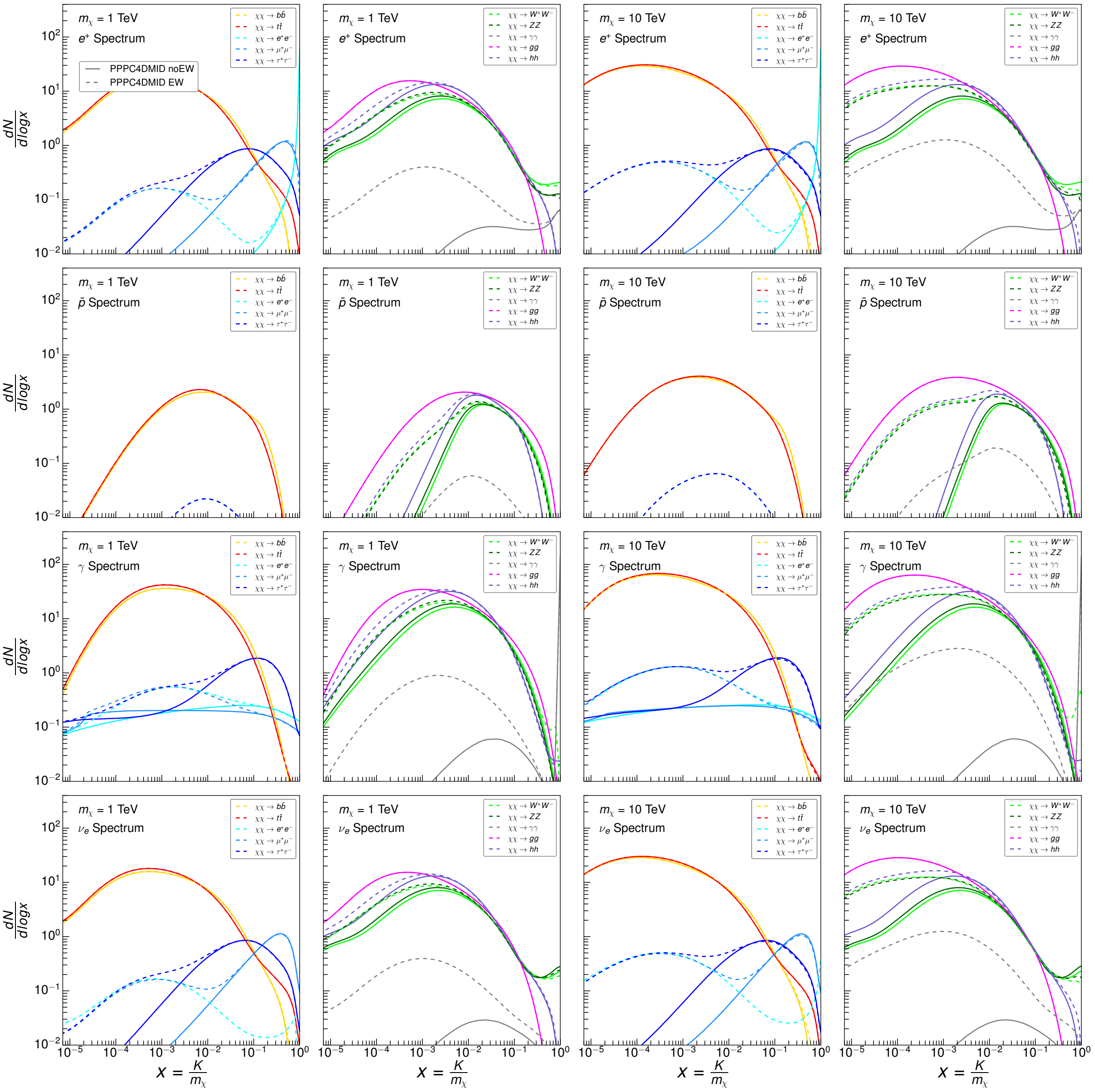

FIGURE H.1: Comparison of the energy spectra (dN/dlogx) at source as a function of x=E_{kin}/m_χ, for m_χ = (1 TeV, 10 TeV), with and without `Pythia 8` electroweak corrections.

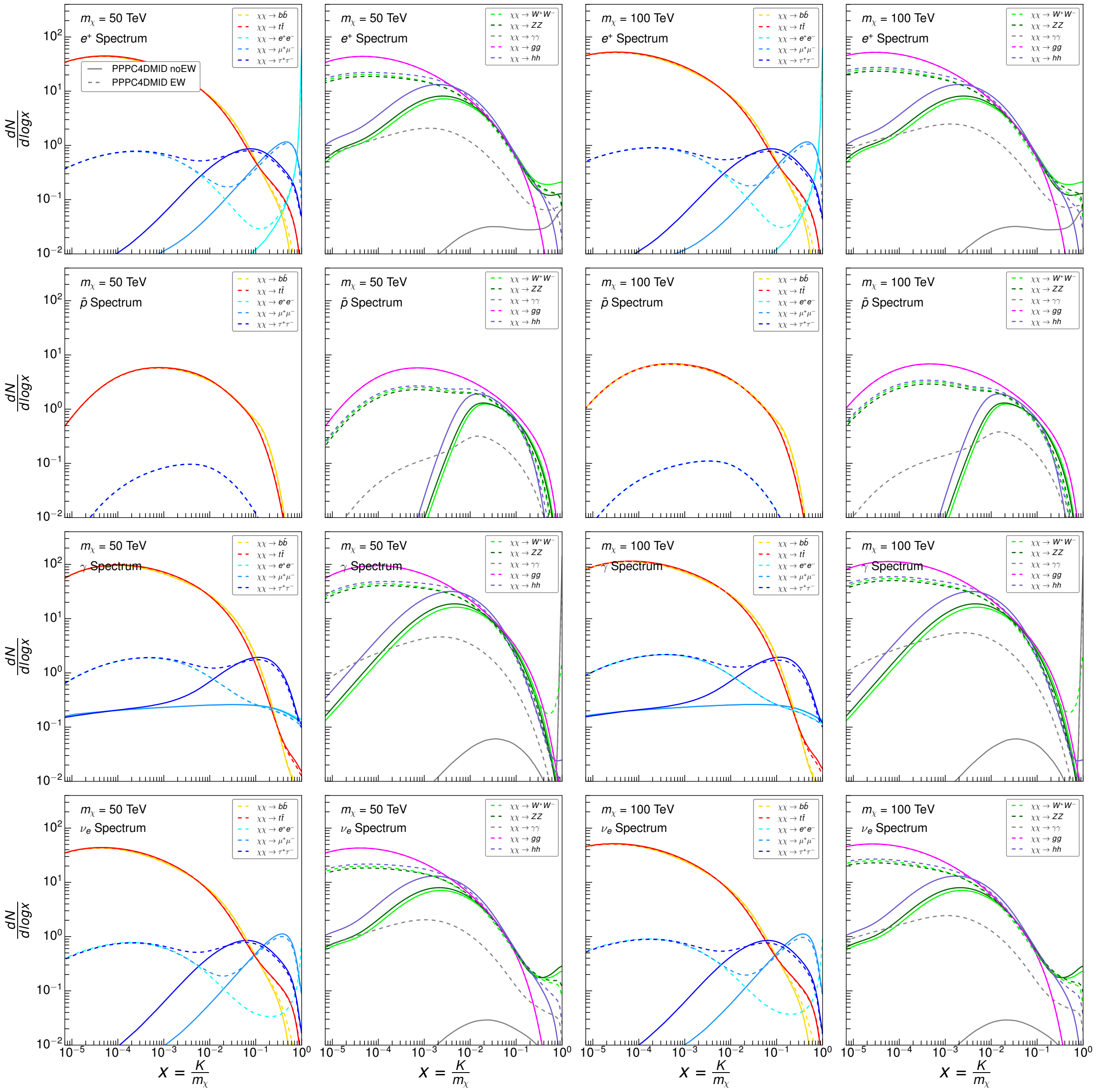

FIGURE H.2: Comparison of the energy spectra (dN/dlogx) at source as a function of x=E_{kin}/m_χ, for m_χ = (50 TeV, 100 TeV), with and without `Pythia 8` electroweak corrections.

Appendix I

Running a `MadDM` Scan

In `MadDM v.3.0`, the scanning over the parameter space of a model can be performed using two different methods. The user can choose to use the implemented module, which uses the experimental likelihoods of some observables, like the relic density or the annihilation cross section, to guide the scan through the parameter space. Alternatively, a simple feature inherited from `MG5_aMC` is the ability the perform sequential scan, or in other words, select a range of variation of some parameter, e.g. the mass of the DM candidate, as well as the binning of such variable, to scan over the selected parameter space. When considering n-variables, `MadDM v.3.0` creates a grid of equally space model points to run over. For details on the module, please refer to the official manual.
The commands to use the sequential grid scan functionality (in this case with the 'precision' method) are:

```
import model DMsimp_s_spin0_MD
define darkmatter ~xd
generate relic_density
add direct_detection
add indirect_detection
output test_y0y0_scalar
launch test_y0y0_scalar
indirect=flux_source
set sigmav_method reshuffling     # (default MadDM option)
set indirect_flux_source pythia8   # (default MadDM option)
set nevents 50000
set MXd scan:[100,200]
set MY0 100
```

The command *set MXd scan:[100,200]* tells `MadDM` to replace the values of the DM mass with 100 and 200 GeV. Very conveniently one can also use a python syntax like *set MXd scan:[100*x for x in range (1,11)]* to select DM mass in the range 100GeV - 1TeV , spaced by 100 GeV, according to the usual python syntax for lists. Likewise a scan on the coupling constants can be performed.

At the end of the run over the two different DM masses, in the 'output' folder inside the project directory 'test_y0y0_scalar' the file *scan_ run_ 01.txt* contains the summary of the results:

```
# [01] : run
# [02] : mass#52
# [03] : Omegah^2
# [04] : x_f
# [05] : sigmav(xf)
# [06] : xsi
# [07] : sigmaN_SI_p
# [08] : lim_sigmaN_SI_p
# [09] : sigmaN_SI_n
# [10] : lim_sigmaN_SI_n
# [11] : sigmaN_SD_p
```

```
# [12] : lim_sigmaN_SD_p
# [13] : sigmaN_SD_n
# [14] : lim_sigmaN_SD_n
# [15] : Nevents
# [16] : smearing
# [17] : xxdxxdb_ccx
# [18] : lim_xxdxxdb_ccx
# [19] : xxdxxdb_ddx
# [20] : lim_xxdxxdb_ddx
# [21] : xxdxxdb_uux
# [22] : lim_xxdxxdb_uux
# [23] : xxdxxdb_bbx
# [24] : lim_xxdxxdb_bbx
# [25] : xxdxxdb_xxcxxcb
# [26] : lim_xxdxxdb_xxcxxcb
# [27] : xxdxxdb_ssx
# [28] : lim_xxdxxdb_ssx
# [29] : xxdxxdb_ttx
# [30] : lim_xxdxxdb_ttx
# [31] : xxdxxdb_xxrxxr
# [32] : lim_xxdxxdb_xxrxxr
# [33] : xxdxxdb_y0y0
# [34] : lim_xxdxxdb_y0y0
# [35] : tot_Xsec
# [36] : tot_SM_xsec
# [37] : Fermi_sigmav
# [38] : pvalue_th
# [39] : like_th
# [40] : pvalue_nonth
# [41] : like_nonth
# [42] : flux_gammas
# [43] : flux_neutrinos_e
# [44] : flux_neutrinos_mu
# [45] : flux_neutrinos_tau

run_01_01     1.00e+02      6.65e-03      2.40e+01      4.31e-08      5.55e-02      3.24e-15
1.37e-46      3.28e-15      1.37e-46      5.16e-35      5.43e-41      5.14e-35      2.77e-41
0.00e+00      0.00e+00      4.02e-37      2.31e-26      6.34e-42      2.39e-26      1.62e-42
2.39e-26      5.49e-36      2.59e-26      0.00e+00      -1.00e+00     2.55e-39      2.39e-26
0.00e+00      1.00e-15      0.00e+00      -1.00e+00     1.45e-40      -1.00e+00     5.90e-36
-3.46e-05     5.05e-26      1.09e-06      -1.76e+01     1.97e-05      -1.76e+01     2.06e-21
6.60e-22      7.18e-22      6.46e-22

run_01_02     2.00e+02      1.93e-02      2.40e+01      1.17e-08      1.61e-01      3.27e-15
2.60e-46      3.31e-15      2.60e-46      0.00e+00      9.13e-41      0.00e+00      5.24e-41
0.00e+00      0.00e+00      7.89e-38      4.54e-26      1.24e-42      4.67e-26      3.18e-43
4.67e-26      1.08e-36      5.00e-26      0.00e+00      -1.00e+00     4.99e-40      4.67e-26
1.91e-34      6.08e-26      0.00e+00      -1.00e+00     3.05e-33      -1.00e+00     3.24e-33
-3.46e-05     4.76e-26      8.02e-05      -1.76e+01     4.98e-04      -1.76e+01     1.22e-17
1.59e-19      1.73e-19      1.55e-19 }
```

At the top of the file, a list of the variables appearing in the columns is provided. The variables are the same appearing as in the output text file for single point runs, with the addition of two statistical quantities related to the indirect detection, i.e. the likelihood and the p-value for the Fermi-LAT limits, provided in both the 'All DM' and 'Thermal' cases depending on the rescaling by $'\xi^2$ of $\langle\sigma v\rangle$.

Acknowledgements

Peu m'importe si tu m'aimes
Je me fous du monde entier

È. Piaf

Tu hai l'x factor
e non capisco perché voglia ostinarti
coi telescopi e le galassie

A Michele

Thanks, Danke, Merci, Grazie

Here I am at the toughest/easiest piece to write to complete this journey. I have been thinking about a nice metaphor to describe it, and I came up with 'rollercoaster' which I admit being quite mainstream but works quite well with its ups, downs, left and right turns and unexpected changes of direction.

Of course I must start by thanking Wolfgang for giving me the ticket for the ride, and for supervising that I was not getting stuck upside-down. I really appreciate the trust you had in me, and I am still surprised that you always keep calm and smile, danke and grazie for that! I am grateful to Prof. Hoang for accepting me as his student, and for helping me getting through my PhD with important advice.
I owe much to Suchita, who taught me a lot of what I needed for my work. I am also grateful to the other SModelS developers I had the fortune to collaborate with. André, thanks for your endless patience and for your clarity. Thank you Ursula, it was always a pleasure talking to you, you always had interesting point of views I had not considered before. Sabine, thanks for teaching me how to be meticulous and accurate, for all the time we spent discussing physics and not, and for the enjoyable trips to Grenoble. Jory, you gave me some very important support, and I was always amazed by the enthusiasm you put in everything we were doing! I also thank Benjamin Fuks and Dipan Sengupta for helping me with the many useful discussions regarding the MadAnalysis 5 code.

To all the other students at Wohllebengasse →Apostelgasse, huge thanks (short list: Daniel, Navid, Mateusz, Johannes, Lukas L. and S., all the master students, ...)! I enjoyed talking about our own struggles and then ending up having some good laughs and chocolate. I learned a lot from our endless discussions, probably much more than from anywhere else. To the CMS experimentalists: the passion you put in your work, your sleepless nights before the conferences, the thousands of hours spent listening to unbearable meetings, I think all of this makes you particle physics heroes. CERN is an amazing place because of you and your passionate dedication. Thanks to all the other colleagues of the HEPHY institute, that create such an enjoyable place to work at. And specially to our Director, Jochen Schieck. Je réserve un gross orange merci à Nathalie, pour ta gentilesse, tes sourires et t' aide fondamentale. Ilse, it is always a pleasure when you are around, with your overflowing positivity. A big thanks to Andreas Goudelis for the lots of friendly and smart advice.

I remember with joy my experience in Louvain-La-Neuve. I am grateful to Fabio for giving me the opportunity to spend 6 beautiful months at CP3, but most of all to Chiara: you patiently explained me so many new things and were always there to help. I really felt we were working together on our project and that I was part of the collaboration. Merci to Olivier, always ready to quickly fix my python bugs, and try to explain me how a developer should do his job. And of course to all the students and people working at CP3.

I want to give a special thank to CERN and its people. I do believe it is one of the most amazing places on Earth, and there is much more to learn there than just the most brilliant ideas in particle physics. Thank you Kati and Sezen, it was really a pleasure working with you there!

But nothing would have been possible without the support of my Family and Friends.
Let's start with the ones who were geographically closer. Razvan, you get the prize for best Viennese flatmate. Thanks for the teas, the cleanings, the Christmas parties, the hair cuts, the card games in which I suspect your were playing tricks, the translations and everything.
Ece Asylar, intentionally misspelled, big thanks. With time I understood how to deal with your creative chaos and the huge amount of positive energy you put in everything you do. And thanks for your comfortable couch!
Mamma e Papà, beh... Sono arrivato qui perché mi avete sempre spinto a essere determinato ed a scegliere la strada migliore che non sempre, anzi quasi mai, é quella facile. Davide Fratello, sorry ancora una volta: neanche in questa tesi parlo di buchi neri. Davide Patato, grazie per esserci sempre, per i consigli, per il supporto, per il sopporto e per contraddirmi quando serve. Cara famiglia, sapere che siete li' per me é la fortuna più grande e più importante. La dedica in francese é tutta per voi.
Mirka, come vedi ho finalmente finito la 'tesina' di dottorato! Attendo con estrema ansia il giorno in cui mi chiederai di spiegartela. Betta, grazie per aver condiviso l'esperienza del dottorato anche se a distanza, e soprattutto per aver adottato anni fa con me la filosofia del 'shitte kudasai'. Siamo ancora qui, dopo tanti anni! Amish, grazie per il supporto psicologico a distanza, e per le fondamentali consulenze di programmazione.

Finally, a global thank you to all the people who shared this exciting ride with me!

Bibliography

[1] F. Ambrogi and J. Sonneveld, *MadAnalysis 5 recast of CMS-SUS-16-033 doi:10.7484/INSPIREHEP.DATA.77YH.NBR3*, .

[2] F. Ambrogi, S. Kraml, S. Kulkarni, U. Laa, A. Lessa, V. Magerl, J. Sonneveld, M. Traub, and W. Waltenberger, *SModelS v1.1 user manual: Improving simplified model constraints with efficiency maps*, *Comput. Phys. Commun.* **227** (2018) 72–98, [arXiv:1701.06586].

[3] F. Ambrogi et al., *SModelS v1.2: long-lived particles, combination of signal regions, and other novelties*, arXiv:1811.10624.

[4] F. Ambrogi, S. Kraml, S. Kulkarni, U. Laa, A. Lessa, and W. Waltenberger, *On the coverage of the pMSSM by simplified model results*, *Eur. Phys. J.* **C78** (2018), no. 3 215, [arXiv:1707.09036].

[5] F. Ambrogi, C. Arina, M. Backovic, J. Heisig, F. Maltoni, L. Mantani, O. Mattelaer, and G. Mohlabeng, *MadDM v.3.0: a Comprehensive Tool for Dark Matter Studies*, arXiv:1804.00044.

[6] **Particle Data Group** Collaboration, M. T. et al. (Particle Data Group), *Review of particle physics*, *Phys. Rev. D* **98** (Aug, 2018) 030001.

[7] P. W. Higgs, *Broken symmetries and the masses of gauge bosons*, *Phys. Rev. Lett.* **13** (Oct, 1964) 508–509.

[8] F. Englert and R. Brout, *Broken symmetry and the mass of gauge vector mesons*, *Phys. Rev. Lett.* **13** (Aug, 1964) 321–323.

[9] G. S. Guralnik, C. R. Hagen, and T. W. B. Kibble, *Global conservation laws and massless particles*, *Phys. Rev. Lett.* **13** (Nov, 1964) 585–587.

[10] A. Djouadi, *The Anatomy of electro-weak symmetry breaking. I: The Higgs boson in the standard model*, *Phys. Rept.* **457** (2008) 1–216, [hep-ph/0503172].

[11] **ATLAS** Collaboration, G. Aad et al., *Observation of a new particle in the search for the Standard Model Higgs boson with the ATLAS detector at the LHC*, *Phys. Lett.* **B716** (2012) 1–29, [arXiv:1207.7214].

[12] **CMS** Collaboration, S. Chatrchyan et al., *Observation of a new boson at a mass of 125 GeV with the CMS experiment at the LHC*, *Phys. Lett.* **B716** (2012) 30–61, [arXiv:1207.7235].

[13] **Planck** Collaboration, P. A. R. Ade et al., *Planck 2015 results. XIII. Cosmological parameters*, *Astron. Astrophys.* **594** (2016) A13, [arXiv:1502.01589].

[14] R. Bernabei et al., *Searching for WIMPs by the annual modulation signature*, *Phys. Lett.* **B424** (1998) 195–201.

[15] I. Esteban, M. C. Gonzalez-Garcia, M. Maltoni, I. Martinez-Soler, and T. Schwetz, *Updated fit to three neutrino mixing: exploring the accelerator-reactor complementarity*, *JHEP* **01** (2017) 087, [arXiv:1611.01514].

[16] M. Lindner, T. Ohlsson, and G. Seidl, *Seesaw mechanisms for Dirac and Majorana neutrino masses*, *Phys. Rev.* **D65** (2002) 053014, [hep-ph/0109264].

[17] P. Fayet, *Supergauge invariant extension of the higgs mechanism and a model for the electron and its neutrino*, *Nuclear Physics B* **90** (1975) 104 – 124.

[18] P. Fayet, *Spontaneously broken supersymmetric theories of weak, electromagnetic and strong interactions*, *Physics Letters B* **69** (1977), no. 4 489 – 494.

[19] Y. Shirman, *Introduction to Supersymmetry and Supersymmetry Breaking*, in *Proceedings of Theoretical Advanced Study Institute in Elementary Particle Physics on The dawn of the LHC era (TASI 2008): Boulder, USA, June 2-27, 2008*, pp. 359–422, 2010. arXiv:0907.0039.

[20] S. P. Martin, *A Supersymmetry primer*, hep-ph/9709356. [Adv. Ser. Direct. High Energy Phys.18,1(1998)].

[21] R. K. Kaul, *Gauge hierarchy in a supersymmetric model*, *Physics Letters B* **109** (1982), no. 1 19 – 24.

[22] **Super-Kamiokande** Collaboration, H. Nishino et al., *Search for Proton Decay via p —> e+ pi0 and p —> mu+ pi0 in a Large Water Cherenkov Detector*, *Phys. Rev. Lett.* **102** (2009) 141801, [arXiv:0903.0676].

[23] D. Ghosh, M. Guchait, S. Raychaudhuri, and D. Sengupta, *How Constrained is the cMSSM?*, *Phys. Rev.* **D86** (2012) 055007, [arXiv:1205.2283].

[24] P. Bechtle et al., *Killing the cMSSM softly*, *Eur. Phys. J.* **C76** (2016), no. 2 96, [arXiv:1508.05951].

[25] C. Han, K.-i. Hikasa, L. Wu, J. M. Yang, and Y. Zhang, *Status of CMSSM in light of current LHC Run-2 and LUX data*, *Phys. Lett.* **B769** (2017) 470–476, [arXiv:1612.02296].

[26] **MSSM Working Group** Collaboration, A. Djouadi et al., *The Minimal supersymmetric standard model: Group summary report*, in *GDR (Groupement De Recherche) - Supersymetrie, Montpellier, France, April 15-17, 1998*. hep-ph/9901246.

[27] J. A. Casas, J. M. Moreno, S. Robles, K. Rolbiecki, and B. Zaldvar, *What is a Natural SUSY scenario?*, *JHEP* **06** (2015) 070, [arXiv:1407.6966].

[28] R. Barbieri and G. F. Giudice, *Upper bounds on supersymmetric particle masses*, *Nucl. Phys. B* **306** (Aug, 1987) 63–76. 19 p.

[29] https://twiki.cern.ch/twiki/pub/CMSPublic/PhysicsResultsSUS/barplot_Squark.png.

[30] https://atlas.web.cern.ch/Atlas/GROUPS/PHYSICS/CombinedSummaryPlots/SUSY/ATLAS_SUSY_Stop_tLSP/ATLAS_SUSY_Stop_tLSP.png.

[31] K. Schindl, *The injector chain for the LHC*, in *LEP performance. Proceedings, 9th Workshop, Chamonix, France, January 26-29, 1999*, pp. 47–52, 1999.

[32] L. Evans and P. Bryant, *LHC Machine*, *JINST* **3** (2008) S08001.

[33] G. Apollinari, I. Bjar Alonso, O. Brning, M. Lamont, and L. Rossi, *High-Luminosity Large Hadron Collider (HL-LHC) : Preliminary Design Report*, .

[34] **ATLAS** Collaboration, G. Aad et al., *The ATLAS Experiment at the CERN Large Hadron Collider*, *JINST* **3** (2008) S08003.

[35] **CMS** Collaboration, S. Chatrchyan et al., *The CMS Experiment at the CERN LHC*, *JINST* **3** (2008) S08004.

[36] **LHCb** Collaboration, A. A. Alves, Jr. et al., *The LHCb Detector at the LHC*, *JINST* **3** (2008) S08005.

[37] **ALICE** Collaboration, K. Aamodt et al., *The ALICE experiment at the CERN LHC*, *JINST* **3** (2008) S08002.

[38] **TOTEM** Collaboration, G. Anelli et al., *The TOTEM experiment at the CERN Large Hadron Collider*, *JINST* **3** (2008) S08007.

[39] **LHCf** Collaboration, O. Adriani et al., *The LHCf detector at the CERN Large Hadron Collider*, *JINST* **3** (2008) S08006.

[40] **CMS** Collaboration, S. Chatrchyan et al., *Description and performance of track and primary-vertex reconstruction with the CMS tracker*, *JINST* **9** (2014), no. 10 P10009, [`arXiv:1405.6569`].

[41] **CMS Collaboration** Collaboration, *The CMS electromagnetic calorimeter project: Technical Design Report*. Technical Design Report CMS. CERN, Geneva, 1997.

[42] **CMS Collaboration** Collaboration, *The CMS hadron calorimeter project: Technical Design Report*. Technical Design Report CMS. CERN, Geneva, 1997.

[43] T. C. collaboration, *The performance of the cms muon detector in proton-proton collisions at sqrt s = 7 tev at the lhc*, *Journal of Instrumentation* **8** (2013), no. 11 P11002.

[44] **CMS** Collaboration, V. Khachatryan et al., *The CMS trigger system*, *JINST* **12** (2017), no. 01 P01020, [`arXiv:1609.02366`].

[45] **ATLAS, CMS** Collaboration, D. Teyssier, *LHC results and prospects: Beyond Standard Model*, in *International Workshop on Future Linear Colliders (LCWS13) Tokyo, Japan, November 11-15, 2013*, 2014. `arXiv:1404.7311`.

[46] **CMS** Collaboration, S. Chatrchyan et al., *Interpretation of Searches for Supersymmetry with simplified Models*, *Phys. Rev.* **D88** (2013), no. 5 052017, [`arXiv:1301.2175`].

[47] J. Alwall, P. Schuster, and N. Toro, *Simplified Models for a First Characterization of New Physics at the LHC*, *Phys. Rev.* **D79** (2009) 075020, [`arXiv:0810.3921`].

[48] **LHC New Physics Working Group** Collaboration, D. Alves, *Simplified Models for LHC New Physics Searches*, *J. Phys.* **G39** (2012) 105005, [`arXiv:1105.2838`].

[49] **CMS** Collaboration, CMS collaboration, *Search for new physics in the multijet and missing transverse momentum final state in proton-proton collisions at $\sqrt{s} = 8$ TeV*, *JHEP* **06** (Feb, 2014) 055. 37 p.

[50] **ATLAS** Collaboration, G. Aad et al., *Search for direct production of charginos, neutralinos and sleptons in final states with two leptons and missing transverse momentum in pp collisions at $\sqrt{s} = 8$ TeV with the ATLAS detector*, *JHEP* **05** (2014) 071, [`arXiv:1403.5294`].

[51] **ATLAS** Collaboration, G. Aad et al., *Search for the electroweak production of supersymmetric particles in $\sqrt{s}$=8 TeV pp collisions with the ATLAS detector*, *Phys. Rev.* **D93** (2016), no. 5 052002, [`arXiv:1509.07152`].

[52] `https://twiki.cern.ch/twiki/bin/view/CMSPublic/SUSYSummary2017`.

[53] `https://twiki.cern.ch/twiki/bin/view/AtlasPublic/SupersymmetryPublicResultsRetired`.

[54] **CMS** Collaboration, A. M. Sirunyan et al., *Combined search for electroweak production of charginos and neutralinos in proton-proton collisions at* $\sqrt{s}$ *13 TeV*, *JHEP* **03** (2018) 160, [arXiv:1801.03957].

[55] M. Papucci, K. Sakurai, A. Weiler, and L. Zeune, *Fastlim: a fast LHC limit calculator*, *Eur. Phys. J.* **C74** (2014), no. 11 3163, [arXiv:1402.0492].

[56] D. Barducci, A. Belyaev, M. Buchkremer, J. Marrouche, S. Moretti, and L. Panizzi, *XQCAT: eXtra Quark Combined Analysis Tool*, *Comput. Phys. Commun.* **197** (2015) 263–275, [arXiv:1409.3116].

[57] S. Kraml, S. Kulkarni, U. Laa, A. Lessa, W. Magerl, D. Proschofsky-Spindler, and W. Waltenberger, *SModelS: a tool for interpreting simplified-model results from the LHC and its application to supersymmetry*, *Eur. Phys. J.* **C74** (2014) 2868, [arXiv:1312.4175].

[58] M. Drees, H. Dreiner, D. Schmeier, J. Tattersall, and J. S. Kim, *CheckMATE: Confronting your Favourite New Physics Model with LHC Data*, *Comput. Phys. Commun.* **187** (2015) 227–265, [arXiv:1312.2591].

[59] **GAMBIT** Collaboration, C. Balzs et al., *ColliderBit: a GAMBIT module for the calculation of high-energy collider observables and likelihoods*, *Eur. Phys. J.* **C77** (2017), no. 11 795, [arXiv:1705.07919].

[60] E. Conte, B. Dumont, B. Fuks, and C. Wymant, *Designing and recasting LHC analyses with MadAnalysis 5*, *Eur. Phys. J.* **C74** (2014), no. 10 3103, [arXiv:1405.3982].

[61] http://smodels.hephy.at/wiki/SmodelsTalks.

[62] **ATLAS, CMS** Collaboration, P. de Jong, *Supersymmetry searches at the LHC*, in *Proceedings, 32nd International Symposium on Physics in Collision (PIC 2012): Strbske Pleso, Slovakia, September 12-15, 2012*, pp. 241–254, 2012. arXiv:1211.3887.

[63] **DELPHES 3** Collaboration, J. de Favereau, C. Delaere, P. Demin, A. Giammanco, V. Lematre, A. Mertens, and M. Selvaggi, *DELPHES 3, A modular framework for fast simulation of a generic collider experiment*, *JHEP* **02** (2014) 057, [arXiv:1307.6346].

[64] B. Dumont, B. Fuks, S. Kraml, S. Bein, G. Chalons, E. Conte, S. Kulkarni, D. Sengupta, and C. Wymant, *Toward a public analysis database for LHC new physics searches using MADANALYSIS 5*, *Eur. Phys. J.* **C75** (2015), no. 2 56, [arXiv:1407.3278].

[65] J. Alwall, M. Herquet, F. Maltoni, O. Mattelaer, and T. Stelzer, *MadGraph 5 : Going Beyond*, *JHEP* **06** (2011) 128, [arXiv:1106.0522].

[66] T. Sjostrand, S. Ask, J. R. Christiansen, R. Corke, N. Desai, P. Ilten, S. Mrenna, S. Prestel, C. O. Rasmussen, and P. Z. Skands, *An Introduction to PYTHIA 8.2*, *Comput. Phys. Commun.* **191** (2015) 159–177, [arXiv:1410.3012].

[67] M. Bahr et al., *Herwig++ Physics and Manual*, *Eur. Phys. J.* **C58** (2008) 639–707, [arXiv:0803.0883].

[68] C. Degrande, C. Duhr, B. Fuks, D. Grellscheid, O. Mattelaer, and T. Reiter, *UFO - The Universal FeynRules Output*, *Comput. Phys. Commun.* **183** (2012) 1201–1214, [arXiv:1108.2040].

[69] M. Cacciari, G. P. Salam, and G. Soyez, *FastJet User Manual*, *Eur.Phys.J.* **C72** (2012) 1896, [arXiv:1111.6097].

[70] A. L. Read, *Presentation of search results: The CL(s) technique*, *J. Phys.* **G28** (2002) 2693–2704. [,11(2002)].

[71] T. Junk, *Confidence level computation for combining searches with small statistics*, *Nucl. Instrum. Meth.* **A434** (1999) 435–443, [`hep-ex/9902006`].

[72] `https://cds.cern.ch/record/2242860/`.

[73] `https://madanalysis.irmp.ucl.ac.be/wiki/PublicAnalysisDatabase`.

[74] `https://madanalysis.irmp.ucl.ac.be/raw-attachment/wiki/PublicAnalysisDatabase/ma5_atlas_1405_7875.pdf`.

[75] http://madanalysis.irmp.ucl.ac.be/raw-attachment/wiki/PublicAnalysisDatabase/ma5_validation_CMS-SUS-13-012.pdf.

[76] **CMS** Collaboration, A. M. Sirunyan et al., *Search for supersymmetry in multijet events with missing transverse momentum in proton-proton collisions at 13 TeV*, *Phys. Rev.* **D96** (2017), no. 3 032003, [`arXiv:1704.07781`].

[77] J. Alwall, R. Frederix, S. Frixione, V. Hirschi, F. Maltoni, O. Mattelaer, H. S. Shao, T. Stelzer, P. Torrielli, and M. Zaro, *The automated computation of tree-level and next-to-leading order differential cross sections, and their matching to parton shower simulations*, *JHEP* **07** (2014) 079, [`arXiv:1405.0301`].

[78] J. Alwall et al., *Comparative study of various algorithms for the merging of parton showers and matrix elements in hadronic collisions*, *Eur. Phys. J.* **C53** (2008) 473–500, [`arXiv:0706.2569`].

[79] S. Hoeche, F. Krauss, N. Lavesson, L. Lonnblad, M. Mangano, A. Schalicke, and S. Schumann, *Matching parton showers and matrix elements*, in *HERA and the LHC: A Workshop on the implications of HERA for LHC physics: Proceedings Part A*, pp. 288–289, 2005. `hep-ph/0602031`.

[80] M. Cacciari, G. P. Salam, and G. Soyez, *The Anti-k(t) jet clustering algorithm*, *JHEP* **0804** (2008) 063, [`arXiv:0802.1189`].

[81] `https://cds.cern.ch/record/2138504/files/BTV-15-001-pas.pdf`.

[82] `http://madanalysis.irmp.ucl.ac.be/raw-attachment/wiki/PublicAnalysisDatabase/ma5_validation_cms_sus_16_033.pdf`.

[83] S. Kraml, S. Kulkarni, U. Laa, A. Lessa, V. Magerl, W. Magerl, D. Proschofsky-Spindler, M. Traub, and W. Waltenberger, *SModelS v1.0: a short user guide*, `arXiv:1412.1745`.

[84] J. Dutta, S. Kraml, A. Lessa, and W. Waltenberger, *SModelS extension with the CMS supersymmetry search results from Run 2*, *LHEP* **1** (2018), no. 1 5–12, [`arXiv:1803.02204`].

[85] `http://smodels.hephy.at/wiki/SmsDictionary`.

[86] P. Z. Skands et al., *SUSY Les Houches accord: Interfacing SUSY spectrum calculators, decay packages, and event generators*, *JHEP* **07** (2004) 036, [`hep-ph/0311123`].

[87] J. Alwall et al., *A Standard format for Les Houches event files*, *Comput. Phys. Commun.* **176** (2007) 300–304, [`hep-ph/0609017`].

[88] T. Sjostrand, S. Mrenna, and P. Z. Skands, *PYTHIA 6.4 Physics and Manual*, *JHEP* **0605** (2006) 026, [`hep-ph/0603175`].

[89] `http://pauli.uni-muenster.de/~akule_01/nllwiki/index.php/NLL-fast`.

[90] W. Beenakker, R. Hopker, M. Spira, and P. Zerwas, *Squark and gluino production at hadron colliders*, *Nucl.Phys.* **B492** (1997) 51–103, [`hep-ph/9610490`].

[91] **ATLAS** Collaboration, G. Aad et al., *Search for squarks and gluinos with the ATLAS detector in final states with jets and missing transverse momentum using* $\sqrt{s} = 8$ *TeV proton–proton collision data*, *JHEP* **1409** (2014) 176, [arXiv:1405.7875].

[92] **ATLAS** Collaboration, G. Aad et al., *Search for new phenomena in final states with large jet multiplicities and missing transverse momentum at* $\sqrt{s} = 8$ *TeV proton-proton collisions using the ATLAS experiment*, *JHEP* **1310** (2013) 130, [arXiv:1308.1841].

[93] **ATLAS** Collaboration, G. Aad et al., *Search for supersymmetry at* $\sqrt{s}$*=8 TeV in final states with jets and two same-sign leptons or three leptons with the ATLAS detector*, *JHEP* **06** (2014) 035, [arXiv:1404.2500].

[94] **ATLAS** Collaboration, G. Aad et al., *Search for strong production of supersymmetric particles in final states with missing transverse momentum and at least three b-jets at* $\sqrt{s}$*= 8 TeV proton-proton collisions with the ATLAS detector*, *JHEP* **10** (2014) 024, [arXiv:1407.0600].

[95] **ATLAS** Collaboration, G. Aad et al., *Search for squarks and gluinos in events with isolated leptons, jets and missing transverse momentum at* $\sqrt{s} = 8$ *TeV with the ATLAS detector*, *JHEP* **04** (2015) 116, [arXiv:1501.03555].

[96] **ATLAS** Collaboration, G. Aad et al., *Search for direct third-generation squark pair production in final states with missing transverse momentum and two b-jets in* $\sqrt{s} =$ *8 TeV pp collisions with the ATLAS detector*, *JHEP* **1310** (2013) 189, [arXiv:1308.2631].

[97] **ATLAS** Collaboration, G. Aad et al., *Search for direct top squark pair production in events with a Z boson, b-jets and missing transverse momentum in sqrt(s)=8 TeV pp collisions with the ATLAS detector*, *Eur. Phys. J.* **C74** (2014), no. 6 2883, [arXiv:1403.5222].

[98] **ATLAS** Collaboration, G. Aad et al., *Search for top squark pair production in final states with one isolated lepton, jets, and missing transverse momentum in* $\sqrt{s}$ *=8 TeV pp collisions with the ATLAS detector*, *JHEP* **11** (2014) 118, [arXiv:1407.0583].

[99] **ATLAS** Collaboration, G. Aad et al., *Search for direct pair production of the top squark in all-hadronic final states in proton-proton collisions at* $\sqrt{s} = 8$ *TeV with the ATLAS detector*, *JHEP* **09** (2014) 015, [arXiv:1406.1122].

[100] **ATLAS** Collaboration, G. Aad et al., *Search for direct top-squark pair production in final states with two leptons in pp collisions at* $\sqrt{s} =$ *8TeV with the ATLAS detector*, *JHEP* **06** (2014) 124, [arXiv:1403.4853].

[101] **ATLAS** Collaboration, G. Aad et al., *Search for pair-produced third-generation squarks decaying via charm quarks or in compressed supersymmetric scenarios in pp collisions at* $\sqrt{s} = 8$ *TeV with the ATLAS detector*, *Phys. Rev.* **D90** (2014), no. 5 052008, [arXiv:1407.0608].

[102] **ATLAS** Collaboration, G. Aad et al., *Search for direct production of charginos and neutralinos in events with three leptons and missing transverse momentum in* $\sqrt{s} =$ *8TeV pp collisions with the ATLAS detector*, *JHEP* **1404** (2014) 169, [arXiv:1402.7029].

[103] **ATLAS** Collaboration, G. Aad et al., *Search for direct pair production of a chargino and a neutralino decaying to the 125 GeV Higgs boson in* $\sqrt{s} = 8$ *TeV pp collisions with the ATLAS detector*, *Eur. Phys. J.* **C75** (2015), no. 5 208, [arXiv:1501.07110].

[104] **CMS** Collaboration, CMS collaboration, *Search for supersymmetry in hadronic final states with missing transverse energy using the variables* α_T *and b-quark multiplicity in pp collisions at* $\sqrt{s}$ *= 8 TeV*, *Eur. Phys. J. C* **73** (Mar, 2013) 2568. 45 p.

[105] **CMS** Collaboration, CMS collaboration, *Search for gluino mediated bottom- and top-squark production in multijet final states in pp collisions at 8 TeV*, *Phys. Lett. B* **725** (May, 2013) 243–270. 39 p.

[106] **CMS** Collaboration, CMS collaboration, *Searches for supersymmetry using the* M_{T2} *variable in hadronic events produced in pp collisions at 8 TeV*, *JHEP* **05** (Feb, 2015) 078. 51 p.

[107] **CMS** Collaboration, CMS collaboration, *Search for supersymmetry using razor variables in events with b-tagged jets in pp collisions at* $\sqrt{s} = 8$ *TeV*, *Phys. Rev. D* **91** (Feb, 2015) 052018. 45 p.

[108] **CMS** Collaboration, *Search for Supersymmetry in pp collisions at 8 TeV in events with a single lepton, multiple jets and b-tags*, Tech. Rep. CMS-PAS-SUS-13-007, CERN, Geneva, Mar, 2013.

[109] **CMS** Collaboration, *Search for supersymmetry in pp collisions at sqrt(s) = 8 Tev in events with two opposite sign leptons, large number of jets, b-tagged jets, and large missing transverse energy.*, Tech. Rep. CMS-PAS-SUS-13-016, CERN, Geneva, 2013.

[110] **CMS** Collaboration, CMS collaboration, *Search for new physics in events with same-sign dileptons and jets in pp collisions at* $\sqrt{s}$*=8 TeV*, *JHEP* **01** (Nov, 2013) 163. 43 p.

[111] **CMS** Collaboration, CMS collaboration, *Searches for supersymmetry based on events with b jets and four W bosons in pp collisions at 8 TeV*, *Phys. Lett. B* **745** (Dec, 2014) 5. 35 p.

[112] **CMS** Collaboration, *Search for top squarks in multijet events with large missing momentum in proton-proton collisions at 8 TeV*, Tech. Rep. CMS-PAS-SUS-13-015, CERN, Geneva, 2013.

[113] **CMS** Collaboration, *A Search for Scalar Top Quark Production and Decay to All Hadronic Final States in pp Collisions at sqrt(s) = 8 TeV*, Tech. Rep. CMS-PAS-SUS-13-023, CERN, Geneva, 2015.

[114] **CMS** Collaboration, CMS collaboration, *Search for top-squark pair production in the single-lepton final state in pp collisions at* $\sqrt{s} = 8$ *TeV*, *Eur. Phys. J. C* **73** (Aug, 2013) 2677. 61 p.

[115] **CMS** Collaboration, *Search for direct production of bottom squark pairs*, Tech. Rep. CMS-PAS-SUS-13-018, CERN, Geneva, 2014.

[116] **CMS** Collaboration, CMS collaboration, *Search for supersymmetry in events with soft leptons, low jet multiplicity, and missing transverse energy in proton-proton collisions at* $\sqrt{s} = 8$ *TeV*, *Phys. Lett. B* **759** (Dec, 2015) 9–35. 40 p.

[117] **CMS** Collaboration, CMS collaboration, *Searches for electroweak production of charginos, neutralinos, and sleptons decaying to leptons and W, Z, and Higgs bosons in pp collisions at 8 TeV*, *Eur. Phys. J. C* **74** (May, 2014) 3036. 61 p.

[118] `http://fastlim.web.cern.ch/`.

[119] **ATLAS** Collaboration, *Search for squarks and gluinos with the ATLAS detector in final states with jets and missing transverse momentum and 20.3* fb^{-1} *of* $\sqrt{s} = 8$ *TeV proton-proton collision data*, Tech. Rep. ATLAS-CONF-2013-047, CERN, Geneva, May, 2013.

[120] **ATLAS** Collaboration, *Search for new phenomena using final states with large jet multiplicities and missing transverse momentum with ATLAS in 20* fb^{-1} *of* $\sqrt{s} = 8$ *TeV proton-proton collisions*, Tech. Rep. ATLAS-CONF-2013-054, CERN, Geneva, May, 2013.

[121] **ATLAS** Collaboration, *Search for squarks and gluinos in events with isolated leptons, jets and missing transverse momentum at* $\sqrt{s} = 8$ *TeV with the ATLAS detector*, Tech. Rep. ATLAS-CONF-2013-062, CERN, Geneva, Jun, 2013.

[122] **ATLAS** Collaboration, *Search for strong production of supersymmetric particles in final states with missing transverse momentum and at least three b-jets using 20.1 fb?1 of pp collisions at sqrt(s) = 8 TeV with the ATLAS Detector*, Tech. Rep. ATLAS-CONF-2013-061, CERN, Geneva, Jun, 2013.

[123] **ATLAS** Collaboration, *Search for direct production of the top squark in the all-hadronic ttbar + etmiss final state in 21 fb-1 of p-pcollisions at sqrt(s)=8 TeV with the ATLAS detector*, Tech. Rep. ATLAS-CONF-2013-024, CERN, Geneva, Mar, 2013.

[124] **ATLAS** Collaboration, *Search for direct top squark pair production in final states with one isolated lepton, jets, and missing transverse momentum in sqrts* $= 8,$*TeV pp collisions using 21* fb^{-1} *of ATLAS data*, Tech. Rep. ATLAS-CONF-2013-037, CERN, Geneva, Mar, 2013.

[125] **ATLAS** Collaboration, *Search for direct top squark pair production in final states with two leptons in* $\sqrt{s} = 8$ *TeV pp collisions using* $20fb^{-1}$ *of ATLAS data*, Tech. Rep. ATLAS-CONF-2013-048, CERN, Geneva, May, 2013. Not published in the proceedings.

[126] **ATLAS** Collaboration, *Search for direct third generation squark pair production in final states with missing transverse momentum and two b-jets in* $\sqrt{s} = 8$ *TeV pp collisions with the ATLAS detector*, Tech. Rep. ATLAS-CONF-2013-053, CERN, Geneva, May, 2013.

[127] **ATLAS** Collaboration, *Search for chargino and neutralino production in final states with one lepton, two b-jets consistent with a Higgs boson, and missing transverse momentum with the ATLAS detector in* 20.3 fb^{-1} *of* $\sqrt{s} = 8$ *TeV pp collisions*, Tech. Rep. ATLAS-CONF-2013-093, CERN, Geneva, Aug, 2013.

[128] **ATLAS** Collaboration, G. Aad et al., *Summary of the ATLAS experiment's sensitivity to supersymmetry after LHC Run 1 interpreted in the phenomenological MSSM*, *JHEP* **10** (2015) 134, [arXiv:1508.06608].

[129] **CMS** Collaboration, V. Khachatryan et al., *Phenomenological MSSM interpretation of CMS searches in pp collisions at sqrt(s) = 7 and 8 TeV*, *JHEP* **10** (2016) 129, [arXiv:1606.03577].

[130] http://hepdata.cedar.ac.uk/view/ins1389857.

[131] B. C. Allanach, *SOFTSUSY: a program for calculating supersymmetric spectra*, *Comput. Phys. Commun.* **143** (2002) 305–331, [hep-ph/0104145].

[132] A. Djouadi, M. M. Muhlleitner, and M. Spira, *Decays of supersymmetric particles: The Program SUSY-HIT (SUspect-SdecaY-Hdecay-InTerface)*, *Acta Phys. Polon.* **B38** (2007) 635–644, [hep-ph/0609292].

[133] J. Heisig, A. Lessa, and L. Quertenmont, *Simplified Models for Exotic BSM Searches*, *JHEP* **12** (2015) 087, [arXiv:1509.00473].

[134] A. Kulesza and L. Motyka, *Threshold resummation for squark-antisquark and gluino-pair production at the LHC*, *Phys.Rev.Lett.* **102** (2009) 111802, [arXiv:0807.2405].

[135] A. Kulesza and L. Motyka, *Soft gluon resummation for the production of gluino-gluino and squark-antisquark pairs at the LHC*, *Phys.Rev.* **D80** (2009) 095004, [arXiv:0905.4749].

[136] W. Beenakker, S. Brensing, M. Kramer, A. Kulesza, E. Laenen, et al., *Soft-gluon resummation for squark and gluino hadroproduction*, *JHEP* **0912** (2009) 041, [arXiv:0909.4418].

[137] W. Beenakker, S. Brensing, M. Kramer, A. Kulesza, E. Laenen, et al., *Squark and Gluino Hadroproduction*, *Int.J.Mod.Phys.* **A26** (2011) 2637–2664, [`arXiv:1105.1110`].

[138] W. Beenakker, M. Kramer, T. Plehn, M. Spira, and P. Zerwas, *Stop production at hadron colliders*, *Nucl.Phys.* **B515** (1998) 3–14, [`hep-ph/9710451`].

[139] W. Beenakker, S. Brensing, M. Kramer, A. Kulesza, E. Laenen, et al., *Supersymmetric top and bottom squark production at hadron colliders*, *JHEP* **1008** (2010) 098, [`arXiv:1006.4771`].

[140] G. Chalons and D. Sengupta, *Closing in on compressed gluino-neutralino spectra at the LHC*, *JHEP* **12** (2015) 129, [`arXiv:1508.06735`].

[141] S. Bein and D. Sengupta, *MadAnalysis 5 implementation of CMS-SUS-13-012*, .

[142] G. Chalons and D. Sengupta, *Madanalysis 5 implementation of the ATLAS multi jet analysis documented in arXiv:1405.7875, JHEP 1409 (2014) 176*, .

[143] **ATLAS** Collaboration, M. Aaboud et al., *Search for squarks and gluinos in final states with jets and missing transverse momentum using 36 fb^{-1} of $\sqrt{s} = 13$ TeV pp collision data with the ATLAS detector*, *Phys. Rev.* **D97** (2018), no. 11 112001, [`arXiv:1712.02332`].

[144] B. Fuks, M. Blanke, and I. Galon, *MadAnalysis5 implementation of ATLAS-SUSY-2013-04*, .

[145] `http://madanalysis.irmp.ucl.ac.be/raw-attachment/wiki/PublicAnalysisDatabase/GFV.pdf`.

[146] A. Buckley, *PySLHA: a Pythonic interface to SUSY Les Houches Accord data*, *Eur. Phys. J.* **C75** (2015), no. 10 467, [`arXiv:1305.4194`].

[147] J. M. Cline, Z. Liu, and W. Xue, *Millicharged Atomic Dark Matter*, *Phys. Rev.* **D85** (2012) 101302, [`arXiv:1201.4858`].

[148] F. Zwicky, *Die Rotverschiebung von extragalaktischen Nebeln*, *Helv. Phys. Acta* **6** (1933) 110–127. [Gen. Rel. Grav.41,207(2009)].

[149] M. Milgrom, *A Modification of the Newtonian dynamics as a possible alternative to the hidden mass hypothesis*, *Astrophys. J.* **270** (1983) 365–370.

[150] C. L. Bennett et al., *Cosmic temperature fluctuations from two years of COBE differential microwave radiometers observations*, *Astrophys. J.* **436** (1994) 423–442, [`astro-ph/9401012`].

[151] D. Clowe, M. Bradac, A. H. Gonzalez, M. Markevitch, S. W. Randall, C. Jones, and D. Zaritsky, *A direct empirical proof of the existence of dark matter*, *Astrophys. J.* **648** (2006) L109–L113, [`astro-ph/0608407`].

[152] G. Arcadi, M. Dutra, P. Ghosh, M. Lindner, Y. Mambrini, M. Pierre, S. Profumo, and F. S. Queiroz, *The waning of the WIMP? A review of models, searches, and constraints*, *Eur. Phys. J.* **C78** (2018), no. 3 203, [`arXiv:1703.07364`].

[153] J. F. Navarro, C. S. Frenk, and S. D. M. White, *A Universal Density Profile from Hierarchical Clustering*, *Astrophys. J.* **490** (1997) 493–508, [`astro-ph/9611107`].

[154] B. Moore, S. Ghigna, F. Governato, G. Lake, T. R. Quinn, J. Stadel, and P. Tozzi, *Dark matter substructure within galactic halos*, *Astrophys. J.* **524** (1999) L19–L22, [`astro-ph/9907411`].

[155] T. Marrodn Undagoitia and L. Rauch, *Dark matter direct-detection experiments*, *J. Phys.* **G43** (2016), no. 1 013001, [`arXiv:1509.08767`].

[156] **XENON** Collaboration, E. Aprile et al., *First Dark Matter Search Results from the XENON1T Experiment*, `arXiv:1705.06655`.

[157] **XENON** Collaboration, E. Aprile et al., *Dark Matter Search Results from a One Tonne× Year Exposure of XENON1T*, `arXiv:1805.12562`.

[158] M. Backovič, A. Martini, O. Mattelaer, K. Kong, and G. Mohlabeng, *Direct Detection of Dark Matter with MadDM v.2.0*, *Phys. Dark Univ.* **9-10** (2015) 37–50, [`arXiv:1505.04190`].

[159] **LUX** Collaboration, D. S. Akerib et al., *Limits on spin-dependent WIMP-nucleon cross section obtained from the complete LUX exposure*, *Phys. Rev. Lett.* **118** (2017), no. 25 251302, [`arXiv:1705.03380`].

[160] **PICO** Collaboration, C. Amole et al., *Dark Matter Search Results from the PICO-60 C_3F_8 Bubble Chamber*, *Phys. Rev. Lett.* **118** (2017), no. 25 251301, [`arXiv:1702.07666`].

[161] J. D. Simon, M. Geha, Q. E. Minor, G. D. Martinez, E. N. Kirby, J. S. Bullock, M. Kaplinghat, L. E. Strigari, B. Willman, P. I. Choi, E. J. Tollerud, and J. Wolf, *A Complete Spectroscopic Survey of the Milky Way Satellite Segue 1: The Darkest Galaxy*, **733** (May, 2011) 46, [`arXiv:1007.4198`].

[162] **Fermi-LAT** Collaboration, M. Ackermann et al., *Searching for Dark Matter Annihilation from Milky Way Dwarf Spheroidal Galaxies with Six Years of Fermi Large Area Telescope Data*, *Phys. Rev. Lett.* **115** (2015), no. 23 231301, [`arXiv:1503.02641`].

[163] G. Belanger, F. Boudjema, A. Pukhov, and A. Semenov, *MicrOMEGAs: A Program for calculating the relic density in the MSSM*, *Comput. Phys. Commun.* **149** (2002) 103–120, [`hep-ph/0112278`].

[164] P. Gondolo, J. Edsjo, P. Ullio, L. Bergstrom, M. Schelke, and E. A. Baltz, *DarkSUSY: Computing supersymmetric dark matter properties numerically*, *JCAP* **0407** (2004) 008, [`astro-ph/0406204`].

[165] **GAMBIT Dark Matter Workgroup** Collaboration, T. Bringmann et al., *DarkBit: A GAMBIT module for computing dark matter observables and likelihoods*, `arXiv:1705.07920`.

[166] M. Backovič, K. Kong, and M. McCaskey, *MadDM v.1.0: Computation of Dark Matter Relic Abundance Using MadGraph5*, *Physics of the Dark Universe* **5-6** (2014) 18–28, [`arXiv:1308.4955`].

[167] C. Evoli, D. Gaggero, D. Grasso, and L. Maccione, *Cosmic-Ray Nuclei, Antiprotons and Gamma-rays in the Galaxy: a New Diffusion Model*, *JCAP* **0810** (2008) 018, [`arXiv:0807.4730`]. [Erratum: JCAP1604,no.04,E01(2016)].

[168] B. Robertson and A. Zentner, *Dark Matter Annihilation Rates with Velocity-Dependent Annihilation Cross Sections*, *Phys. Rev.* **D79** (2009) 083525, [`arXiv:0902.0362`].

[169] F. Ferrer and D. R. Hunter, *The impact of the phase-space density on the indirect detection of dark matter*, *JCAP* **1309** (2013) 005, [`arXiv:1306.6586`].

[170] `http://www.marcocirelli.net/PPPC4DMID.html`.

[171] M. Cirelli, G. Corcella, A. Hektor, G. Hutsi, M. Kadastik, P. Panci, M. Raidal, F. Sala, and A. Strumia, *PPPC 4 DM ID: A Poor Particle Physicist Cookbook for Dark Matter Indirect Detection*, *JCAP* **1103** (2011) 051, [`arXiv:1012.4515`]. [Erratum: JCAP1210,E01(2012)].

[172] P. Ciafaloni, D. Comelli, A. Riotto, F. Sala, A. Strumia, and A. Urbano, *Weak Corrections are Relevant for Dark Matter Indirect Detection*, *JCAP* **1103** (2011) 019, [`arXiv:1009.0224`].

[173] `http://home.thep.lu.se/Pythia/pythia82html/WeakShowers.html`.

[174] **DES, Fermi-LAT** Collaboration, A. Albert et al., *Searching for Dark Matter Annihilation in Recently Discovered Milky Way Satellites with Fermi-LAT*, *Astrophys. J.* **834** (2017), no. 2 110, [`arXiv:1611.03184`].

[175] `https://www.glast.stanford.edu/pub_data/1203/`.

[176] A. Geringer-Sameth, S. M. Koushiappas, and M. Walker, *Dwarf galaxy annihilation and decay emission profiles for dark matter experiments*, *Astrophys. J.* **801** (2015), no. 2 74, [`arXiv:1408.0002`].

[177] A. Geringer-Sameth, M. G. Walker, S. M. Koushiappas, S. E. Koposov, V. Belokurov, G. Torrealba, and N. W. Evans, *Indication of Gamma-ray Emission from the Newly Discovered Dwarf Galaxy Reticulum II*, *Phys. Rev. Lett.* **115** (2015), no. 8 081101, [`arXiv:1503.02320`].

[178] D. Hooper and T. Linden, *On The Gamma-Ray Emission From Reticulum II and Other Dwarf Galaxies*, *JCAP* **1509** (2015), no. 09 016, [`arXiv:1503.06209`].

[179] G. Belanger, F. Boudjema, A. Pukhov, and A. Semenov, *Dark matter direct detection rate in a generic model with micrOMEGAs 2.2*, *Comput. Phys. Commun.* **180** (2009) 747–767, [`arXiv:0803.2360`].

[180] **GAMBIT** Collaboration, P. Athron et al., *GAMBIT: The Global and Modular Beyond-the-Standard-Model Inference Tool*, *Eur. Phys. J.* **C77** (2017), no. 11 784, [`arXiv:1705.07908`]. [Addendum: Eur. Phys. J.C78,no.2,98(2018)].

[181] P. Bechtle, S. Belkner, D. Dercks, M. Hamer, T. Keller, M. Krmer, B. Sarrazin, J. Schtte-Engel, and J. Tattersall, *SCYNet: Testing supersymmetric models at the LHC with neural networks*, *Eur. Phys. J.* **C77** (2017), no. 10 707, [`arXiv:1703.01309`].

[182] `http://smodels.readthedocs.io/en/latest/`.

[183] B. Dumont, "MadAnalysis 5 implementation of ATLAS-SUSY-2013-11: di-leptons plus MET." `http://doi.org/10.7484/INSPIREHEP.DATA.HLMR.T56W.2`.

[184] "MadAnalysis5 Public Analysis Database ATLAS-SUSY-2013-11 validation." `http://madanalysis.irmp.ucl.ac.be/raw-attachment/wiki/PublicAnalysisDatabase/ma5_validation_ATLAS-SUSY-2013-11_v2.pdf`.